



**ACOUSTIC TEST AND ANALYSIS
OF A
COUNTERROTATING PROP-FAN MODEL**

**By: Bernard Magliozzi
Paul Brown
David Parzych**

**HAMILTON STANDARD
UNITED TECHNOLOGIES CORPORATION**

October 1987

NASA

Prepared for

**National Aeronautics and Space Administration
NASA-Lewis Research Center
Cleveland, Ohio 44135**



FOREWORD

All of the testing reported here was conducted in the Acoustic Research Tunnel at the United Technologies Research Center. The authors wish to express their thanks for the support provided by the personnel of the United Technologies Research Center.

Special acknowledgement is extended to the McDonnell Douglas Corporation (DAC) for providing the pylon and nacelle used for Counterrotating Prop-Fan (CRP) pusher configuration testing and for providing microphone measurement and support equipment. Furthermore, DAC is gratefully acknowledged for consenting to include within the body of this report pusher CRP, zero degree angle-of-attack acoustic data and results acquired jointly under DAC and Hamilton Standard funding.



CONTENTS

<u>SECTION</u>	<u>PAGE</u>
FOREWORD	i
TABLE OF CONTENTS	iii
SUMMARY	1
INTRODUCTION	3
TEST PROGRAM	5
<u>Model Description</u>	5
Counterrotating Prop-Fan (CRP-X1)	5
Drive System	5
Pylon and Nacelle	6
Test Configurations	6
<u>Facility Description</u>	7
Facility Arrangement	7
Flow Capability	7
Location of Tunnel Shear Layer	7
<u>Instrumentation</u>	8
Acoustic Data Acquisition System	8
Microphone Locations	9
Shear-Layer Survey Instrumentation	10
Tunnel Instrumentation	10
CRP Drive System Instrumentation	10
Blade Vibratory Strain	11
<u>Data Reduction and Analysis</u>	11
Acoustic Data	11
Shear Layer Data	12
CRP-X1 Operating Parameters	12
Blade Vibratory Strain	13

PRECEDING PAGE BLANK NOT FILMED

CONTENTS (CONTINUED)

<u>SECTION</u>	<u>PAGE</u>
<u>Test Procedure</u>	13
Test Configurations	13
Background Noise	13
Single-Rotation Test	14
Counterrotation Test	14
DISCUSSION OF TEST RESULTS	17
<u>Background Noise</u>	17
<u>Comparison of SRP and CRP Noise</u>	17
Single-Rotation Prop-Fan Noise	17
Counterrotating Prop-Fan Noise	18
Aerodynamic Interaction Noise	18
<u>CRP Noise Trends</u>	19
Tractor at Zero Degrees Angle-of-Attack	19
Tractor at 4 Degrees Angle-of-Attack	21
Pusher Configurations at Zero Degrees Angle-of-Attack	23
Pusher Configurations at 4 Degrees Angle-of Attack	24
Pusher Versus Tractor Comparison	25
<u>Summary of Configuration Effects on Noise</u>	26
Rotor-Rotor Spacing Effects	26
Tractor Angle-of-Attack Effects	27
Pusher Pylon Spacing Effects	27
Pusher Versus Tractor Effects	27
NOISE PREDICTIONS AND COMPARISON WITH MEASUREMENTS	29
<u>Prediction Methodology</u>	29
<u>Comparison of Predictions and Measurements</u>	29
Far-Field Noise Directivities	29
Scaled Far-Field Perceived Noise Level	30
Near-Field Noise Directivities	30

CONTENTS (CONTINUED)

<u>SECTION</u>	<u>PAGE</u>
<u>Full Scale Noise Predictions</u>	31
Far-Field Noise During Low Speed Flight	31
Near-Field Noise at Cruise Conditions	31
CONCLUSIONS	33
APPENDIX A SYMBOLS AND ABBREVIATIONS	147
REFERENCES	

SUMMARY

Hamilton Standard, under contract to NASA-Lewis, has completed an acoustic evaluation of a 62.2 cm (24.5 in.) diameter model of a counterrotating Prop-Fan (CRP). Tests were conducted on the rear rotor alone (to simulate a single rotation Prop-Fan) and on the counterrotating Prop-Fan as a tractor and as a pusher (with a pylon and nacelle installed upstream) both at zero degrees and at 4 degrees angle-of-attack. The effects of spacing between rotors and between the pylon and the front rotor on noise were also measured.

The objective of the program was to obtain test data necessary to define the acoustic characteristics of counterrotating Prop-Fans in the far-field at take-off conditions and in the near-field at cruise conditions. In obtaining data for cruise conditions, measurements were made at a 0.2 diameter tip clearance, similar to the location expected for the fuselage. However, the flight speed was limited to 0.26 Mach number due to facility fan capacity. Therefore, the model was oversped to achieve an operating condition with a tip helical Mach number similar to the full-scale cruise condition. Far-field noise measurements were obtained at approximately three Prop-Fan diameters distance. Representative take-off flight speeds, tip speeds, and power loadings were used.

Test results in the far-field show that the most important parameter affecting noise is the tip speed. Reducing tip speed reduces noise until about 200 m/sec (650 ft/sec) when a leveling-off is reached. Reducing the tip speed to levels below this value showed little additional noise reduction. The effect on noise of increased spacing between the rotors was negligible, probably because the nominal spacing was already large enough to avoid significant potential field interaction.

Angle-of-attack effects raise the peak noise of the tractor configuration about 3 to 4 EPNdB when changing the angle from zero degree to 4 degrees. Compared to the tractor configuration, the pusher configuration produces 2 to 3 EPNdB more noise. Relative angle-of-attack effects for the pusher configurations are lower, possibly because the pylon tends to straighten the flow into the rotors. Combinations of pylon-to-rotor spacings and rotor-to-rotor spacings tested show very little effect on the noise.

Comparisons of the noise of the CRP to that of the single rotation Prop-Fan (SRP) show that the CRP produces much higher levels of higher frequency harmonic noise, particularly in the forward direction. The results of this are both increased peak noise levels and increased duration resulting in a higher level of Effective Perceived Noise.

Test results in the near-field at the high helical tip Mach numbers representative of cruise conditions show that the spectrum and directivity characteristics of the CRP are very similar to those of the single rotation Prop-Fan. The peak noise occurs in the visual plane of rotation, with significant reduction in noise levels fore and aft.

Scaling of the measured model data for take-off condition to full scale shows that the CRP-X1 model as a twin-engine, aft mounted pusher would produce an equivalent free-field Effective Perceived Noise Level of 93.1 EPNdB at a point 457 m (1500 ft) to the side of the airplane.

INTRODUCTION

The Counterrotating Prop-Fan (CRP) promises substantial fuel savings compared to turbofans for commercial transport airplanes during high altitude cruise conditions in the 0.7 to 0.8 Mach number range. In addition, the CRP provides relatively better low speed performance, allowing operation from shorter runways and climbing to higher altitudes more quickly. The CRP also provides up to 8% better cruise efficiency than the Single Rotation Prop-Fan (SRP).

Compared to an SRP, a CRP generates noise in a more complex manner. It has the same sources of noise as those of the SRP and in addition a source of aerodynamic interaction noise. The aerodynamic interaction noise results from wakes produced by the front rotor convected into the rear rotor and producing fluctuating loading on the rear rotor blades. This is an efficient source of noise and typically results in significant levels of higher frequency noise. Aircraft must satisfy specified noise limits during take-off and landing to meet certification requirements. In addition, acceptable near-field noise during cruise conditions is important to minimize the weight of acoustic treatment needed to maintain cabin noise levels consistent with those found in turbofan-powered airplanes.

In order to develop a technology base for designing low-noise CRP's, an experimental program was undertaken to define the noise characteristics of CRPs over a range of operating conditions including certain design and installation parameters. The purpose of this program was to obtain test data necessary to define the acoustic characteristics of counterrotating Prop-Fans.

In this report the results of the acoustic tests are presented. Measurements were obtained in an acoustically treated wind tunnel at conditions simulating take-off and landing as well as high-speed cruise conditions. Acoustic measurements were made in the far-field and in the near-field at sufficient fore and aft locations necessary to define the directivity of the noise. This report also compares the measurements with predicted levels. Analytically projected full-scale levels for a CRP in the far-field at take-off and in the near-field in cruise conditions are presented.

TEST PROGRAM

Model Description

Counterrotating Prop-Fan (CRP-X1)

Acoustic testing was conducted using a 62.2 cm (24.5 in.) diameter counterrotating Prop-Fan (CRP) model designated CRP-X1 and is shown in Figure 1. This model was operated as a counterrotating tractor and a counterrotating pusher propulsor. The single rotation configuration was obtained by removing the front blade row and replacing it with a dummy hub. Each blade row has five 235 activity factor (AF) blades with thin NACA series 16 airfoils. The design tip sweep of the CRP-X1 blades is 34 degrees measured on the helix formed by the motion of the advancing blade. A description of the blade design is given in Reference 1. The basic CRP-X1 test configuration was designed for cruise as a CRP tractor operating at 0.72Mn, 10,668 m (35,000 ft) altitude, 228.6 m/sec. (750 fps) tip speed and 297 kW/D² (37 SHP/D²). Each blade row of the CRP-X1 has variable blade pitch capability with approximately 1.5 degrees of resolution. The blades were locked at discrete blade pitch angles. Because the blades are adjusted together through gears the blade angle is uniform and repeatable. The nominal spacing between the front and rear rotors was 0.257 diameters, as defined by the axial spacing between the blade pitch-change axes. Two spacers were fabricated so that the axial separation of the front and rear rotors could be increased from the nominal 0.257D to 0.363D and 0.461D. The spacers were designed to provide a smooth flow transition between rotor hubs. The three rotor to rotor spacing configurations are shown in Figure 2.

Drive System

The counterrotating drive rig (CRDR) consists of two air turbine drives providing power to the Prop-Fan through concentric counterrotating shafts. Each turbine of the CRDR produces a maximum power of 362 kW (485 SHP) at its maximum rotational speed of 12000 RPM. The rear turbine drives the front Prop-Fan in the counterclockwise direction while the front turbine drives the rear Prop-Fan in the clockwise direction as viewed from the front. Pitching of the base support system of the counterrotating drive system allowed the Prop-Fan and nacelle system to be run at angles-of-attack. The variable angle-of-attack capabilities of the drive rig ranged from 0 to -5 degrees in 1 degree increments with an accuracy of approximately 0.1 degree.

ORIGINAL PAGE IS
OF POOR QUALITY

Pylon and Nacelle

A pylon/nacelle simulator was designed and manufactured by the McDonnell Douglas Aircraft Company for pusher configuration testing. The pylon was adjustable to provide variable clearance between the pylon trailing edge and the front rotor leading edge. The pylon/nacelle geometry can be seen in Figure 3. The pylon leading edge sweep is 22.4 degrees while the trailing edge is unswept. The axial distance between the pylon trailing edge and the front rotor pitch change axis is 12.4 cm (4.88 in.) for the 0.1 pylon chord spacing and 17.17 cm (6.76 in.) for the 0.2 pylon chord spacing. A nominal pylon chord (c) of 47.75 cm (18.8 in.) is used to non-dimensionalize the minimum distance measured between the Prop-Fan leading edge and pylon trailing edge.

Test Configurations

The model was tested for a number of configurations in the following sequence:

- Tractor at zero degree angle-of-attack
 - Single rotation (rear rotor alone)
 - Counterrotating
 - 0.257D (nominal) rotor-to-rotor spacing
 - 0.363D rotor/rotor spacing
 - 0.461D rotor/rotor spacing
- Tractor at -4 degrees angle-of-attack
 - Counterrotating at 0.257D rotor/rotor spacing
- Pusher at -4 degrees angle-of-attack
 - Counterrotating
 - 0.257D rotor/rotor spacing, 0.1 pylon chord/rotor spacing
 - 0.257D rotor/rotor spacing, 0.2 pylon chord/rotor spacing
 - 0.363D rotor/rotor spacing, 0.2 pylon chord/rotor spacing
- Pusher at 0 degree angle-of-attack
 - Counterrotating
 - 0.257D rotor/rotor spacing, 0.1 pylon chord/rotor spacing
 - 0.257D rotor/rotor spacing, 0.2 pylon chord/rotor spacing

In addition, configurations with dummy hubs (i.e., without blades) were tested for each of the basic tractor and pusher configuration at 0 and -4 degrees angle-of-attack to determine background noise levels. Figure 4 shows a representative arrangement for the CRP installed as a pusher configuration.

Facility Description

Facility Arrangement

All acoustic testing was performed in the Acoustic Research Tunnel (ART) of the United Technologies Research Center in East Hartford, Connecticut. The facility is an open jet tunnel surrounded by an anechoic chamber. Figure 5 shows the general arrangement of the facility. The anechoic chamber dimensions are 4.9 m (16 ft) high, 5.5 m (18 ft) in axial length and 6.7 m (22 ft) wide. The interior walls and floor of the chamber are lined with triangular fiberglass wedges. The anechoic quality is documented in Reference 2 and shows that broadband noise between 200 and 20,000 Hertz decays at 6dB per doubling of source to observer distance within $\pm 1/2$ dB. Turbulence suppression screens and a high length-to-diameter ratio honeycomb section are used to remove turbulent flow before the inlet test section. The airflow enters the test chamber through a 1.168 m (46 in.) diameter inlet nozzle and exits through an acoustically treated collector ring. The tunnel is driven by a 1120 kW (1500HP) centrifugal fan. The fan noise is prevented from propagating upstream into the anechoic chamber with a muffler section consisting of two right angle bends and parallel treated baffles located between the diffuser and the fan.

Flow Capability

The maximum flow velocity of the tunnel with the 1.168 m (46 in.) inlet nozzle was approximately 0.29 Mach number. The Mach number was obtained by assuming isentropic flow and calculating Mach number using the ratio of the measured total inlet pressure and the static pressure within the anechoic chamber.

Pressure losses due to the honeycomb and turbulence suppression screens were shown to be negligible experimentally. The results of the experiment have been reported in Reference 2.

Location of Tunnel Shear Layer

The open jet nature of the tunnel gives rise to a shear layer between the jet potential core and the surrounding quiescent air in the anechoic test section. The shear layer increases in thickness with increasing axial distance from the nozzle. For this test program the Prop-Fan was located totally within the potential flow so that there would be no interaction between the shear layer and the blade tips. The plane of rotation was located as far downstream of the nozzle as possible to allow the greatest angle of noise measurement forward of the Prop-Fan. The optimum CRDR location was defined as having the maximum axial separation between the tunnel nozzle exit and the plane of rotation while the front and rear blade tips remain free of shear layer turbulence ingestion. The location of the shear layer was measured with a hot wire boundary layer probe.

Hot wire traverses were made in a radial direction both 7.6 cm (3 in.) upstream of the front rotor, between the two rotors, and 7.6 cm (3 in.) downstream of the rear rotor. The CRP model was operated at a high power condition to assure that shear layer ingestion was not occurring when streamline contraction was at a maximum. Both mean velocity and axial turbulence data were obtained. A linearizer was used in the anemometer system to provide accurate measurement of the turbulence intensities at the high levels encountered in shear layers. The criteria used to define the shear layer boundary were 99 percent of the nozzle jet mean velocity and 0.5 percent increase in axial turbulence level. Also, the time varying signal of the shear layer turbulence intermittency was visually monitored with an oscilloscope to aid in determining the shear layer location. The radial traverse covered a range of 5.1 cm (2 in.) to 51 cm (20 in.) from the CRP model blade tips. Figure 6 shows the mean velocity measured as a function of distance for a traverse located axially mid-way between the two rotors and the change in turbulence level as the probe is traversed from within the potential core into the shear layer. It was noted that the onset of shear layer intermittency occurred at approximately 14 cm (5.5 in.) from the blade tips. The point at which the free stream turbulence increased by 0.5% was at about 13 cm (5.1 in.) from the blade tips. The apparent increase in turbulence at a location closer to the blade tips is the result of excitation from the CRP blade potential field. Figure 7 summarizes the results of the shear layer study. The 99 percent mean velocity measurements are shown as 'X', triangles indicate where intermittency was observed and circles indicate where the RMS turbulence level increased 0.5% from potential core values. It can be seen that with all measures of shear layer position the model blades are well inside the shear layer. The clearance was found to be 18.8 cm (7.4 in.) from the blade tips 7.6 cm (3 in.) upstream of the rear rotor to 16.9 cm (6.6 in.) from the blade tips 7.6 cm (3 in.) downstream of the rear rotor.

Instrumentation

Acoustic Data Acquisition System

A schematic diagram of the acoustic data acquisition and signal processing system is shown in Figure 8. For clarity only one microphone channel is shown. Item numbers shown in Figure 8 correspond to item numbers listed in Table I where additional information such as manufacturer and model number can be found. Table II provides the estimated accuracy and ranges of the instrumentation. The microphone signal was recorded at the highest level obtainable without exceeding the maximum tape recorder input signal. The signal strength was determined by monitoring each data channel with an oscilloscope prior to each data run and adjusting the gains accordingly. A real time narrow-band spectrum analyzer was used for on-line data reduction of one microphone channel close to the plane-of-rotation of the front rotor. Prior to the start of testing, a through-system calibration was conducted. This consisted of applying a known signal from a frequency generator that was

verified with a frequency counter and RMS voltage meter. The data was processed through the complete system and recorded on magnetic tape. The calibration data was then played back to the spectrum analyzer. The total system response was found to be flat within ± 1 dB over the frequency range 50 to 10,000 Hz.

Microphone Locations

Noise measurements were made in both the far-field and near-field using several microphone arrays.

Far-field noise measurements were made at a fixed overhead array that included seven microphones located outside the tunnel shear layer (A-1 through A-7) and one microphone located inside the shear layer mounted in the inlet nozzle (N-1). For angle-of-attack testing, an additional transverse array of six microphones (T-1 through T-6) was used. Top and side views of the far-field microphone locations are shown in Figure 9. Table III defines the coordinates of the far-field microphone locations. Also shown in Table III are the corrected visual locations, corrected radiation distances and angles, and ray-path divergence corrections that were applied to the measured levels to account for propagation through the shear-layer.

Prior to the actual acoustic testing of the Prop-Fan noise a far-field background noise test of the facility was conducted. The microphone locations for the background noise test were slightly different than the model test microphone locations discussed previously. A list of the coordinates of the background noise microphone locations can be found in Table IV.

During the pusher configuration testing at simulated cruise conditions, a traversing system supporting four microphones mounted circumferentially at 0.2 rotor diameter tip clearance was added. An end-view looking upstream of the traversing system is shown in Figure 10. The microphones were moved axially from 30.48 cm (12 in.) aft to 60.96 cm (24 in.) forward of the front rotor plane-of-rotation. These four traversing microphones were always totally inside the tunnel flow and do not require any corrections. They are designated 2-1 through 2-4.

Shear-Layer Survey Instrumentation

Figure 11 presents the shear layer survey instrumentation. A Thermo-Systems type 1218-T2 hot wire boundary layer probe was mounted on a UTRC X-Y traverse system. Both A.C. and D.C. linearized anemometer outputs were coupled to a FM tape recorder and on-line analog plotters. Also, an oscilloscope was used to monitor the time varying signal representing the shear layer turbulence.

Tunnel Instrumentation

Figure 12 shows the arrangement for measuring the Acoustic Research Tunnel speed. Additional instrumentation is identified in Figure 13. Table V is a listing of tunnel instrumentation, manufacturers model number and location. The shear layer survey instrumentation is also included in this listing.

The total pressure (P_T) was measuring using a probe upstream of the CRP model in the tunnel inlet. The probe was located outside the tunnel wall boundary layer and downstream of the last inlet screen. The static pressure of the test section was measured by static pressure probes located inside the anechoic chamber in a region of negligible recirculation velocity. The atmospheric pressure (P_A) was obtained prior to each data run from a barometer. The total pressure and static pressure signals were input directly to the on-line data acquisition system shown in Figure 13 while the atmospheric pressure was input manually. From these pressure measurements the tunnel pressure was input manually. From these pressure measurements the tunnel pressure ratio (P_T/P_S) was obtained and the tunnel Mach number was calculated from isentropic flow equations. The uncertainty of the tunnel Mach number was less than 1 percent.

CRP Drive System Instrumentation

A list of model and drive instrumentation along with manufacturers model number and location are shown in Table VI. Rotor speeds were measured using a once-per-revolution shaft signal generator (1P pipper) on each of the two rotors. This was recorded on magnetic tape simultaneously with acoustic data. Also, a separate system to provide rotor speed input to the data acquisition system was used. This incorporated a sixty tooth wheel to obtain RPM over a 1 second time span. Rotor power was obtained from a measurement of shaft torque and rotor RPM. The torque balances were calibrated prior to the start of testing by hanging a series of weights on a lever arm attached to the rotor hubs. To minimize the number of model drive power data points taken, a series of test points (zero angle-of-attack tractor) were run early in the testing with the torque balances operational. This covered all the combinations of advance ratio, tunnel Mach number and blade angles tested in the program. Power was determined for other configurations by matching operating conditions (blade angle combinations and tip rotational Mach numbers) of the test configuration with the power of the baseline configuration. Pylon and angle-of-attack effects on absorbed power were assumed to be negligible.

Blade Vibratory Strain

Prior to the acoustic testing of the tractor and simulated pusher pylon configuration, stress surveys were conducted to structurally clear the rotor blades for operation at high power take-off and simulated cruise (rotational overspeed) conditions. The simulated cruise conditions required the front and rear rotors to be run as high as 11700 RPM depending on ambient temperature conditions. The tractor testing was conducted with the rotor/rotor spacing set to its minimum value of 0.257D. This assured maximum excitation of the blades due to wake interaction. The pusher stress survey was conducted prior to the pusher angle-of-attack acoustic testing. This additional testing was necessary to assure flow distortions due to the installation of the upstream pylon did not increase blade loading beyond tolerable limits. To obtain the worst possible case, pylon spacing and rotor/rotor spacing were set to their closest position. Shown in Figure 14 are the locations of the strain gages for the front and rear rotors. One blade from each rotor was gaged with five transducers. The front and rear blades had three gages located at the 86% (26.85 cm) radial station 45 degrees apart and one parallel to the pitch change axis at the 76% (23.70 cm) radial station. Each blade also had one transducer oriented five degrees from the pitch change axis at the 38% (11.86 cm) radial station on the front rotor and the 42% (13.13 cm) radial station on the rear rotor.

Data Reduction and Analysis

Acoustic Data

The acoustic data were processed in the form of 400-line narrow-band spectra at Hamilton Standard. The system used to accomplish this included playback on an Ampex FR 1900 25.4 mm (1 in.) FM tape system, a General Radio GR2502 spectrum analyzer and a Hamilton Standard design System Corrector Amplifier. The tape system has an amplitude and frequency linearity of ± 0.5 dB and ± 0.2 percent, respectively, with identical linearities for the spectrum analyzer. The system corrector has an amplitude linearity of ± 0.1 percent of full-scale with essentially flat frequency response over the analysis range. The frequency range covered was 0 to 10,000 Hz on a linear frequency scale which gives an effective filter bandwidth of 25 Hz. The digital value of each of the 400 bands was written to magnetic tape. The tape was read and processed by a computer with software that extracted the sound pressure level of the tones associated with the counterrotating Prop-Fan. The software accomplished the tone extractions by first calculating the frequencies of the tones. These occur at harmonics of blade passage frequencies (number blades X RPM/60) of each the front/rear rotors when equal numbers of blades and equal RPM exist. The tones were extracted from the 400-line narrow-band spectra by selecting the sound pressure levels in the bins that contain the frequencies of interest. To account for a small differential RPM of the front and rear rotors, the tone levels were obtained by integrating the sound pressure level from the bin containing blade passage frequency (BPF) of the

front rotor to the bin containing BPF of the rear rotor. This was performed for each harmonic of BPF and is necessary to obtain the aerodynamic interaction tones which occur between the front and rear rotor blade passage frequency harmonics. The interaction tones occur at evenly spaced intervals of $BPF_{FRONT} - BPF_{REAR}$ and fall between the self-generated rotor frequencies starting at 2 times BPF. For the cases where the two rotors were run at substantially different RPMs the tones were identified individually and a complete set of self-generated and interaction tones was obtained. Additional data processing was performed to scale the model data to a full size CRP and to synthesize a flyover. This was done to evaluate trends of noise versus design and operating parameters in terms of Effective Perceived Noise Level (EPNL), which cannot be done in model scale.

The measured noise spectrum (tone frequencies) were corrected for shear layer effects using the method described in Reference 3 and normalized to a radius of one Prop-Fan diameter. The frequencies of the tones were corrected by multiplying them by the ratio of the model-scale diameter to the full size diameter. To simulate actual flight, frequencies were also corrected for Doppler shifting effects. Distance from the source to the observer was calculated using the Prop-Fan diameter as the measurement scale and corrected by $20 \log_{10}(\text{distance})$. Atmospheric attenuation was included to correct for the long source to observer distances of actual flight. The tone spectra were linearly interpolated to 1/2 second increments from which 1/3 octave band spectra, Perceived Noise Levels (PNL) and Tone Corrected Perceived Noise Levels (PNLT) were calculated. The Effective Perceived Noise Level (EPNL) was obtained by integrating PNLT at 1/2 second intervals from $PNLT_{max}$ minus 10 dB before and after the occurrence of the peak noise.

Shear Layer Data

The shear layer data was analyzed to indicate the main nozzle jet flow velocity and the RMS turbulence level as functions of the distance from the blade tips. These quantities were plotted on an X-Y plotter. From the plots the 99% velocity points and the 0.5% turbulence increase points were determined. Intermittency onset was determined from observing the unprocessed hot-wire signal on an oscilloscope. Random, short duration jitters of the signal were interpreted to be evidence of intermittency. Although this is highly subjective, these results compared favorably with the more reliable (but less sensitive) measures of mean velocity drop-off and 0.5% turbulence level rise.

CRP Operating Parameters

All steady-state data parameters were measured and processed using a computer-based system. Measured and computed quantities were tabulated and stored on floppy disk. Identification information, such as test configuration, test point number, and date and time were used to identify each record.

Blade Vibratory Strain

The strain gage data was analyzed to identify the amplitudes of multiples of the once-per-revolution components of blade stress. The only purpose for doing this was to identify that the allowable blade stress would not be exceeded for any operating condition for any test configuration.

Test Procedure

Test Configurations

The test matrix defined take-off operating conditions at 0.26 tunnel Mach number for nominal tip rotational speeds ranging from 198 m/sec (650 ft/sec) to 244 m/sec (800 ft/sec) and nominal power loadings from 160 kW/D² (20 SHP/D²) to 1124 kW/D² (140 SHP/D²). Simulated cruise conditions were run at 0.26 tunnel Mach number with overspeed tip rotational velocities that provided tip helical Mach numbers equivalent to cruise conditions. Power loadings were selected to provide the best match with actual cruise radial lift distribution.

Single rotation noise testing was performed to obtain baseline noise results. This was accomplished by running the CRP-X1 configuration with the front rotor removed and replaced by a dummy hub assembly.

CRP-X1 tractor configurations included front-to-rear rotor axial spacings of 0.257D, 0.363D and 0.461D at a zero degree inflow angle-of-attack. The CRP tractor configuration was also operated at the nominal 0.257D rotor spacing with a four degree angle-of-attack. Shown in Figure 15 is a picture of the tractor configuration installation.

The CRP pusher configuration was simulated by installing a pylon and nacelle combination upstream of the CRP tractor model, as shown in Figure 16. The model was operated at zero and four degree inflow angles-of-attack with pylon-to-front-rotor spacings of 0.1 and 0.2 pylon chords. At the 0.2 pylon chord spacing, two front and rear rotor spacings were tested. The rotor spacings tested were the nominal 0.257D and the intermediate 0.363D spacing.

Background Noise

Background noise was measured for the tractor configuration and the pusher configuration. The CRP-X1 rotor blades were removed and replaced with dummy rotor hubs. The air turbines were operated in a locked position and also in the free-spinning mode. While the tunnel speed was operated at 0.26 Mach number, noise measurements were made in the far-field at the overhead axial microphone array. It should be noted that some of the axial microphone locations were slightly different than the final microphone locations used during the CRP acoustic testing.

Single-Rotation Test

The single rotation Prop-Fan noise was measured at the overhead axial far-field microphone array. The single rotation test conditions cover a range of tip speeds of 183 m/sec (600 ft/sec) to 244 m/sec (800 ft/sec) and a power range of about 40 kW/D² (5 SHP/D²) to 482 kW/D² (60 SHP/D²) in the take-off regime. Simulated cruise testing conditions covered tip helical Mach numbers of approximately 0.766 to 1.158. Test conditions for the single rotation condition are summarized in Figures 17 and 18. Shown next to the symbols are the run numbers corresponding to the condition which can serve as a cross-reference in the analysis section.

Counterrotation Test

Counterrotating noise measurements throughout the testing were made with the front and rear rotors operating at slightly different tip rotational speeds. This was done to obtain diagnostic information by separating the front and rear rotor self-generated frequencies and the frequencies associated with the aerodynamic interaction between rotors. The differential speed was obtained by choosing a nominal tip speed, then raising the front rotor RPM by 2.5 percent and lowering the rear rotor RPM by 2.5 percent. This differential was determined to be large enough to resolve the frequencies without significantly altering the source strength or radiation efficiency. Throughout this section and in the analysis section, any notation of "equal" RPM actually has a 5 percent differential between the front and rear rotors.

Tractor at Zero Degree Angle-of-Attack - The first portion of the CRP noise testing was performed at zero inflow angle-of-attack with a nominal rotor/rotor spacing of 0.257D. The testing included seven blade angle combinations that provided take-off power loadings of 160 kW/D² (20 SHP/D²) to 1124 kW/D² (140 SHP/D²) at tip speeds of approximately 183 m/sec (600 ft/sec) to 244 m/sec (800 ft/sec). Two additional blade angle combinations provided simulated 0.72 and 0.80 Mach number cruise conditions where the tip rotational speed was increased to provide the 1.055 and 1.115 tip helical Mach numbers. The simulated cruise blade angles were selected to provide the best match to the actual cruise blade loading distribution for the front and rear rotors at the ART conditions. Additional take-off conditions were run with front and rear rotor tip speeds that differed by as much as 20 percent (unequal RPM) to determine the effect of differential tip speeds and tone splitting (separation of the self frequencies and unsteady frequencies). During this testing the far-field axial microphone array was operational. The operating conditions and run numbers tested are summarized in Figures 19, 20, and 21. The second phase of the zero degree inflow angle-of-attack tractor testing was with the rotor/rotor spacing set to its maximum distance of 0.461D. Test conditions included blade angle settings to obtain equal RPM data and unequal RPM data. The operating conditions for the maximum rotor/rotor spacing cases are shown in Figures 22 and 23. The final phase of the zero degree inflow angle-of-attack testing was conducted with the rotor/rotor spacing set to its intermediate value of 0.363D. The scope of this testing is similar to the 0.461D configuration. The operating conditions for this configuration are shown in Figures 24 and 25.

Tractor Configuration at Angle-of-Attack - The rig with the CRP model was pitched downward four degrees for the inflow angle-of-attack testing. The rotor/rotor spacing was set to the nominal 0.257D spacing. With the rig pitched downward, a shear layer investigation was performed to determine if there was any CRP-shear layer interaction. The CRP was found to be clear of the shear layer and did not need to be repositioned. Noise measurements were made in the far-field at the axial overhead array and the overhead traverse microphone array to determine circumferential variation effects. The range of testing included take-off conditions with tip speeds ranging from 183 m/sec (600 ft/sec) to 244 m/sec (800 ft/sec) and power loadings of 225 kW/D² (28 SHP/D²) to 1124 kW/D² (140 SHP/D²). No simulated cruise conditions were tested during the 4 degree angle-of-attack tractor testing. Figures 26 and 27 show the operating conditions tested.

Pusher Configuration at Inflow Angle-of-Attack - With the pylon and nacelle installed for the pusher configuration, the rig was pitched at a four degree inflow angle-of-attack attitude. The pylon/nacelle combination was initially set at its closest 0.1 pylon chord position relative to the Prop-Fan front rotor leading edge and the rotor/rotor spacing was set at its nominal 0.257D value. Three sets of take-off conditions shown in Figures 28 and 29 were tested that included equal and unequal RPM conditions. The pylon/nacelle was then moved to the maximum spacing of 0.2 pylon chords. The rotor/rotor spacing was kept at the nominal 0.257D value and the same test matrix as the 0.1 pylon chord spacing was repeated. The run numbers and test conditions are shown in Figures 30 and 31. The rotor/rotor spacing was increased next to the 0.363D distance and again the test matrix was repeated. Shown in Figures 32 and 33 is the summary of test conditions for the CRP-X1 pusher at four degree angle-of-attack and at 0.363D rotor/rotor spacing. Microphone arrays for this testing included the far-field overhead axial and transverse arrays.

Pusher Configuration at Zero Degrees Angle-of-Attack - With the rig pitched at zero degrees relative to the tunnel inflow, a pylon/nacelle combination was installed upstream of the CRP tractor model to simulate a pusher configuration. The rotor/rotor spacing of the CRP model was set to its nominal 0.257D value throughout the testing. The initial setting of the pylon trailing edge spacing relative to the front rotor leading edge was 0.1 pylon chords. Noise testing included take-off and simulated cruise operating conditions. The test matrix defining the operating conditions for this configuration can be seen in Figures 34 and 35. After completion of the 0.1 pylon chord spacing testing, the pylon/nacelle was moved to its maximum spacing of 0.20 pylon chords. The test matrix for this configuration is similar to the 0.1 pylon chord testing, although slightly reduced in scope. The operating conditions for the 0.2 pylon chord spacing testing are shown in Figures 36 and 37. Noise measurements were taken in the far-field at the overhead axial array. During the simulated cruise testing the 0.2 rotor diameter near-field traversing microphone array was included. Also, the traversing array was used during the 44.06°/42.84° and 41.21°/38.55° take-off blade angle combinations, 0.1 pylon chord spacing testing.

DISCUSSION OF TEST RESULTS

Background Noise

Background noise was measured for two major test configurations: during tractor testing and during pusher testing. In both cases, dummy hubs were installed. Noise was measured with the tunnel operating at the nominal 0.26 Mach number. In addition, the two turbines were run with no load over a range of speeds. Finally, the shafts were locked and 1.034×10^6 N/M² (150 PSI) air pressure applied to the turbine inlets. Figures 38 to 41 show the background noise sound pressure levels (SPL) at four locations spanning the forward to aft range of noise measurement positions. Also shown on the figures are the spectra measured for the CRP operating at lower power and low tip speed. At the forward locations, Figures 38 and 39, the air turbines do not significantly contribute to the background noise below about 5000 Hz. In any case, the total background noise is significantly below that of the CRP plus background noise. The tunnel plus turbine noise appears to contribute to the total above 6000 Hz, but the levels of the CRP tones are essentially uncontaminated up to about the 12th harmonic of BPF.

Figure 40 shows that the turbine noise is beginning to contribute to the total noise at the higher frequencies aft of the plane-of-rotation.

Figure 41 shows that at this aft-most location the locked-turbine noise levels dominate the broadband noise floor. However, the CRP tones still are relatively uncontaminated to beyond the 10th harmonic of BPF.

Since the data analysis consisted of extracting the CRP tone noise only and that there was essentially uncontaminated tone noise levels to beyond the 10th harmonic of BPF for a low power, low tip speed CRP operating condition, it was concluded that facility and drive-turbine background noise was not a problem. Therefore, no corrections to the data were made for background noise.

Comparison of SRP and CRP Noise

Single-Rotation Prop-Fan Noise

Single-rotation Prop-Fan (SRP) noise data were acquired primarily to provide a basis for comparison with Counterrotating Prop-Fan (CRP) noise characteristics. It is not the objective of this discussion to provide detailed definition of SRP noise characteristics, but rather to provide enough background information on SRP and CRP so that the added sources of noise in CRP, namely the aerodynamic interaction noise, can be identified in quality and importance.

Figure 42 shows representative spectra of SRP noise at a forward directivity, near the plane-of-rotation, and at an aft directivity. It is readily apparent that the SRP has no significant higher frequency harmonics at the

PRECEDING PAGE BLANK NOT FILMED

forward directivity. The second harmonic is barely discernable, at a level more than 20 dB lower than that of the fundamental. In the plane-of-rotation, more harmonics are seen, but the higher harmonics are still 20 dB or more below the fundamental. Similar characteristics can be seen in the aft radiated noise.

It is apparent that SRP noise is characterized by a blade passing frequency harmonic that peaks in the plane-of-rotation and a few higher harmonics that are 20dB or more below the fundamental.

Counterrotating Prop-Fan Noise

Representative counterrotating Prop-Fan noise spectra are shown in Figure 43. The first impression is that the CRP is significantly richer in harmonics than is the SRP. In the forward direction the levels of the second and third harmonics are nearly equal to that of the fundamental. Harmonics to the sixth are readily apparent. In the aft direction, the levels of the second and third harmonics exceed that of the fundamental.

It is thus apparent that the noise spectrum of a CRP contains many higher harmonics which radiate effectively at forward and aft angles.

Aerodynamic Interaction Noise

Figure 44 shows the comparison of SRP and CRP noise spectra at the three directivity angles. The SRP and each rotor of the CRP are operating at approximately 198 m/sec (650 ft/sec) tip speed and 82 kW (110 SHP). However, to provide an equal basis of comparison, the single rotation data has been increased by 3dB to account for one rotor versus two. This provides a means of obtaining free-field noise of two noninteracting rotors and allows the noise due to rotor/rotor aerodynamic interaction to be extracted. It can be seen that at the three directivities the blade passage frequency (BPF) harmonic is approximately equal to CRP and SRP. However, the CRP higher harmonics are clearly much higher than those of the SRP. The forward and aft directivities show higher levels at the second harmonic and above. In the plane-of-rotation the CRP and SRP spectra do not diverge until the third harmonic.

The difference between the spectra is caused by the aerodynamic interaction between the two CRP rotors. This source of noise is the major difference between CRP and SRP. Because the aerodynamic interaction noise results in higher levels of higher harmonics, its effect on a metric such as A-weighted overall noise or Effective Perceived Noise Level will be significant. It thus would appear that the difference in overall noise level between SRP and CRP might be relatively small, whereas the difference in dBA or EPNdB would be considerably larger.

CRP Noise Trends

Tractor at Zero Degrees Angle-of-Attack

Power and Tip Speed Effects - This section will discuss the effects of power and tip speed on the noise levels of the CRP-X1 model while operating in the tractor configuration at the minimum rotor/rotor spacing (0.257D) and at equal front and rear rotor tip speeds. Five test points were selected for discussion. The operating conditions for these points are shown in Figure 45.

Figure 46 shows two plots of sound pressure level (SPL) for several harmonics of blade passing frequency (BPF) as a function of emission angle. Also shown on this figure are the calculated Effective Perceived Noise Levels (EPNL) based on geometric scaling of the data to an equivalent diameter of 4.0 m (13.1 ft) and synthesizing a 457 m (1500 ft) flyover at 0.26 Mx. This is needed, as EPNLs are dependent on frequency and do not scale. The plots represent test points 46.2 and 45.3. Both have a tip speed of approximately 201 m/sec (660 ft/sec) and both have approximately the same front-rear power split. For these plots only the first four harmonics and the tenth harmonic will be presented. Harmonics 5 through 9 were omitted because of difficulty in interpreting the directivity results of these harmonics. Run 46.2 was at 511 kW/D² (63.7 SHP/D²) and run 45.3 was at 696 kW/D² (86.7 SHP/D²). Blade passage frequency levels and levels of the upper harmonics increased with power loading.

Figure 47 shows the effect of power loading on noise at a constant tip speed of 232 m/sec (760 ft/sec). The major effect is the increase in SPL levels at blade passage frequency, the higher harmonics show only subtle differences. The results at this higher tip speed are similar to the 201 m/sec (660 ft/sec) case. In both cases the scaled EPNdB levels increase approximately 1.0 dB for an 80 kW/D² (10 SHP/D²) increase in power loading.

The effect of tip speed at constant power loading is shown in Figure 48. For these plots the power loading is approximately 700 kW/D² (87 SHP/D²) and the power split held to approximately 58/42. Blade passage frequency noise level is shown to increase with the increase in tip speed. For this case the higher harmonics changed significantly with tip speed.

Figure 49 shows the effects of the tip speed at a lower power loading of approximately 480 kW/D² (60 SHP/D²) and a front-rear power split similar to the previous plots, near 58/42. Again the most noticeable increase in noise level was at blade passage frequency with significant changes seen in the second and fourth harmonic of BPF. The tenth harmonic did not show significant change for this case as was seen for the 700 kW/D² (87 SHP/D²) case. Both examples of the effect of tip speed show that the scaled EPNdB levels increase approximately 3.5 dB with a 30 m/sec (100 ft/sec) increase in tip speed.

A summary of the effects of tip speed and power loading on scaled EPNdB levels is shown in Figure 50. The effective perceived noise levels are scaled for a 4.0 m (13.1 ft) diameter Prop-Fan to a distance of 457 m (1500 ft). All the curves have been adjusted empirically to a 45/55 front/rear power split. Noise levels decrease as tip speed and power loading are reduced. A minimum level is reached as tip speed is reduced to 183 m/sec (600 ft/sec). In the 198 to 229 m/sec (650 to 750 ft/sec) range the EPNdB levels are most sensitive to changes in tip speed. Above 229 m/sec (750 ft/sec) the slope of the curves decrease, indicating that the sensitivity of the levels to tip speed decreases above 229 m/sec (750 ft/sec).

Rotor Power Split Effects - The effect of front-to-rear power split is shown in Figure 51. These data are also for the nominal rotor/rotor spacing of 0.257D and for equal front and rear rotor tip speeds. Run 49.2 had a front/rear power split of 49/51 and run 41.2 had a split of 67/33. Both test points had an approximate power loading of 305 kW/D² (38 SHP/D²) and a tip speed of 195 m/sec (640 ft/sec). Increasing the front power increased blade passage frequency levels a small amount. All the harmonics above BPF, including the tenth harmonic, had small increases in SPL over the entire emission angle range.

Figure 52 contains the effect of front/rear power split at approximately 673 kW/D² (84 SHP/D²) and 232 m/sec (760 ft/sec) tip speed. For this case there is no change in level at blade passage frequency. At the second, third, and fourth harmonics, levels increased at far forward and aft emission angles and decreased or remained the same at the emission angles of 52.8 and 67.2 degrees. The tenth harmonic increased at all emission angles, except for the far forward microphone position.

Figures 51 and 52 lead to the conclusion that increasing front horsepower has a small adverse effect on noise levels, approximately 0.7 dB per 10% increase in front rotor power.

Rotor-Rotor Spacing Effects - The effects of rotor-rotor spacing on the harmonic directivity is shown in Figure 53 for an operating condition of 303 kW/D² (37.8 SHP/D²), 49/51 power split and 193 m/sec (633 ft/sec) tip speed. It can be seen that there is a minor effect on the noise levels resulting from increased rotor-rotor spacing. The blade passage frequency level did not change with spacing, although the higher harmonic levels increased at forward directivity angles. As can be seen from the figure the minor changes of the harmonics did not change the scaled EPNL values which were essentially the same at the three rotor-rotor spacings.

Figure 54 shows the directivity plots for the three rotor-rotor spacings at a power loading and tip speed similar to the previous case with a 67/33 power split. These plots show the same results as the previous plots, where blade passage frequency levels did not change appreciably and the higher harmonics increased in level at the forward directivity angles. EPNL levels were almost constant, increasing only slightly with increased spacing. The higher front SHP loading and small increase in tip speed caused the EPNL level to increase about 2 dB.

Directivity plots for a higher power loading and tip speed case with a 48/52 power split for the three rotor-rotor spacing are shown in Figure 55. Again the results show only subtle effects on the harmonic levels and no change in EPNL levels for different rotor-rotor spacings.

Rotor-Rotor spacing effects are summarized in Figure 56 for the 50/50 power split conditions. Each of the four conditions have the same front and rear rotor blade angles, with the RPM varying. Increasing rotor-rotor spacing from 0.257D to 0.461D shows small decreases in noise levels, less than 0.5 db. The effect appears to be independent of tip speed. Figure 57 shows similar results for a 57/43 power split. For these cases it is seen that the minimum noise occurred at the 0.363D spacing. However, the differences between the minimum and maximum levels is less than 2 dB.

From these data it appears that for the rotor-rotor spacings investigated, there is no substantial effect on CRP noise over a wide range of power loading and tip speeds.

Unequal RPM Effects - The effects on noise while operating at unequal front and rear rotor speeds were investigated. Measurements were made for a range of RPM ratios (RPM front/RPM rear) from 0.8 to 1.2. The front and rear rotor blade angles were adjusted to maintain a reasonable power split.

Figure 58 summarizes the results of the unequal RPM analysis. This shows a plot of scaled Effective Perceived Noise Level versus the front-to-rear rotor RPM ratio. All the data used in Figure 58 were adjusted empirically to the CRP-XI design power split of 45/55. The EPNL were calculated based on scaling all the tones to a full-scale diameter of 4.0 m (13.1 ft), as was the case for the equal RPM cases previously discussed.

The scaled relative EPNL are shown for four conditions spanning low loading (289 kW/D^2 (36 SHP/D^2)) to high loading (738 kW/D^2 (92 SHP/D^2)) at low average tip speed (194 m/sec (637 ft/sec)) to high average tip speed (239 m/sec (785 ft/sec)). It should be noted that in this plot the average tip speed of the two rotors was held constant. Thus, at the 1.0 RPM ratio point the two rotors have the same tip speed while at the 1.2 RPM ratio the front rotor has a tip speed which is 10 percent higher than at the 1.0 RPM ratio and the rear rotor has a tip speed which is 10 percent lower than at the 1.0 RPM ratio. It is apparent that increasing the front rotor tip speed while decreasing the rear rotor tip speed decreases noise whereas increasing the rear rotor tip speed while decreasing the front rotor tip speed raises noise. The effect, however, is relatively small. It appears that the total effect for an RPM ratio change of ± 20 percent is about 2 EPNdB.

Tractor at 4 Degrees Angle-of-Attack.

The tractor configuration was tested at an angle-of-attack of 4 degrees for the nominal 0.257D rotor-rotor spacing. For this testing, the same rotor blades angles, tip speeds, and tunnel speed as for the tractor at zero angle-of-attack were used. This allows a direct comparison to extract the inflow angle effects of the CRP noise.

Axial Directivity Effects - Figure 59 shows the axial directivity comparison between 0 and 4 degrees angle-of-attack at the nominal rotor-rotor spacing of 0.257D for a tip speed of 193 m/sec (633 ft/sec), power loading of 303 kW/D² (37.8 SHP/D²), and power split of 49/51. There appears to be a substantial increase in level at all harmonics from 0 to 4 degrees.

Figure 60 shows the 0 to 4 degree angle-of-attack comparison at approximately the same power loading and tip speed as the previous figure with a power split of 67/33. Results are similar to the results that were found in the previous example. For both this case and the previous case EPNL levels increased about 3 to 5 dB with the 0 to 4 degree angle-of-attack change.

Directivity plots of Figure 61 are for a tip speed of 231 m/sec (758 ft/sec) and power loading of 701 kW/D² (87.3 SHP/D²) at minimum rotor-rotor spacing with a 48/52 front/rear power split. As in the previous cases, the levels at all harmonics increases substantially. The scaled EPNL increased 4 dB in level for a change in angle-of-attack from 0 to 4 degrees.

Figures 59, 60, and 61 show that varying power loading, tip speed and power split had little influence on the effect of angle-of-attack. The noise increment for angle-of-attack effects remained constant over a large range of power loadings, tip speeds and power splits.

Transverse Directivity Effects - The effects of angle-of-attack on far-field noise transverse directivity was also evaluated. The convention used in the following discussion is illustrated in Figure 62. It assumes an aircraft altitude of 800 ft which might be similar to that used during aircraft noise certification tests. For this geometry, the angle relative to the horizontal is 28.5 degrees on the starboard side and 151.5 degrees on the port side.

Figure 63 contains harmonic directivity plots for transverse microphone locations that compare the tractor 0 degree angle-of-attack case to the tractor 4 degree angle-of-attack case. For this comparison the power loading was 303 kW/D² (37.8 SHP/D²), the tip speed was 193 m/sec (633 ft/sec) and the front/rear power split was 49/51. The 0 degree angle-of-attack plot shows nearly constant SPL levels at all transverse angles except for a drop in level that occurred at the 165 degree microphone position. At 4 degrees angle-of-attack all harmonic levels increased with the largest increase occurring in the range 70 to 140 degrees. The 4 degree angle of attack data SPL levels show a reduction at the far port and starboard microphone position, especially at blade passage frequency. Figure 64 shows directivity plots comparing the tractor 0 and 4 degree angle-of-attack cases for approximately the same power loading and tip speed as those of Figure 63 but at a different power split of 67/33. Results are similar to those stated previously. At 0 degree angle-of-attack, harmonic levels showed little change with transverse angle. At 4 degrees angle-of-attack, levels increased substantially near 90 degrees and decreased at microphone locations toward the sideline.

Figure 65 shows the transverse microphone data angle-of-attack comparison for conditions of 701 kW/D^2 (87.3 SHP/D^2), 231 m/sec (758 ft/sec) tip speed and a power split of 48/52. Again the 4 degrees angle-of-attack case shows higher noise levels directly below the flight path which decrease at microphone locations near the sideline. The 0 degree angle-of-attack data shows a dip in noise level at the highest transverse angle and also at the 90 degrees location at BPF.

Figures 63, 64, and 65 show that there is evidence that during 4 degrees angle-of-attack conditions there is a decreasing noise level trend at microphone locations near the sideline. This result is consistent with conventional Prop-Fan data in that noise levels decrease at the sideline due to the non-uniform blade loading that occurs during angle-of-attack operation.

Pusher Configurations at Zero Degrees Angle-of-Attack

The geometry of the pylon and the definition of spacing of the pylon to the front rotor is defined in Figure 66. The purpose of the pylon and extended spinner shown in the figure was to simulate a pusher Prop-Fan configuration using basic tractor hardware. Two pylon chord spacings were tested, a .1 chord and .2 chord spacing.

Pusher Versus Tractor Effects - Comparisons are made in Figure 67 between the noise of the tractor configuration and the pusher configuration, both at zero degrees angle-of-attack. This comparison was done for the nominal rotor-rotor spacing of $0.257D$. BPF levels increased when operating as a pusher compared to the tractor configuration. The higher harmonics showed some changes in directivity with the SPL levels remaining roughly the same. Figure 68 shows the same comparison for a test condition with a higher power loading and tip speed. For this case the BPF levels decreased during pusher operation. Higher harmonic directivity changed especially at the far forward positions during pusher operation. The tenth harmonic showed a noticeable decrease in level from tractor to pusher operation at the far forward microphone locations. The above plots suggest that the pylon in the pusher test configuration did not have a significant effect on the harmonic SPL noise levels.

Cruise Tip Speed Simulation - Cruise noise was simulated in the low speed wind tunnel environment by overspeeding the rotor to match the cruise tip helical Mach number. Because the operating conditions do not match the actual cruise conditions, the noise measurements are not the same as those for the actual cruise flight conditions. However, matching the tip helical Mach number and approximating the blade loading distribution results in noise levels which show the general characteristics of an actual cruise condition. It is to be noted that these data cannot be scaled directly to an actual cruise condition (as was the case for the take-off conditions). Cruise noise levels need to be calculated using a noise prediction methodology. The overspeed data can be calculated using a noise prediction methodology. The overspeed data can be used to "calibrate" the methodology which then can be used to calculate the actual cruise noise. This was done and will be described in a later section.

Figures 69 to 73 summarize the measured directivity for the first five harmonics of BPF, respectively. These are for the tunnel condition which most closely matches the tip helical Mach number and blade loading distribution of the actual CRP-X1 cruise design condition of 0.72 Mn, 229 m/sec (750 ft/sec) tip speed, and 10668 m (35,000 ft) altitude.

Figure 69 shows the BPF peaking near the plane of rotation, with fairly significant reductions in levels at forward distances. The forward data shows some effect of circumferential directivity, which is probably a result of the presence of the pylon. At one diameter forward, the levels are down about 15 dB from the peak. Similar results are seen for the higher harmonics in Figures 70 to 73. At the higher harmonics, the forward directivity tends to flatten beyond about 0.5 diameter. This could be an indication of the presence of aerodynamic interaction noise. However, these levels are again about 15 dB down from the peak

Pusher Configurations at 4 Degrees Angle-of-Attack

Pylon Spacing Effects - Figures 74 to 76 show the measured effect on the axial directivity of the noise of the pylon spacing. The pylon spacing parameter was previously defined in Figure 66. These cases represent equal front and rear rotor RPM, 0.257D (nominal) rotor-rotor spacing, and the rotor/pylon at 4 degrees angle-of-attack.

The spectra comparisons in these figures show a very small effect of pylon spacing on the measured levels up to the 10th harmonic. This is reflected in the calculated PNL. A weak effect can be seen. At the two higher power conditions, Figures 75 and 76, increasing the pylon spacing from 0.1 to 0.2 chords results in a decrease in EPNdB of about 0.5. The lower power condition shows a slight increase in noise as the pylon spacing is increased. The observed effects are small and may not be statistically significant. It can thus be stated that pylon spacing over the range tested has negligible effect on noise.

Rotor-Rotor Spacing Effects - The effect on noise of rotor-rotor spacing was measured at the 0.2 pylon chord spacing at 4 degrees angle-of-attack.

The directivity plots of Figure 77 compare the 0.257D rotor-rotor spacing case to the 0.363D rotor-rotor spacing case for a low power, low tip speed case. There was little change in level at BPF with the increased spacing. The higher harmonics showed some directivity changes but the levels are approximately the same.

Figure 78 shows the same comparison for a greater power loading. The results are the same: the level of BPF noise was not affected and the levels of the higher harmonics showed only subtle changes. A high tip speed case is plotted in Figure 79. For this case BPF levels increased with increased rotor-rotor spacing. Higher harmonic levels were not substantially affected by the increased rotor/rotor spacing. As seen by the directivity plots and the EPNdB comparisons, increasing the rotor-rotor spacing had little or no effect on noise levels over a wide range of operating conditions for the range measured.

Angle-of-Attack Effects - A comparison can be made between the pusher at zero degrees angle-of-attack and the pusher at 4 degrees angle-of-attack, as was previously discussed for the tractor configuration.

The effect of angle-of-attack on harmonic noise levels during pusher operation is shown in Figure 80 for an operating condition of 511 kW/D² (63.7 SHP/D²), 202 m/sec (662 ft/sec) tip speed and a 59/41 power split. As can be seen, all harmonic SPL levels remained approximately the same. BPF levels increased slightly with increased angle-of-attack. The tenth harmonic levels increased at the forward microphone locations and decreased at the aft microphone locations. All other harmonic levels remained about the same with subtle changes in directivity. Figure 81 shows the angle-of-attack effect for a higher power loading and tip speed than was shown in the previous figure. BPF levels increased substantially at the 4 degrees attack angle at microphone locations near the plane of rotation. The second, third and fourth harmonics decreased in level at forward microphone locations. The tenth harmonic increased at the forward location and decreased at the aft locations as in the previously discussed figure. Results of the data analysis suggests that the angle-of-attack effect was not as substantial as was observed during tractor testing. This may be explained by the pylon acting to turn part of the inlet flow in a direction more nearly parallel to that of the Prop-Fan axis during pusher operation.

Pusher Versus Tractor Comparison

The comparison can also be made between the pusher at 4 degrees angle-of-attack and the tractor at zero degrees angle-of-attack. This comparison has significance in that the configuration with the pylon at 4 degrees angle-of-attack represents an installed pusher configuration during a take-off climb condition (i.e., modeling reality) while the tractor at zero degrees angle-of-attack represents a configuration with minimal inflow disturbances (i.e., the laboratory). It is to be noted that the most noise prediction methods would address the latter case.

The comparison between tractor at zero degrees angle-of-attack and pusher at 4 degrees angle-of-attack is shown in Figure 82 for a low power, low tip speed condition having a front-to-rear power split of 59/41. The pusher data clearly shows higher levels at BPF and changes in harmonic directivities. The pusher at 4 degrees angle-of-attack shows an increase of 1.3 EPNdB compared to the level of the tractor at zero degrees angle-of-attack.

Figure 83 contains the directivity plots of the pusher at angle-of-attack compared to those of the tractor at zero degrees angle-of-attack for approximately the same tip speed and power split (58/42) as the previous figure, but at a higher power loading. Comparisons at this power loading gave similar results, the pusher installation at four degrees angle-of-attack had a substantial increase in noise level at BPF. The higher harmonics had substantial changes in directivity and the tenth harmonic increased in level. Comparison based on EPNL indicates that the pusher is 2.9 EPNdB higher than the tractor. This is higher than was seen in the previous figure, indicating that the installation effects may have a larger influence on noise at higher power.

Figure 84 shows the comparison of the pusher at four degrees angle-of-attack to the tractor at zero degrees angle-of-attack for approximately the same power loading and power split as the previous figure, but at a higher tip speed. Results from this case are very similar to those of the previous figure that was discussed.

In summarizing the three cases it was observed that the pusher at four degrees angle-of-attack configuration had higher noise levels when compared to the tractor configuration at zero degree angle-of-attack. It is also evident that the increase in EPNL for the pusher at four degrees angle-of-attack is more at the higher power loading condition.

Summary of Configuration Effects on Noise

The previous discussion presented the results of configuration changes on noise in some detail. However, the appropriate metric for airplane noise certification is Effective Perceived Noise Level (EPNL), since current regulations require that aircraft noise levels not exceed the specified EPNL limits in order to be certified. To be meaningful, EPNL must be in full-scale, since propeller tone frequencies vary inversely with diameter for a specified tip speed. For the purposes of the following discussion the CRP-XI model data was geometrically scaled to 4.0 m (13.1 ft) in diameter. Although a full-scale CRP might be a different size depending on the actual airplane, this is an acceptable size to show reliable effects.

The results of configuration changes on EPNL are summarized in Table VII for operating conditions covering a large range in power loading and tip speed. The following comparisons can be made:

Rotor-Rotor Spacing Effects

At zero degrees angle-of-attack, the tractor configuration shows no consistent, significant trend in noise with rotor-rotor spacing. A small effect is seen in increasing the spacing to 0.363D, but the level for 0.461D spacing is the same as that for the 0.257D spacing cases. On an average, the rotor-rotor spacing effect shows a decrease of 0.3 EPNdB from 0.257D to 0.363D, and an increase of 0.1 EPNdB between 0.257D and 0.461D. The pusher

at 4 degrees angle-of-attack at the 0.2 pylon chord spacing shows an average increase of 0.1 EPNdB for a rotor-rotor spacing change from 0.257D to 0.363D. It can thus be concluded that over the range tested rotor-rotor spacing changes had negligible effect on noise.

Tractor Angle-of-Attack Effects

For the tractor configuration, angle-of-attack effects were significant. A consistent increase of 3 to 5 EPNdB is seen for almost all operating conditions. It can thus be concluded that angle-of-attack effects for the tractor configuration are significant, raising the noise by an average of 3.5 EPNdB for angle-of-attack increase of four degrees.

Pusher Pylon Spacing Effects

At zero degrees angle-of-attack increasing the pylon-to-rotor spacing shows a small increase in noise. An average increase of 0.5 EPNdB can be seen for a doubling of pylon spacing. At four degrees angle-of-attack, a smaller effect is seen, showing an average reduction of 0.3 EPNdB for a doubling of pylon spacing. Again, it can be concluded that for the range tested, pylon spacing has small effect on noise.

Pusher Versus Tractor Effects

At zero degrees angle-of-attack, the installation of the pylon results in an average increase of 1.0 EPNdB for the close pylon spacing, or 1.5 EPNdB for the far pylon spacing. It can be concluded that the pylon effect at zero degrees angle-of-attack is a little more than 1 EPNdB. At four degrees angle-of-attack, however, the effect is significantly different. The effect of adding a pylon is a decrease in noise compared to that for the tractor at four degrees angle-of-attack. On average, the presence of the pylon for the four degree angle-of-attack pusher decreases noise by slightly more than 1 EPNdB, depending on pylon spacing and rotor-rotor spacing. It is thus apparent that adding a pylon at angle-of-attack has a small beneficial effect on noise. It was expected that the effect would be much greater, since adding a pylon increases noise by about 1 EPNdB at zero degrees angle-of-attack and increasing angle-of-attack increases noise by about 3.5 EPNdB. Thus, combining the effects would result in an increase of 4.5 EPNdB for the pylon at four degrees angle-of-attack compared to the tractor at zero degrees angle-of-attack. The actual measured effect is about 2.5 EPNdB. The difference may be attributed to the fact that the pylon tends to straighten the flow into the rotors, since it is aligned with the axis of rotation, and thus reduces the angle-of-attack effect seen by the tractor configuration.

NOISE PREDICTIONS AND COMPARISON WITH MEASUREMENTS

Prediction Methodology

The method used for predicting the noise of CRPs is one developed at Hamilton Standard. It is based on a frequency domain method (Reference 4) originally developed for SRP. This method calculates steady sources including thickness (monopole) noise, steady loading (dipole) noise, and non-linear (quadrupole) noise. Each of these sources contributes in differing amounts depending on design and operating condition. In 1984 the method was extended to include unsteady loading noise (Reference 5), as needed for inclusion of the CRP aerodynamic interaction noise source. This method includes the unsteady loading noise at the rear rotor resulting from viscous and potential wakes generated by the front rotor and convected into the rear rotor.

Initial correlation of the method with CRP-XI noise measurements showed some deficiencies at the higher harmonics, which for low speed take-off conditions are due to aerodynamic interaction. An empirical factor was added to the rear rotor blade lift response function, which is used in the calculation of fluctuating blade loads at the rear rotor resulting from the upstream rotor wakes, to improve the correlation. This method was used to make the noise predictions discussed in the following sections.

Comparison of Predictions and Measurements

Far-field Noise Directivities

Harmonic directivity predictions were made for a representative low-speed condition to evaluate the prediction method. For this evaluation the directivities of the first ten harmonics were calculated and compared to the CRP-XI noise measurements. The measured data were corrected for shear-layer propagation and adjusted to a constant sideline distance.

Figure 85 shows the agreement between prediction and measurement for BPF. The prediction is seen to be slightly higher in level than the measurement, but the fore and aft directivity shows quite good agreement. This harmonic is dominated by steady loading noise.

Figure 86 shows the comparison of prediction and measurement at 2 times BPF. The measurement exceeds the prediction. In general, the shape of the curve in the forward arc shows similar characteristics between the measurement and prediction. Aft of the plane of rotation, particularly aft of the 120 degree emission angle, there is a significant underprediction of the measurement. At further aft locations the agreement becomes better.

The comparison of predictions and measurements at 3 times BPF is shown in Figure 87. The level and directivity of the prediction agrees reasonably well with measurements particularly in the forward quadrant. However, there is some underprediction of the peak aft of the 120 degree emission angle.

Figure 88 shows the comparison of measurement and prediction at 4 times BPF. The measurement exceeds the prediction around 100 degrees. However, at fore and aft directivities, the agreement is quite good.

Figure 89 shows a comparison of prediction and measurement at 5, 6 and 7 times BPF. The agreement for 5 times BPF is quite good. At 6 times BPF, there is some underprediction near 140 degrees emission angle. At 7 times BPF the agreement is quite good except near the plane of rotation where there is some underprediction.

The comparison of prediction and measurement for 8, 9 and 10 times BPF is shown in Figure 90. Some underprediction can be seen around the 80 degree emission angle for 8, 9 and 10 times BPF. However, the other directivities show reasonable agreement.

Scaled Far-Field Perceived Noise Level

As a means for evaluating the combined effects of spectral characteristics and directivities, comparisons were made between predicted and measured Effective Perceived Noise Levels. The measured EPNL are based on geometric scaling of the measured CRP-X1 noise levels. Scaling was necessary to provide harmonic frequencies that are correct because EPNL is frequency dependent. Free-field flyovers were synthesized from the data assuming level flight at the speed of the tunnel. The calculations were done for the scaled conditions.

Figure 91 summarizes the comparison. For this figure the difference between predicted and measured EPNL was plotted against tip speed, since the tip speed showed a mild trend. Also, an effect of front rotor power can be seen. From Figure 91 it can be seen that the measured levels are fairly well predicted (within about 1 EPNdB) for tip speeds from 180 m/sec (590 ft/sec) to 200 m/sec (650 ft/sec) with some underprediction at higher tip speeds. There is some tendency to underpredict the noise as the front rotor power is reduced, but this error is generally less than 1 dB.

Near-Field Noise Directivities

Noise predictions were made for the model operating at a flight Mach number of 0.26 with the rotational tip speed increased to match the helical tip Mach number which occurs in actual cruise. Because the noise measurements were made in the flow, no shear-layer transmission corrections were made to the measurements. Thus, the calculations and measurements can be compared directly.

Comparisons of the overspeed ($M_{t,n} = 1.054$) 0.2 diameter tip clearance data and theoretical calculations are shown in Figures 92 through 96 for BPF harmonics 1 through 5, respectively. It can be seen that in general the agreement between the measured and calculated levels is very good. The directivities agree quite well except for the forward locations at 2 times BPF, where the predicted levels show a more rapid decrease in level than do

The measurements. For all five harmonics the peak noise levels are in close agreement, typically within 2 dB. The aft directivity shows essentially perfect agreement in all cases. At the forward locations the predicted levels generally fall within the range of measured levels, except for the most forward location where an underprediction of about 5 to 6 dB is seen at BPF, 4 x BPF, and 5 x BPF. At the most forward location, 2 x BPF shows an underprediction of about 8 dB, but at 3 x BPF the calculation overpredicts by about 5 dB. These underpredictions may possibly be associated with reflections from the pylon, which are not predicted in the existing methodology.

It is thus concluded that the noise prediction method shows good comparison with the measurements and that there is no need for any empirical adjustments to the near-field noise prediction methodology.

Full-Scale Noise Predictions

Far-Field Noise During Low Speed Flight

Because the CRP-X1 model was tested at the tip speeds and power loadings representative of a full-size CRP, the test data can be scaled geometrically to represent the full-scale noise for a level flyover at 0.26 Mn. Several scaled predictions were presented in earlier discussions.

As a representative full-scale take-off condition noise estimate, the 5 x 5 bladed CRP-X1 was scaled to a full-size diameter of 4.0 m (13.1 ft). Table VIII summarizes the estimated noise levels for a level flyover of two CRPs. The installation effects are the average measured during this test program. Therefore the estimated level of 93.1 EPNdB should be very close to the actual full-scale measurement.

Near-Field Noise at Cruise Conditions

Near-field noise estimates were made for two cruise conditions: 0.72 Mn (the CRP-X1 design condition) and 0.80 Mn, both at 10668 m (35,000 ft) altitude. The powers for the two flight speeds are the CRP-X1 design power loadings of 311 kW/D² (38.8 SHP/D²) at 0.72 Mn and 336 kW/D² (41.9 SHP/D²) at 0.8 Mn. Both cases were run at the design tip speed of 229 m/sec (750 ft/sec) and at a reduced tip speed of 198 m/sec (650 ft/sec). Estimated levels are along a line parallel to the CRP axis of rotation with a 0.2 diameter tip clearance under free-field conditions. In both cases, the noise levels were estimated using the analytical noise prediction method.

Figure 97 shows the noise levels calculated for the 0.72 Mn, 229 m/sec (750 ft/sec) tip speed condition. The estimated levels show that the peak noise occurs at the midpoint between the two rotors where the sound pressure level at BPF is about 143 dB. Noise levels roll off quickly forward of the peak, where levels drop by 14 to 30 dB at 0.5 diameters forward.

Figure 98 summarizes the 0.80 Mn, 229 m/sec (750 ft/sec) tip speed calculated noise levels as a function of harmonic and directivity. The peak noise occurs at the midpoint between the two rotors, at a sound pressure level at BPF of 147 dB. However, the noise levels roll off rapidly forward, where levels are down more than 20 dB at 0.5 diameters forward of the midpoint between the rotors.

Figures 99 and 100 show the estimated levels for the 198 m/sec (650 ft/sec) tip speed conditions at 0.72 Mn and 0.8 Mn, respectively. At the power tip speeds, it can be seen that the peak noise levels are lower than those for the 229 m/sec (750 ft/sec) tip speed condition shown in Figures 97 and 98. Also, the levels of the higher harmonics are relatively lower than was the case for the higher tip speed conditions. At the 198 m/sec (650 ft/sec) tip speed conditions, the peak levels at BPF are 138 dB at 0.72 Mn and 143 dB at 0.8 Mn.

CONCLUSIONS

As a result of the analyses described in this report, the following conclusions were reached. Because of the scope of the analyses, the conclusions have been arranged in several logical categories.

Tractor Configuration at Zero Degree Angle-of-Attack, Nominal Rotor/Rotor Spacing

1. As power and tip speed were increased, noise levels increased. A minimum noise level was reached as tip speed decreased to 183 m/sec (600 ft/sec).
2. The change in noise level with tip speed was greatest in the range from 198 m/sec (650 ft/sec) to 229 m/sec (750 ft/sec).
3. Increasing front rotor power relative to that of the rear rotor showed a small adverse effect on noise. Conversely, reducing front rotor power relative to that of the rear rotor showed a small noise benefit. This effect was less pronounced as total power increased.
4. Increasing the front rotor tip speed while decreasing the rear rotor tip speed lowers noise whereas increasing the rear rotor tip speed while decreasing the front rotor tip speed raises noise. The effect, however, is relatively small. The total effect for an RPM ratio change of ± 20 percent is about 2 EPNdB.

Other Tractor Configuration Effects

1. Noise level differences for the three rotor-rotor spacings tested were less than 2 dB. For most cases, rotor-rotor spacing effects were negligible.
2. The tractor configuration noise levels increased 3 to 4 EPNdB when the angle-of-attack was changed from 0 to 4 degrees. A larger increase in level was seen in the blade passing frequency tone than in the higher harmonics.
3. Angle-of-attack effects showed a greater increase in noise underneath the flight path than at sideline locations.

Pusher Configuration Effects

1. Installation of the pylon in front of the CRP raised noise levels 1 to 1.5 EPNdB at zero angle-of-attack. However, installation of the pylon at 4 degrees angle-of-attack showed an average increase of only 2.5 EPNdB compared to the tractor at zero angle-of-attack.
2. Pylon-to-rotor spacing had little effect on noise levels.
3. Rotor-to-Rotor spacing alone and in combination with pylon-to-rotor spacing had little or no effect on noise.

CRP Noise Predictions

1. The far-field noise prediction method used to make CRP noise predictions showed good agreement for cases in the 198 m/sec (600 ft/sec) tip speed range. Approximately 2 EPNdB underprediction was seen at higher tip speed conditions.
2. The near-field noise prediction method showed good agreement with measurements over the full directivity range.
3. Scaling of the CRP-X1 to 4.0 m (13.1 ft) diameter full-scale installations gave estimated noise levels of 93.1 EPNdB for a twin engine airplane during take-off on a 457 m (1500 ft) sideline.
4. Near-field noise estimates during cruise showed peak noise levels of 143 dB, dropping by 14 dB at 0.5 diameter forward, for the CRP-X1 operating at 229 m/sec (750 ft/sec) tip speed at 0.72 flight Mach number and 147 dB, dropping by more than 20 dB at 0.5 diameter forward, for the CRP-X1 operating at 229 m/sec (750 ft/sec) tip speed at 0.80 flight Mach number. At a tip speed of 198 m/sec (650 ft/sec) the estimated peak noise levels are 138 and 143 dB for the 0.72 Mn and 0.8 Mn conditions, respectively.

TABLE I. ACOUSTIC DATA INSTRUMENTATION

<u>Item No.</u>	<u>Item</u>	<u>Manufacturer</u>	<u>Manufacturer's Designation</u>	<u>Location</u>
1	1/4" Microphone	Bruel and Kjaer	4135/4136	T.C.*
2	Microphone Adapter	Bruel and Kjaer	UA0035	T.C.
3	Preamplifier	Bruel and Kjaer	2619	T.C.
4	Power Supply	Bruel and Kjaer	2801	T.C.
4A	2 Cha. Mic Power Supply	Hamilton Standard	-	C.R.**
5	Pistonphone	Bruel and Kjaer	4220	T.C.
6	Adapter	Bruel and Kjaer	JJ2615	T.C.
7	RMS Volt Meter	TSI	1076	C.R.
8	Signal Generator	Hewlett Packard	3311A	C.R.
9	Frequency Counter	Fluke	1900A	C.R.
10	Amplifier System	UTRC	-	C.R.
10A	Amplifier System	Hamilton Standard	-	C.R.
11	RMS Volt Meter	TSI	1076	C.R.
12	Oscilloscope	Tektronix	D105A14N	C.R.
12A	Oscilloscope - 4 Cha.	Tektronix	-	C.R.
13	F.M. Tape Recorder	Honeywell	96	C.R.
13A	F.M. Tape Recorder	Ampex	AR200	C.R.
14	Spectrum Analyzer	Wavetek	660B	C.R.
15	Digital Plotter	Nicolet	136A	C.R.

*T.C. = Test Chamber

**C.R. = Control Room

TABLE II. INSTRUMENTATION ACCURACY AND RANGE

<u>Item No.</u>	<u>Item</u>	<u>Range</u>	<u>Accuracy</u>
1	1/4" Microphone	1 Hz to 100 KHz	Response = \pm .5 dB to 10 KHz
5	Pistonphone	124 dB SPL	+/- .25 dB
7	RMS Volt Meter	0 to 100 volts	+/- 1% of reading
9	Frequency Counter	5 Hz to 80 MHz	.1, 1, 10, 100 Hz resolution (manually selectable)
10	Amplifier System	0-50 dB Gain, 0-30 dB Attenuation	+/- .5 dB
11	RMS Volt Meter	0 to 100 Volts	+/- 1% of reading
13	Tape Recorder	Dynamic Range = 60 dB Frequency Range = 0 to 100 KHz	+/- .25 dB to 10 KHz
14	Spectrum Analyzer	1 Hz to 100 KHz	+/- .5 dB
21	Barometer	0 to 31 inches Hg	+/- 1.0 mm Hg
30	Aerodynamic Wedge Probe	-10° to +10°	+/- .25°
31	Inclinometer	0° to 90°	+/- .02°
32	Manometer	0 to 5 inches H ₂ O	+/- .02 inches H ₂ O
33	Differential Pressure Transducer	-5 to +5 psid	+/- .15% of range
37	A/D Converter	-100 to +100 Volts	+/- .01% +2 least sig. digits
52	500 psi Pressure Transducer	0 to 500 psia	+/- .25% of reading

TABLE II. INSTRUMENTATION ACCURACY AND RANGE (Continued)

<u>Item No.</u>	<u>Item</u>	<u>Range</u>	<u>Accuracy</u>
53	500 psi Pressure Transducer	0 to 500 psia	+/- .25% of reading
54	15 psid Pressure Transducer	-15 to +15 psid	+/- .25% of reading
55	15 psid Pressure Transducer	-15 to +15 psid	+/- .25% of reading

TABLE III. CRP-X1 FAR-FIELD MICROPHONE LOCATIONS AND SHEAR LAYER CORRECTIONS

Microphone Designation*	X_M	Y_M	Z_M	X_C	Y_C	Z_C	Δ_R	Corrected Emission Values R_R	Divergence Radiation ΔdB^*
A-1	1.219	0.990	0	0.871	1.308	0	43.85	1.726	4.31
A-2	1.219	1.537	0	0.779	1.800	0	52.80	2.101	2.97
A-3	0.752	1.988	-0.010	0.293	2.105	-0.010	67.15	2.190	1.62
A-4	-0.010	1.988	-0.010	-0.376	1.952	-0.010	86.12	1.992	0.24
A-5	-0.606	1.988	-0.010	-0.935	1.856	-0.010	103.31	2.038	-0.78
A-6	-1.359	1.988	-0.010	-1.690	1.715	-0.010	123.92	2.311	-1.92
A-7	-2.388	1.988	-0.010	-2.745	1.454	-0.010	145.10	2.925	-2.94
N-1	1.413	0	-0.572	1.413	0	-0.572	16.40	2.024	0+(-6.0)
T-1	0.321	1.048	-3.931	-0.597	1.040	-3.900	83.50	4.095	0.47
T-2	0.321	2.057	-2.921	-0.473	2.066	-2.933	82.64	3.604	0.52
T-3	0.194	2.026	-0.889	-0.244	2.013	-0.884	81.33	2.239	0.57
T-4	0.171	1.829	0.718	-0.201	1.826	0.717	80.87	1.991	0.58
T-5	0.098	0.711	0.876	-0.054	0.713	0.879	77.68	1.157	0.63
T-6	0.089	0.267	0.994	-0.037	0.267	0.997	76.97	1.058	0.63

* See Figure 10 for pictorial location

** To be added to measured levels

+ Inside shear layer flush with nozzle. -6 BD for pressure doubling.

NOTES: Dimensions in meters, angles in degrees. Origin is on axis mid-way between pitch change axes. X is along axis of rotation, positive forward. Y is positive up. Z is positive forward right facing forward. θ is zero on axis in forward direction.

TABLE IV. CRP-X1 MICROPHONE LOCATIONS
DURING BACKGROUND NOISE TEST

<u>Microphone Designation</u>	<u>Visual Locations</u>		
	<u>X_M</u>	<u>Y_M</u>	<u>Z_M</u>
A-1	1.219	0.991	0
A-2	1.219	1.537	0
A-3	0.752	1.988	-0.010
A-4	0.324	1.988	-0.010
A-5	-0.086	1.988	-0.010
A-6	-0.994	1.988	-0.010
A-7	-2.388	1.988	-0.010
T-1	0.321	1.048	-3.931
T-2	0.321	2.057	-2.921
T-3	0.321	2.026	-0.889
T-4	0.321	1.829	0.718
T-5	0.321	0.711	0.876
T-6	0.321	0.267	0.994

NOTE: Dimensions in meters. Origin is on axis mid-way between pitch change axes. X is along axis of rotation, positive forward. Y is positive up. Z is positive forward right facing forward.

TABLE V. ACOUSTIC TUNNEL FACILITY INSTRUMENTATION

<u>Item No.</u>	<u>Item</u>	<u>Manufacturer</u>	<u>Manufacturer's Designation</u>	<u>Location</u>
16	Pitot Probe	UTRC	--	Tunnel Inlet
17	Thermocouple	Project Inc.	CH-A1	Tunnel Inlet
18	Differential Pressure Gage	Wallace and Tiernan	62B	C.R. *
19	Static Pressure Probes	UTRC	--	T.C.**
20	Thermocouple	Project Inc.	CH-A1	T.C.
21	Barometer	Sergeant Welch	1215	C.R.
22	Thermocouple Readout	Omega	199-KFAD	C.R.
23	Hot Wire Probe	TSI	1218-T2	T.C.
24	Linearized Anemometer System	TSI	1054A	C.R.
25	10:1 D.C. Attenuator	UTRC	--	C.R.
26	Oscilloscope	Tektronix	5440	C.R.
27	X-Y Analog Plotter	Hewlett Packard	7035B	C.R.
28	X-Y Analog Plotter	Hewlett Packard	7035B	C.R.
29	Traverse Potition	UTRC	--	C.R.
30	Aerodynamic Wedge Probe	United Sensor	W-187-24-F-22-CD	C.R.

*C.R. = Control Room
 **T.C. = Test Chamber

TABLE V. ACOUSTIC TUNNEL FACILITY INSTRUMENTATION (Continued)

<u>Item No.</u>	<u>Item</u>	<u>Manufacturer</u>	<u>Manufacturer's Designation</u>	<u>Location</u>
31	Inclinometer	Hilger and Watts	TB108-1	C.R.*
32	Manometer	Dwyer	424	C.R.
33	Differential Pressure Transducer	Data Sensors	PB419	C.R.
34	Humidity Gage Readout	Texas Electronics	803	T.C.**
35	Humidity Gage	Texas Electronics	803	C.R.
36	Digital Computer	Hewlett Packard	9836	C.R.
37	Data Acquisition/Control Unit	Hewlett Packard	3497A	C.R.
38	400 psi Pressure Gage	Heise	CMM 58628	C.R.
39	400 psi Pressure Gage	Heise	CMM 58628	C.R.
40	400 psi Pressure Gage	Heise	CMM 58628	C.R.
41	Thermocouple Readout	Omega	199-KFAD	C.R.
42	Thermocouple Readout	Omega	199-KFAD	C.R.
43	Thermocouple Readout	Omega	199-KFAD	C.R.
44	Static Pressure Probe	UTRC	--	J.B.T.S.
45	Static Pressure Probe	UTRC	--	J.B.T.S.
46	Static Pressure Probe	UTRC	--	J.B.T.S.

*C.R. = Control Room

**T.C. = Test Chamber

TABLE V. ACOUSTIC TUNNEL FACILITY INSTRUMENTATION (Continued)

<u>Item No.</u>	<u>Item</u>	<u>Manufacturer</u>	<u>Manufacturer's Designation</u>	<u>Location</u>
47	Thermocouple	Project Inc.	CH-A1	J.B.T.S.
48	Thermocouple	Project Inc.	CH-A1	J.B.T.S.
49	Thermocouple	Project Inc.	CH-A1	J.B.T.S.
50	Signal Conditioner	UTRC	--	C.R.
51	Amplifier	Preston	DX-A1	C.R.

T.C. = Test Chamber

C.R. = Control Room

J.B.T.S. = Jet Burner Test Stand 400 psi Air Piping

TABLE VI. CRP DRIVE SYSTEM INSTRUMENTATION

<u>Item No.</u>	<u>Item</u>	<u>Manufacturer</u>	<u>Manufacturer's Designation</u>	<u>Location</u>
52	500 PSI Pressure Transducer	Bytrex	MPA500	On Drive Rig
53	500 PSI Pressure Transducer	Bytrex	MPA500	On Drive Rig
54	15 PSID Pressure Transducer	Microdot Inc.	DPT175-15PC	On Drive Rig
55	15 PSID Pressure Transducer	Microdot Inc.	DPT175-15PC	On Drive Rig
56	Static Pressure Probe	UTRC	--	On Drive Rig
57	Static Pressure Probe	UTRC	--	On Drive Rig
58	Static Pressure Probe	UTRC	--	On Drive Rig
59	Static Pressure Probe	UTRC	--	On Drive Rig
60	Thermocouple	Project Inc.	CH-A1	On Drive Rig
61	Thermocouple	Project Inc.	CH-A1	On Drive Rig
62	Signal Conditioner	UTRC	--	C.R.*
63	Signal Conditioner	UTRC	--	C.R.
64	Signal Conditioner	UTRC	--	C.R.
65	Signal Conditioner	UTRC	--	C.R.
66	Amplifier	Preston	DX-A1	C.R.
67	Amplifier	Preston	DX-A1	C.R.

*C.R. = Control Room

TABLE VI. CRP DRIVE SYSTEM INSTRUMENTATION (Continued)

<u>Item No.</u>	<u>Item</u>	<u>Manufacturer</u>	<u>Manufacturer's Designation</u>	<u>Location</u>
68	Amplifier	Preston	DX-A1	C.R.*
69	Amplifier	Preston	DX-A1	C.R.
70	Total Pressure Probe	UTRC	--	On Drive Rig
71	Total Pressure Probe	UTRC	--	On Drive Rig

*C.R. = Control Room

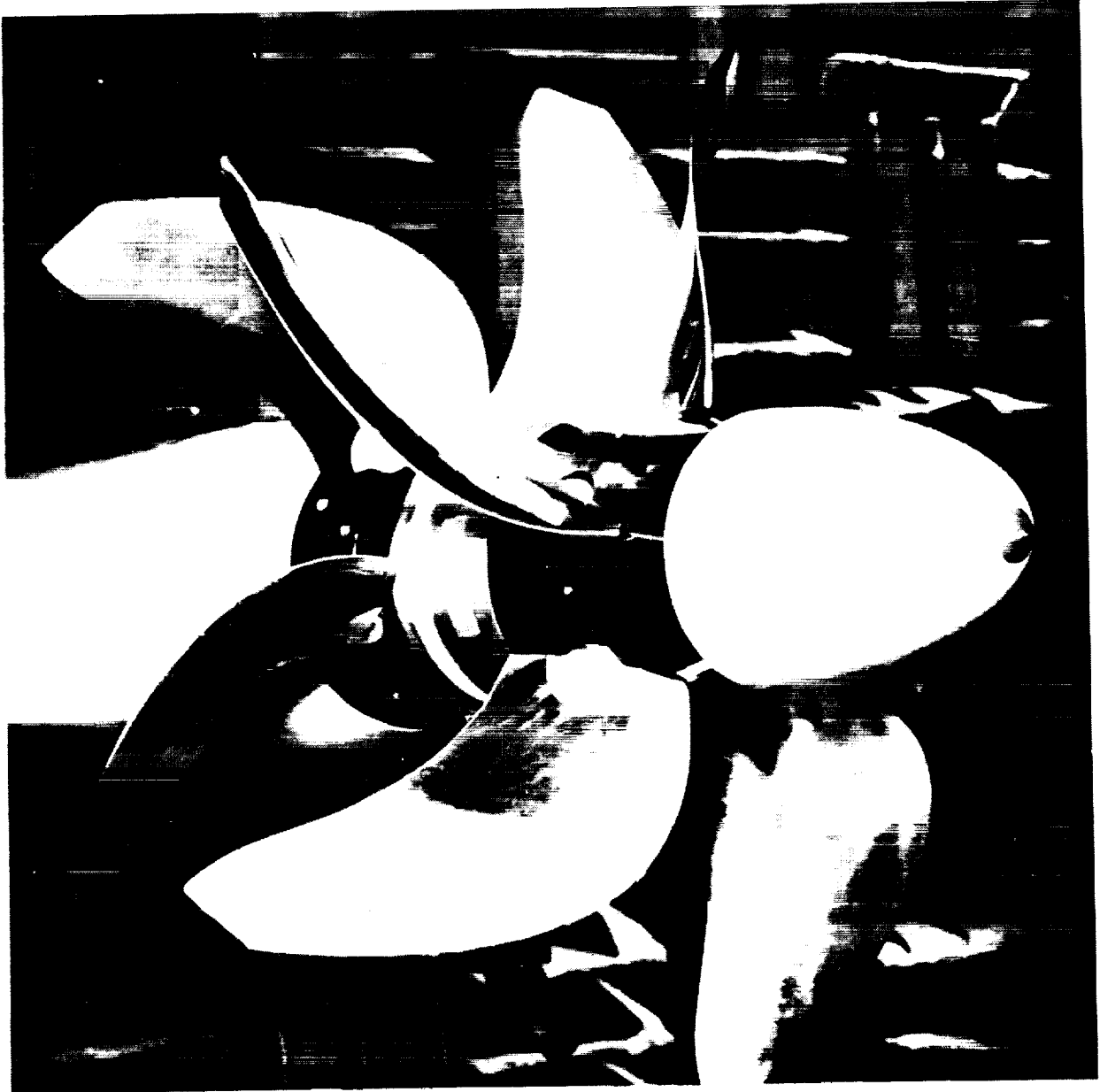
TABLE VII
 SUMMARY OF Δ EPNdB COMPARISONS FOR FULL-SCALE CRP-X1
 (Referenced to tractor configuration with 0.257D rotor-to-rotor spacing at 0° angle-of-attack)

Point	Blade Angle BF/BR	Tip Speed		Power Loading		Tractor Configuration			Pusher Configuration					
		m/sec	ft/sec	kW/D²	SHP/D²	$\alpha = 0^\circ$		$\alpha = 4^\circ$		$\alpha = 4^\circ$				
						0.257D	0.363D	0.461D	0.257D	0.257D	0.257D	0.257D	0.257D	0.363D
						No Pylon			Pylon Chord Spacing					
						0.1	0.2	0.1	0.2	0.1	0.2	0.2	0.2	
						Rotor-To-Rotor Spacing			Rotor-To-Rotor Spacing					
						0.257D	0.257D	0.257D	0.257D	0.257D	0.257D	0.257D	0.363D	
1	41.2/38.6	181	593	205	25.5	0.0	1.1	0.4	3.5	1.2	2.9	3.2	2.7	3.0
2	39.8/41.4	180	592	214	26.7	0.0	0.0	-0.2	3.5	-	-	-	-	-
3	44.1/42.8	183	599	323	40.3	0.0	-0.9	-0.3	3.3	0.7	1.4	0.6	1.1	1.8
4	49.8/44.3	184	604	509	63.4	0.0	-	-	-	1.7	2.4	2.7	2.4	1.7
5	49.8/44.3	190	624	580	72.3	0.0	-	-	-	2.4	2.3	3.3	3.0	2.3
6	39.8/41.4	193	633	303	37.8	0.0	0.1	0.3	5.2	-	-	-	-	-
7	41.2/38.6	197	645	307	38.3	0.0	-0.4	2.1	4.6	1.1	2.5	2.8	1.9	2.3
8	44.1/42.8	202	662	511	63.7	0.0	-0.8	0.0	1.7	0.6	-0.5	1.2	1.5	1.9
9	49.8/44.3	199	652	696	86.7	0.0	-	-	-	1.9	3.0	2.9	2.3	1.3
10	41.2/38.6	212	694	437	54.4	0.0	0.1	0.2	2.7	1.3	1.3	3.4	2.6	2.9
11	39.8/41.4	212	696	484	60.3	0.0	-0.8	-0.2	4.6	-	-	-	-	-
12	44.1/42.8	218	716	714	89.0	0.0	-1.3	-0.5	-0.4	-1.3	-0.7	2.2	1.6	2.0
13	49.8/44.3	215	705	939	117.0	0.0	-	-	-	1.2	1.6	3.4	2.4	2.2
14	41.2/38.6	232	760	648	80.7	0.0	-0.4	0.0	2.0	1.2	-0.8	2.8	2.4	2.8
15	39.8/41.4	231	758	701	87.3	0.0	-0.2	-0.3	5.3	-	-	-	-	-
16	44.1/42.8	233	766	934	116.3	0.0	-0.7	-0.2	3.7	0.4	2.2	1.9	1.6	2.1
17	39.8/41.4	240	789	831	103.5	0.0	0.1	-0.2	5.7	-	-	-	-	-
AVERAGE						0.0	-0.3	0.1	3.5	1.0	1.5	2.5	2.1	2.2

TABLE VIII. ESTIMATED FULL-SCALE CRP-X1 NOISE LEVELS
FOR A LEVEL FLYOVER AT 0.26 Mn

Configuration:	2 CRP-X1 Prop-Fans 4.0 m (13.1 ft) diameter Pusher configuration at 4 deg angle-of-attack	
Operating Condition:	198 m/sec (650 ft/sec) tip speed 618 kW/D ² (77 SHP/D ²) power 0.26 Mn flight speed	
Measurement Conditions:	457 m (1500 ft) altitude Free-field conditions	
Estimated Levels:	Level of one CRP	87.6 EPNdB
	Increment for 2 CRP	3.0
	Increment for Pylon	<u>2.5</u>
	Total estimated level	93.1 EPNdB

ORIGINAL PAGE IS
OF POOR QUALITY



ORIGINAL PAGE
BLACK AND WHITE PHOTOGRAPH

FIGURE 1. CRP-XI COUNTERROTATING PROP-FAN MODEL

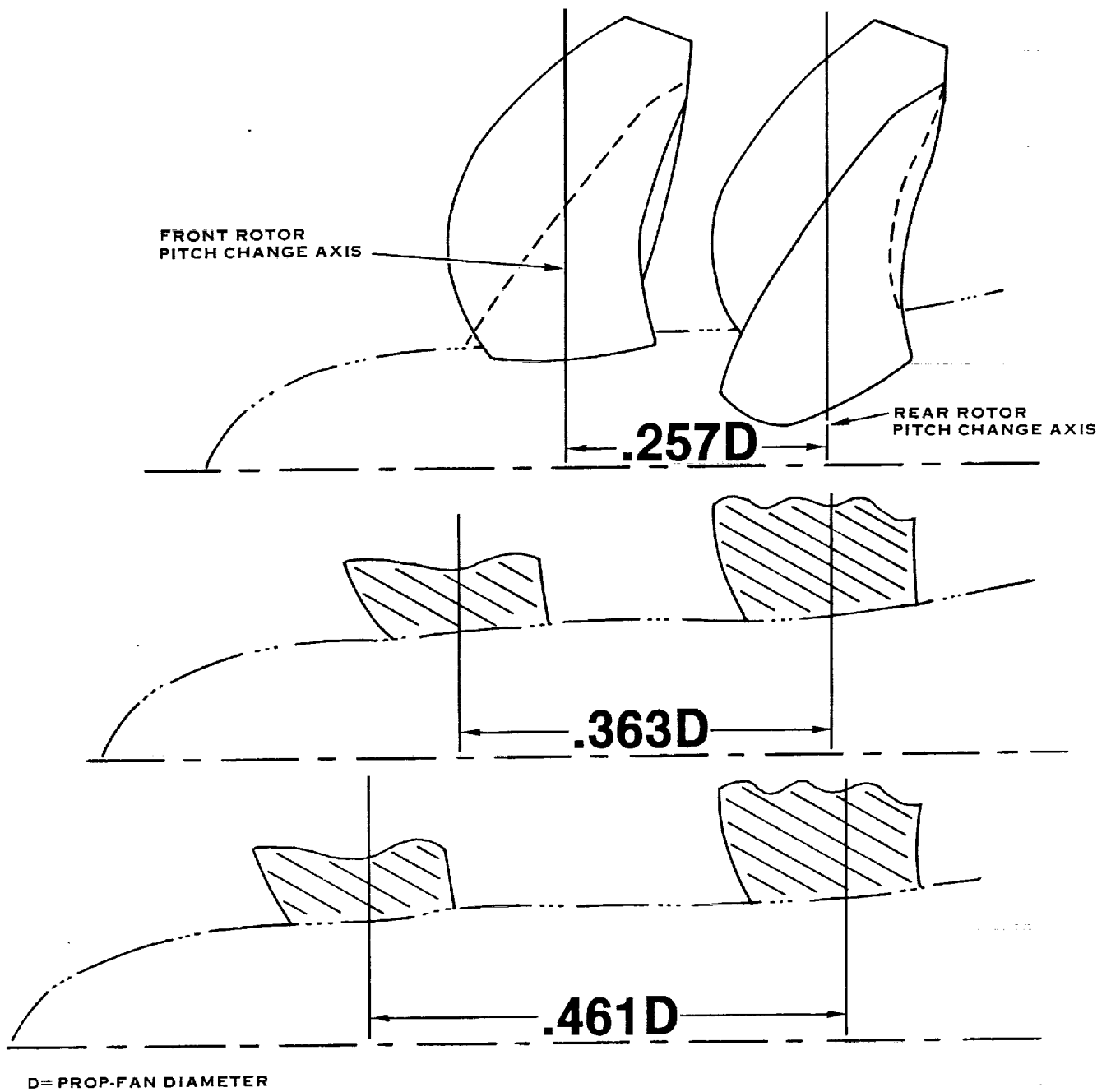


FIGURE 2. ROTOR-TO-ROTOR SPACING TEST CONFIGURATIONS

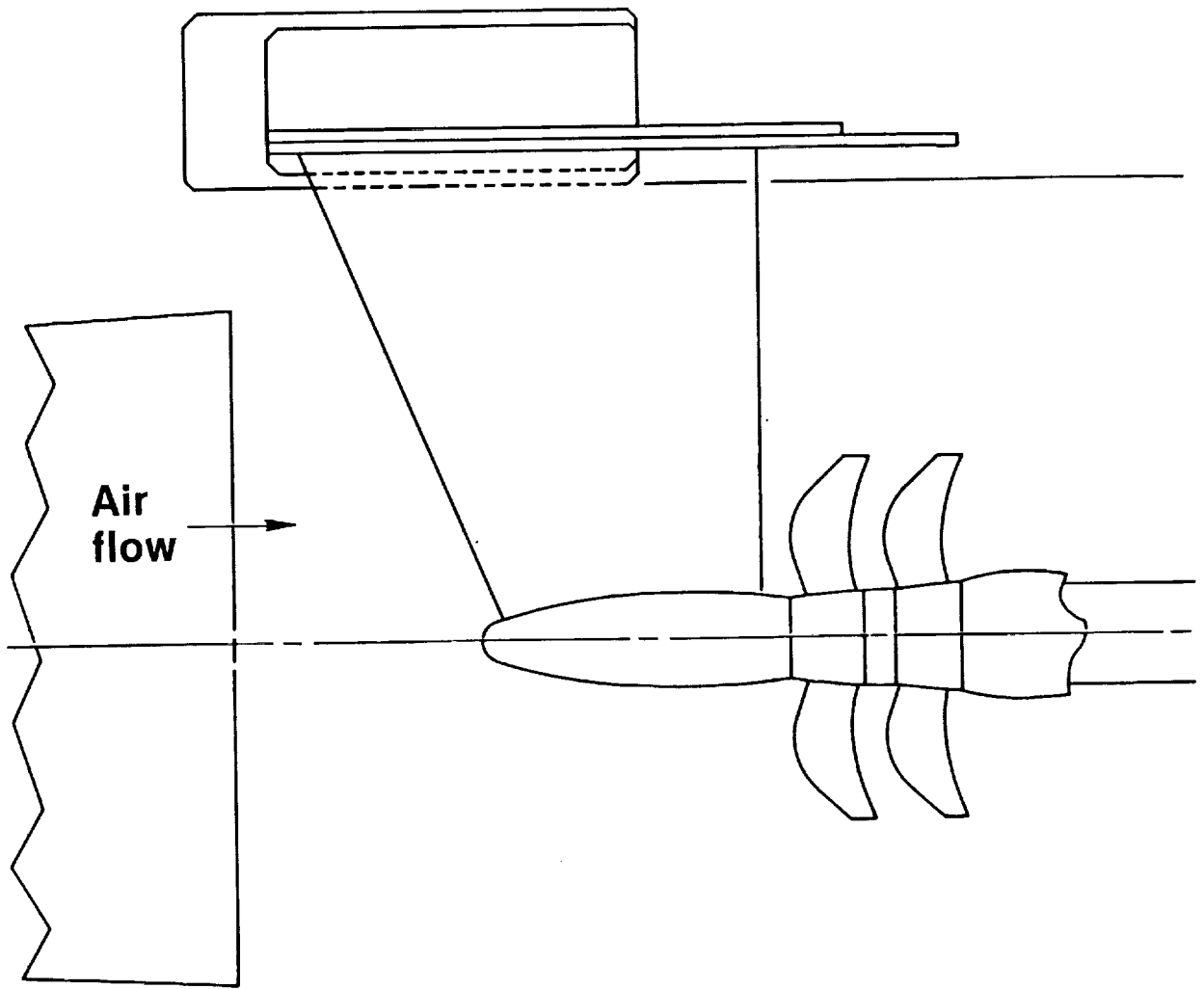
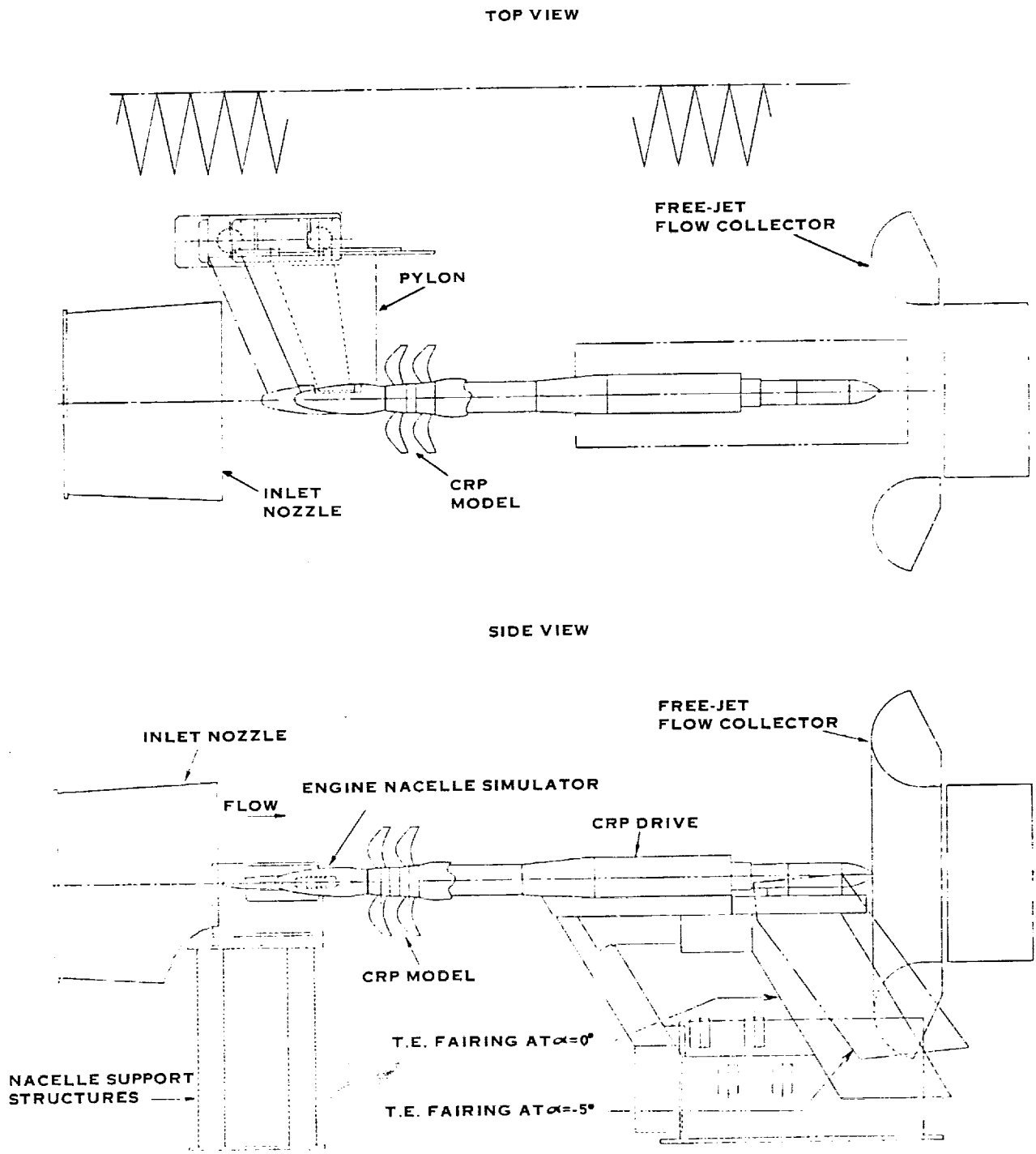


FIGURE 3. PYLON AND NACELLE ARRANGEMENT FOR PUSHER CONFIGURATIONS



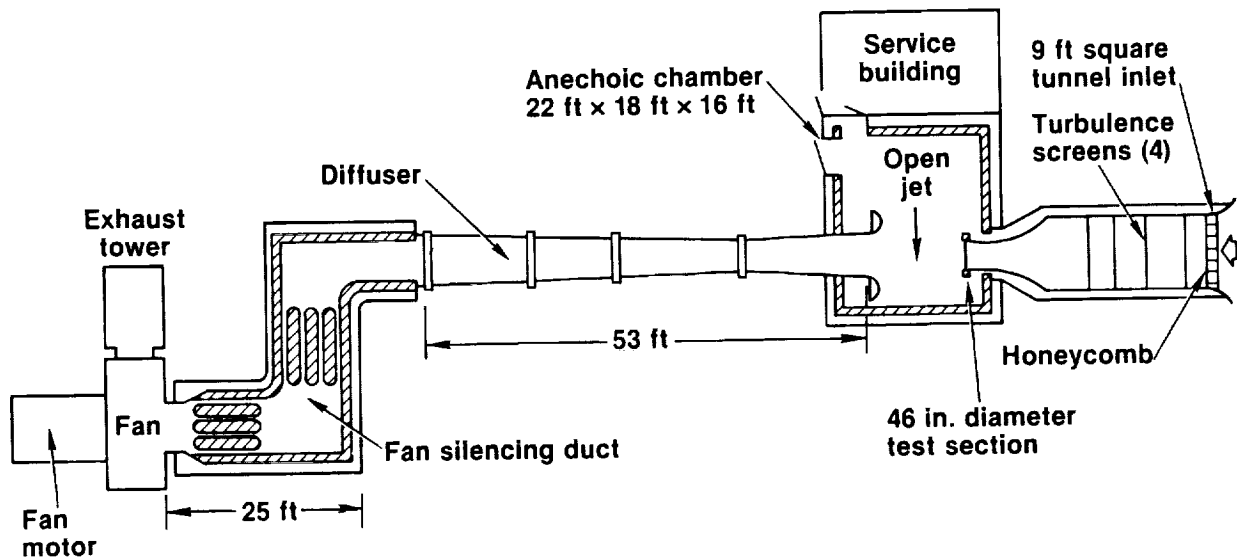


FIGURE 5. UNITED TECHNOLOGIES RESEARCH CENTER ACOUSTIC RESEARCH TUNNEL

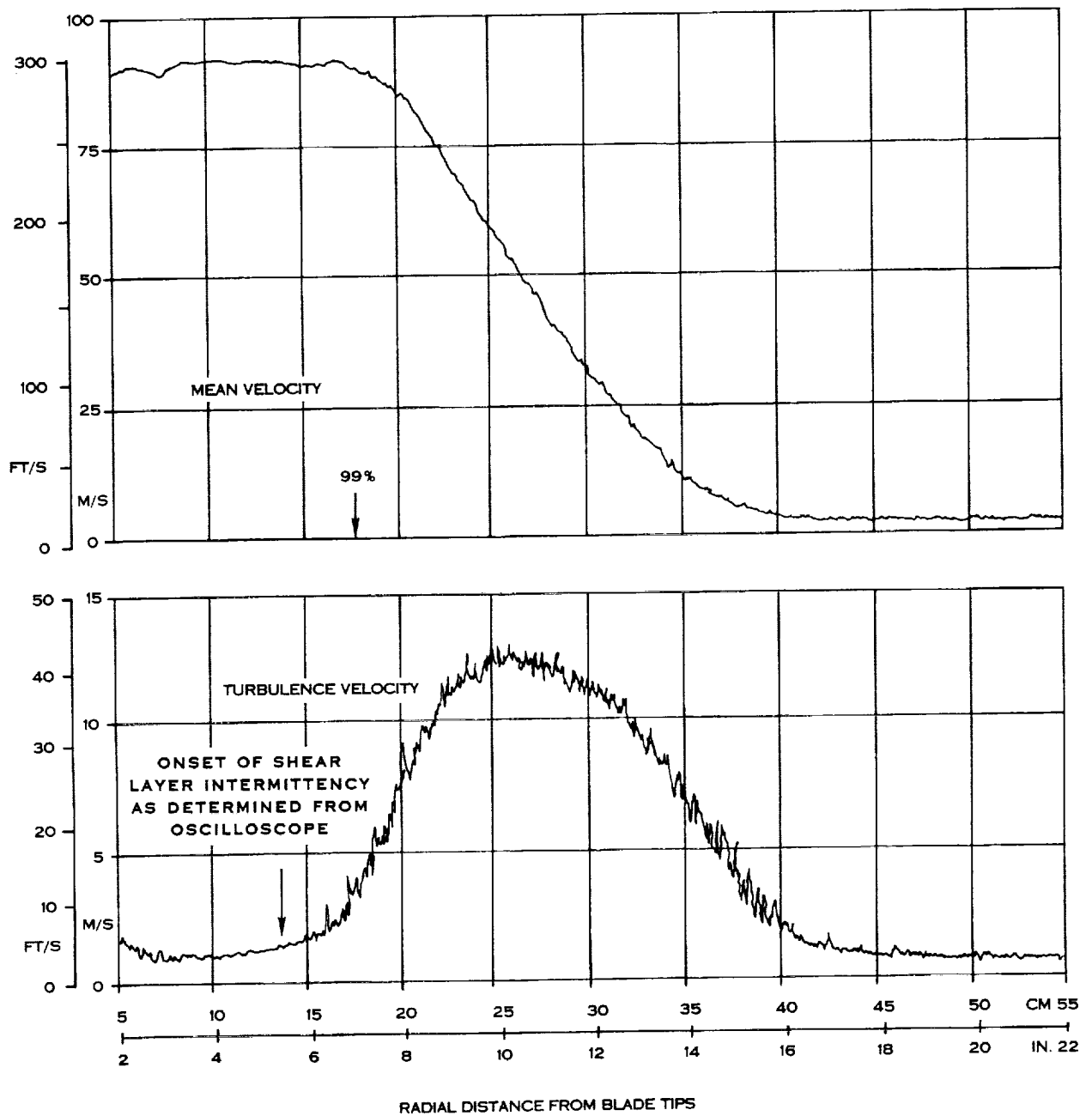


FIGURE 6. SHEAR LAYER VELOCITY SURVEY RESULTS AT MID POINT BETWEEN ROTORS

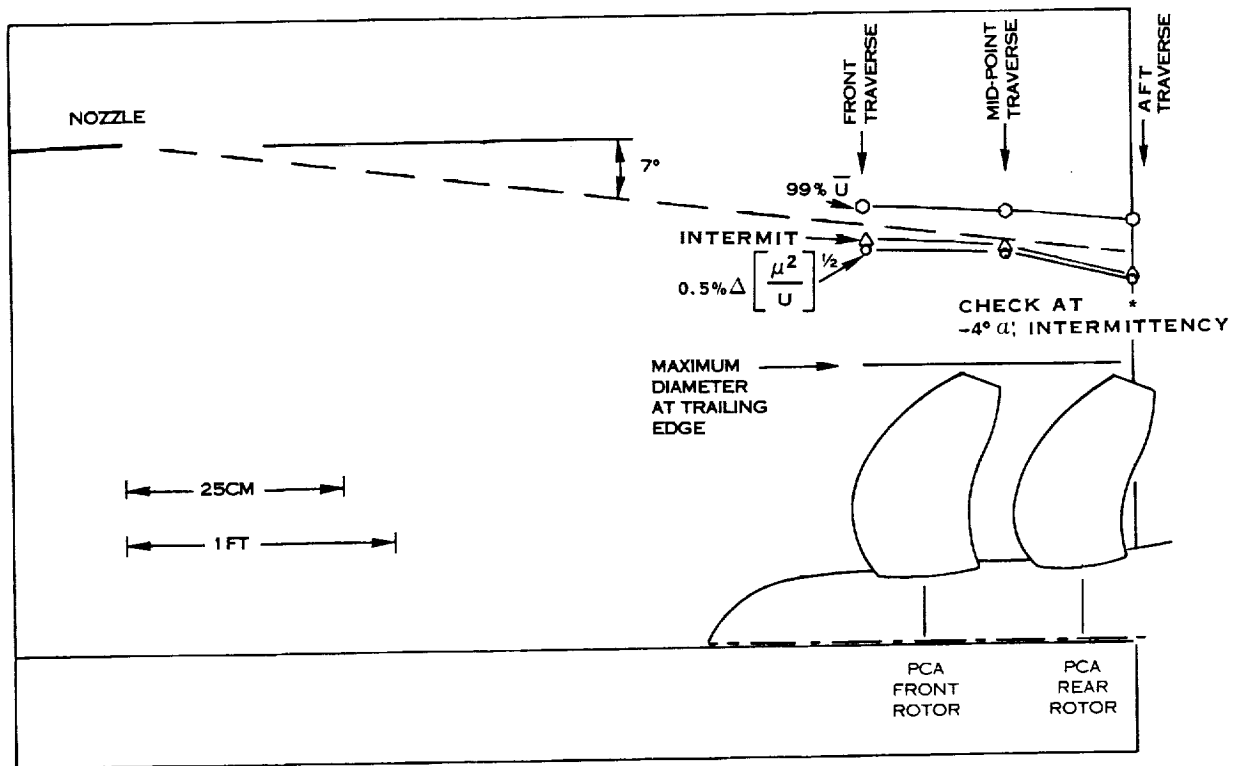


FIGURE 7. SUMMARY OF SHEAR LAYER EVALUATION

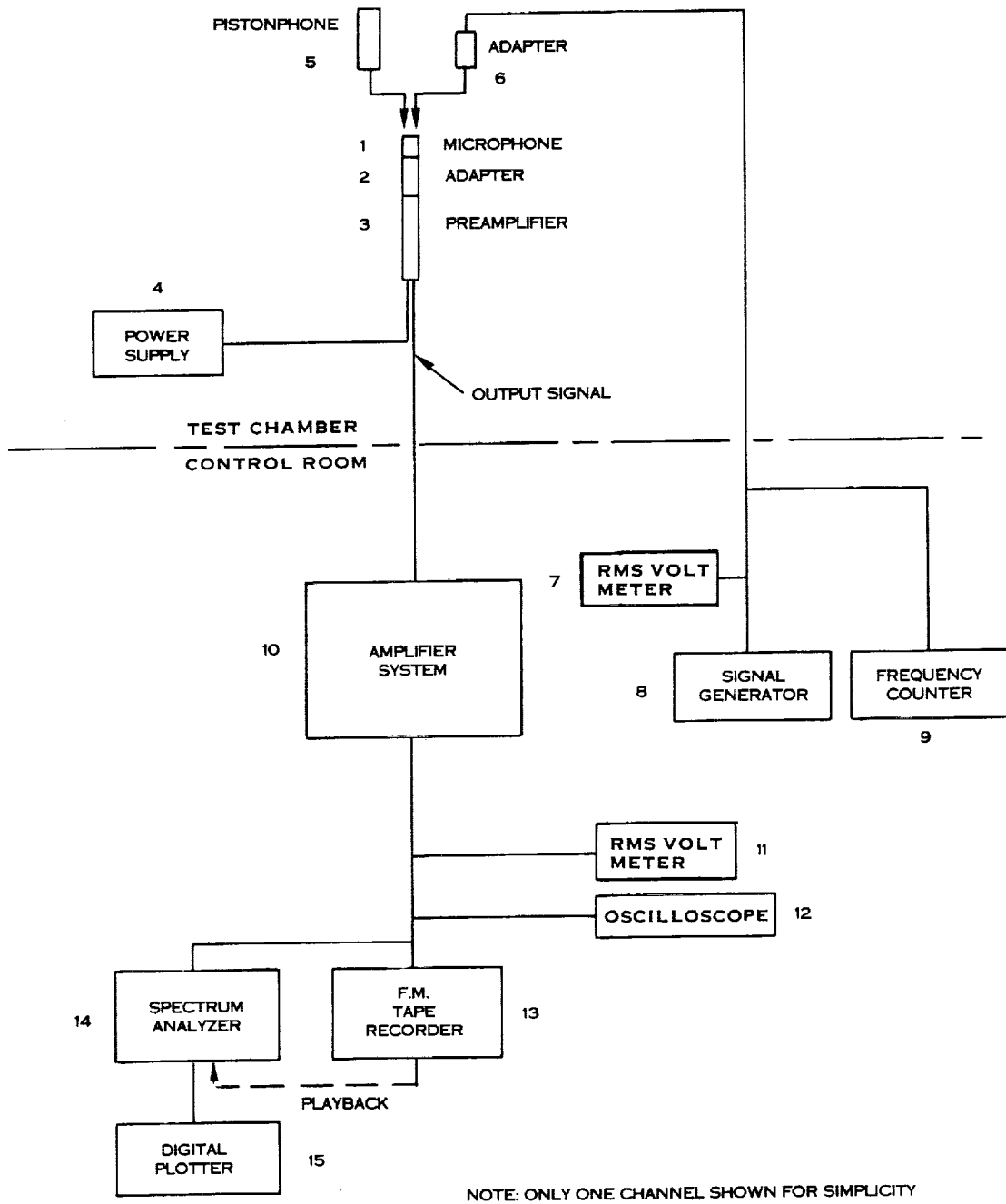


FIGURE 8. ACOUSTIC DATA ACQUISITION SYSTEM

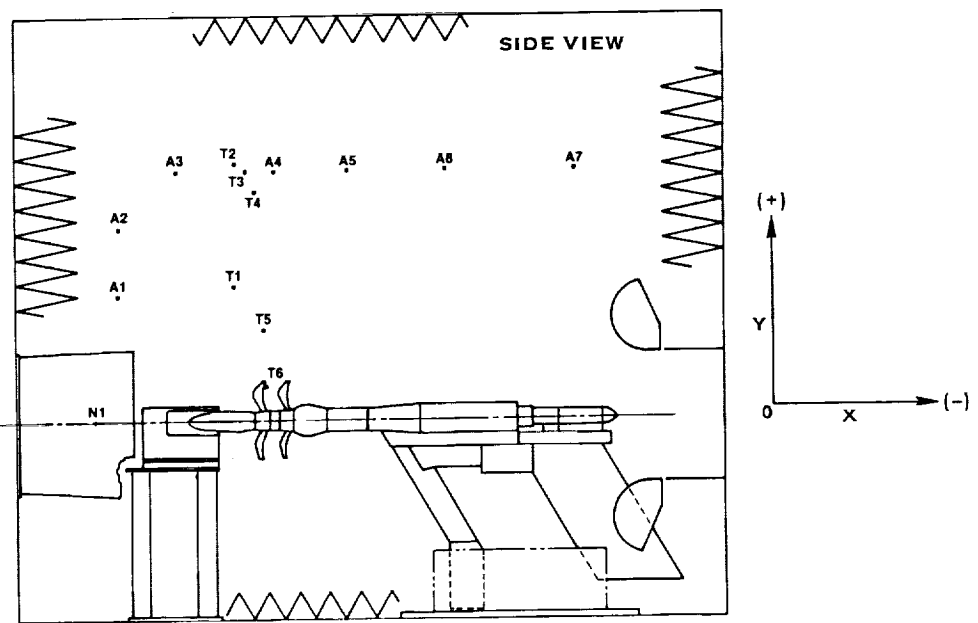
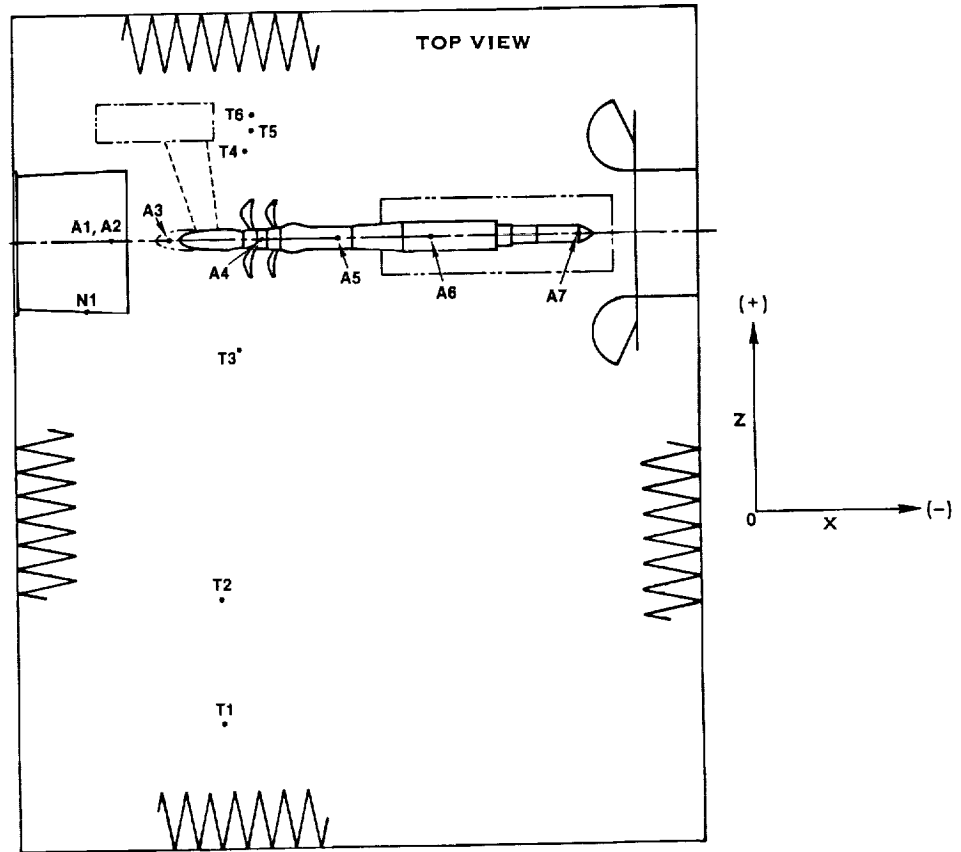


FIGURE 9. ACOUSTIC TEST CHAMBER WITH MICROPHONE LOCATIONS

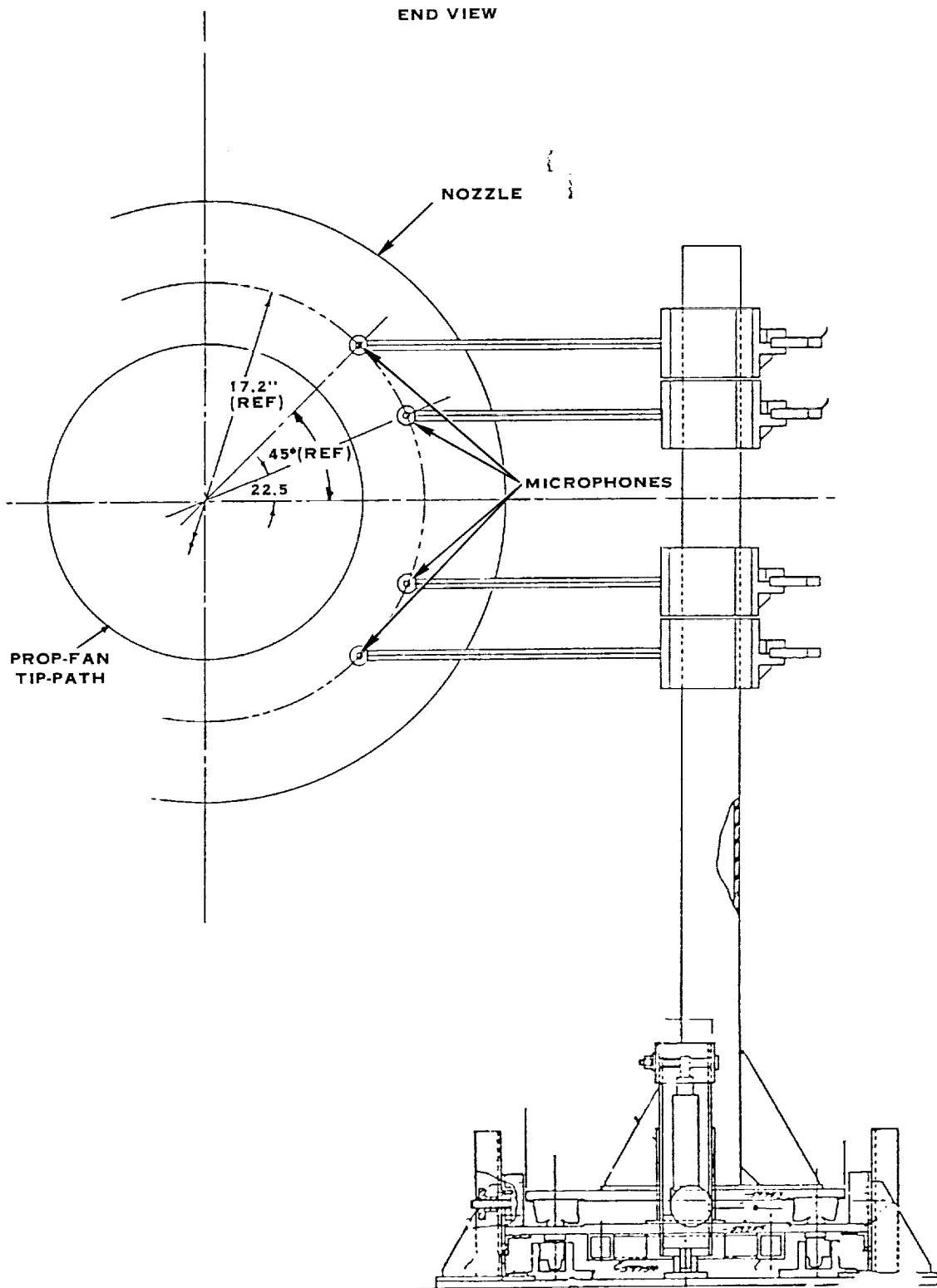


FIGURE 10. IN FLOW TRAVERSING PROBE ASSEMBLY

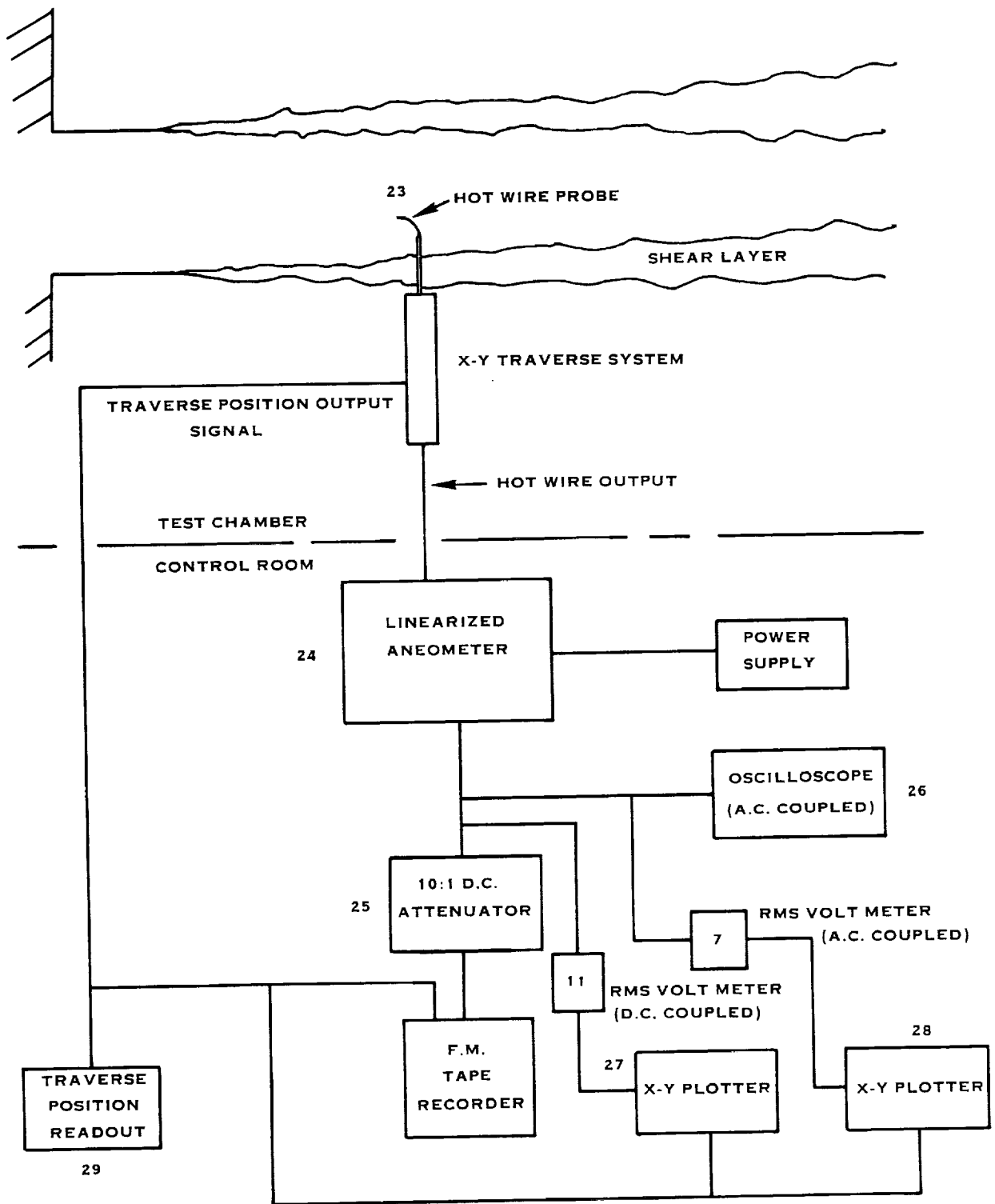


FIGURE 11. SHEAR LAYER SURVEY INSTRUMENTATION

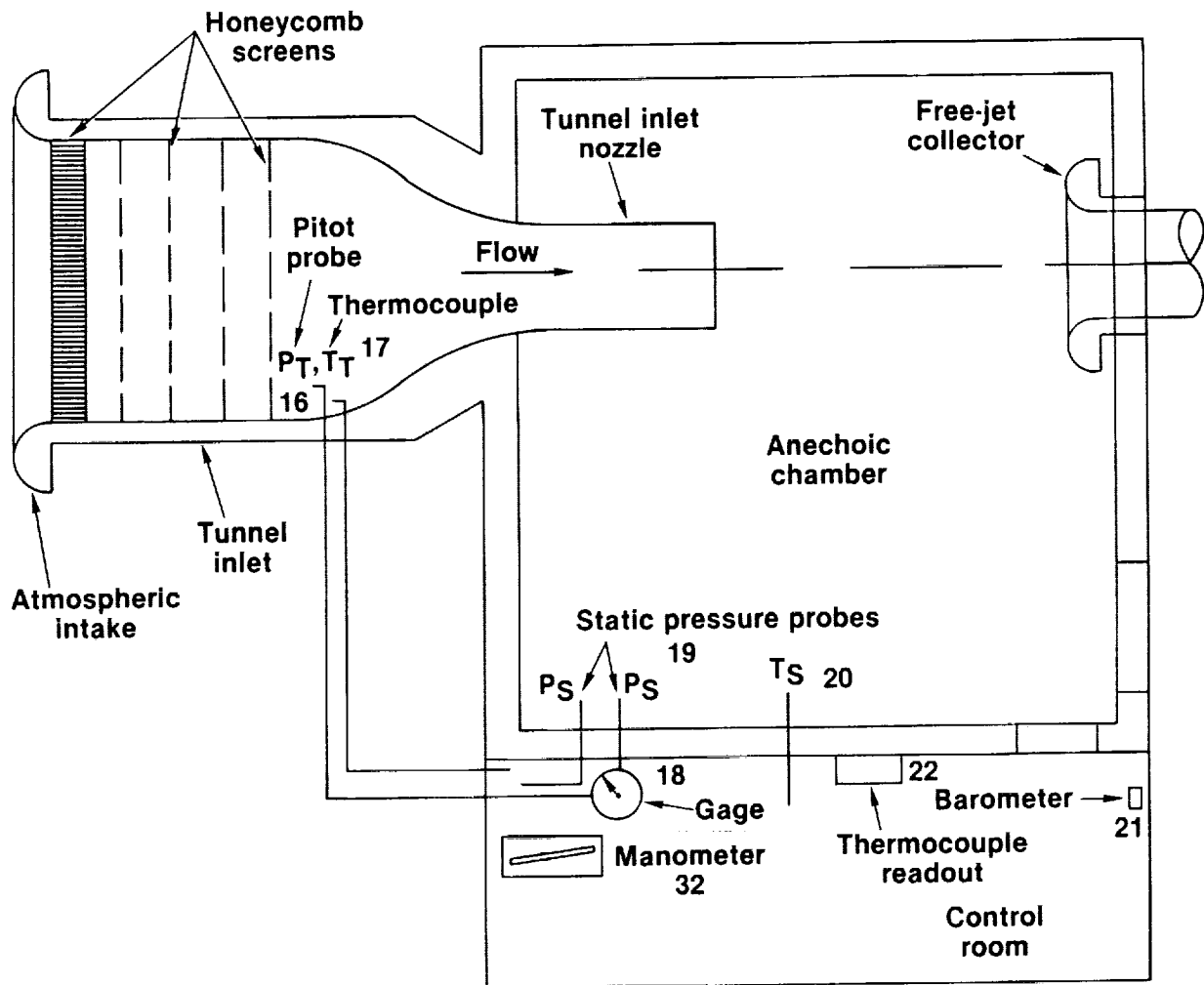


FIGURE 12. ACOUSTIC RESEARCH TUNNEL AND CONTROL ROOM INSTRUMENTATION

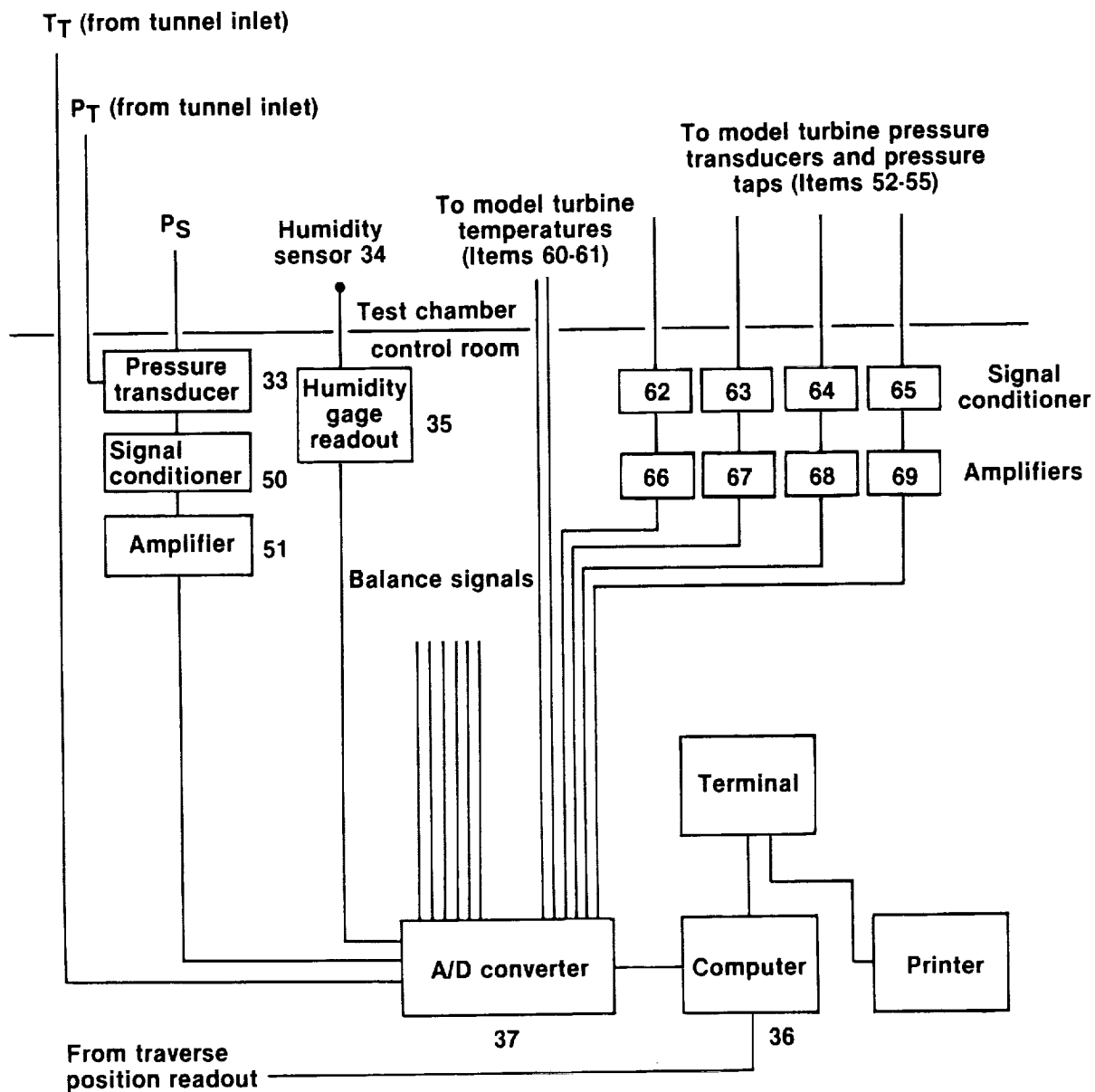


FIGURE 13. DATA ACQUISITION SYSTEM FOR STEADY STATE PARAMETERS

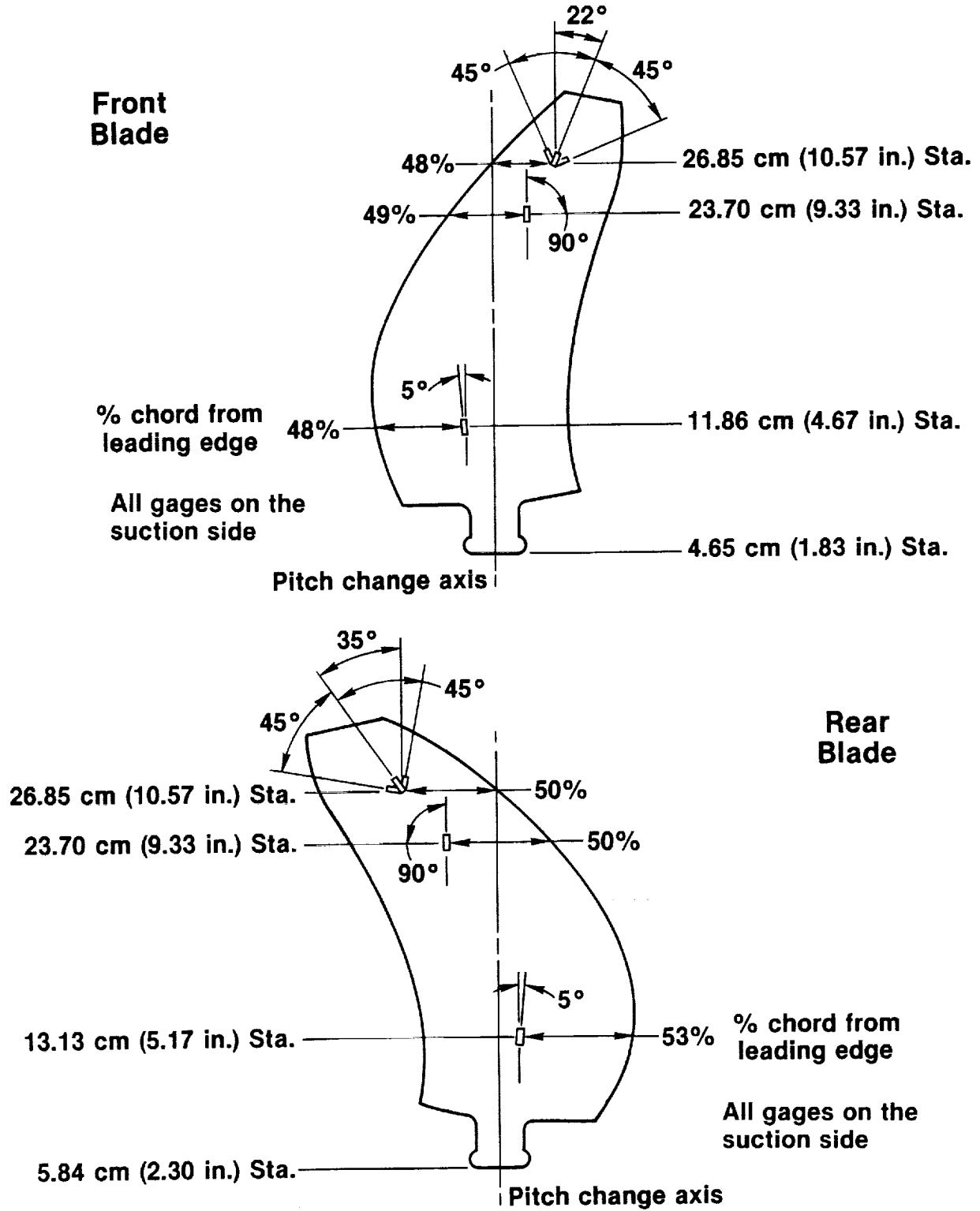


FIGURE 14. CRP-XI MODEL STRAIN GAGE INSTALLATION

~~ORIGINAL PAGE IS
OF POOR QUALITY~~

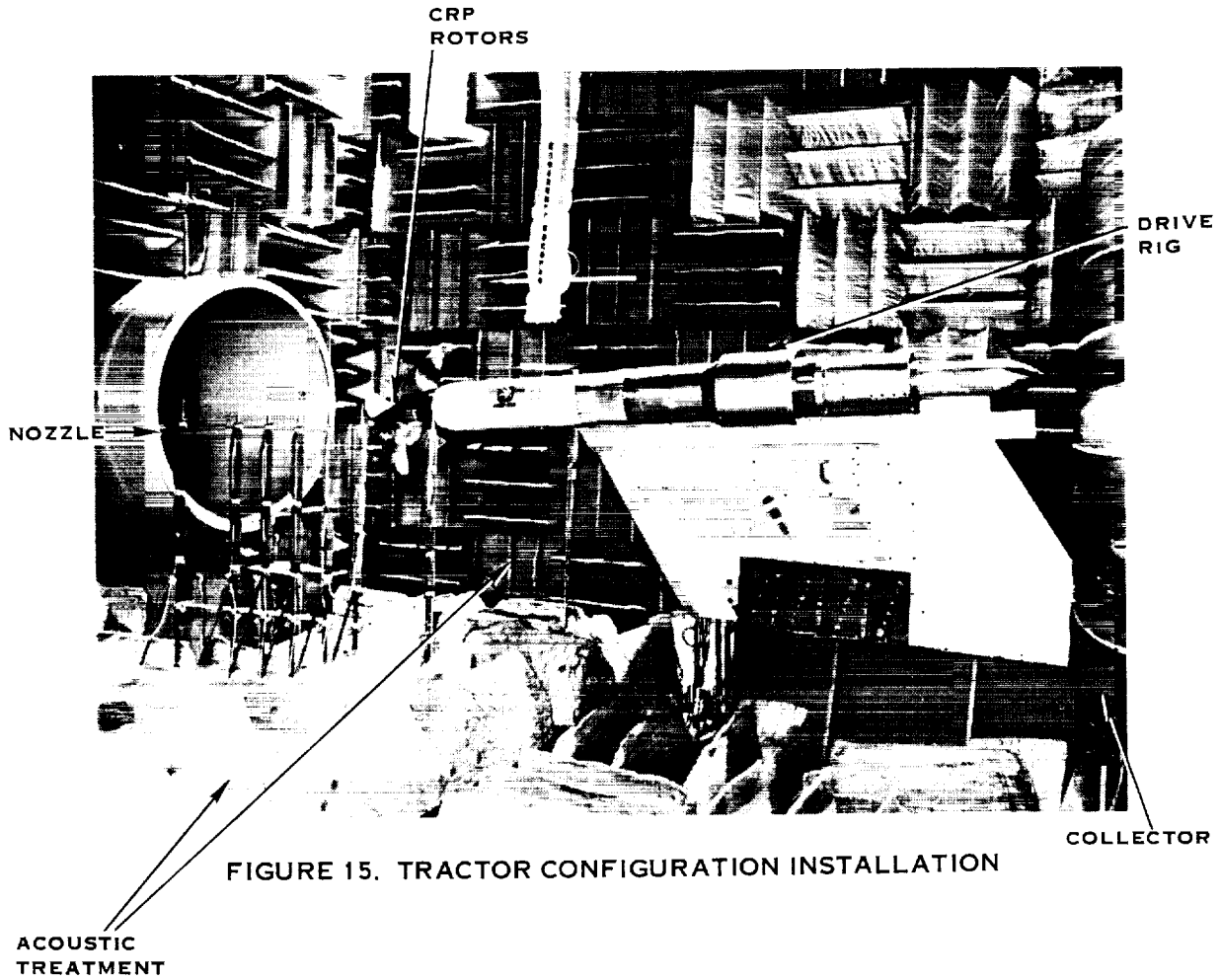


FIGURE 15. TRACTOR CONFIGURATION INSTALLATION

ORIGINAL PAGE
BLACK AND WHITE PHOTOGRAPH

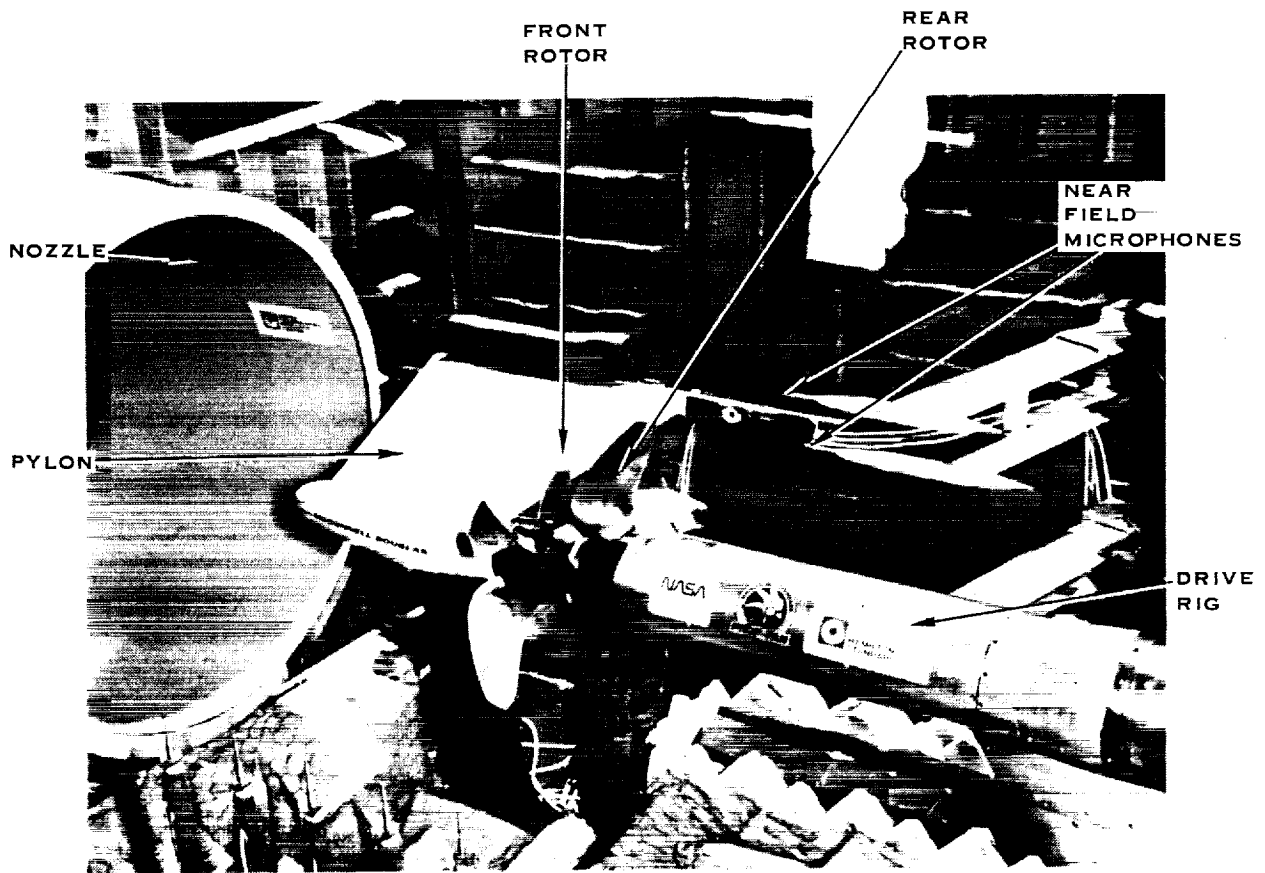


FIGURE 16. PUSHER CONFIGURATION INSTALLATION

ORIGINAL PAGE
BLACK AND WHITE PHOTOGRAPH

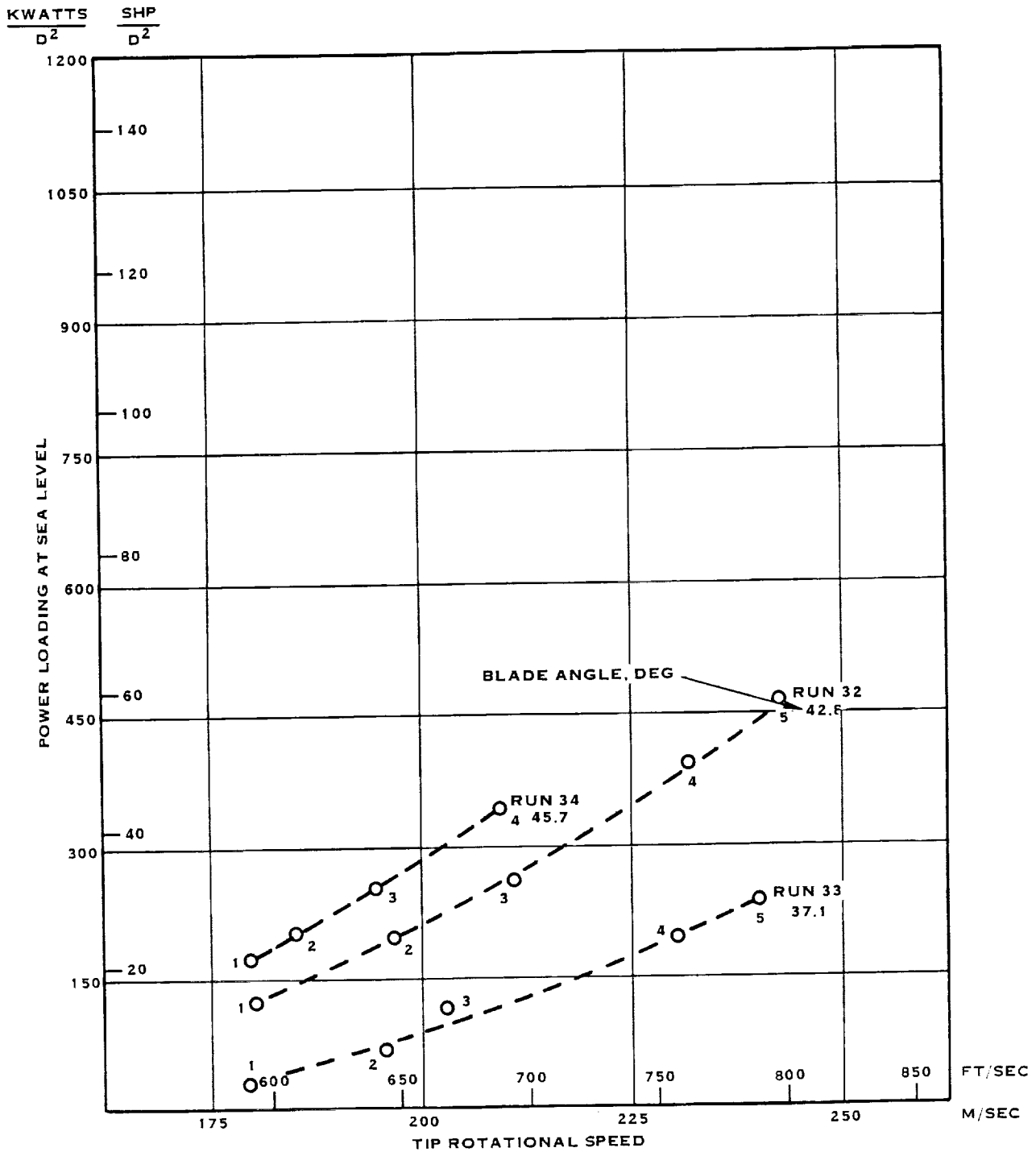


FIGURE 17. CRP-XI SINGLE ROTATION (REAR ROTOR) DATA

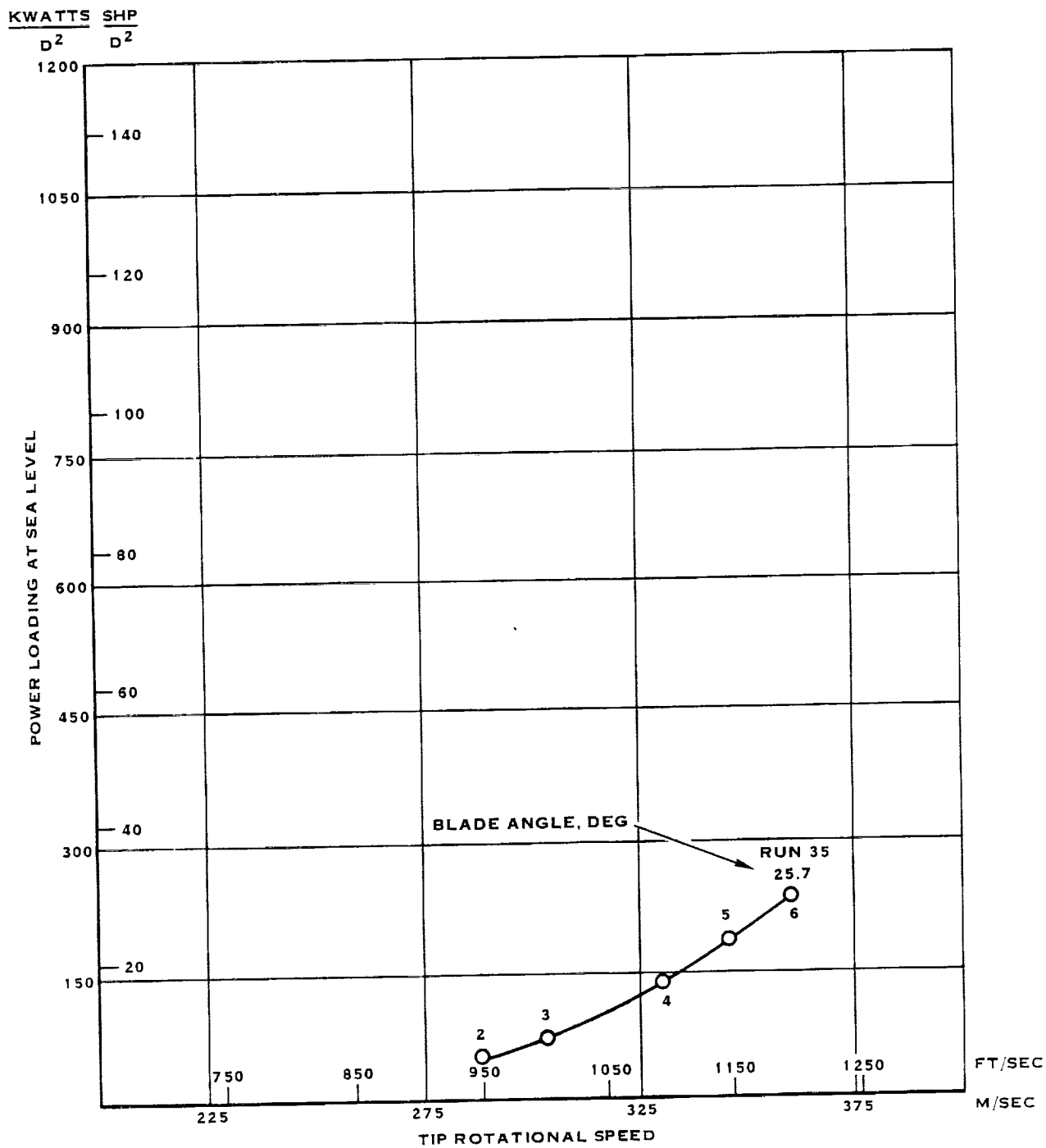


FIGURE 18. CRP-XI SINGLE ROTATION (REAR ROTOR) DATA - CRUISE SIMULATION

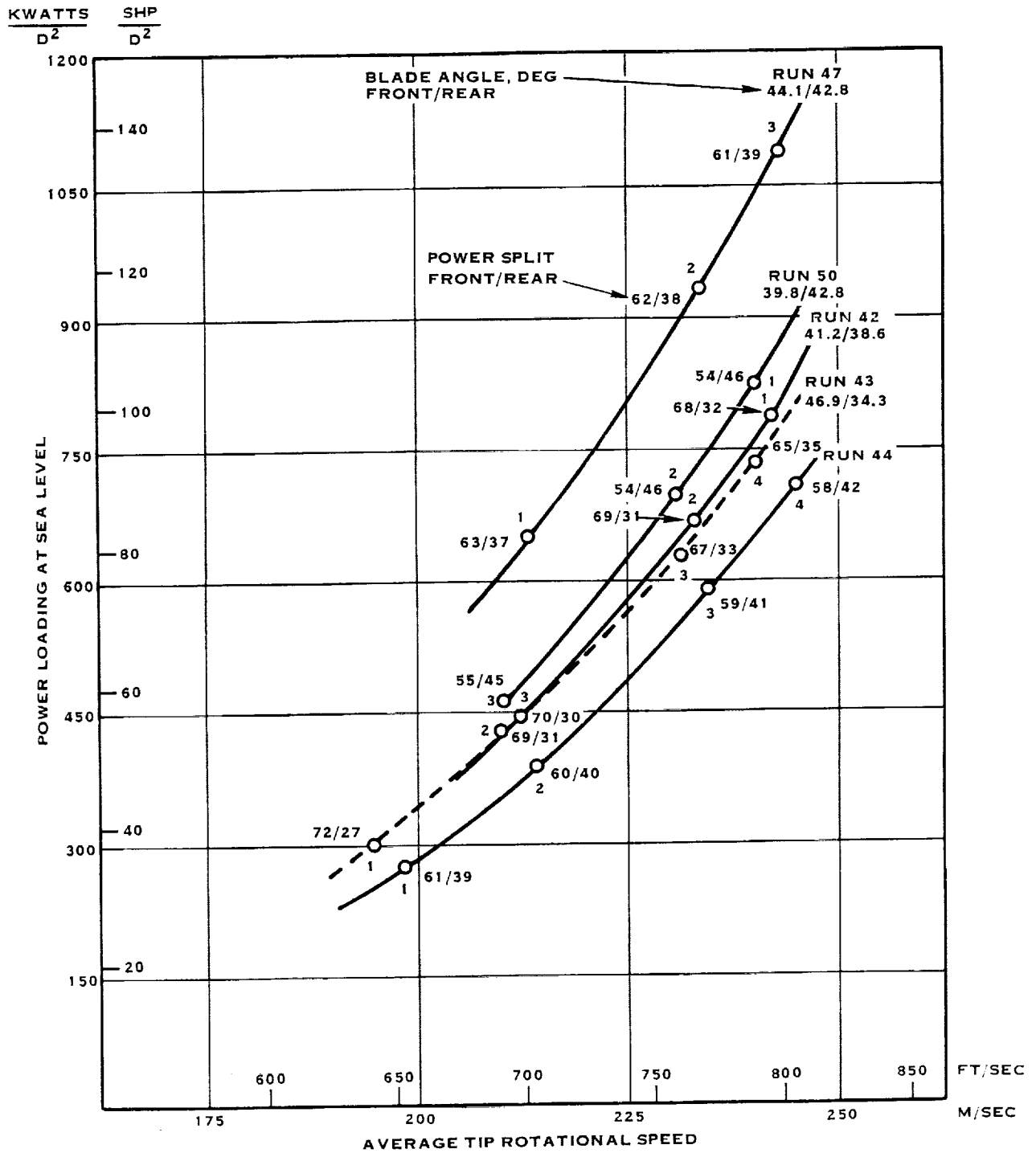


FIGURE 20. CRP-XI "UNEQUAL" RPM TRACTOR DATA - 0° ANGLE-OF-ATTACK, 0.257D SPACING

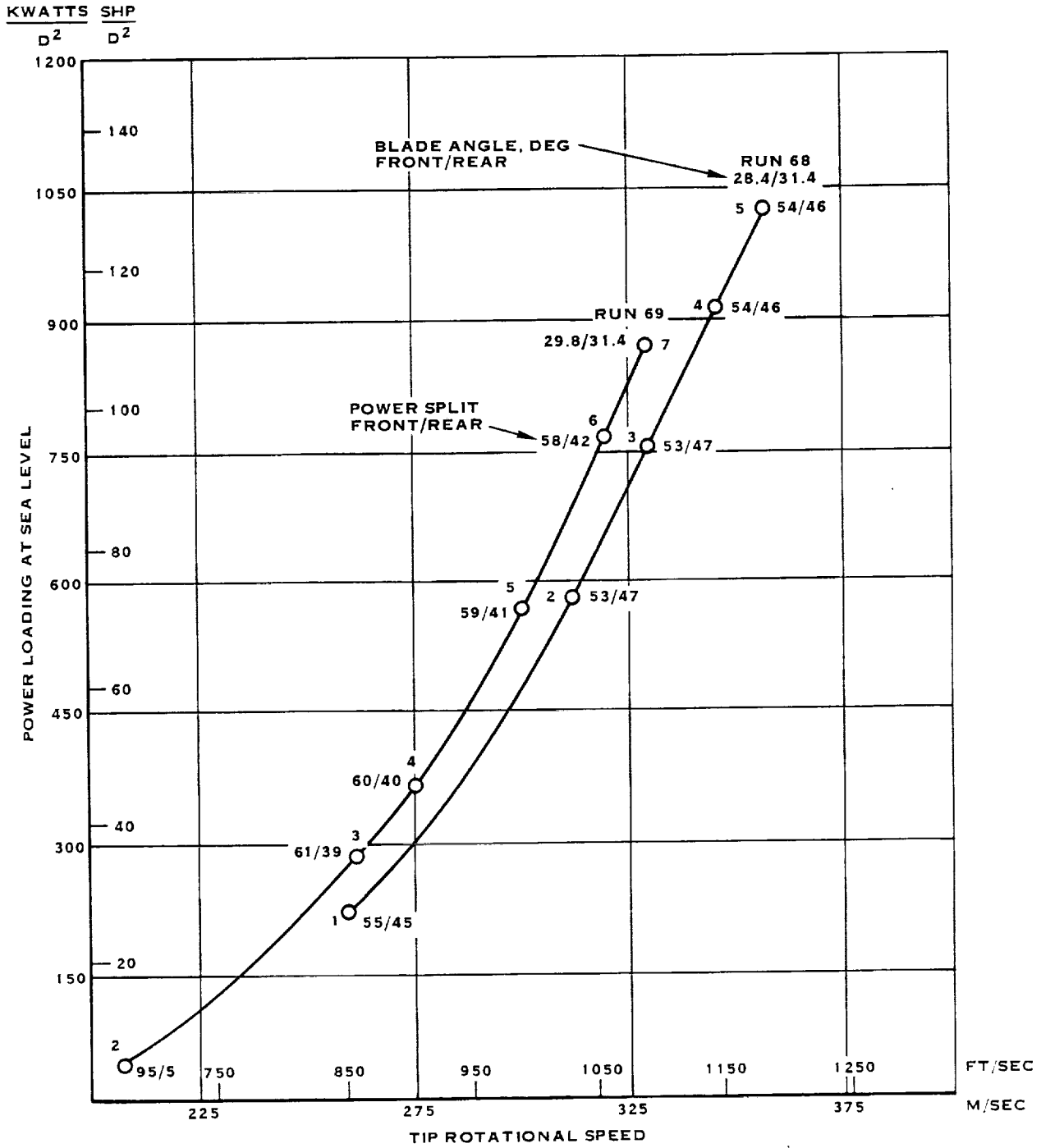


FIGURE 21. CRP-XI CRUISE SIMULATION DATA - 0° ANGLE-OF-ATTACK TRACTOR, 0.257D SPACING

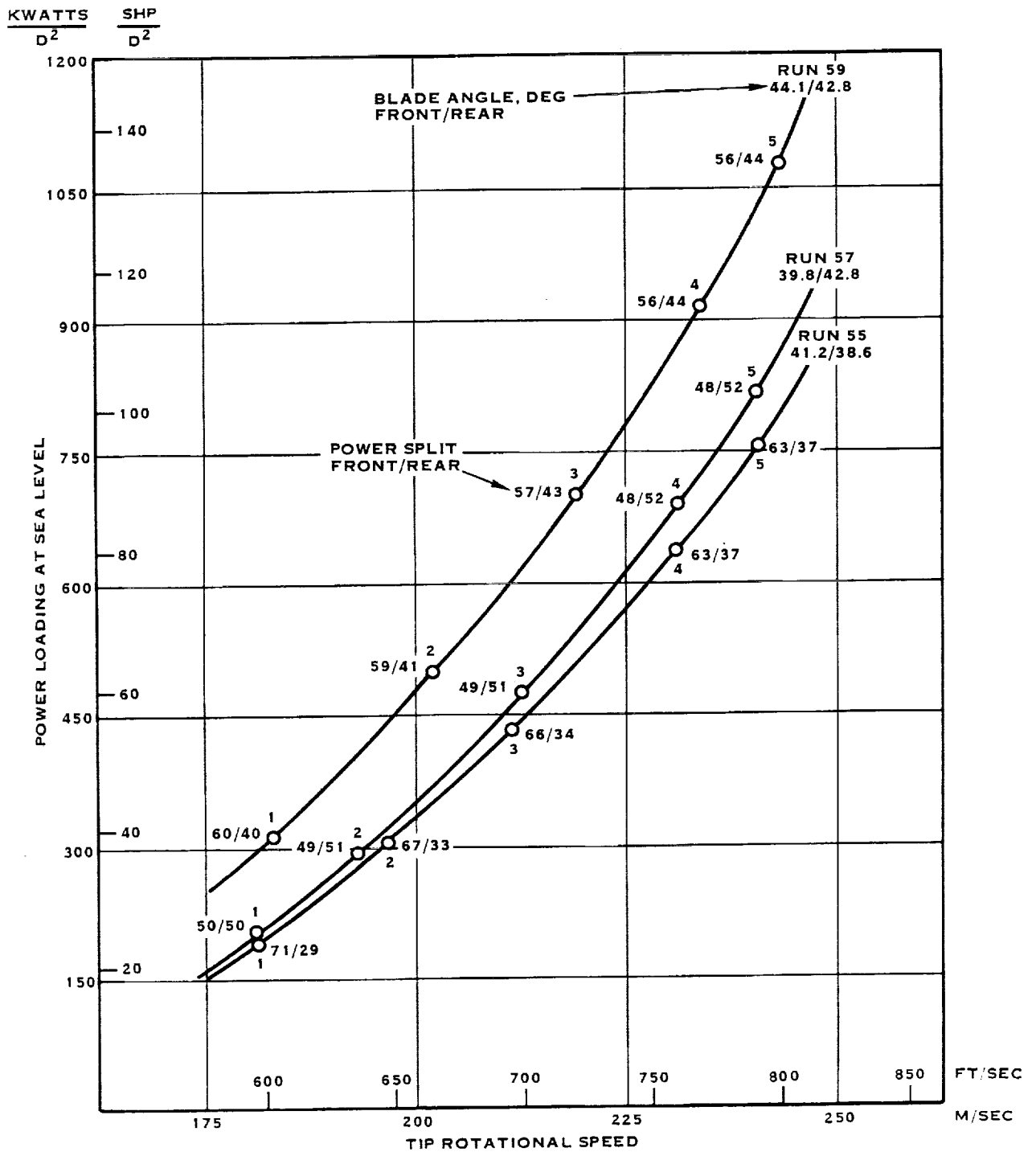


FIGURE 22. CRP-XI "EQUAL" RPM TRACTOR DATA - 0° ANGLE-OF-ATTACK, 0.461D SPACING

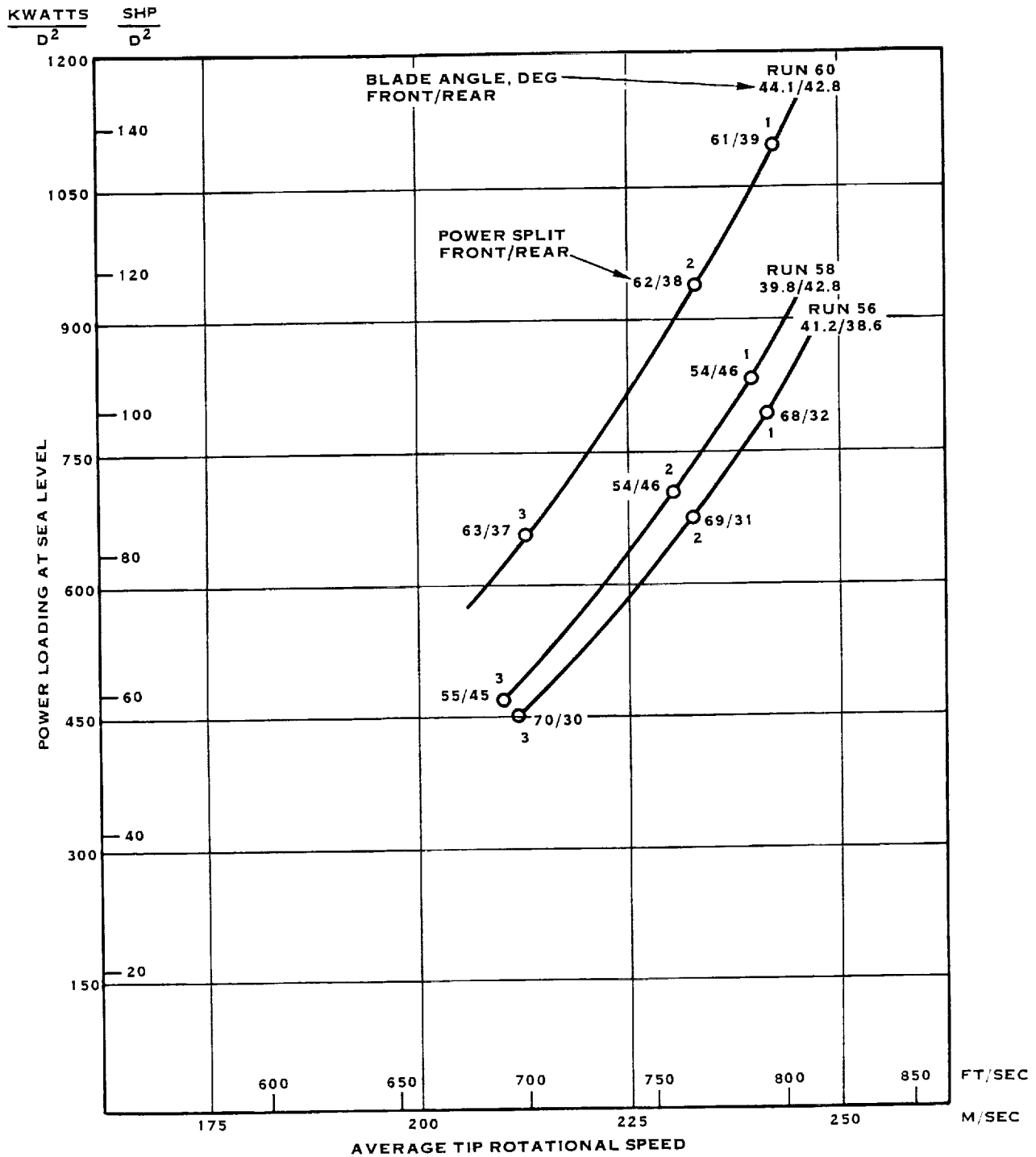


FIGURE 23. CRP-XI "UNEQUAL" RPM TRACTOR DATA - 0° ANGLE-OF-ATTACK, 0.461D SPACING

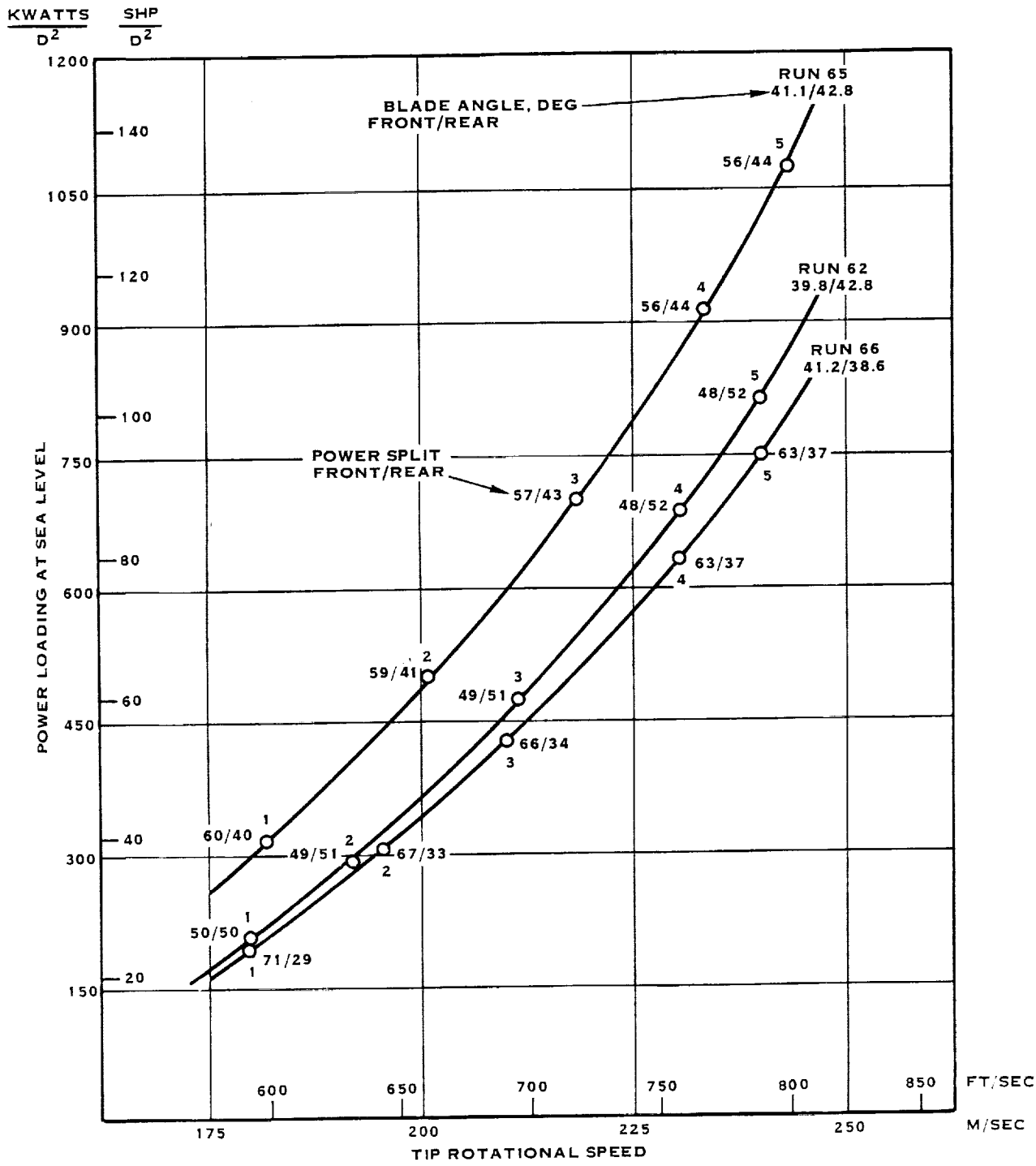


FIGURE 24. CRP-XI "EQUAL" RPM TRACTOR DATA - 0° ANGLE-OF-ATTACK, 0.363D SPACING

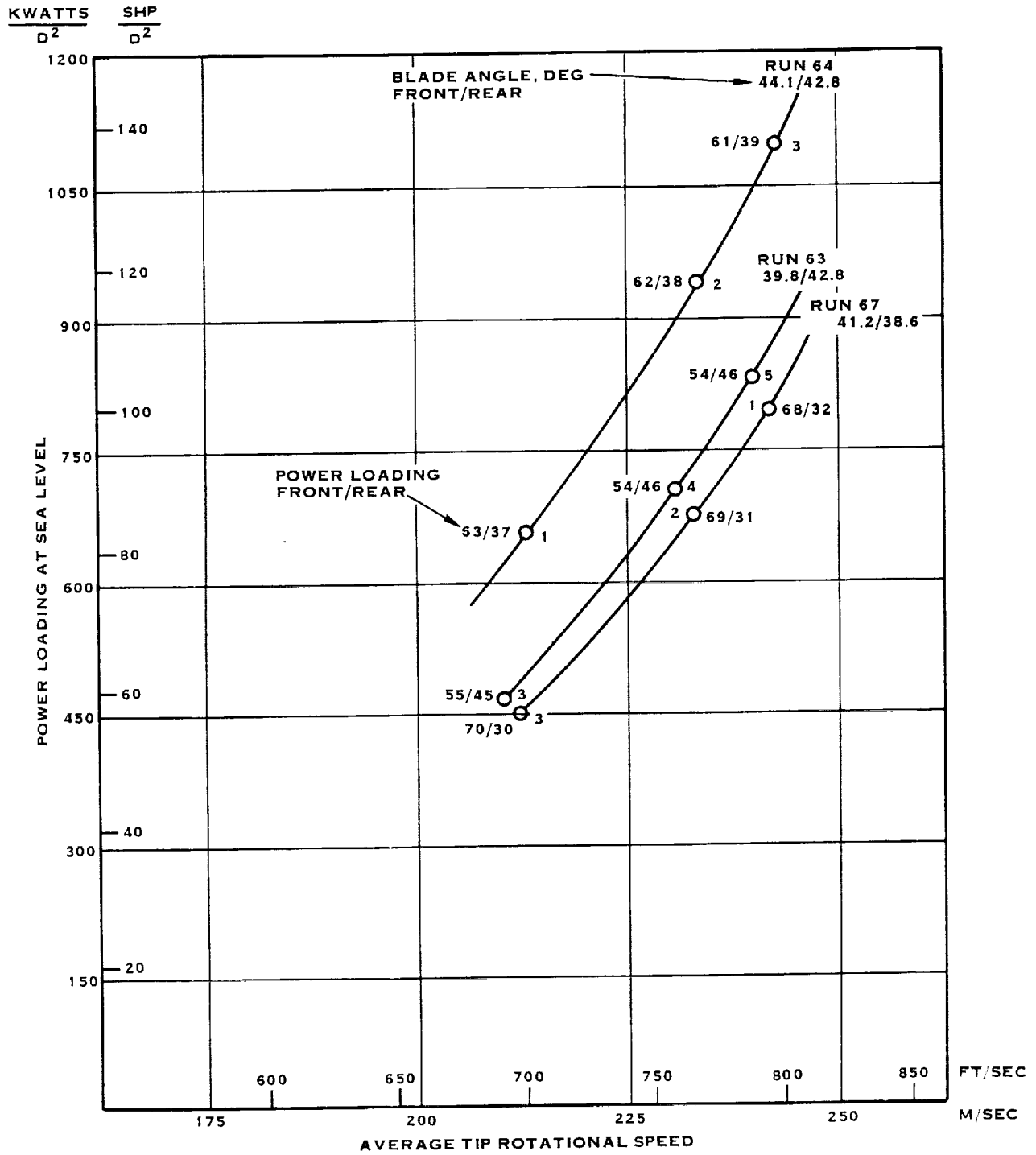


FIGURE 25. CRP-XI "UNEQUAL" RPM TRACTOR DATA - 0° ANGLE-OF-ATTACK, 0.363D SPACING

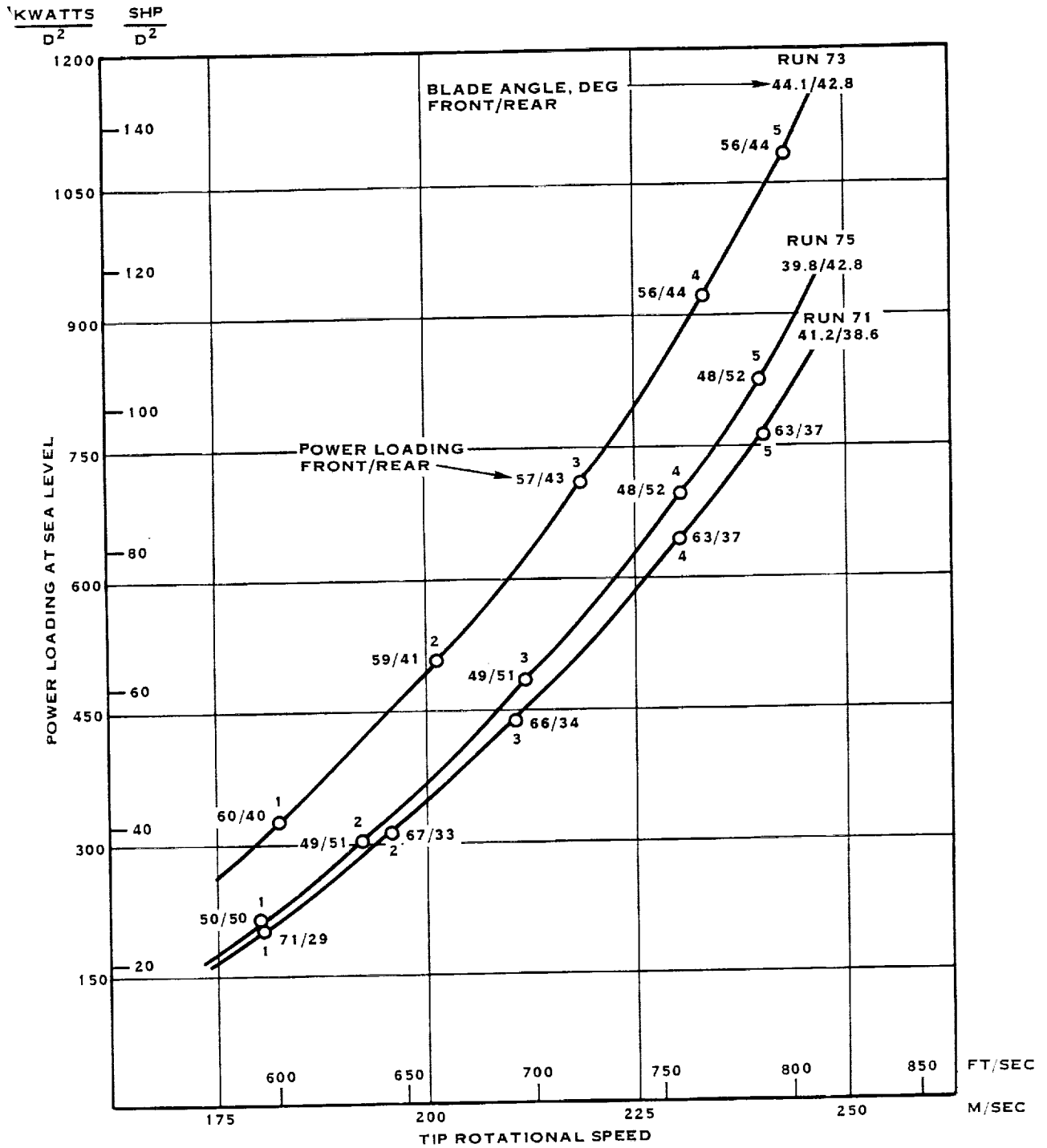


FIGURE 26. CRP-XI "EQUAL" RPM TRACTOR DATA - 4° ANGLE-OF-ATTACK, 0.257D SPACING

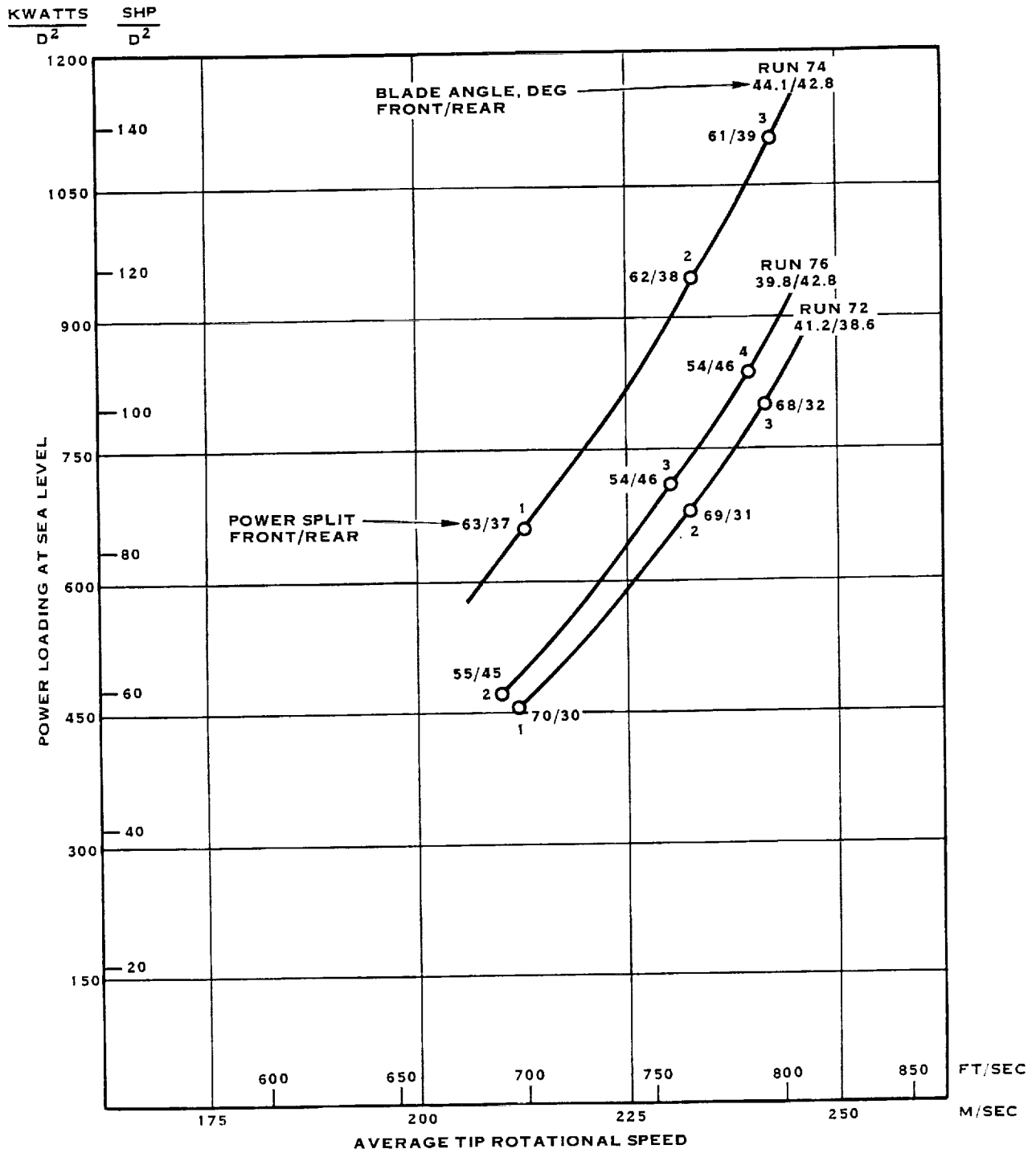


FIGURE 27. CRP-XI "UNEQUAL" RPM TRACTOR DATA - 4° ANGLE-OF-ATTACK, 0.257D SPACING

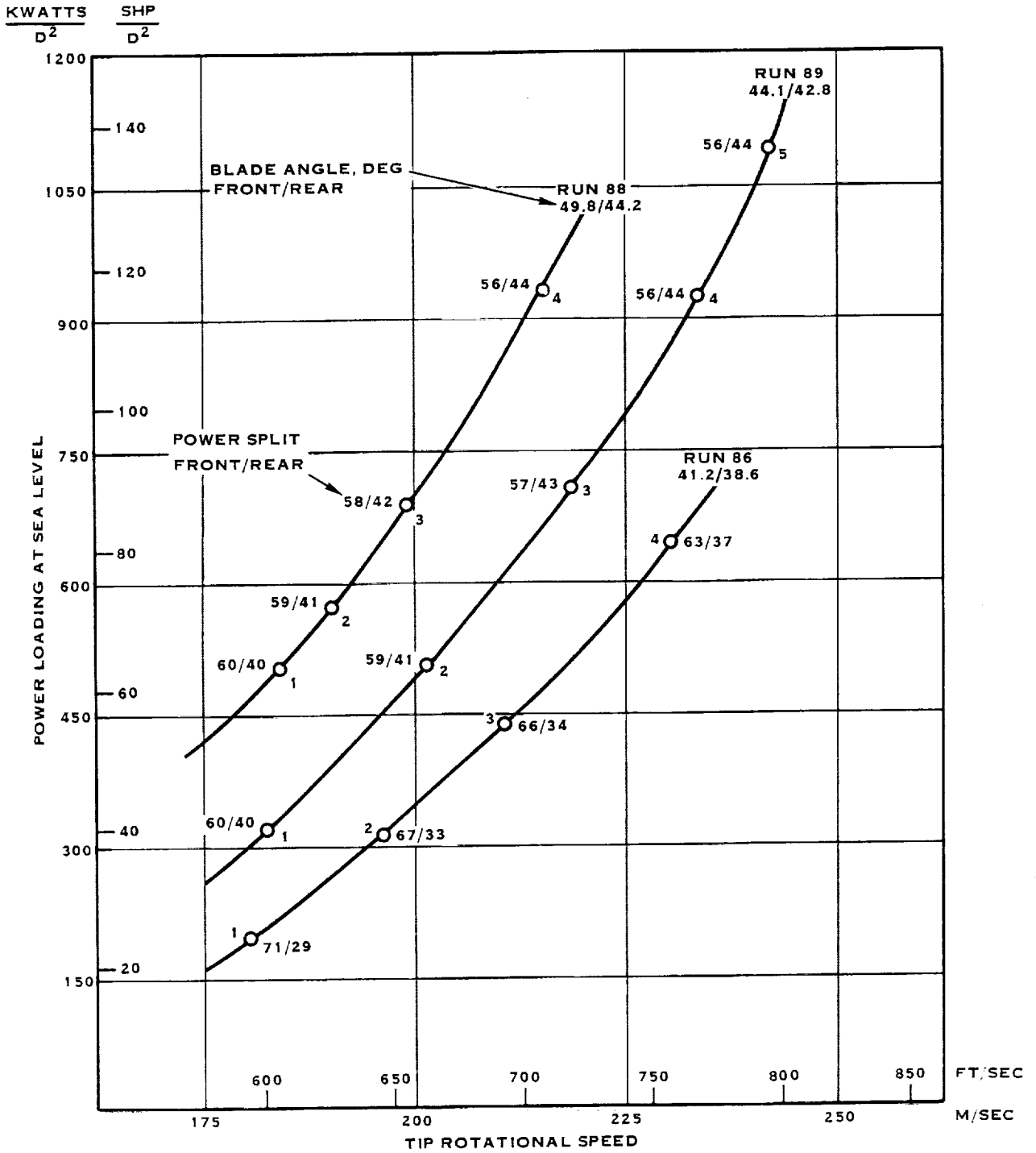


FIGURE 28. CRP-XI "EQUAL" RPM PUSHER DATA - 4° ANGLE-OF-ATTACK, 0.257D ROTOR SPACING, 0.1C PYLON SPACING

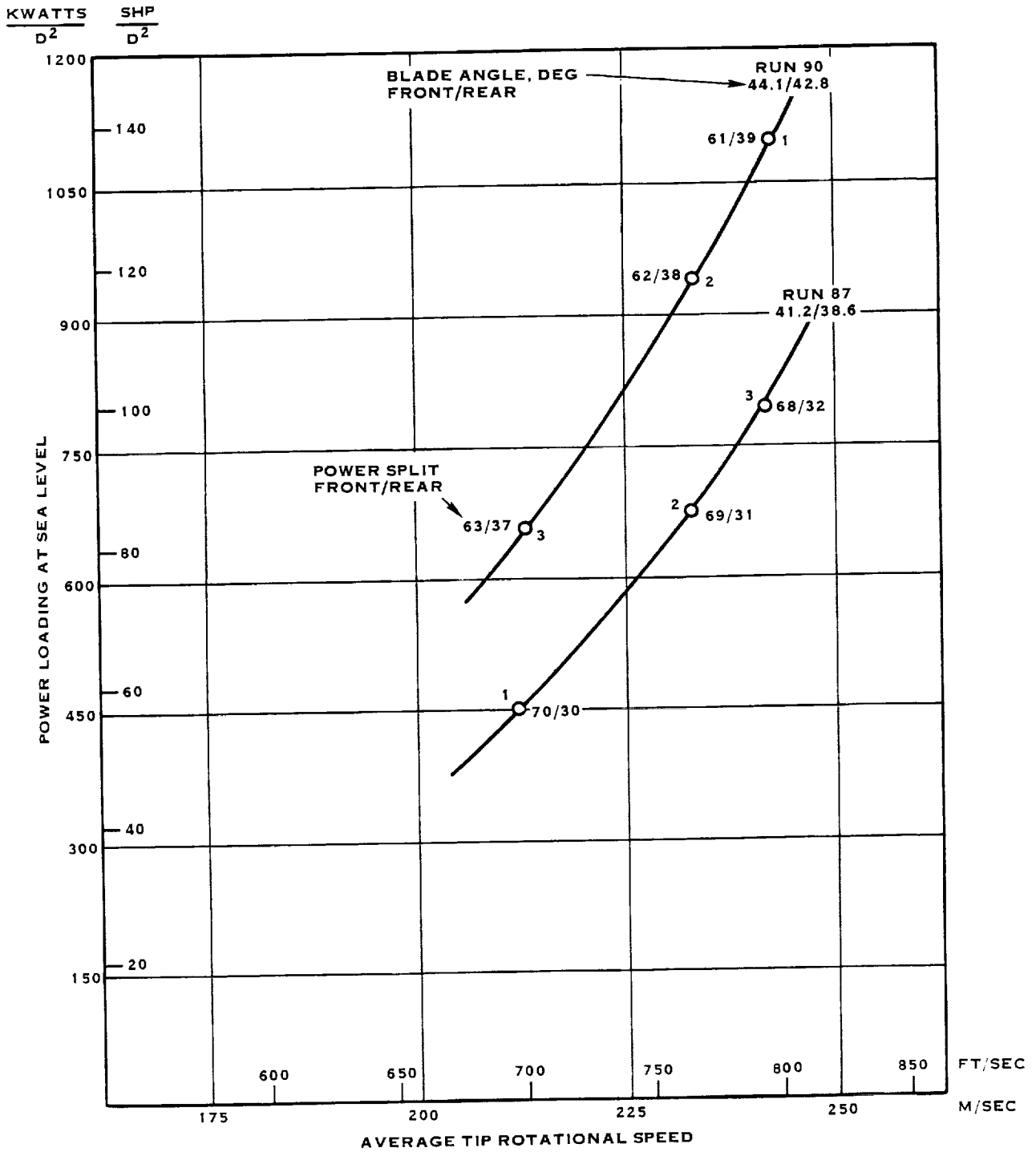


FIGURE 29. CRP-XI "UNEQUAL" RPM PUSHER DATA - 4° ANGLE-OF-ATTACK, 0.257D ROTOR SPACING, 0.1C PYLON SPACING

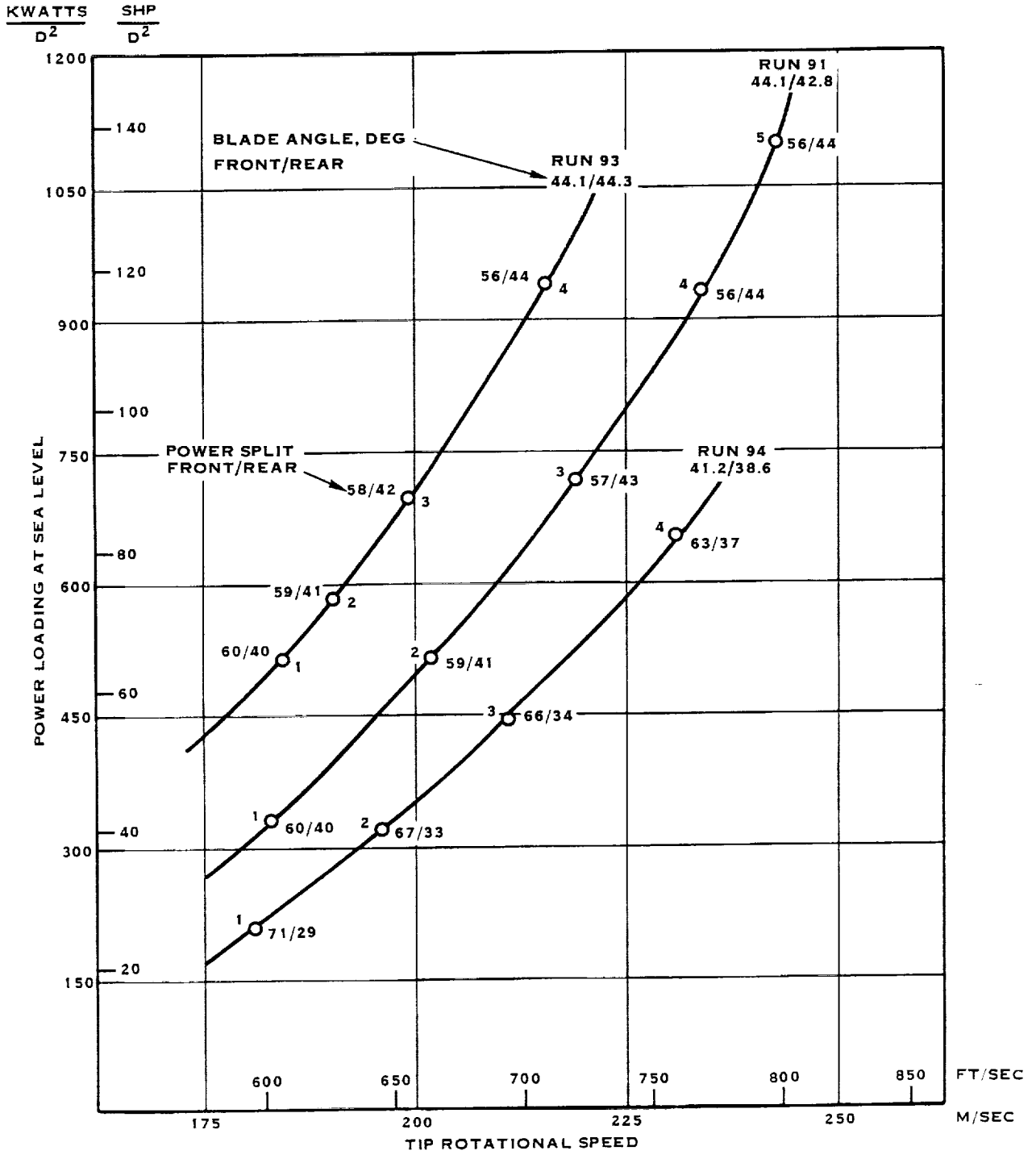


FIGURE 30. CRP-XI "EQUAL" PUSHER DATA - 4° ANGLE-OF-ATTACK, 0.257D ROTOR SPACING, 0.2C PYLON SPACING

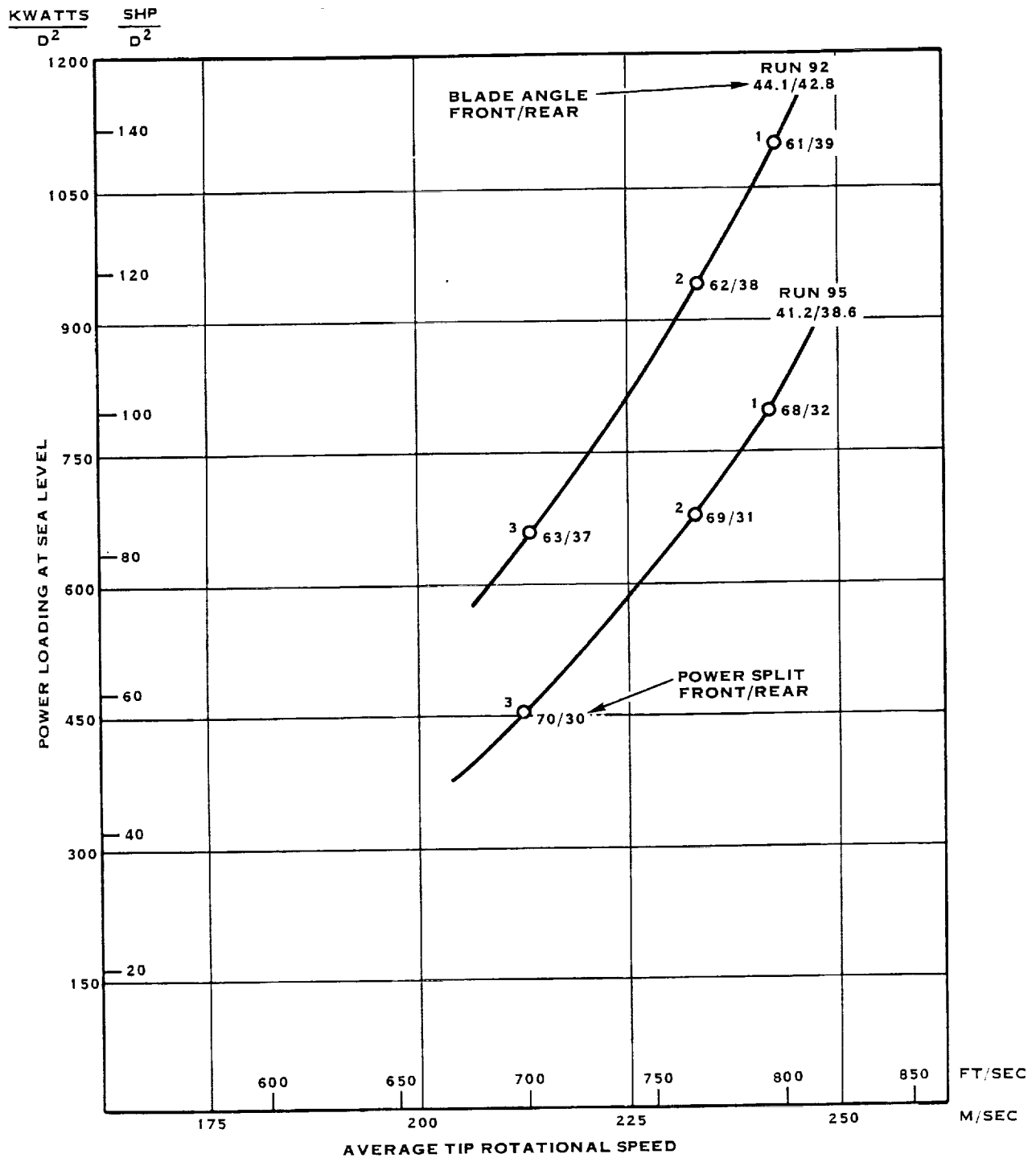


FIGURE 31. CRP-XI "UNEQUAL" RPM PUSHER DATA - 4° ANGLE-OF-ATTACK, 0.257D ROTOR SPACING, 0.2C PYLON SPACING

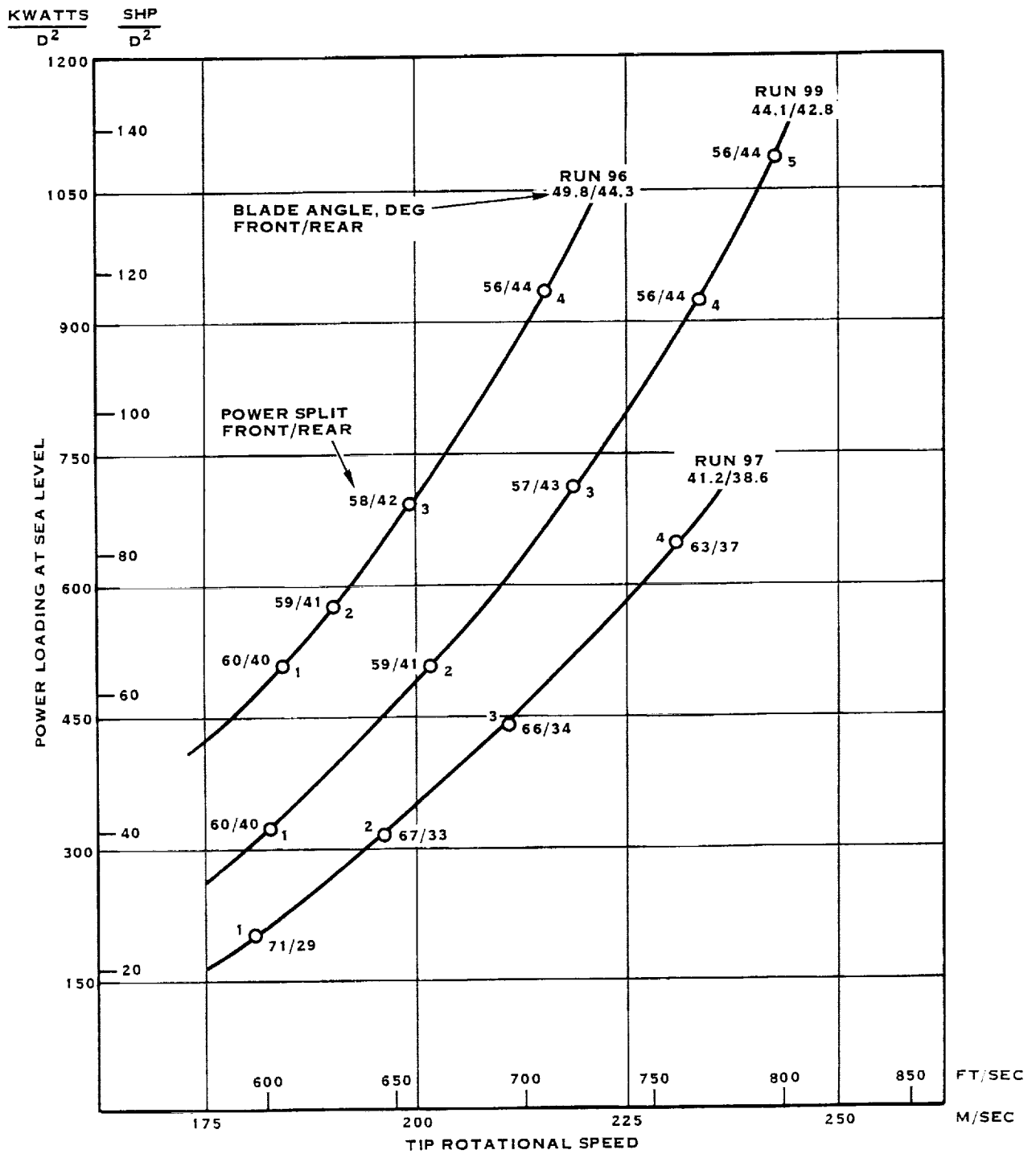


FIGURE 32. CRP-XI "EQUAL" RPM PUSHER DATA - 4° ANGLE-OF-ATTACK, 0.363D ROTOR SPACING, 0.2C PYLON SPACING

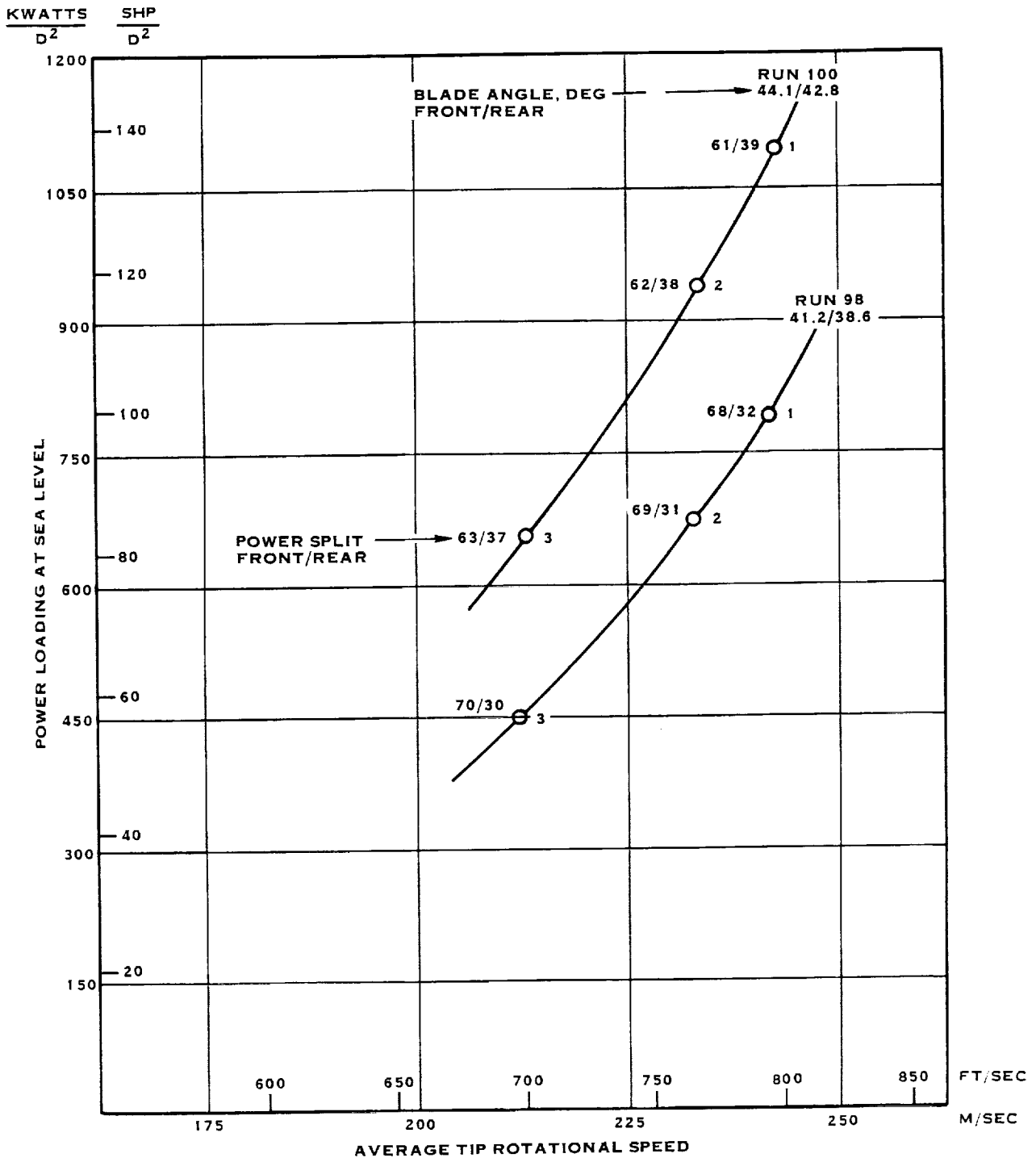


FIGURE 33. CRP-XI "UNEQUAL" RPM PUSHER DATA - 4° ANGLE-OF-ATTACK, 0.363D ROTOR SPACING, 0.2C PYLON SPACING

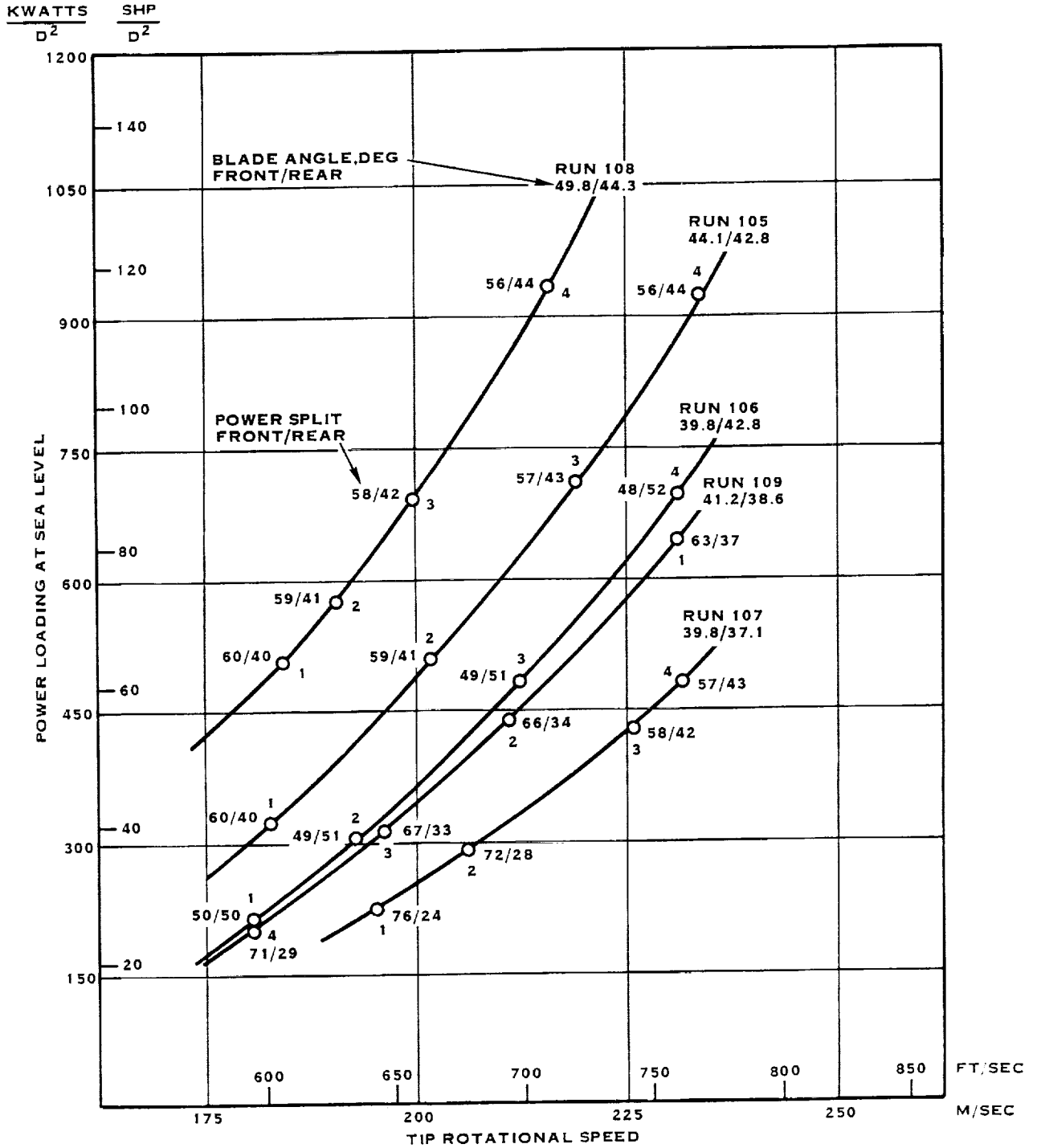


FIGURE 34. CRP-XI "EQUAL" RPM PUSHER DATA - 0° ANGLE-OF-ATTACK, 0.257D ROTOR SPACING, 0.1C PYLON SPACING

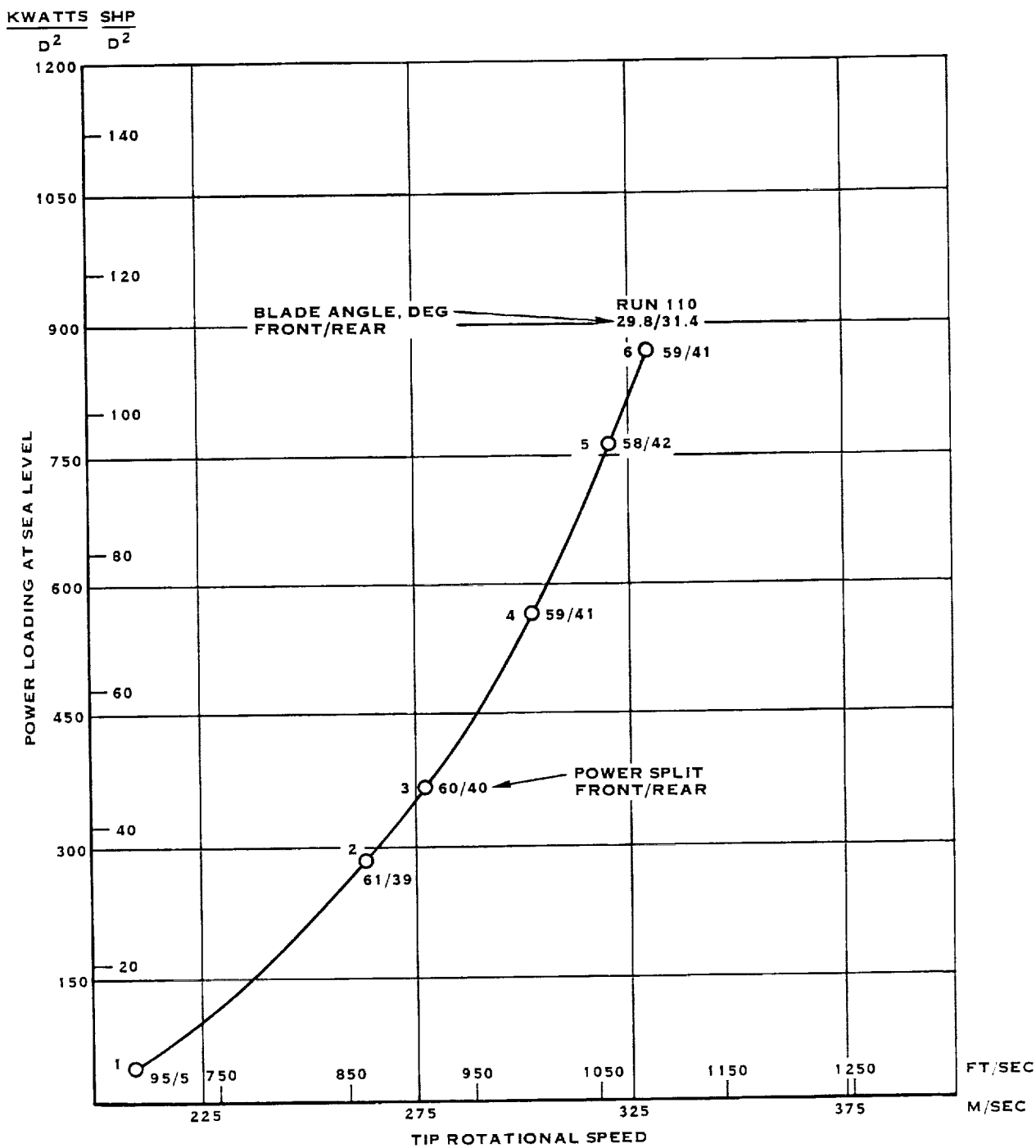


FIGURE 35. CRP-XI CRUISE SIMULATION DATA - 0° ANGLE-OF-ATTACK PUSHER, 0.257D ROTOR SPACING, 0.1C PYLON SPACING

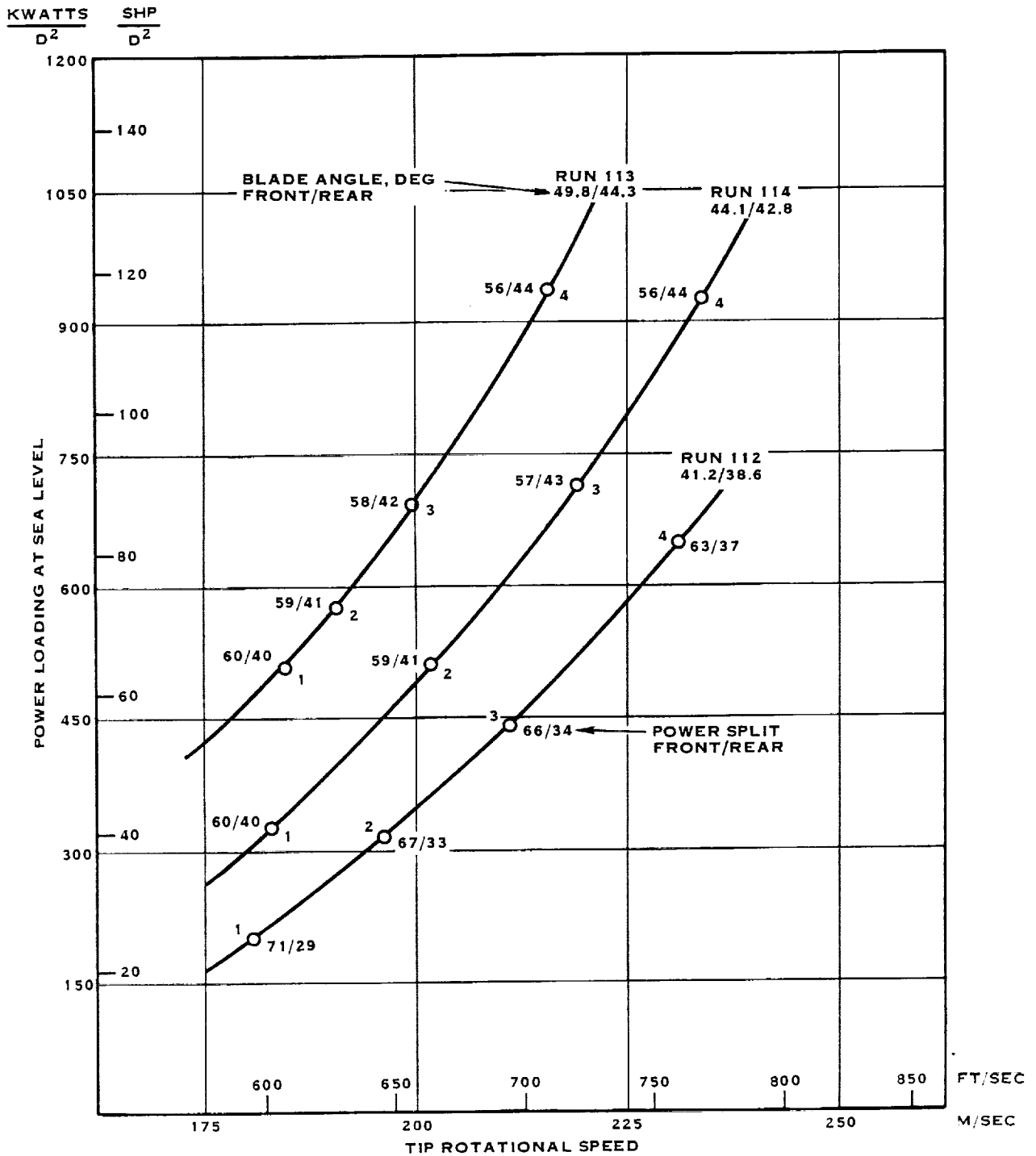


FIGURE 36. CRP-XI "EQUAL" RPM PUSHER DATA - 0° ANGLE-OF-ATTACK, 0.257D ROTOR SPACING, 0.2C PYLON SPACING

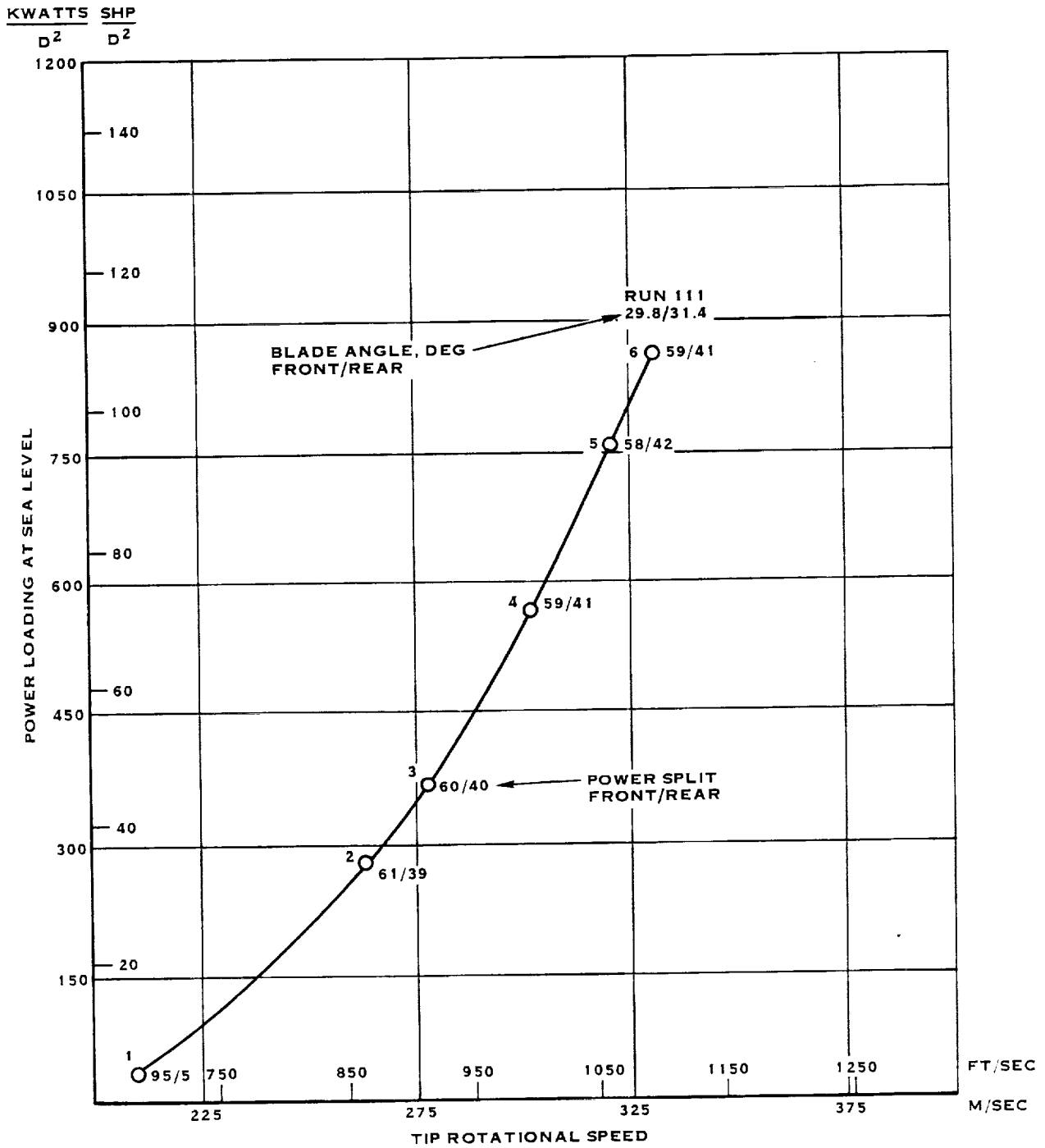
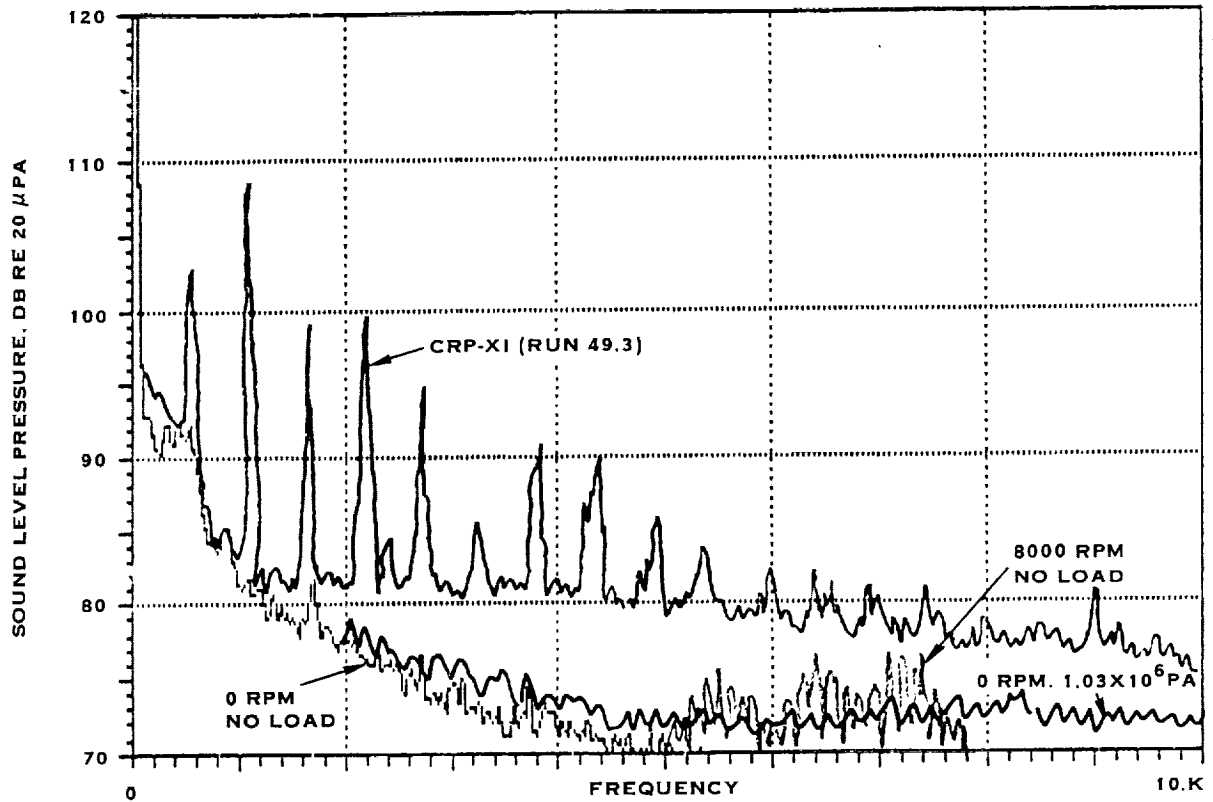


FIGURE 37. CRP-XI CRUISE SIMULATION DATA - 0° ANGLE-OF-ATTACK PUSHER, 0.257D ROTOR SPACING, 0.2C PYLON SPACING



NOTE: ALL BACKGROUND
NOISE IS AT 0.26 MN
WITH DUMMY HUBS
INSTALLED ON RIG

FIGURE 38. BACKGROUND NOISE AT A FORWARD LOCATION

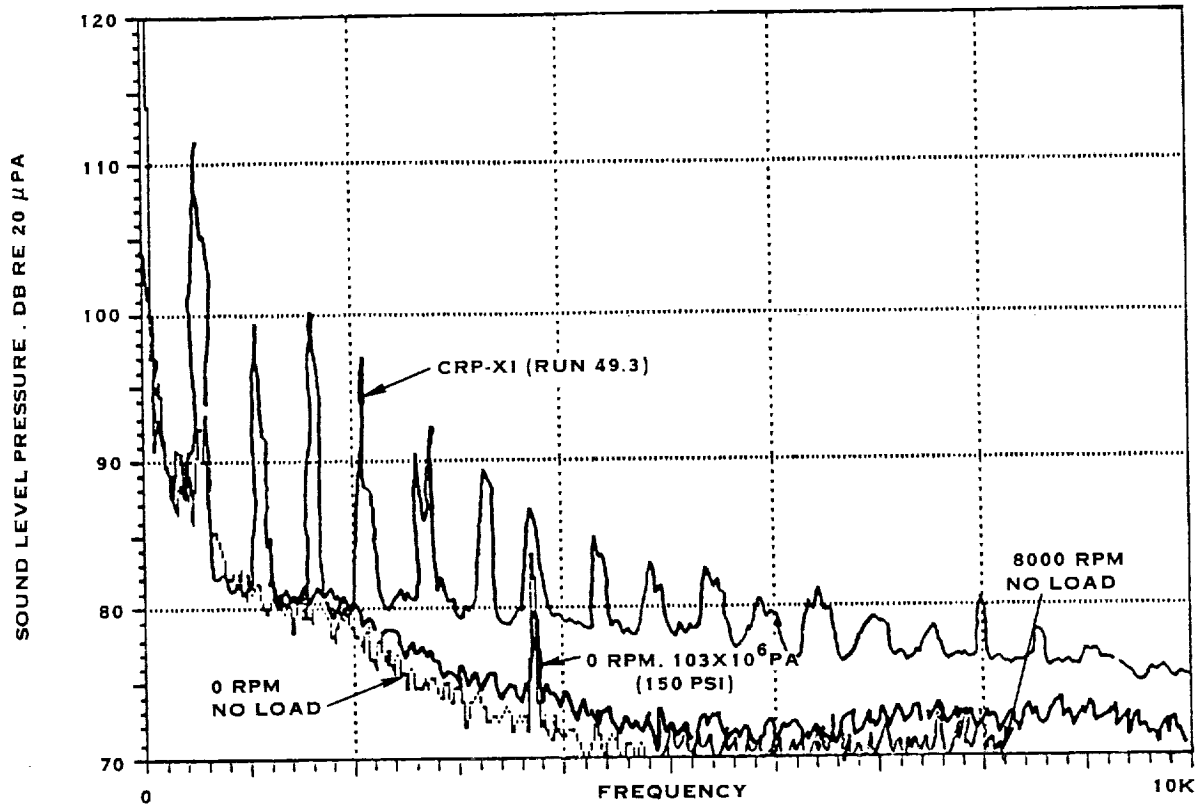


FIGURE 39. BACKGROUND NOISE SLIGHTLY FORWARD OF THE PLANE-OF-ROTATION

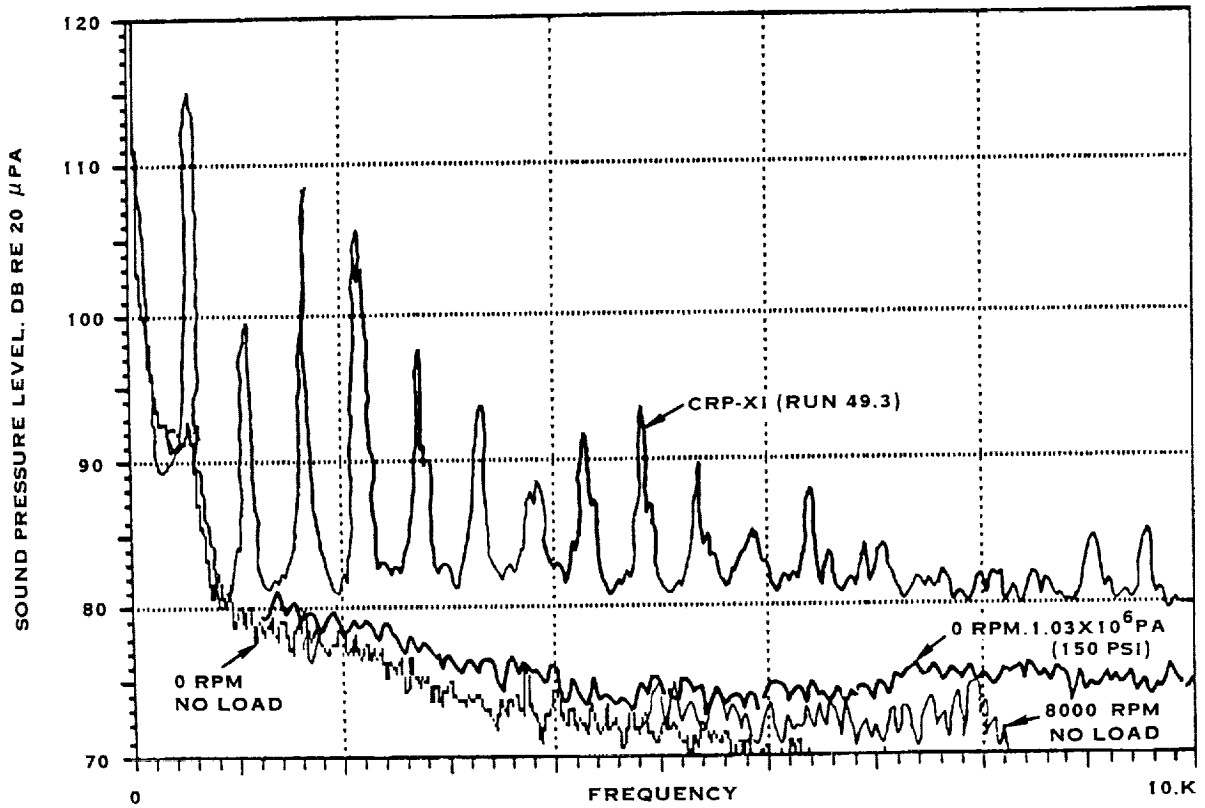


FIGURE 40. BACKGROUND NOISE SLIGHTLY AFT OF THE PLANE-OF-ROTATION

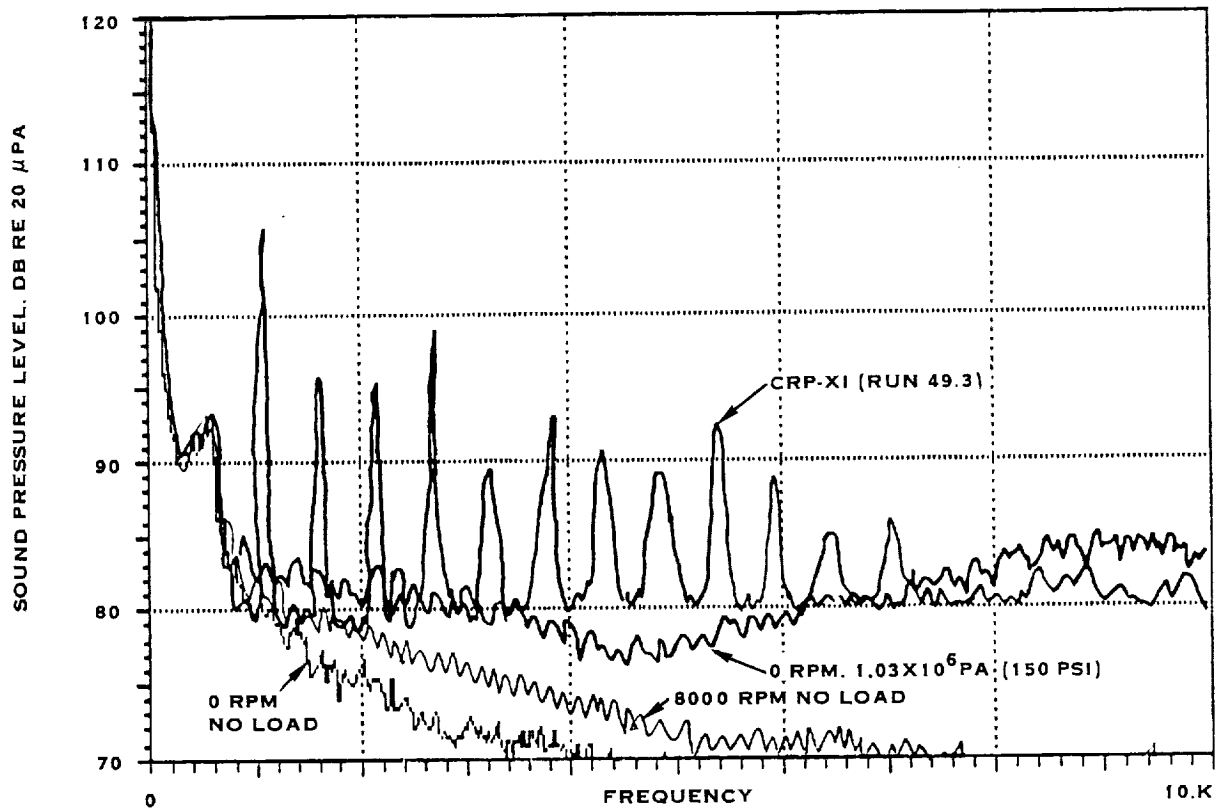


FIGURE 41. BACKGROUND NOISE AT AN AFT LOCATION

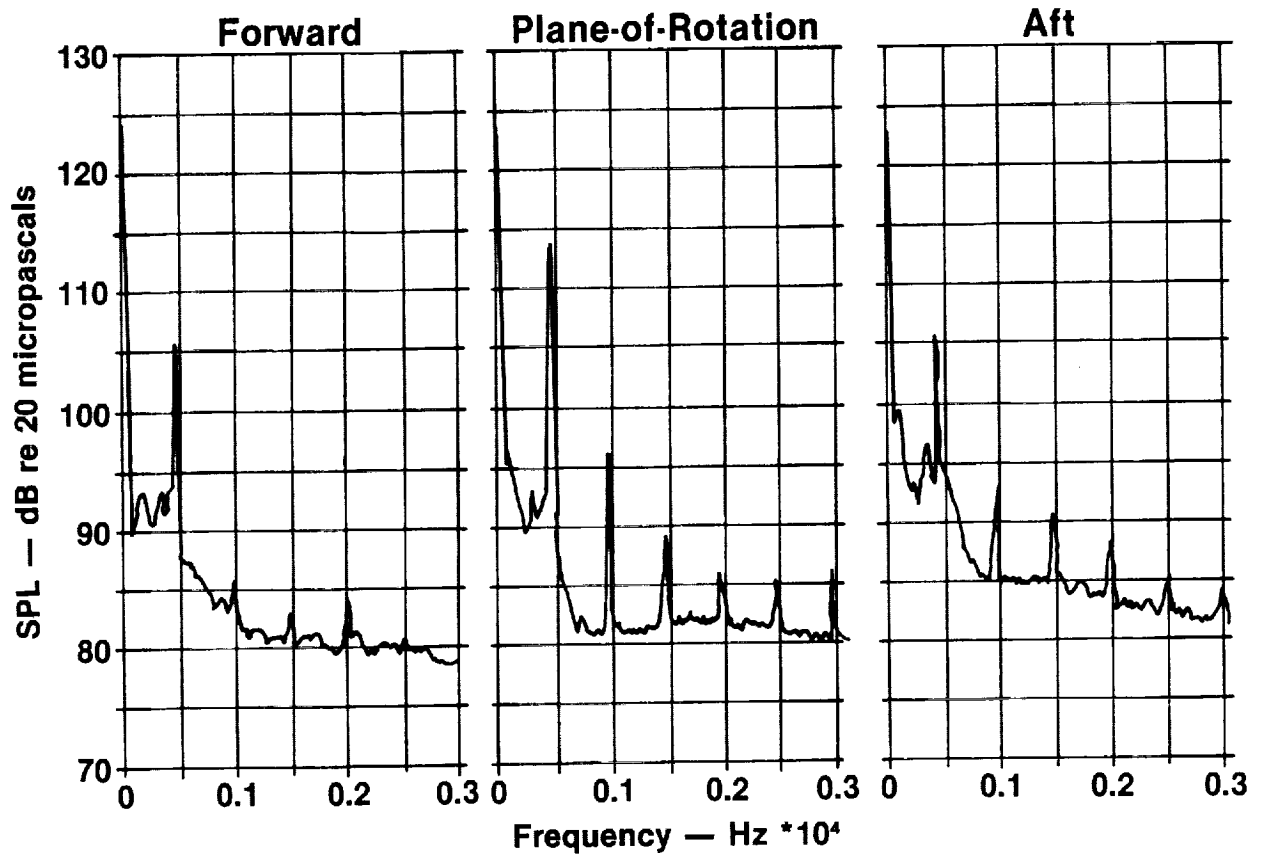


FIGURE 42. REPRESENTATIVE SINGLE-ROTATION PROP-FAN NOISE SPECTRA

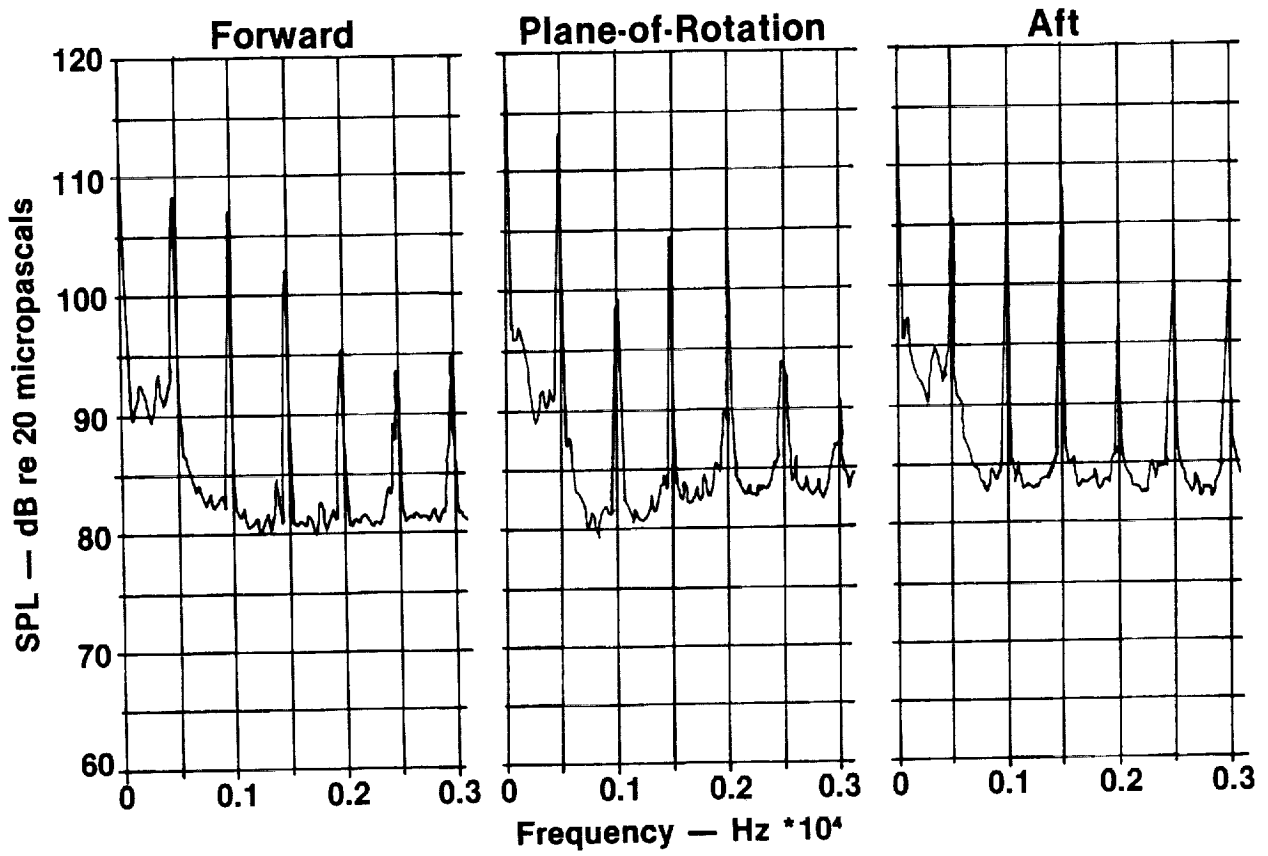


FIGURE 43. REPRESENTATIVE COUNTERROTATING PROP-FAN NOISE SPECTRA

198 M/SEC (650 FT/SEC) TIP SPEED
 82 K-WATTS (100 SHP) PER ROTOR

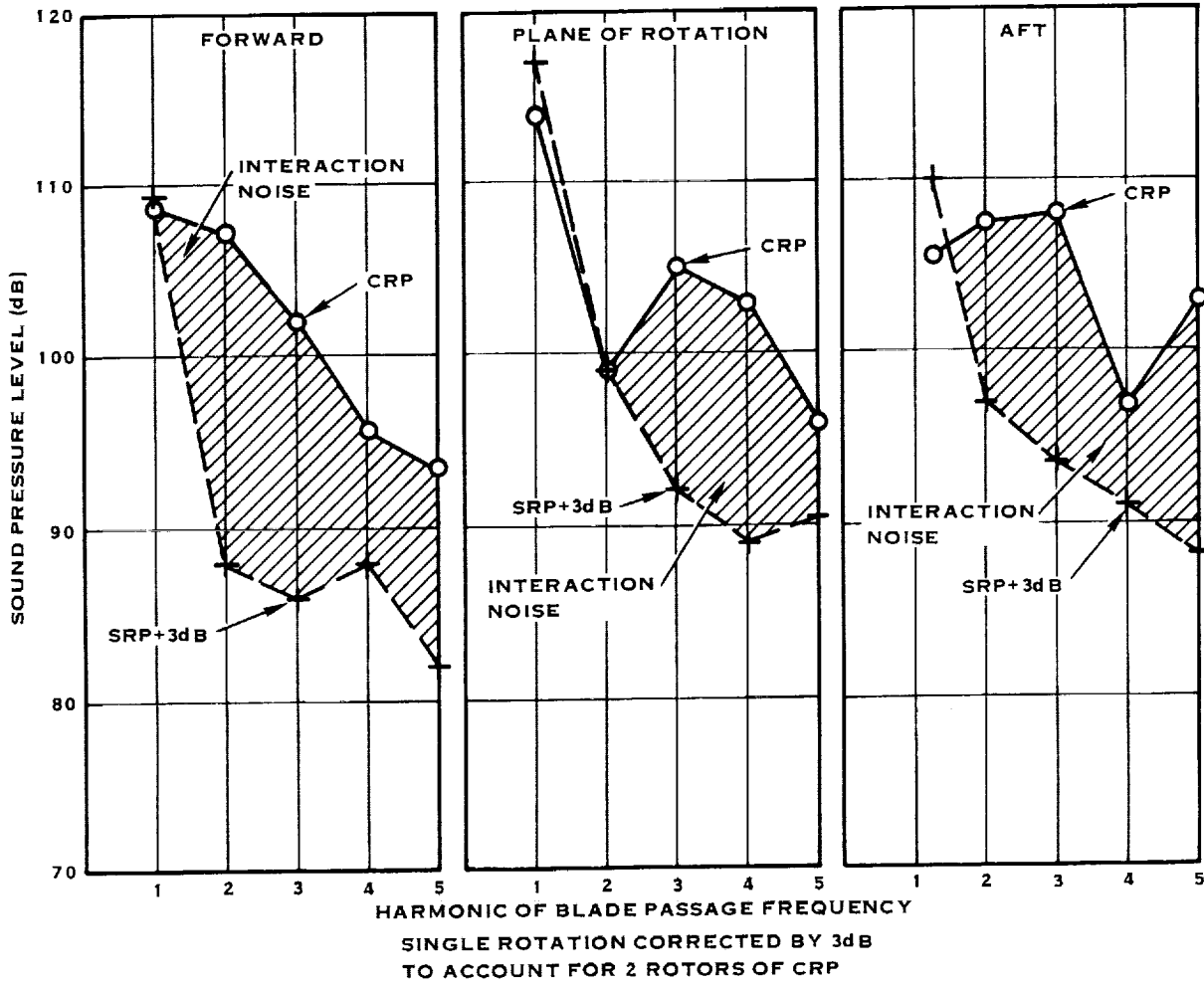


FIGURE 44. COMPARISON OF SINGLE ROTATION AND COUNTERROTATION NOISE LEVELS

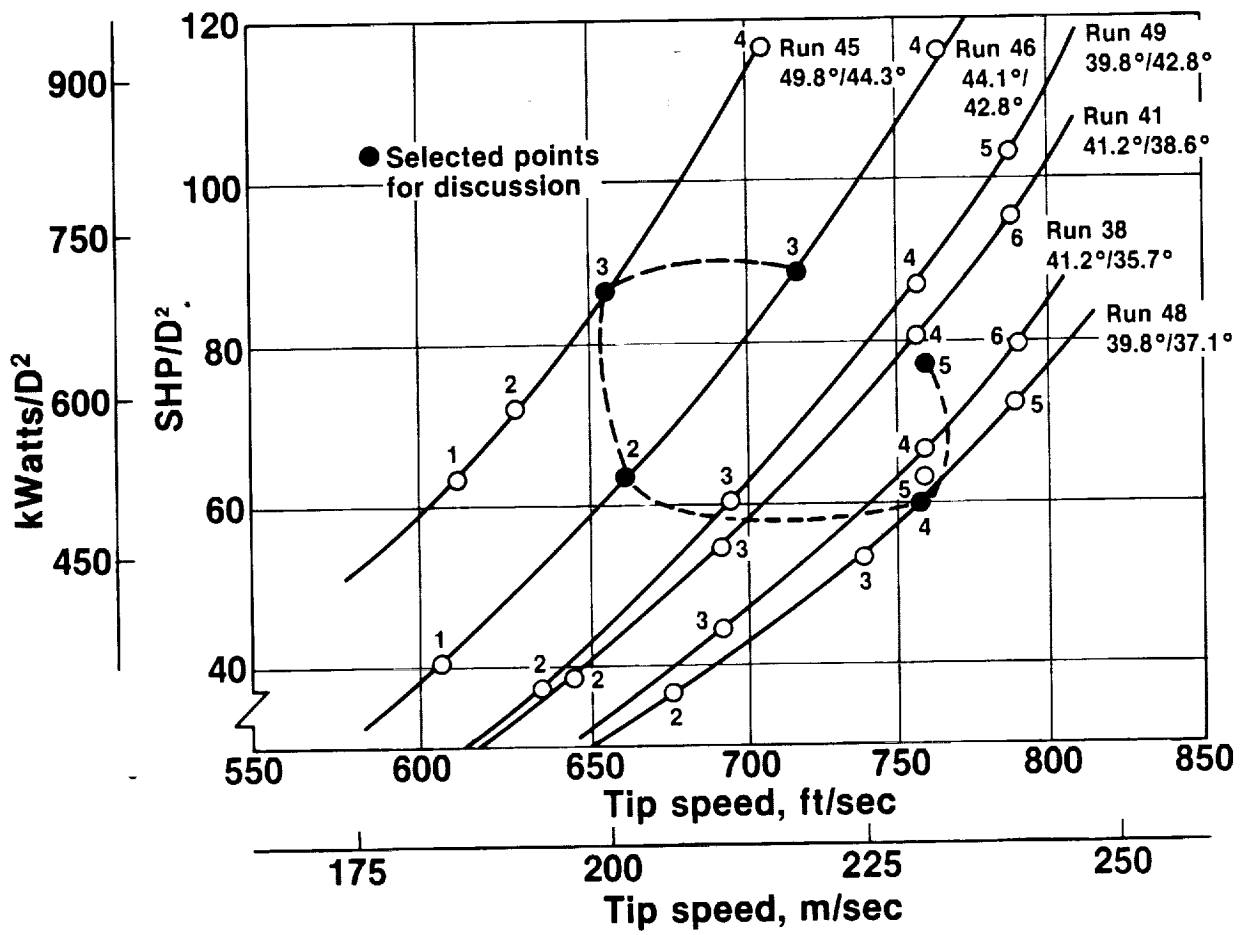


FIGURE 45. EQUAL RPM TRACTOR DATA FOR EVALUATING TIP SPEED AND POWER EFFECTS ON NOISE

ORIGINAL PAGE IS
OF POOR QUALITY

RUN 46.2
511 KW/D² (63.7 SHP/D²)
202 M/SEC (662 FT/SEC) TIP SPEED
59/41 POWER SPLIT

RUN 45.3
696 KW/D² (86.7 SHP/D²)
199 M/SEC (652 FT/SEC) TIP SPEED
58/42 POWER SPLIT

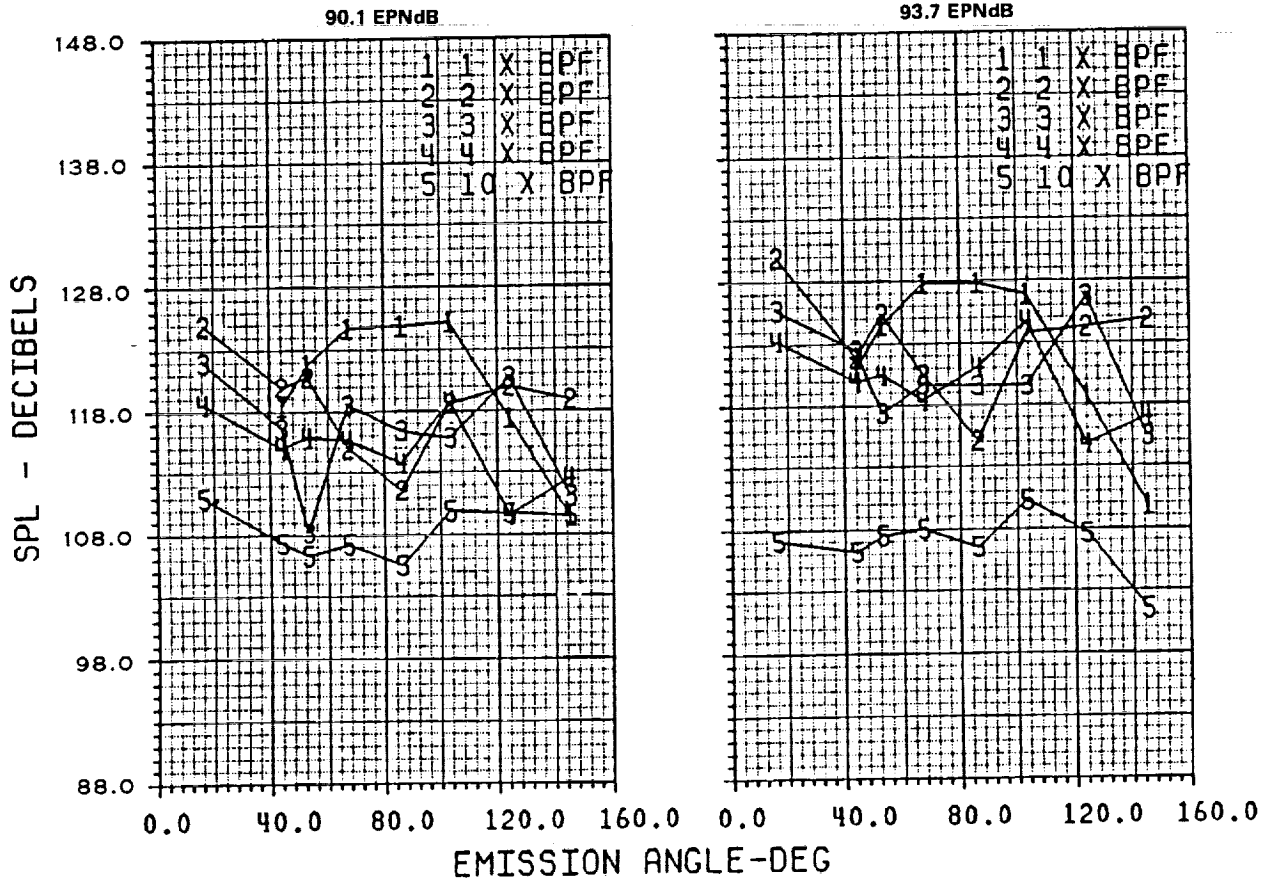


FIGURE 46. EFFECT OF POWER LOADING ON NOISE AT LOW TIP SPEED

ORIGINAL PAGE IS
OF POOR QUALITY

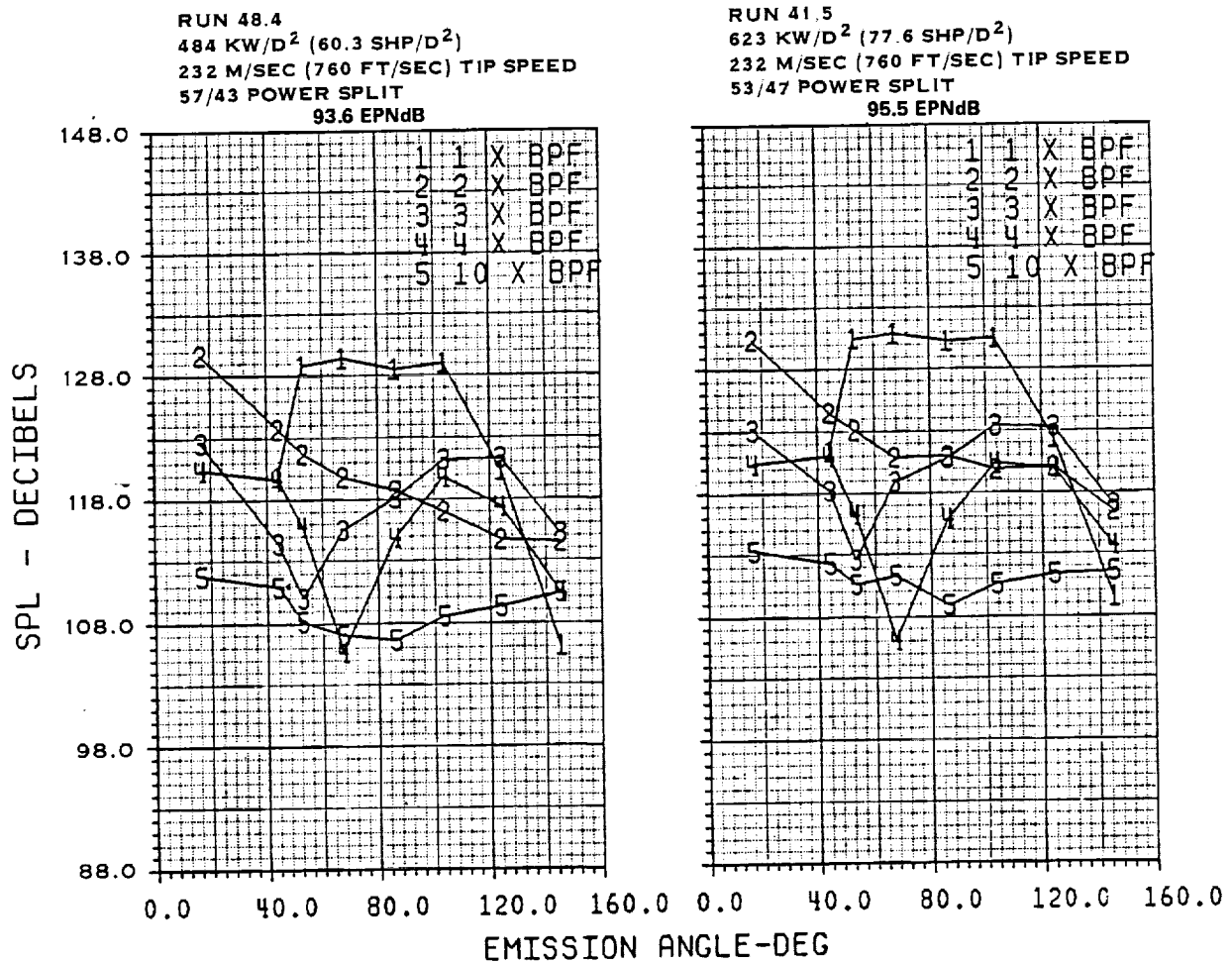


FIGURE 47. EFFECT OF POWER LOADING ON NOISE AT HIGH TIP SPEED

ORIGINAL PAGE IS
OF POOR QUALITY

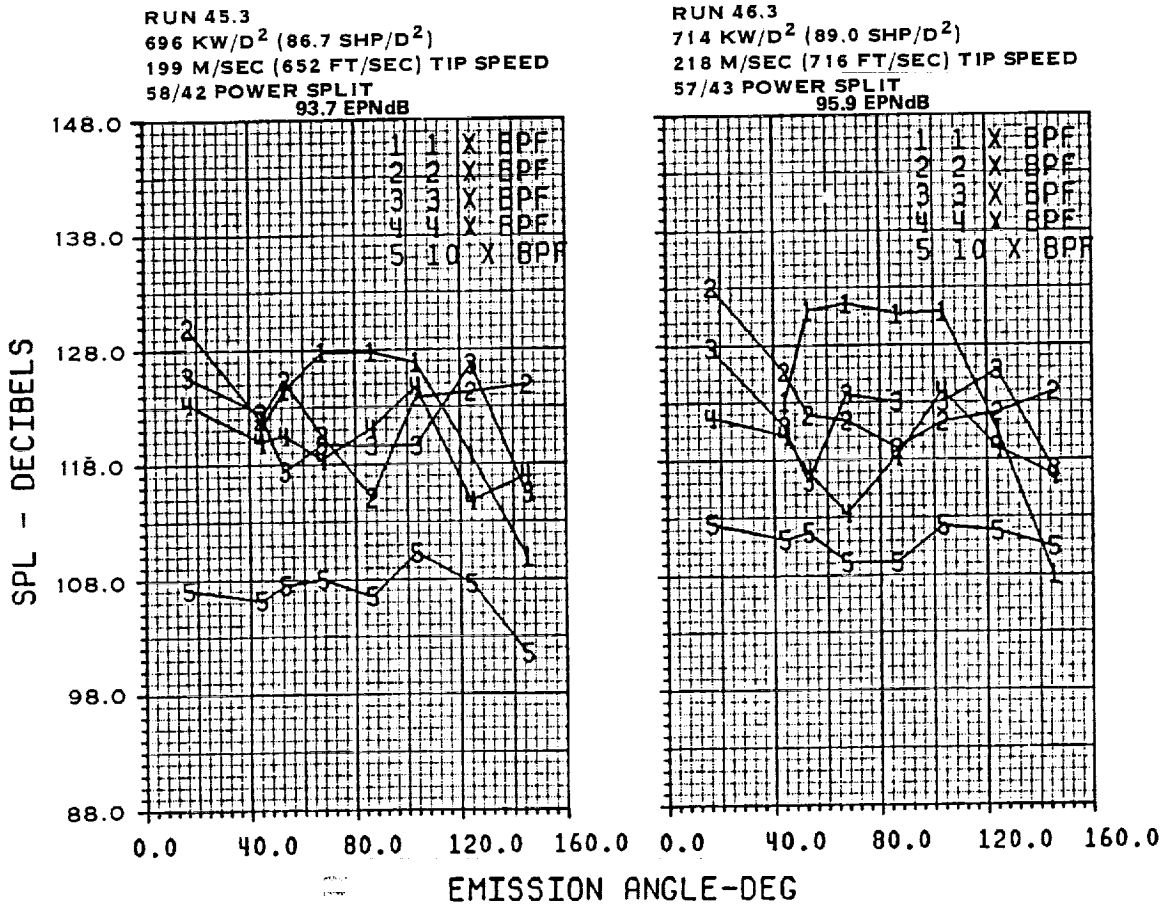


FIGURE 48. EFFECT OF TIP SPEED ON NOISE AT MODERATE POWER LOADING

ORIGINAL PAGE IS
OF POOR QUALITY

RUN 46.2
511 KW/D² (63.7 SHP/D²)
202 M/SEC (662 FT/SEC) TIP SPEED
59/41 POWER SPLIT

RUN 48.4
484 KW/D² (60.3 SHP/D²)
232 M/SEC (760 FT/SEC) TIP SPEED
57/43 POWER SPLIT

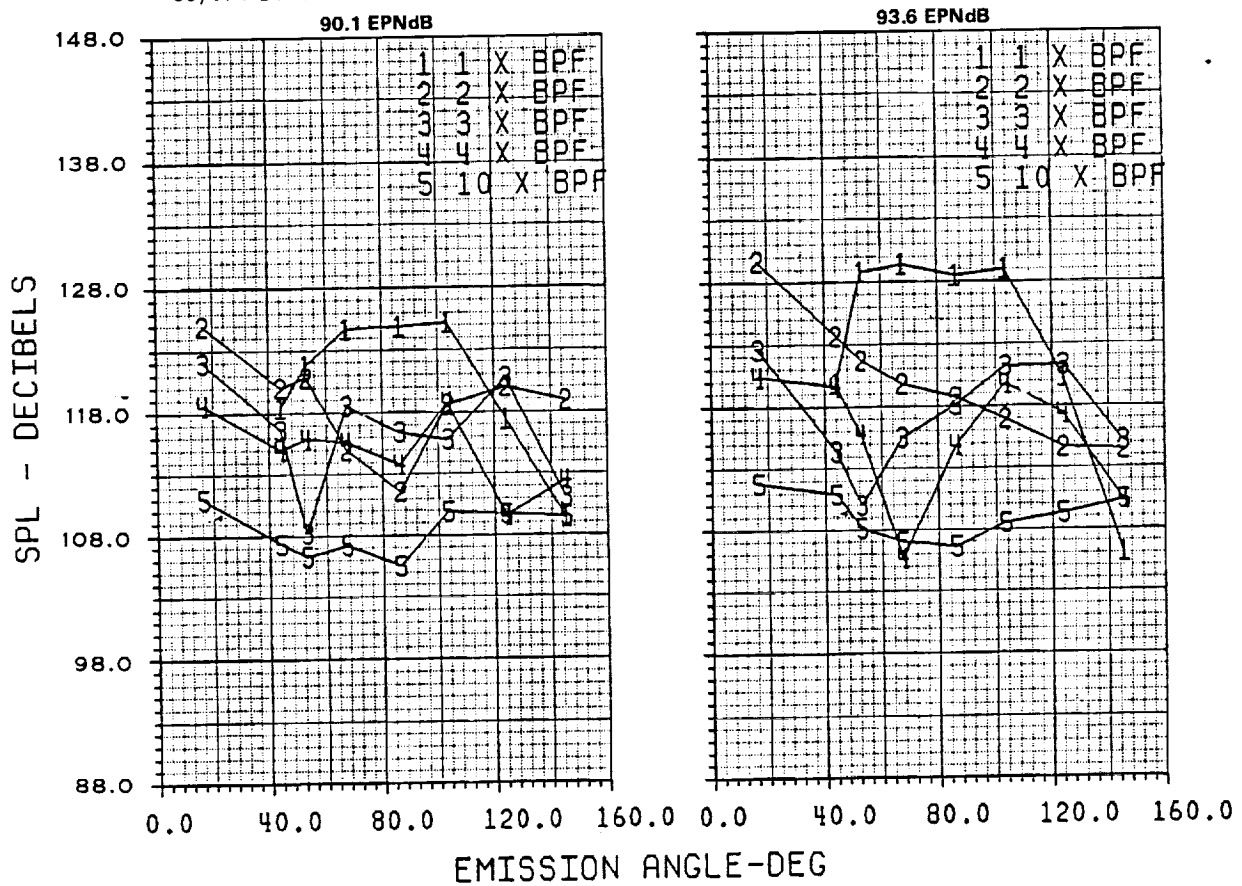
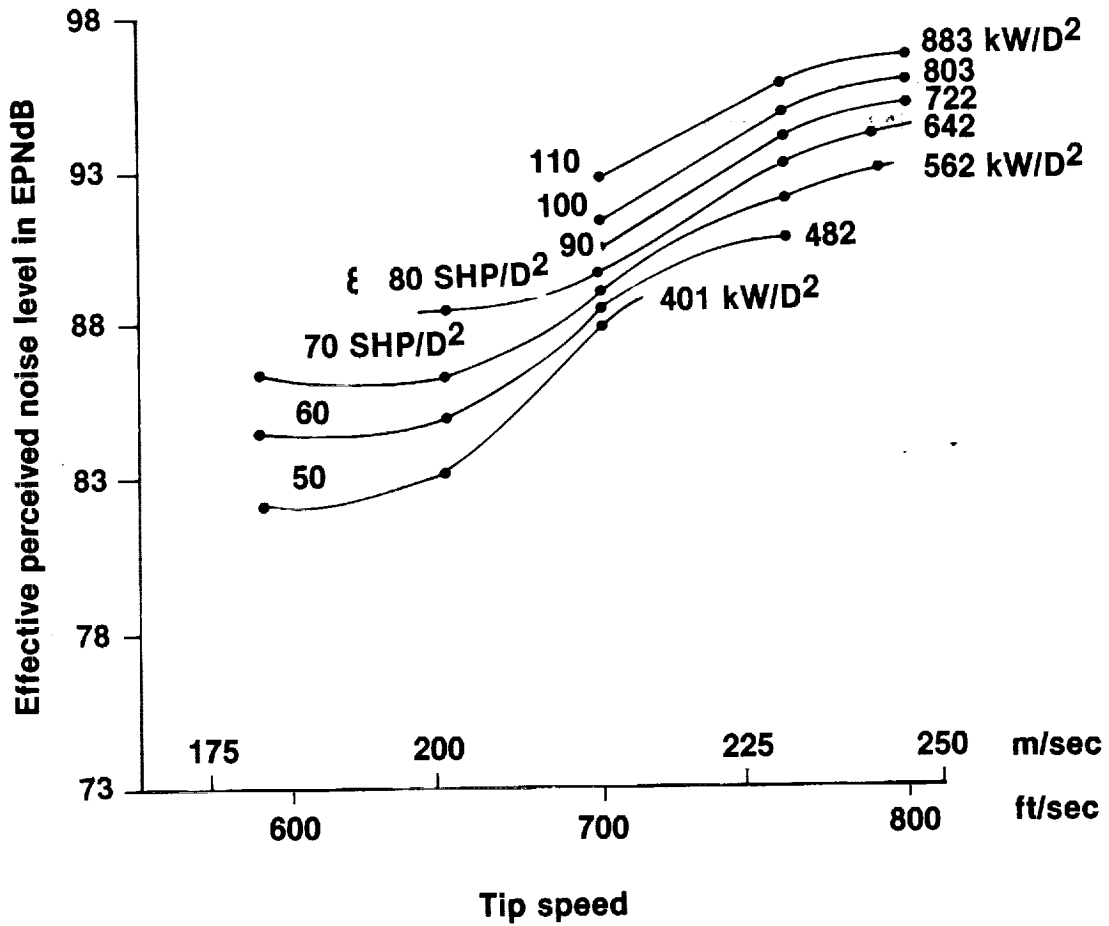


FIGURE 49. EFFECT OF TIP SPEED AT LOW POWER LOADING



Equal rpm tractor data
 Scaled to 4.0m (13.1 ft) diameter
 Adjusted to 45/55 power split
 0° angle-of-attack
 0.257D rotor/rotor spacing
 457m (1500 ft) distance

FIGURE 50. EFFECTIVE PERCEIVED NOISE LEVEL TRENDS WITH TIP SPEED AND POWER LOADING

RUN 49.2
 303 KW/D² (37.8 SHP/D²)
 193 M/SEC (633 FT/SEC) TIP SPEED
 49/51 POWER SPLIT

RUN 41.2
 307 KW/D² (38.3 SHP/D²)
 197 M/SEC (645 FT/SEC) TIP SPEED
 67/33 POWER SPLIT

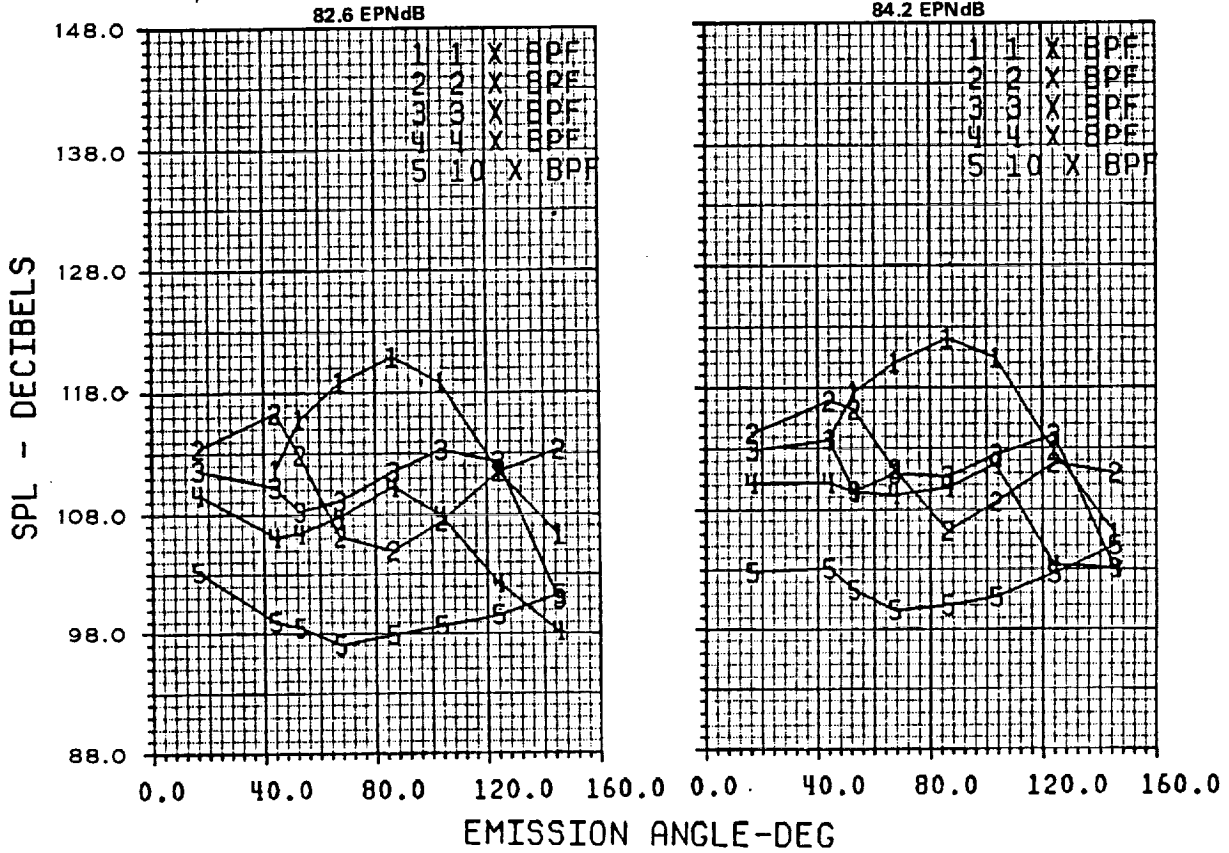
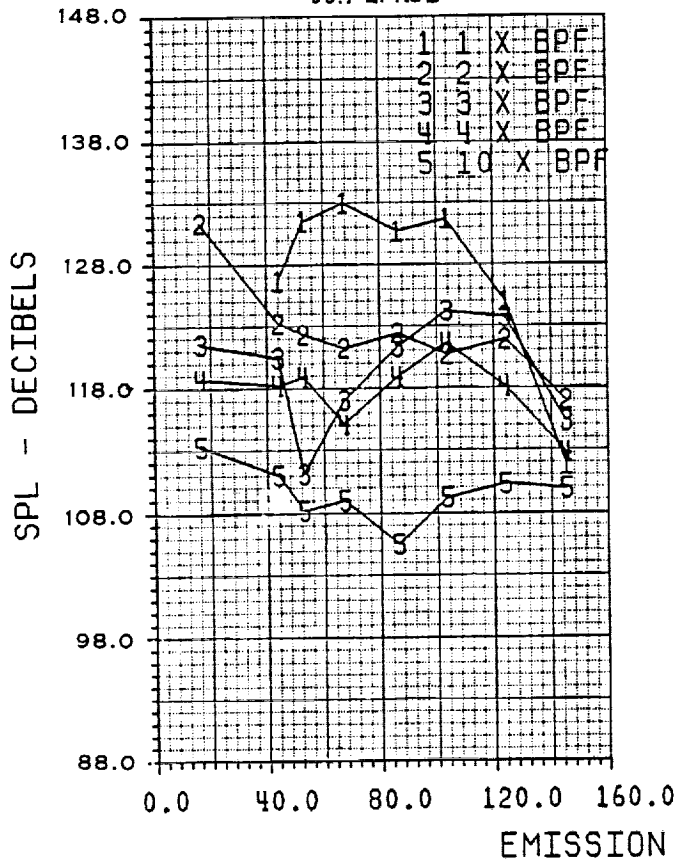


FIGURE 51. EFFECT OF POWER SPLIT ON CRP NOISE AT LOW TIP SPEED

RUN 49.4
 701 KW/D² (87.3 SHP/D²)
 231 M/SEC (758 FT/SEC) TIP SPEED
 48/52 POWER SPLIT

95.7 EPNdB



RUN 41.4
 648 KW/D² (80.7 SHP/D²)
 232 M/SEC (760 FT/SEC) TIP SPEED
 63/37 POWER SPLIT

96.6 EPNdB

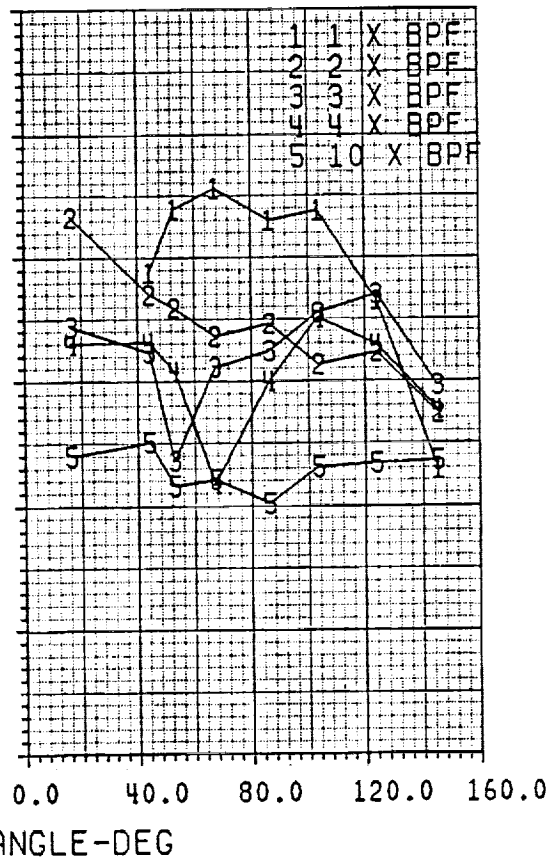
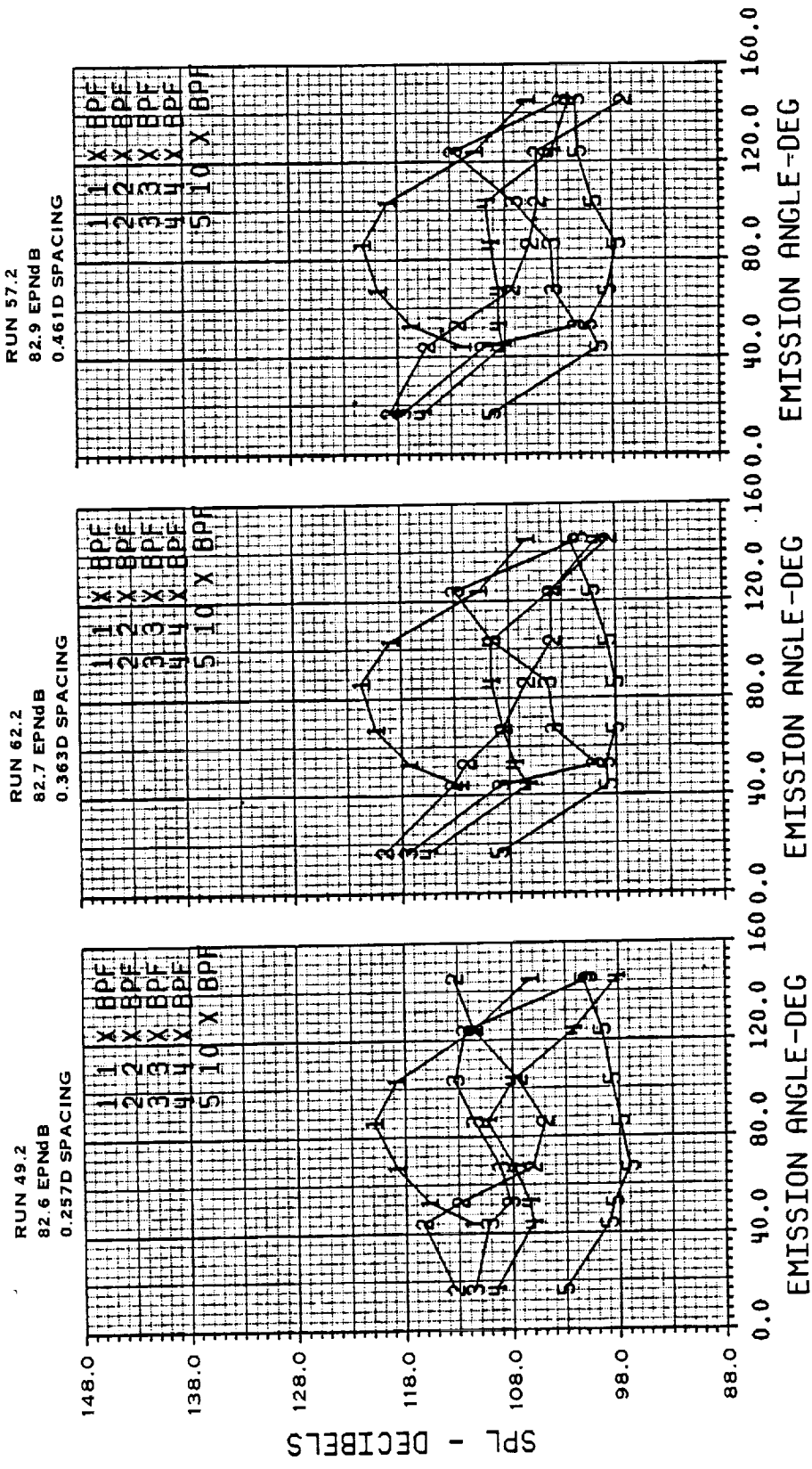
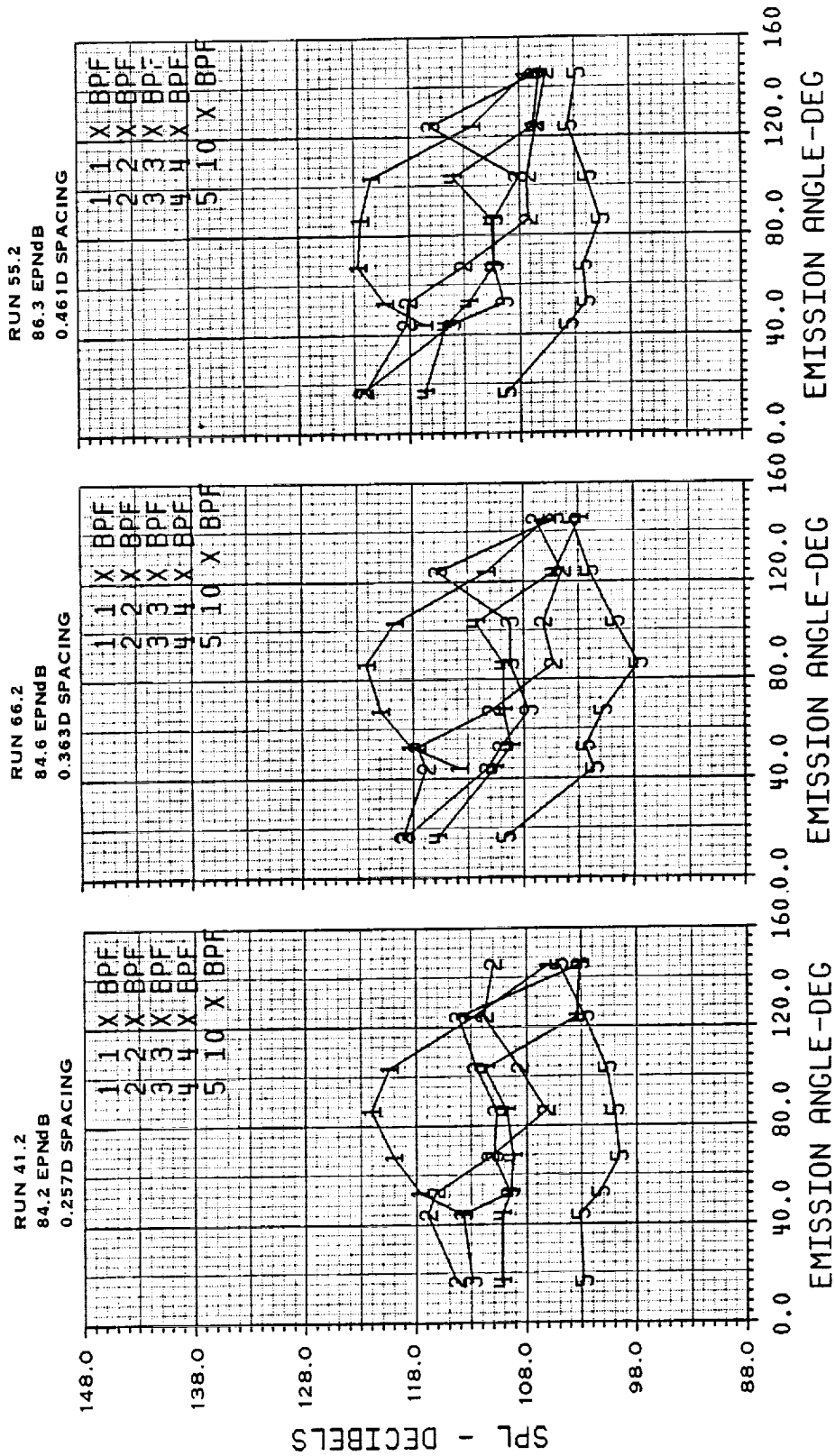


FIGURE 52. EFFECT OF POWER SPLIT ON NOISE AT HIGH TIP SPEED



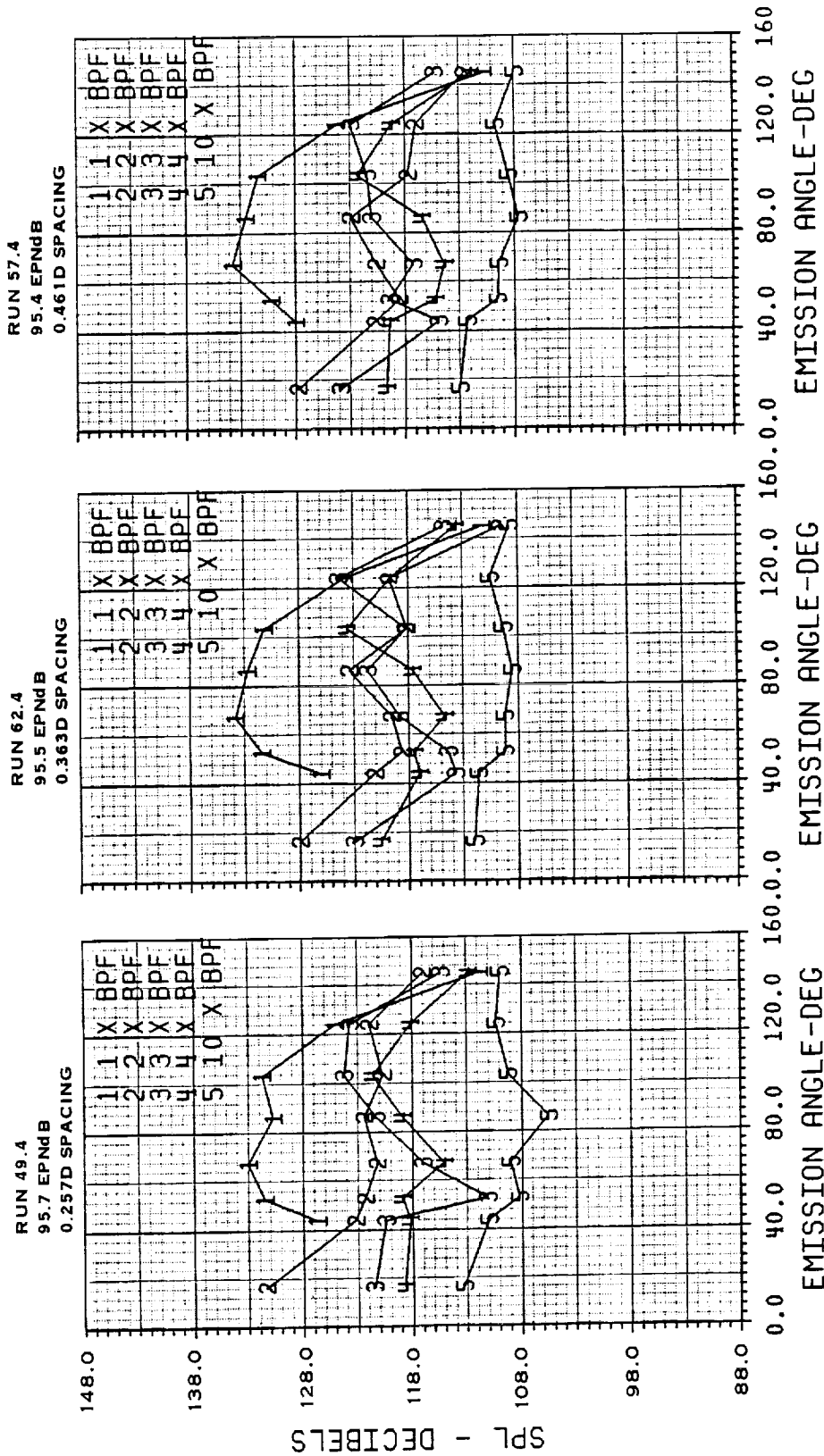
EQUAL RPM TRACTOR, 0° ANGLE OF ATTACK
 303 KWATTS/D2 (37.8 SHP/D²), 193 M/SEC (633 FT/SEC) TIP SPEED, 49/51 POWER SPLIT

FIGURE 53. EFFECT OF ROTOR-ROTOR SPACING AT EQUAL POWER SPLIT, LOW POWER, AND LOW TIP SPEED



EQUAL RPM TRACTOR, 0° ANGLE OF ATTACK
 307 KWATTS/D² (38.3 SHP/D²), 197 M/SEC (645 FT/SEC) TIP SPEED, 67/33 POWER SPLIT

FIGURE 54. EFFECT OF ROTOR-ROTOR SPACING AT UNEQUAL POWER SPLIT, LOW POWER, AND LOW TIP SPEED



EQUAL RPM TRACTOR, 0° ANGLE OF ATTACK
701 KWATTS/D² (87.3 SHP/D²), 231 M/SEC (758 FT/SEC) TIP SPEED, .48/52 POWER SPLIT

FIGURE 55. EFFECT OF ROTOR-ROTOR SPACING AT EQUAL POWER SPLIT, HIGH POWER, AND HIGH TIP SPEED

EQUAL RPM TRACTOR, 50/50 POWER SPLIT

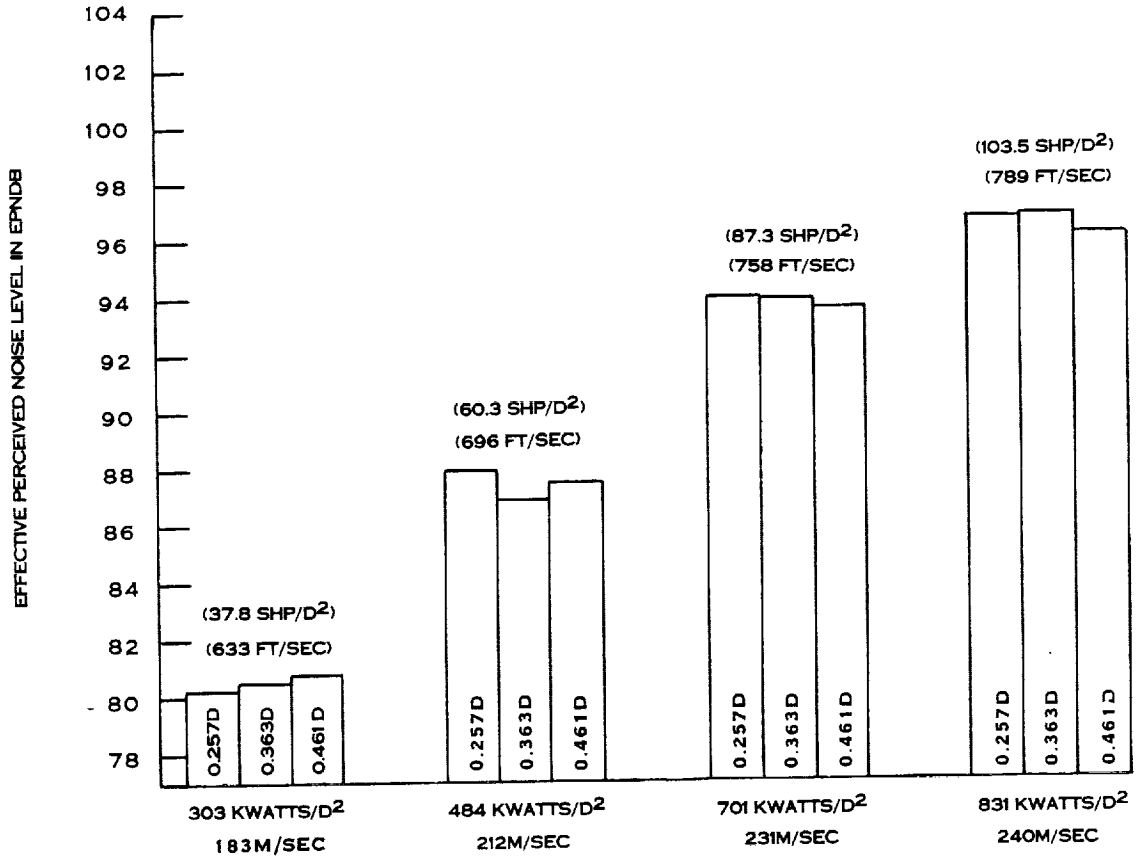


FIGURE 56. EFFECT OF ROTOR/ROTOR SPACING ON SCALED EPNL FOR 50/50 POWER SPLIT

EQUAL RPM TRACTOR, 57/43 POWER SPLIT

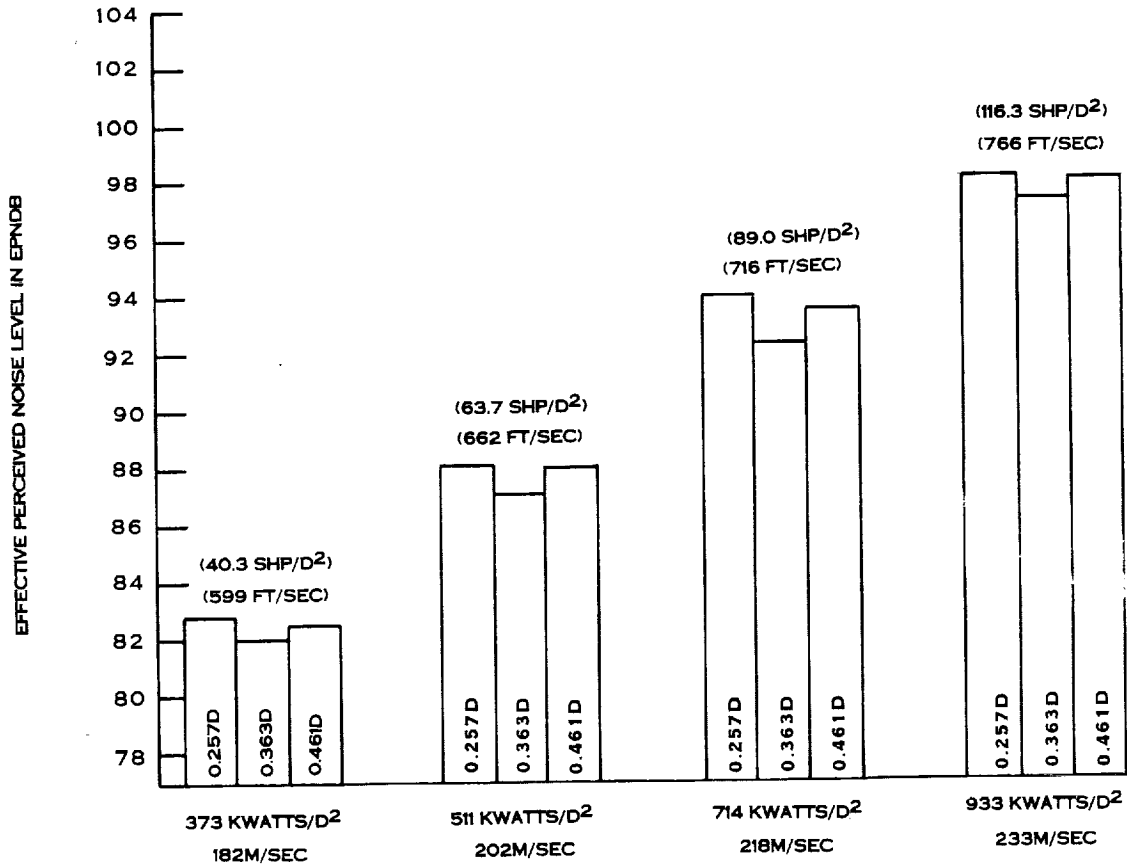
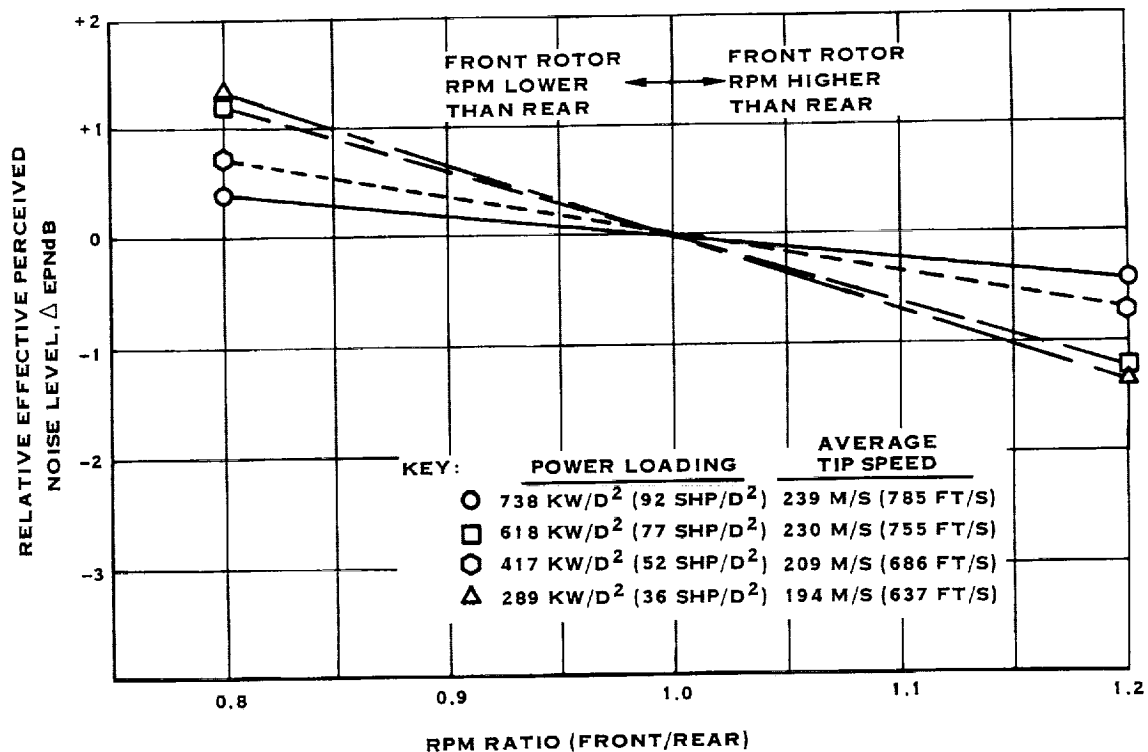


FIGURE 57. EFFECT OF ROTOR/ROTOR SPACING ON SCALED EPNL FOR 57/43 POWER SPLIT



TRACTOR DATA
 SCALED TO 4.0M (13.1 FT) DIAMETER
 55/45 POWER SPLIT
 0° ANGLE-OF-ATTACK
 0.257D ROTOR/ROTOR SPACING
 457M (1500 FT) DISTANCE

FIGURE 58. EFFECT OF FRONT-TO-REAR RPM RATIO ON SCALED PERCEIVED NOISE

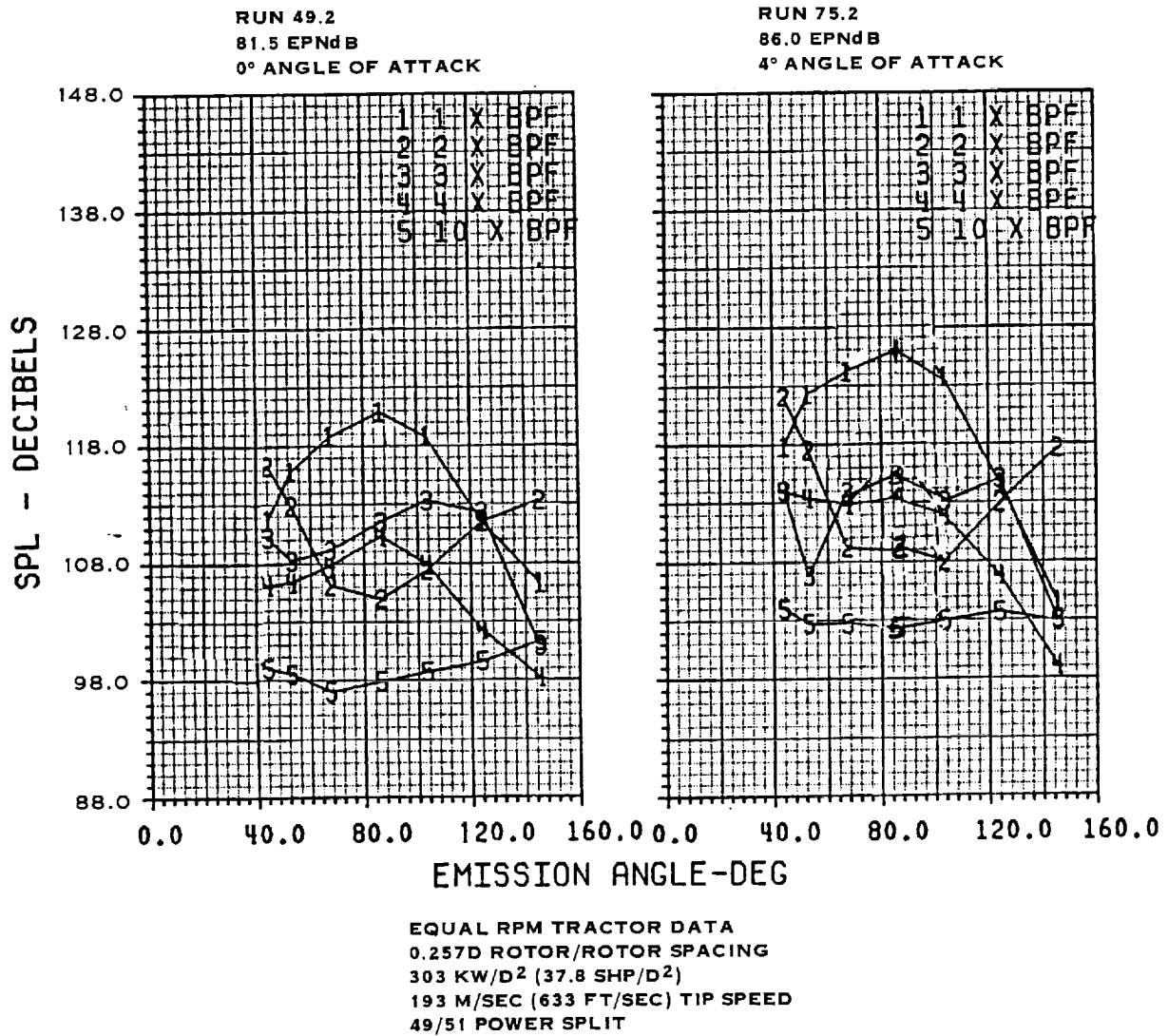


FIGURE 59. EFFECT OF ANGLE-OF-ATTACK ON TRACTOR AT LOW POWER AND LOW TIP SPEED FOR A 49/51 POWER SPLIT

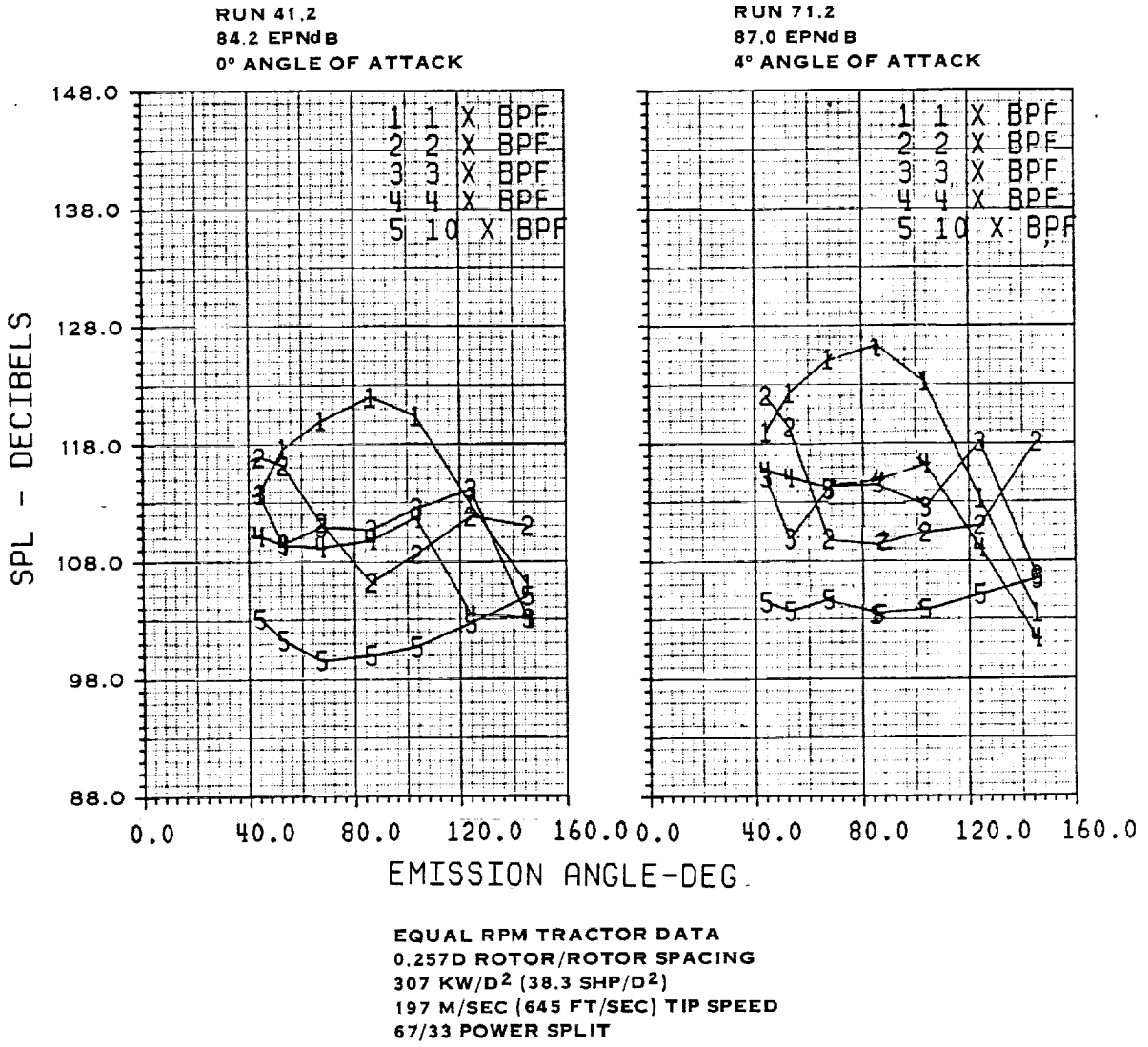
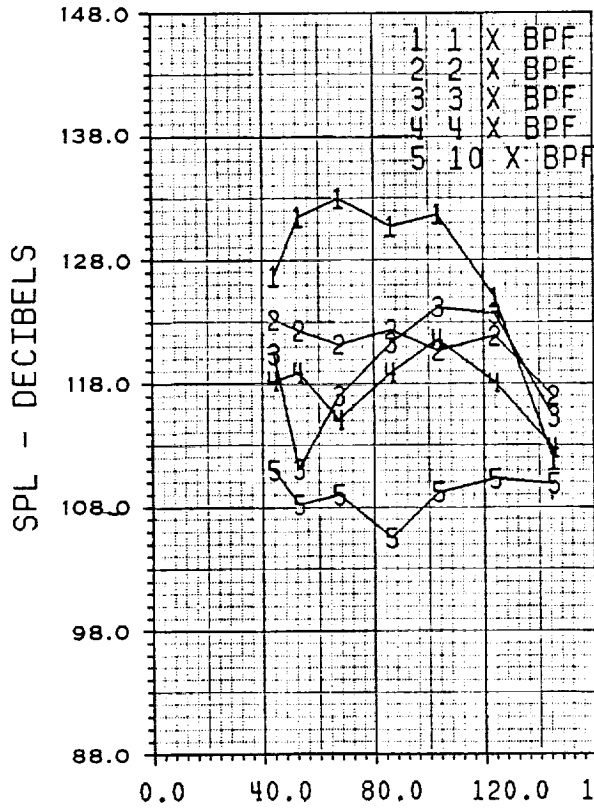
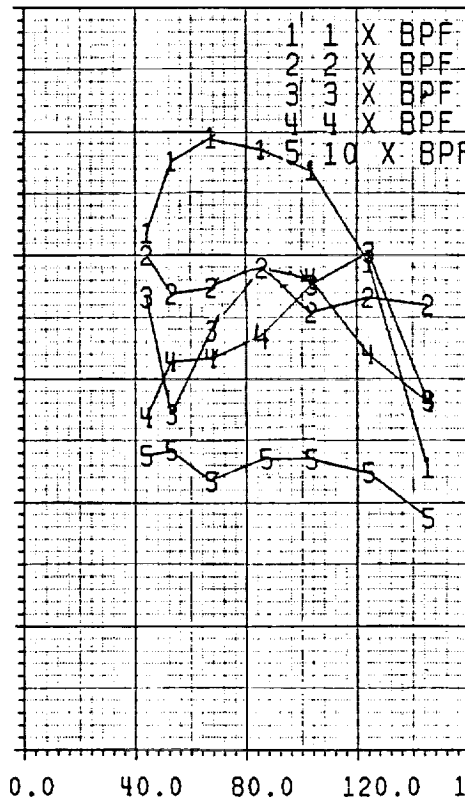


FIGURE 60. EFFECT OF ANGLE-OF-ATTACK ON TRACTOR AT LOW POWER AND LOW TIP SPEED FOR A 67/33 POWER SPLIT.

RUN 49.4
94.5 EPNdB
0° ANGLE OF ATTACK



RUN 75.4
98.6 EPNdB
4° ANGLE OF ATTACK



EQUAL RPM TRACTOR DATA
0.257D ROTOR/ROTOR SPACING
701 KW/D² (87.3 SHP/D²)
231 M/SEC (758 FT/SEC) TIP SPEED
48/52 POWER SPLIT

FIGURE 61. EFFECT OF ANGLE-OF-ATTACK ON TRACTOR AT HIGH POWER AND HIGH TIP SPEED FOR A 48/52 POWER SPLIT

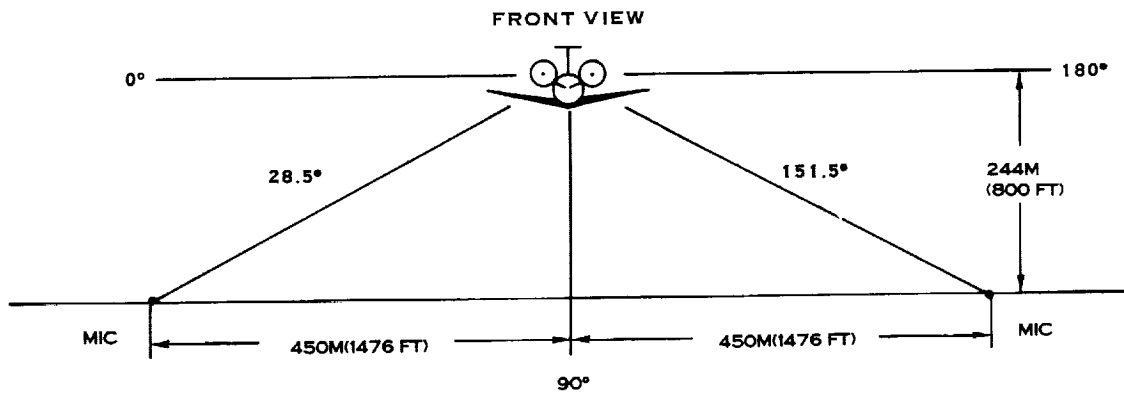
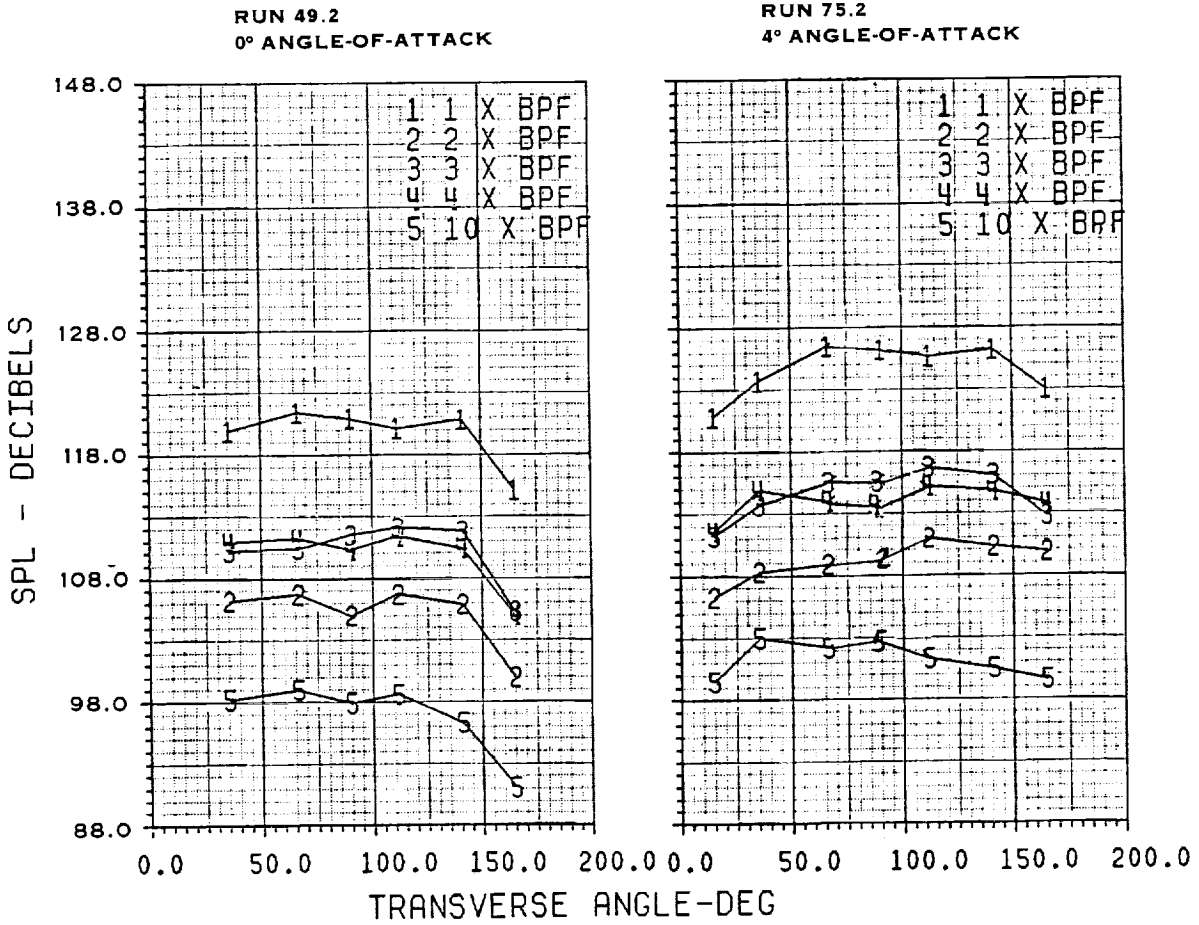


FIGURE 62. MICROPHONE LOCATIONS FOR SIDELINE NOISE MEASUREMENTS



EQUAL RPM TRACTOR DATA
 0.257D ROTOR/ROTOR SPACING
 303 KW/D² (37.8 SHP/D²)
 193 M/SEC (633 FT/SEC) TIP SPEED
 49/51 POWER SPLIT

FIGURE 63. EFFECT OF ANGLE-OF-ATTACK ON TRACTOR SIDELINE NOISE AT LOW POWER, LOW TIP SPEED, AND 49/51 POWER SPLIT

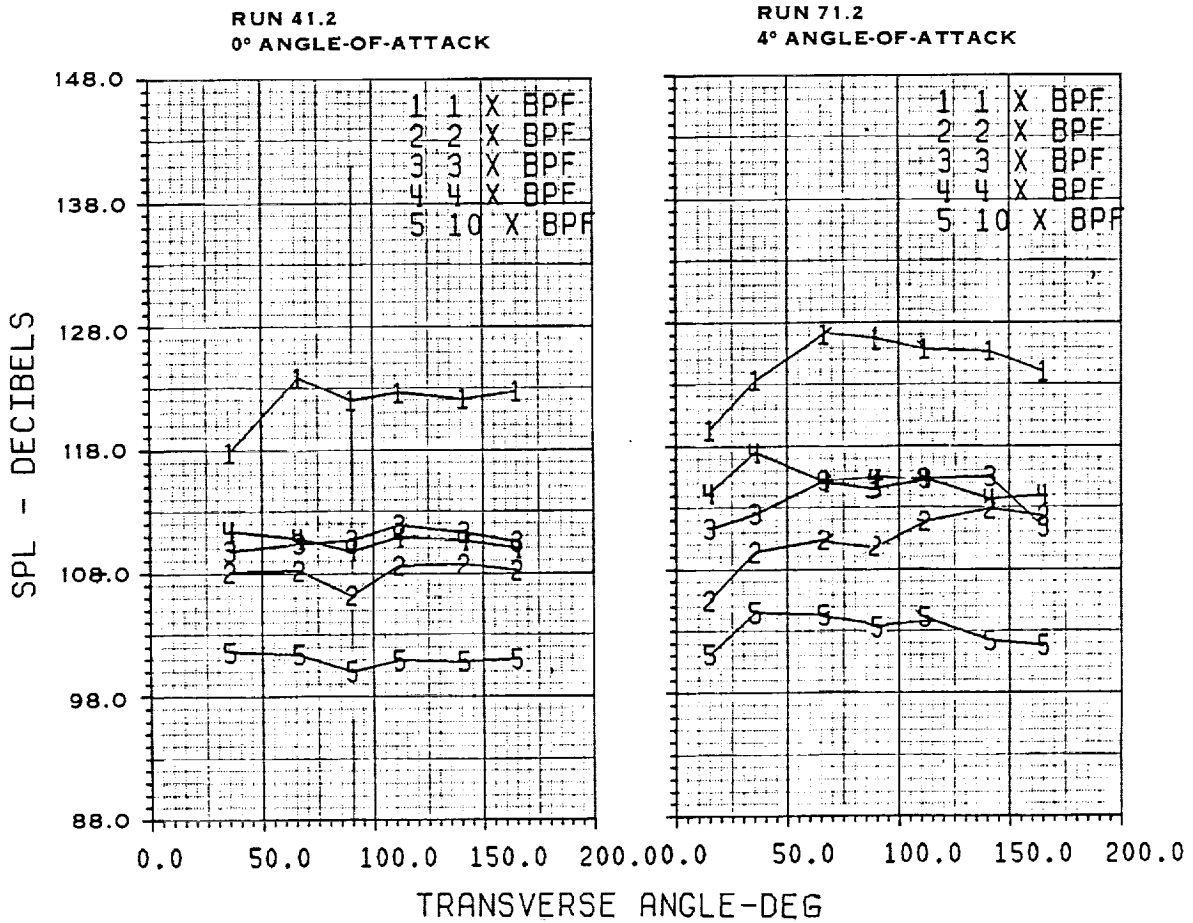
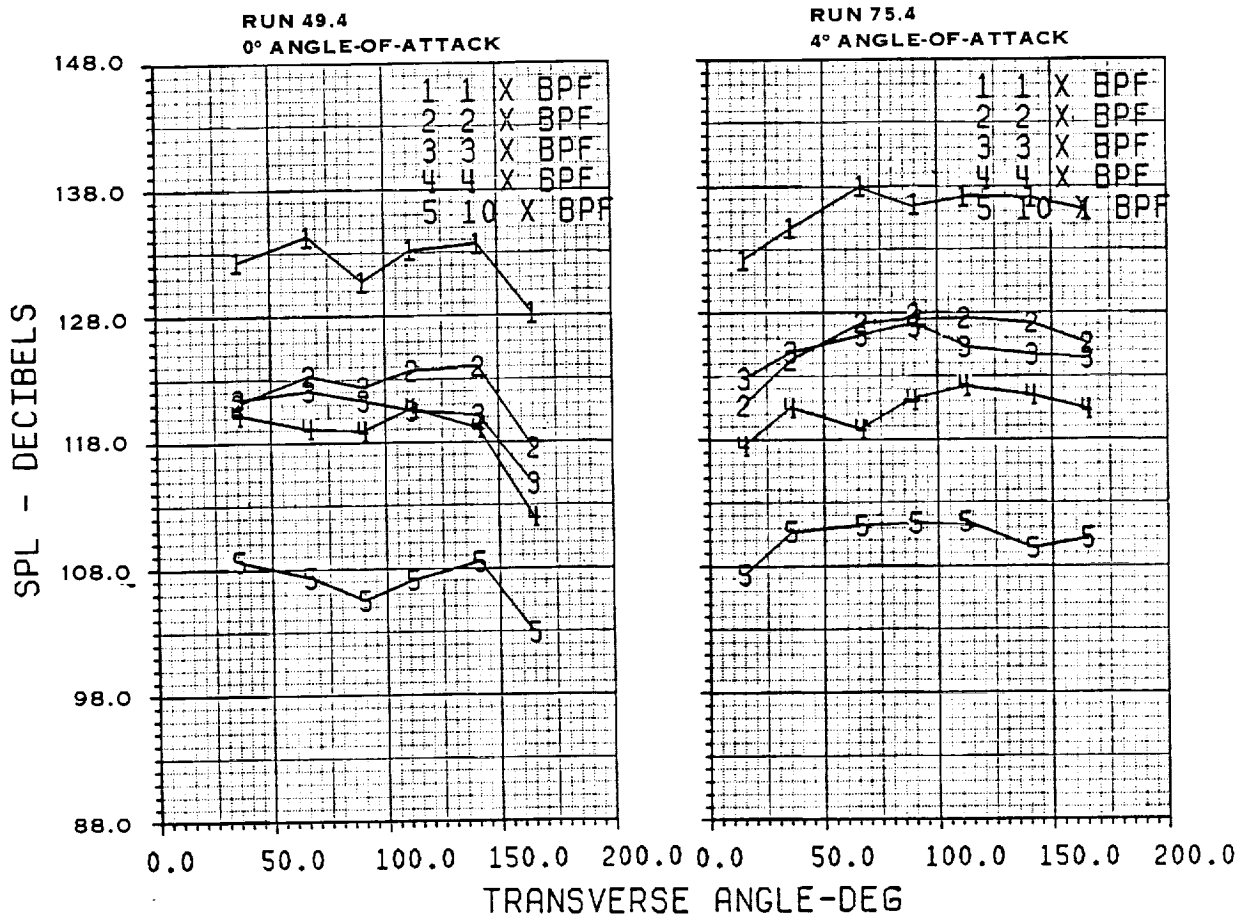
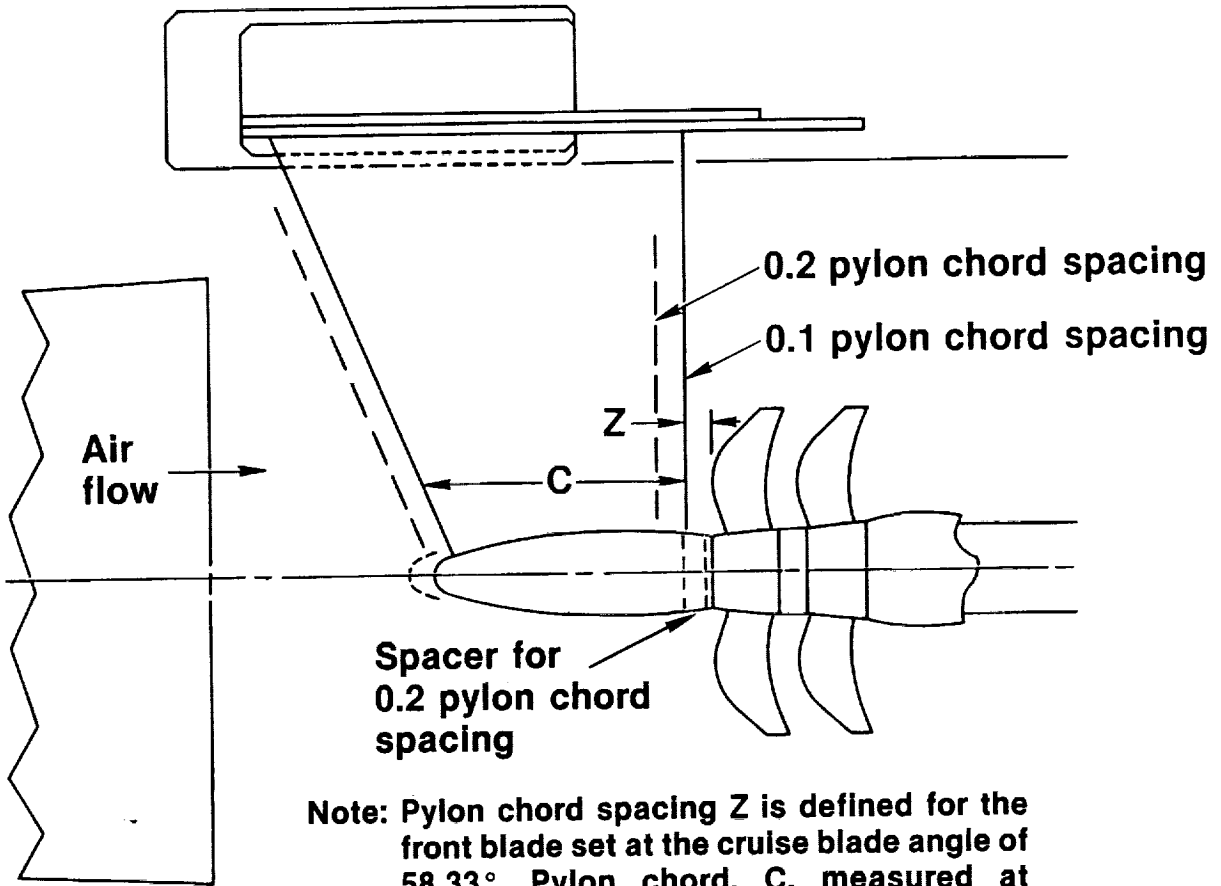


FIGURE 64. EFFECT OF ANGLE-OF-ATTACK ON TRACTOR SIDELINE NOISE AT LOW POWER, LOW TIP SPEED, AND 67/33 POWER SPLIT



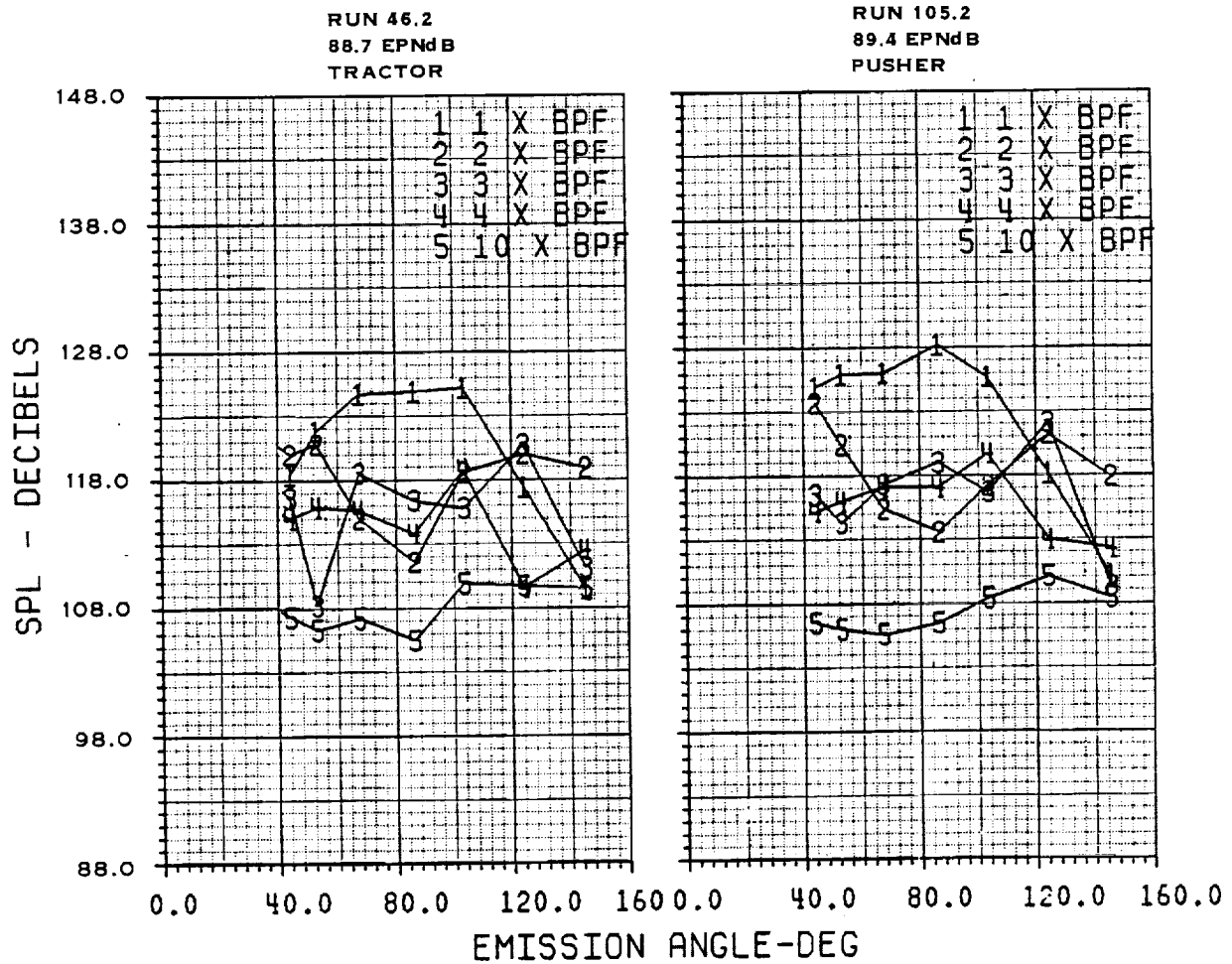
EQUAL RPM TRACTOR DATA
 0.257D ROTOR/ROTOR SPACING
 701 KW/D² (87.3 SHP/D²)
 231 M/SEC (758 FT/SEC) TIP SPEED
 48/52 POWER SPLIT

FIGURE 65. EFFECT OF ANGLE-OF-ATTACK ON TRACTOR SIDELINE NOISE AT HIGH POWER, HIGH TIP SPEED, AND 48/52 POWER SPLIT



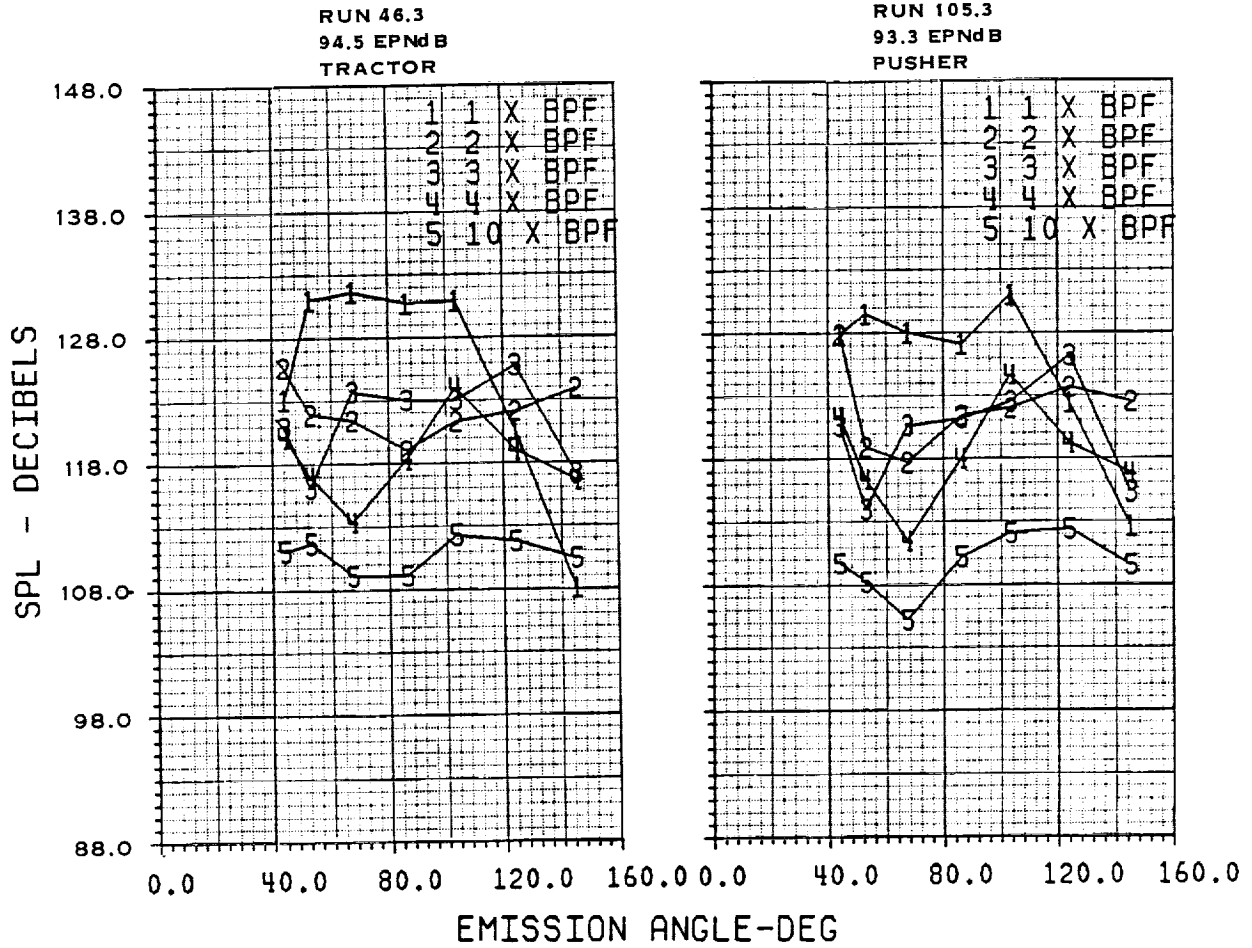
Note: Pylon chord spacing Z is defined for the front blade set at the cruise blade angle of 58.33° . Pylon chord, C , measured at minimum Z .

FIGURE 66. PYLON LOCATIONS FOR PUSHER TESTING



EQUAL RPM DATA
 0° ANGLE-OF-ATTACK
 0.257D ROTOR/ROTOR SPACING
 511 KW/D² (63.7 SHP/D²)
 202 M/SEC (662 FT/SEC) TIP SPEED
 59/41 POWER SPLIT

FIGURE 67. EFFECT OF PYLON AT LOW POWER AND LOW TIP SPEED



EQUAL RPM DATA
 0° ANGLE-OF-ATTACK
 0.257D ROTOR/ROTOR SPACING
 714 KW/D² (89.0 SHP/D²)
 218 M/SEC (716 FT/SEC) TIP SPEED
 57/43 POWER SPLIT

FIGURE 68. EFFECT OF PYLON AT HIGH POWER AND HIGH TIP SPEED

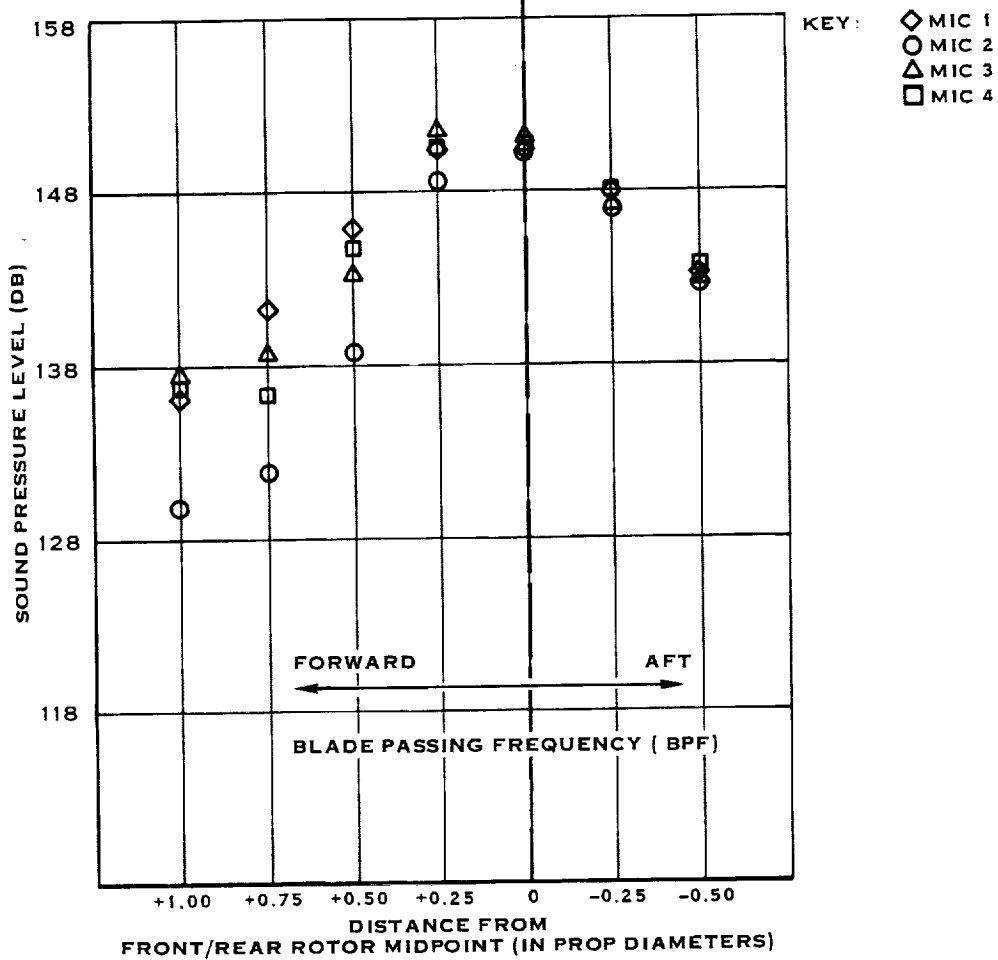
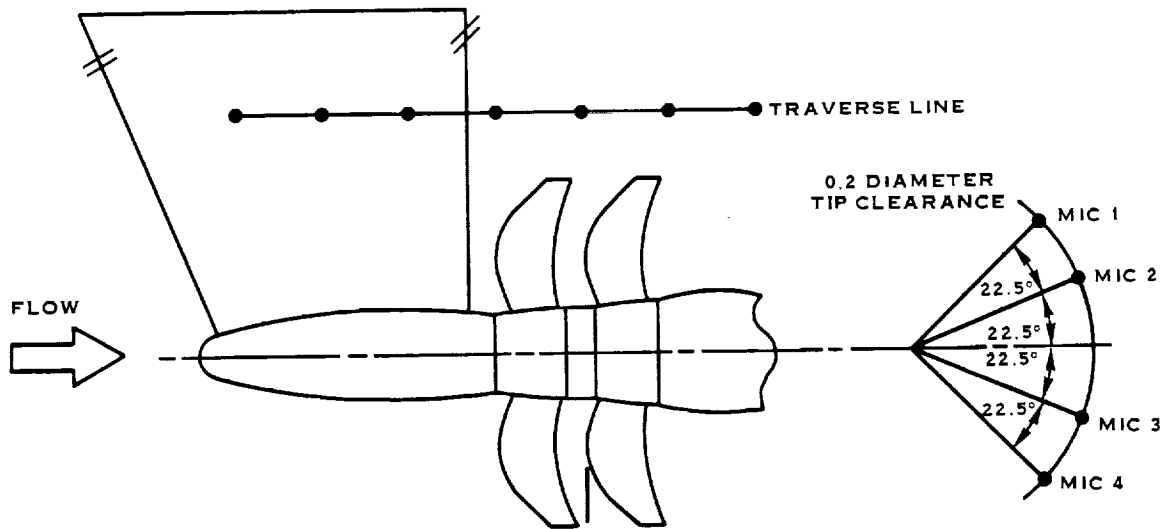


FIGURE 69. NEAR-FIELD NOISE LEVELS AT CRUISE TIP MACH NUMBER FOR BPF

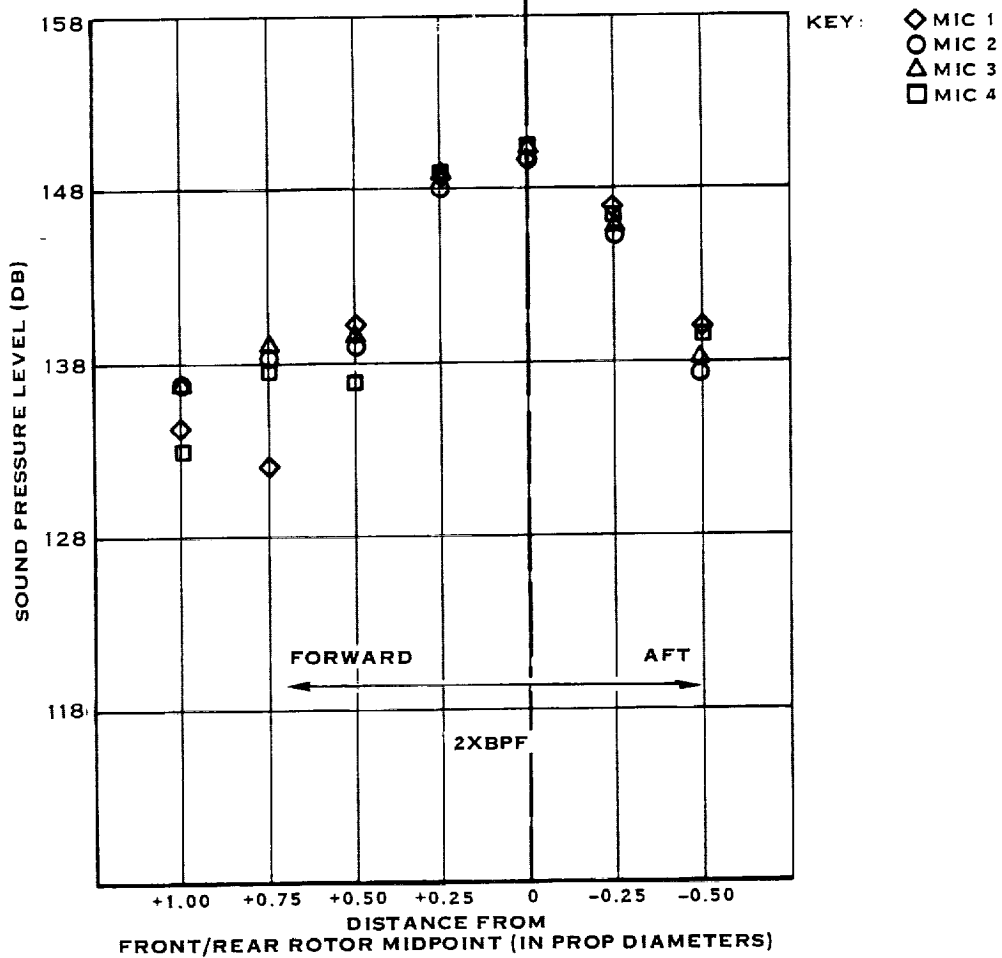
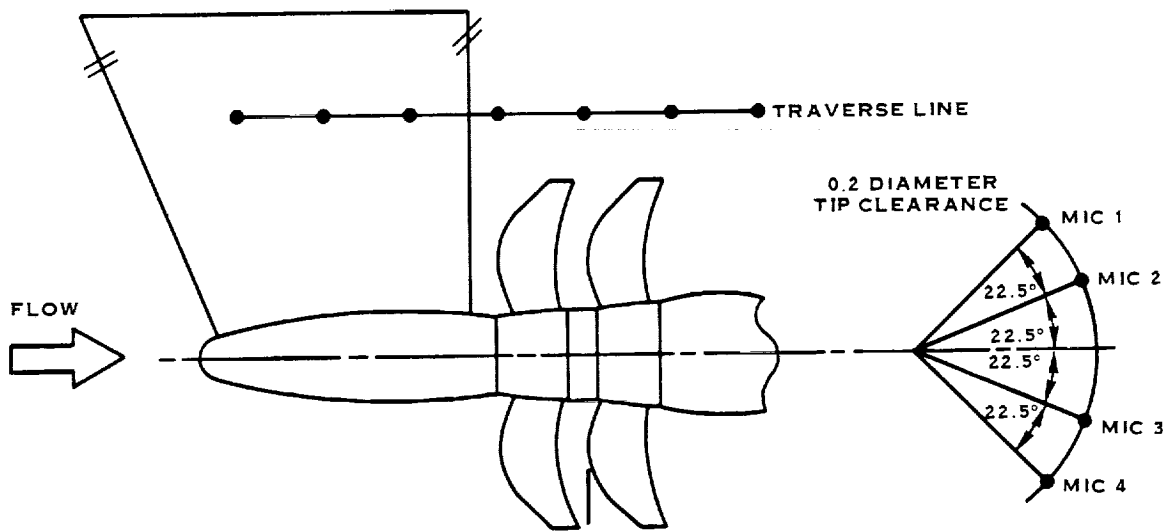


FIGURE 70. NEAR-FIELD NOISE LEVELS AT CRUISE TIP MACH NUMBER FOR 2X BPF

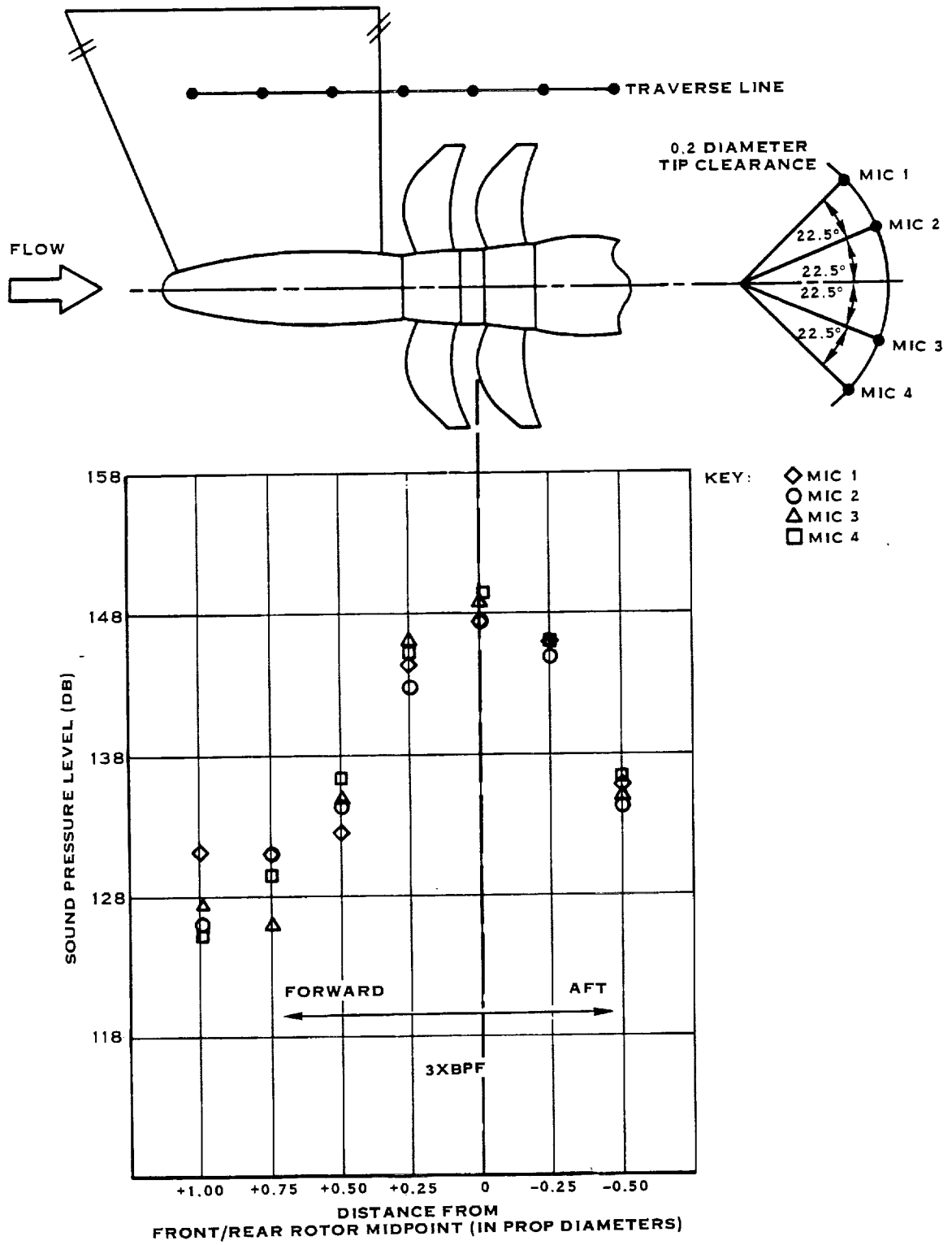


FIGURE 71. NEAR-FIELD NOISE LEVELS AT CRUISE TIP MACH NUMBER FOR 3X BPF

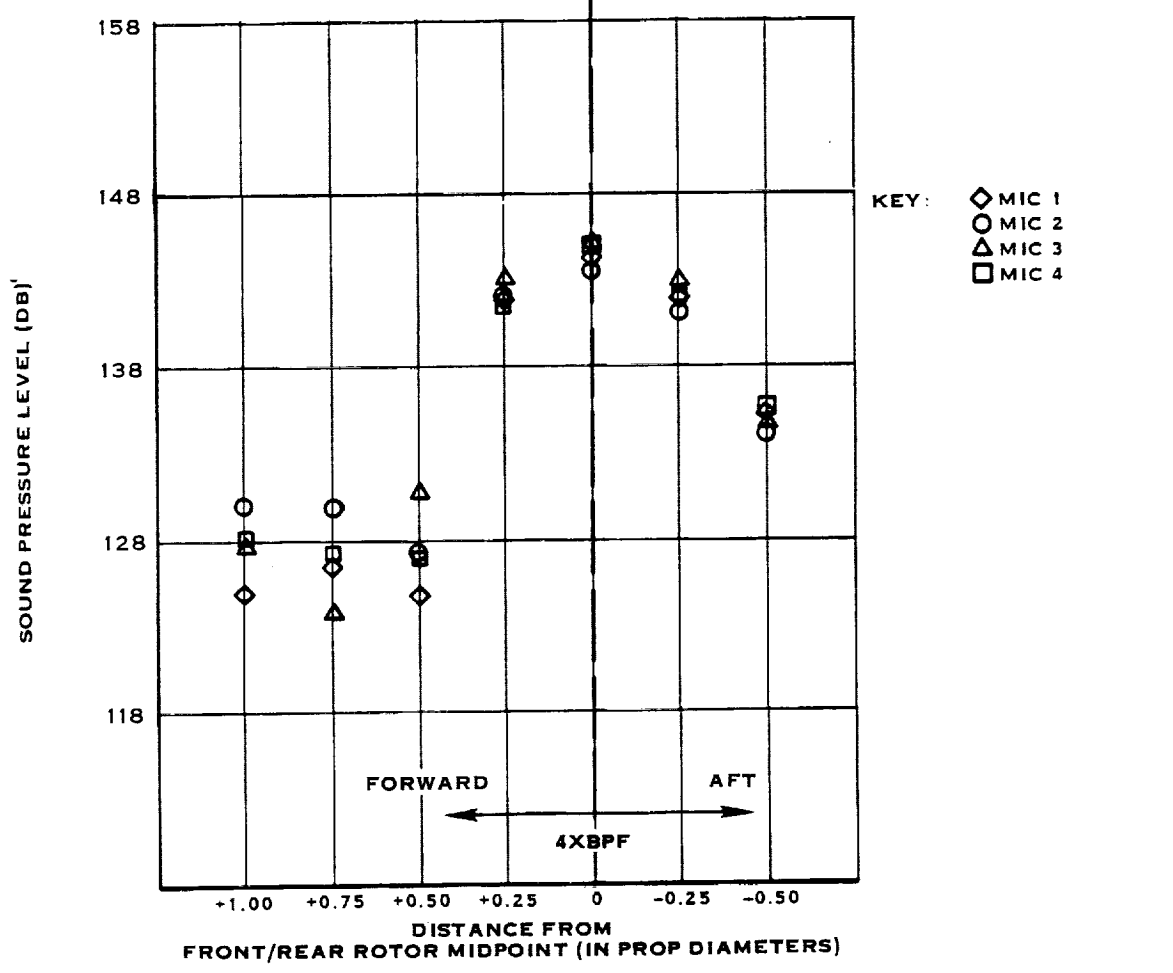
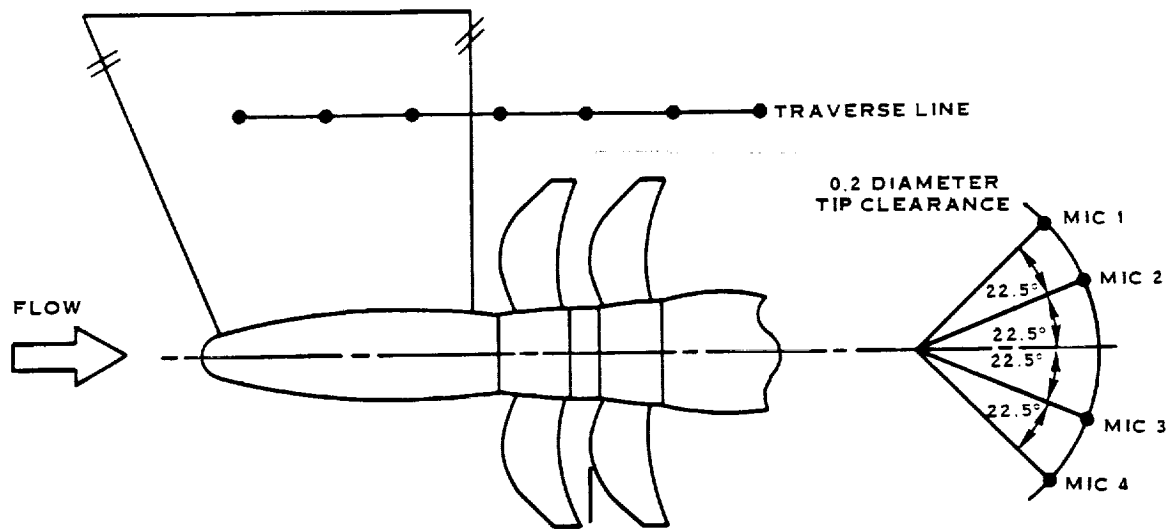


FIGURE 72. NEAR-FIELD NOISE LEVELS AT CRUISE TIP MACH NUMBER FOR 4X BPF

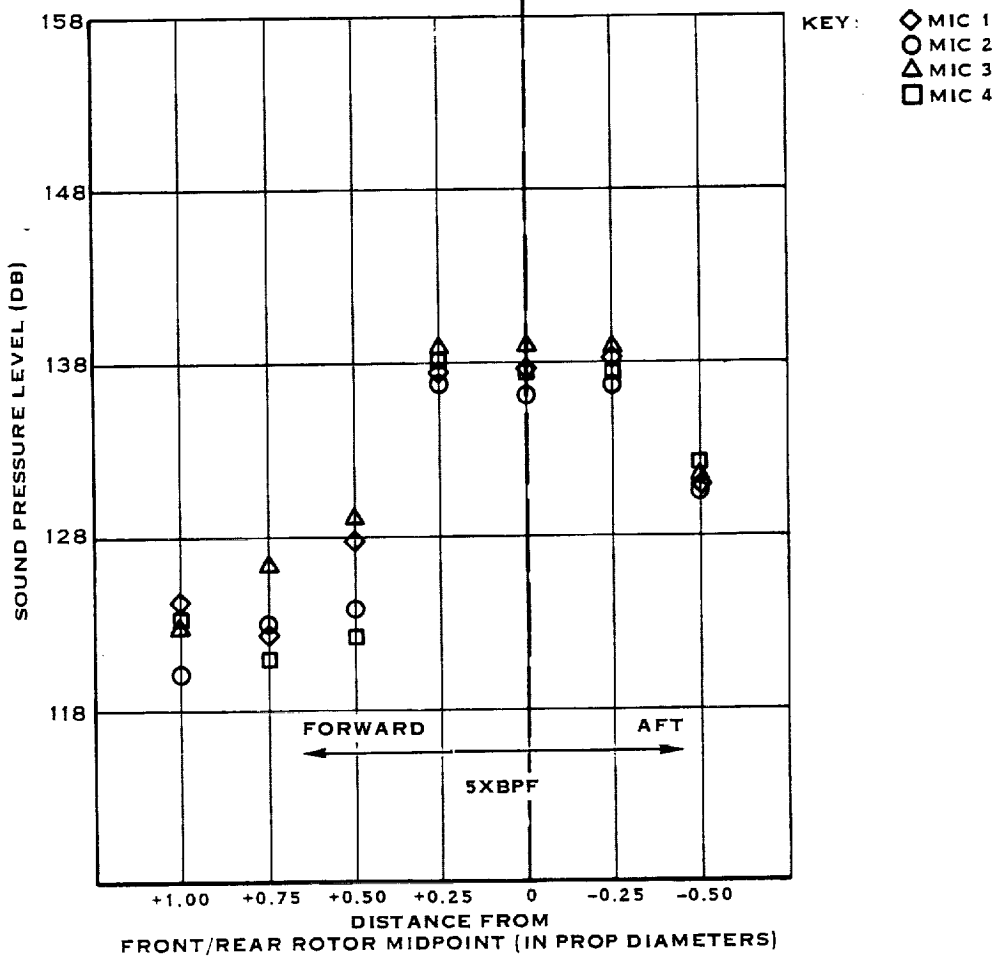
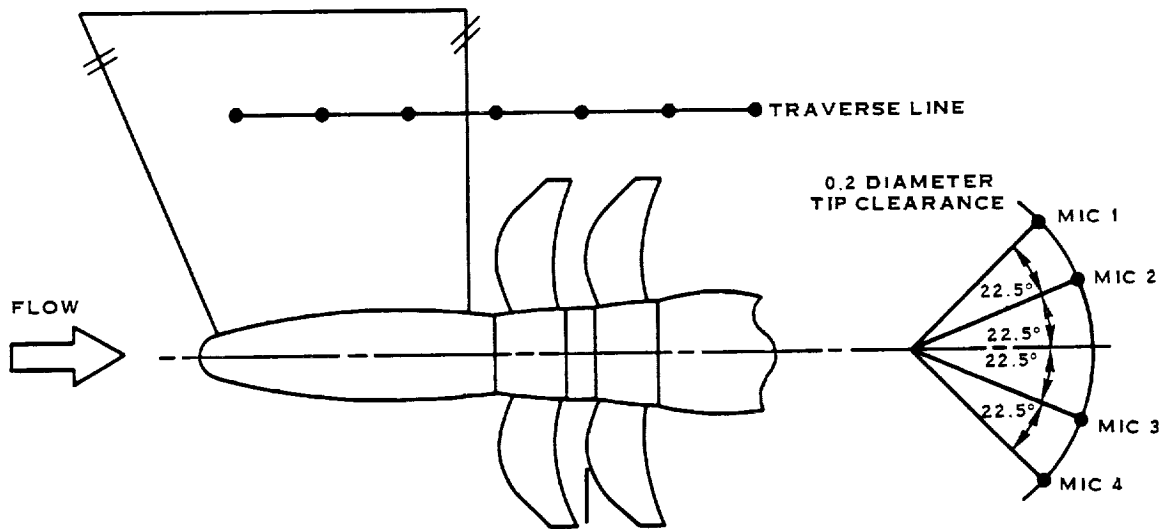
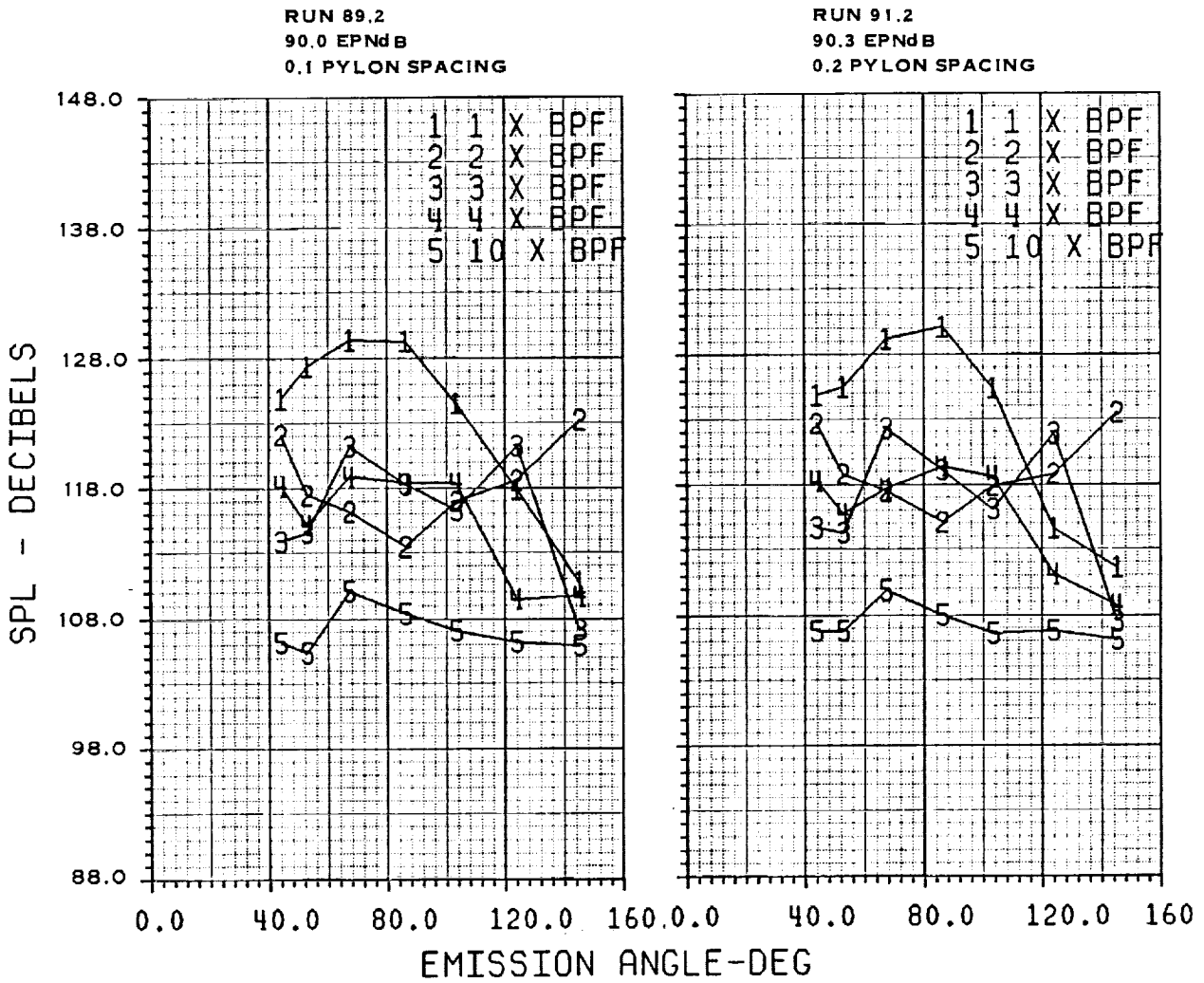
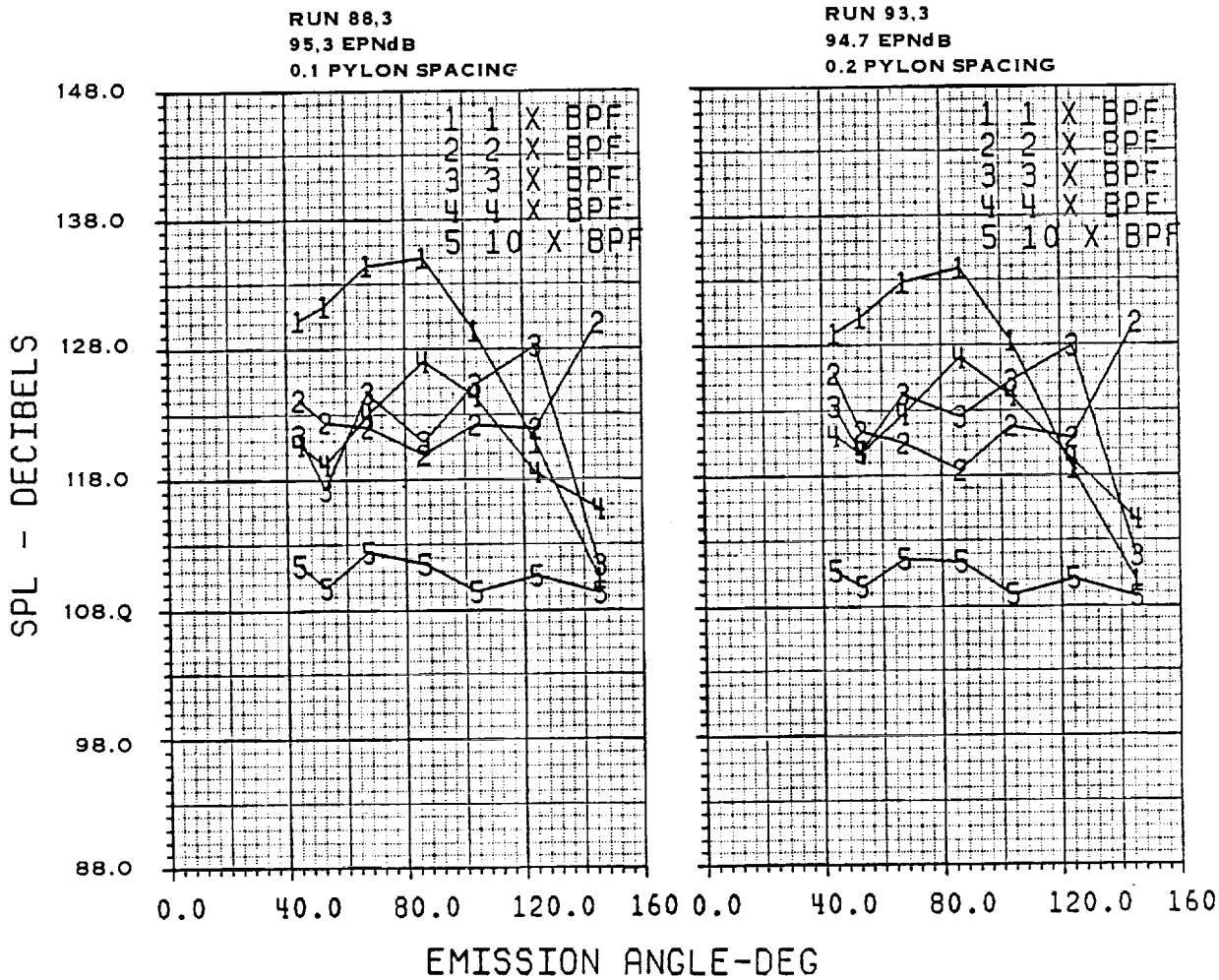


FIGURE 73. NEAR-FIELD NOISE LEVELS AT CRUISE TIP MACH NUMBER FOR 5X BPF



EQUAL RPM DATA
 4° ANGLE-OF-ATTACK
 0.257D ROTOR/ROTOR SPACING
 511 KW/D² (63.7 SHP/D²)
 202 M/SEC (662 FT/SEC) TIP SPEED
 59/41 POWER SPLIT

FIGURE 74. EFFECT OF PYLON SPACING ON PUSHER AT 4° ANGLE-OF-ATTACK FOR LOW POWER AND LOW TIP SPEED



EQUAL RPM DATA
 4° ANGLE-OF-ATTACK
 0.257D ROTOR/ROTOR SPACING
 696 KW/D² (86.7 SHP/D²)
 199 M/SEC (652 FT/SEC) TIP SPEED
 58/42 POWER SPLIT

FIGURE 75. EFFECT OF PYLON SPACING ON PUSHER AT 4° ANGLE-OF-ATTACK FOR HIGH POWER AND LOW TIP SPEED

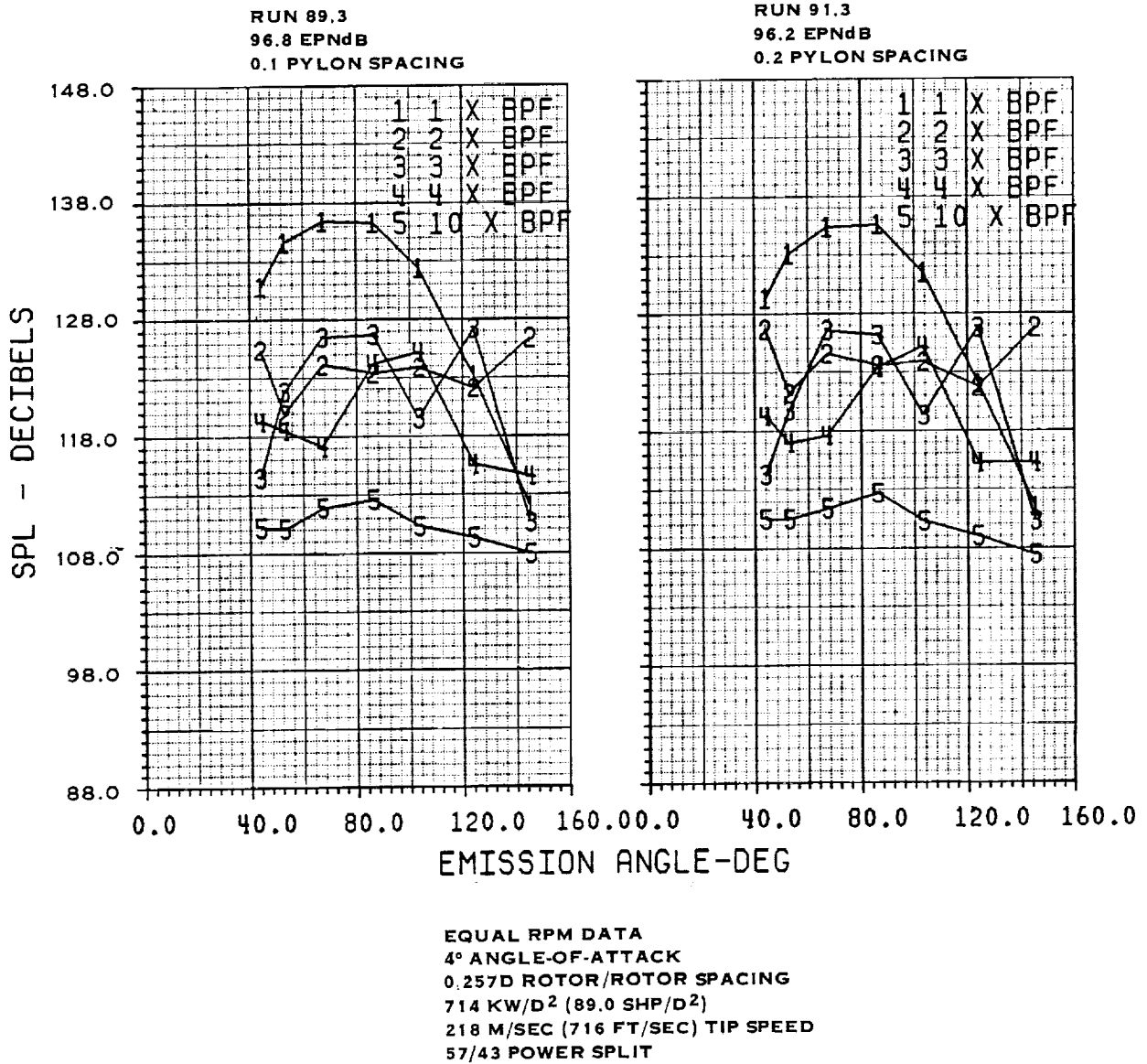
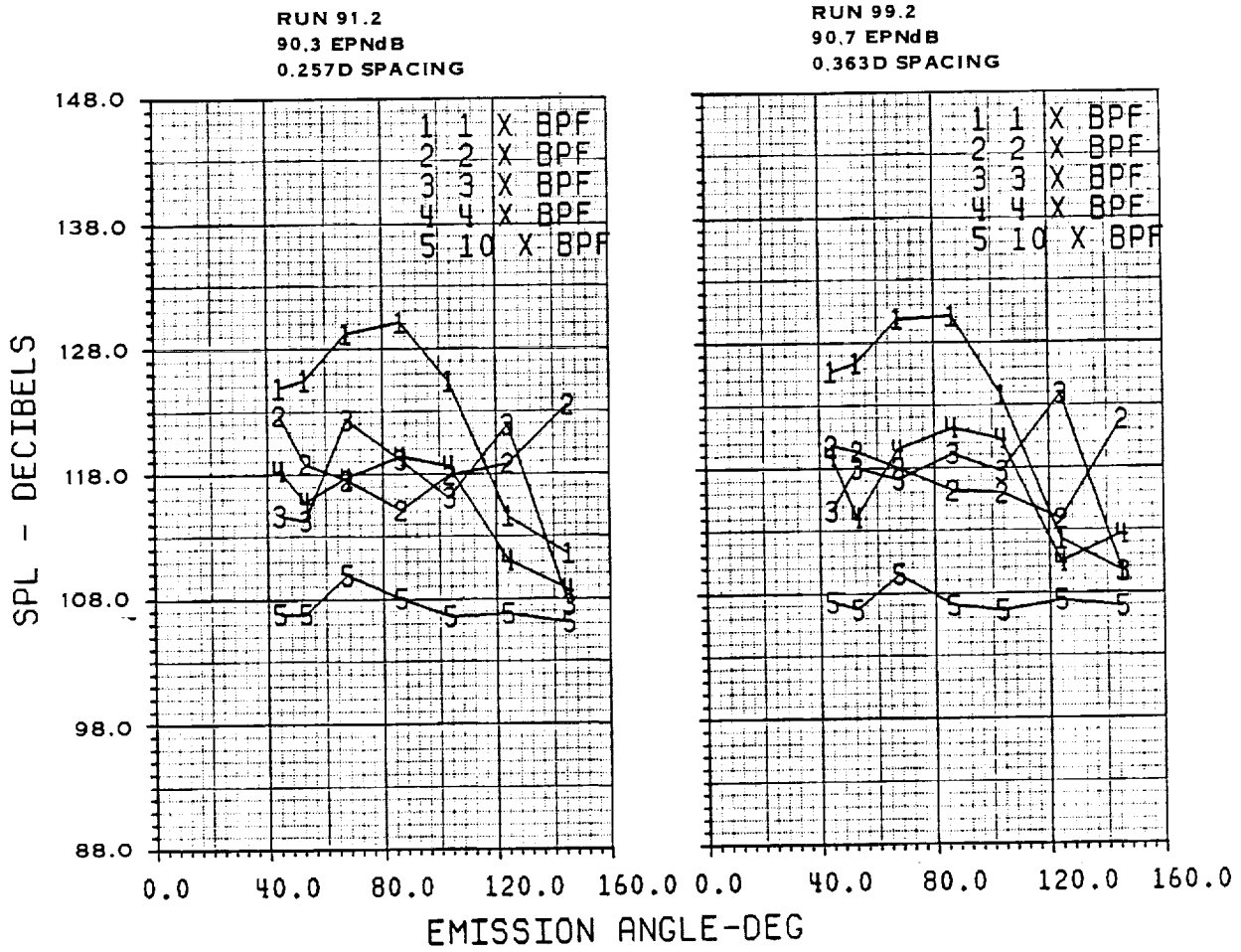


FIGURE 76. EFFECT OF PYLON SPACING ON PUSHER AT 4° ANGLE-OF-ATTACK FOR HIGH POWER AND HIGH TIP SPEED

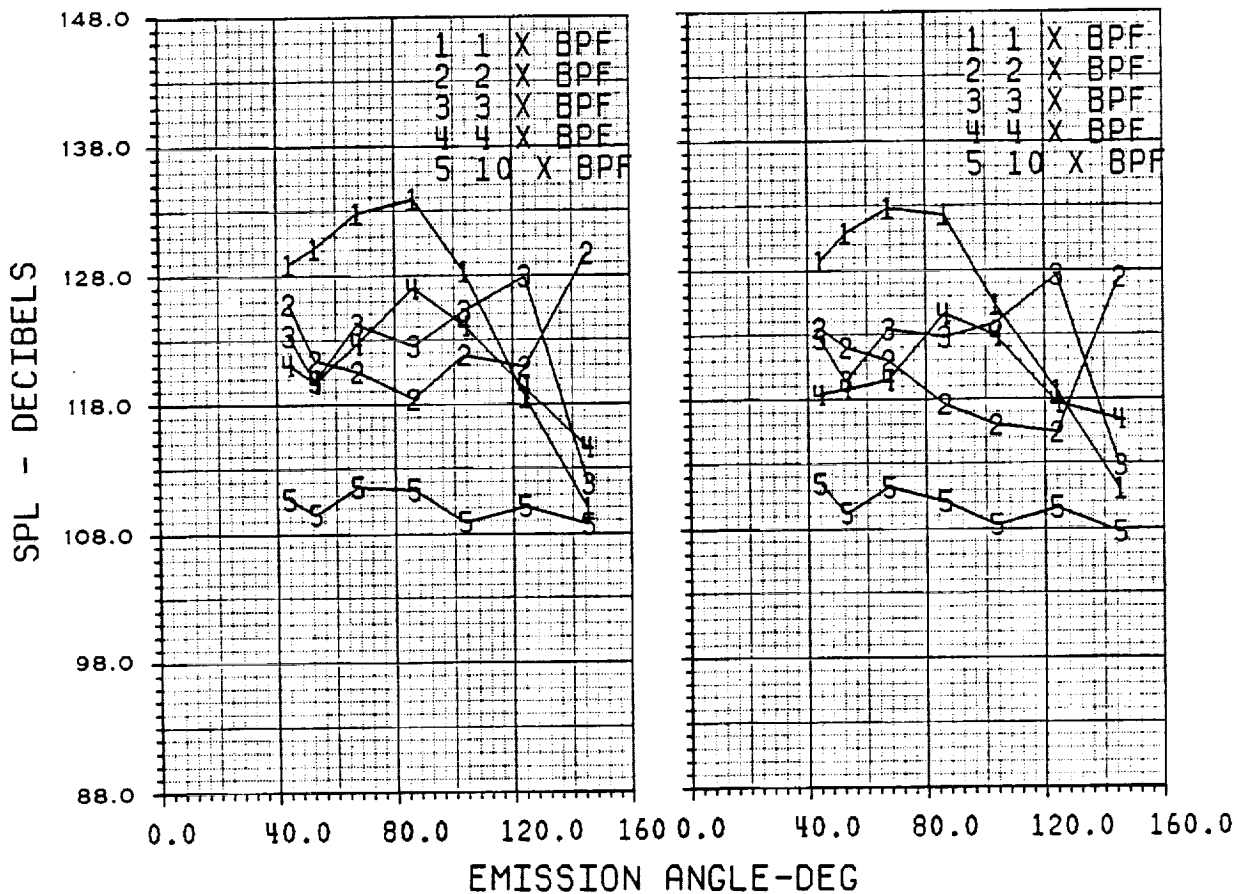


EQUAL RPM PUSHER DATA
 4° ANGLE-OF-ATTACK
 0.2 PYLON SPACING
 511 KW/D² (63.7 SHP/D²)
 202 M/SEC (662 FT/SEC) TIP SPEED
 59/41 POWER SPLIT

FIGURE 77. EFFECT OF ROTOR/ROTOR SPACING ON PUSHER AT 4° ANGLE-OF-ATTACK FOR LOW POWER AND LOW TIP SPEED

RUN 93.3
94.7 EPNdB
0.257D SPACING

RUN 96.3
90.7 EPNdB
0.363 SPACING



EQUAL RPM PUSHER DATA
4° ANGLE-OF-ATTACK
0.2 PYLON SPACING
696 KW/D² (86.7 SHP/D²)
199 M/SEC (652 FT/SEC) TIP SPEED
58/42 POWER SPLIT

FIGURE 78. EFFECT OF ROTOR/ROTOR SPACING ON PUSHER AT 4° ANGLE-OF-ATTACK FOR HIGH POWER AND LOW TIP SPEED

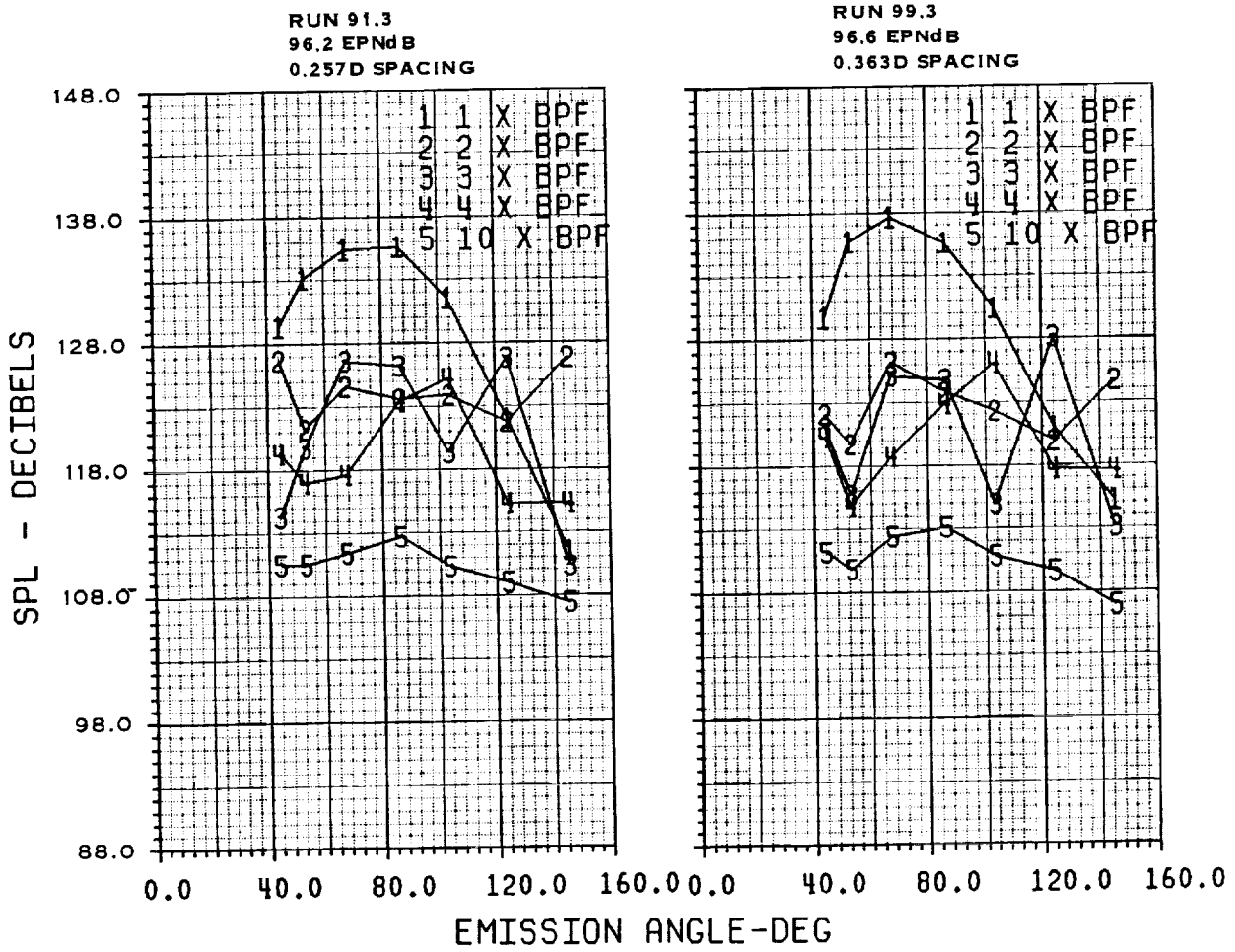
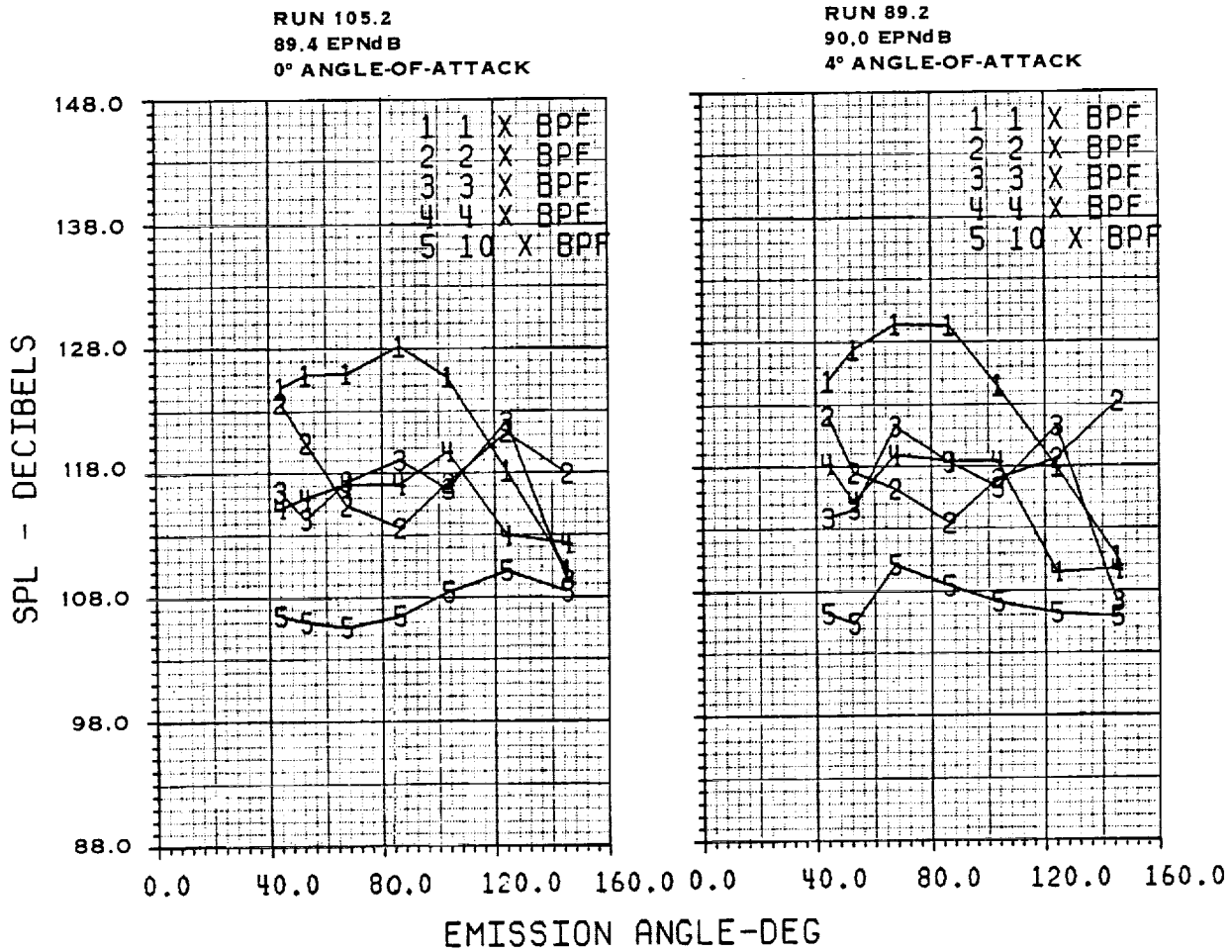
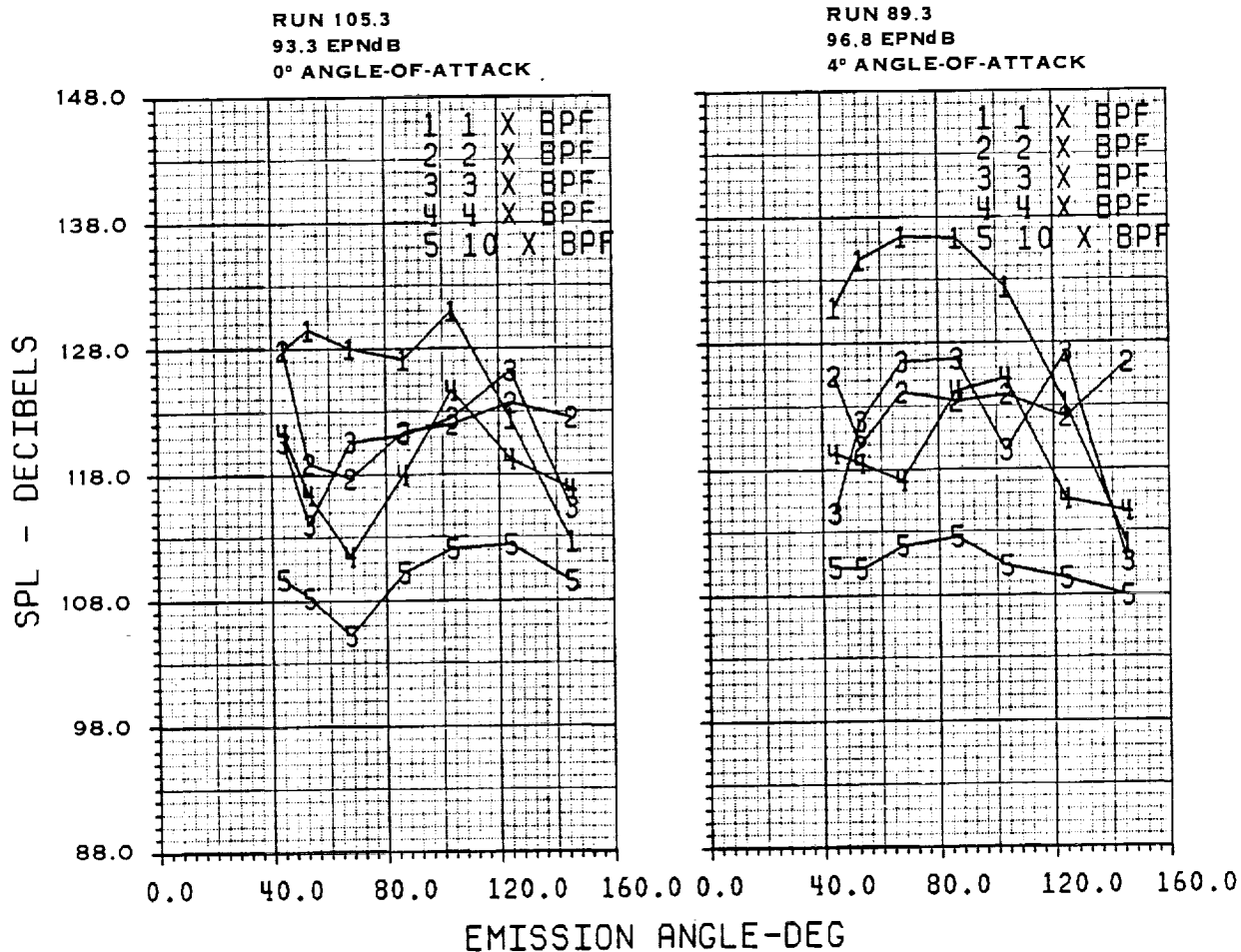


FIGURE 79. EFFECT OF ROTOR/ROTOR SPACING ON PUSHER AT 4° ANGLE-OF-ATTACK FOR HIGH POWER AND HIGH TIP SPEED



EQUAL RPM PUSHER DATA
 0.257D ROTOR/ROTOR SPACING
 0.1 PYLON SPACING
 511 KW/D² (63.7 SHP/D²)
 202 M/SEC (662 FT/SEC) TIP SPEED
 59/41 POWER SPLIT

FIGURE 80. EFFECT OF ANGLE-OF-ATTACK ON PUSHER NOISE AT LOW POWER AND LOW TIP SPEED

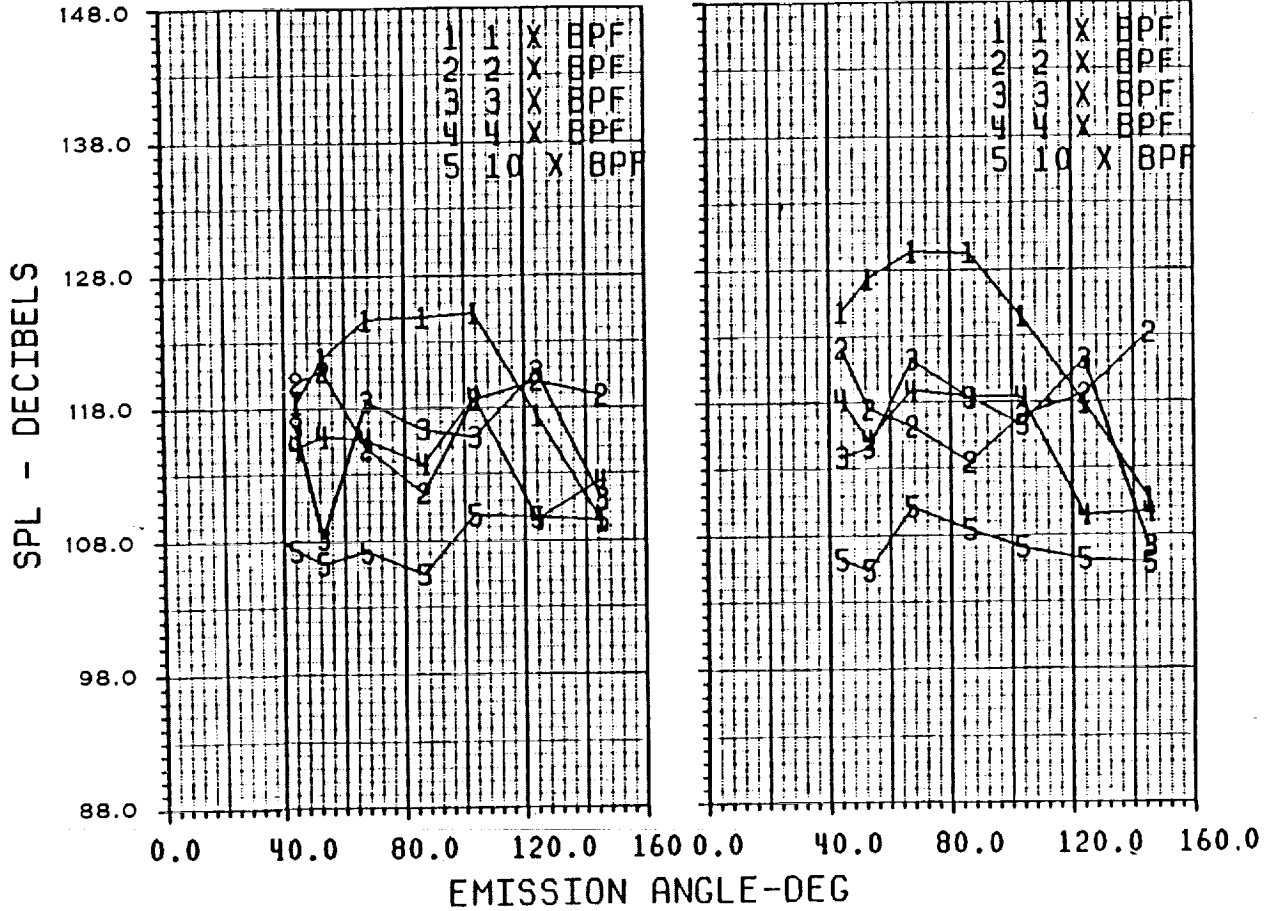


EQUAL RPM PUSHER DATA
 0.257D ROTOR/ROTOR SPACING
 0.1 PYLON SPACING
 714 KW/D² (89.0 SHP/D²)
 218 M/SEC (716 FT/SEC) TIP SPEED
 57/43 POWER SPLIT

FIGURE 81. EFFECT OF ANGLE-OF-ATTACK ON PUSHER NOISE AT HIGH POWER AND LOW TIP SPEED

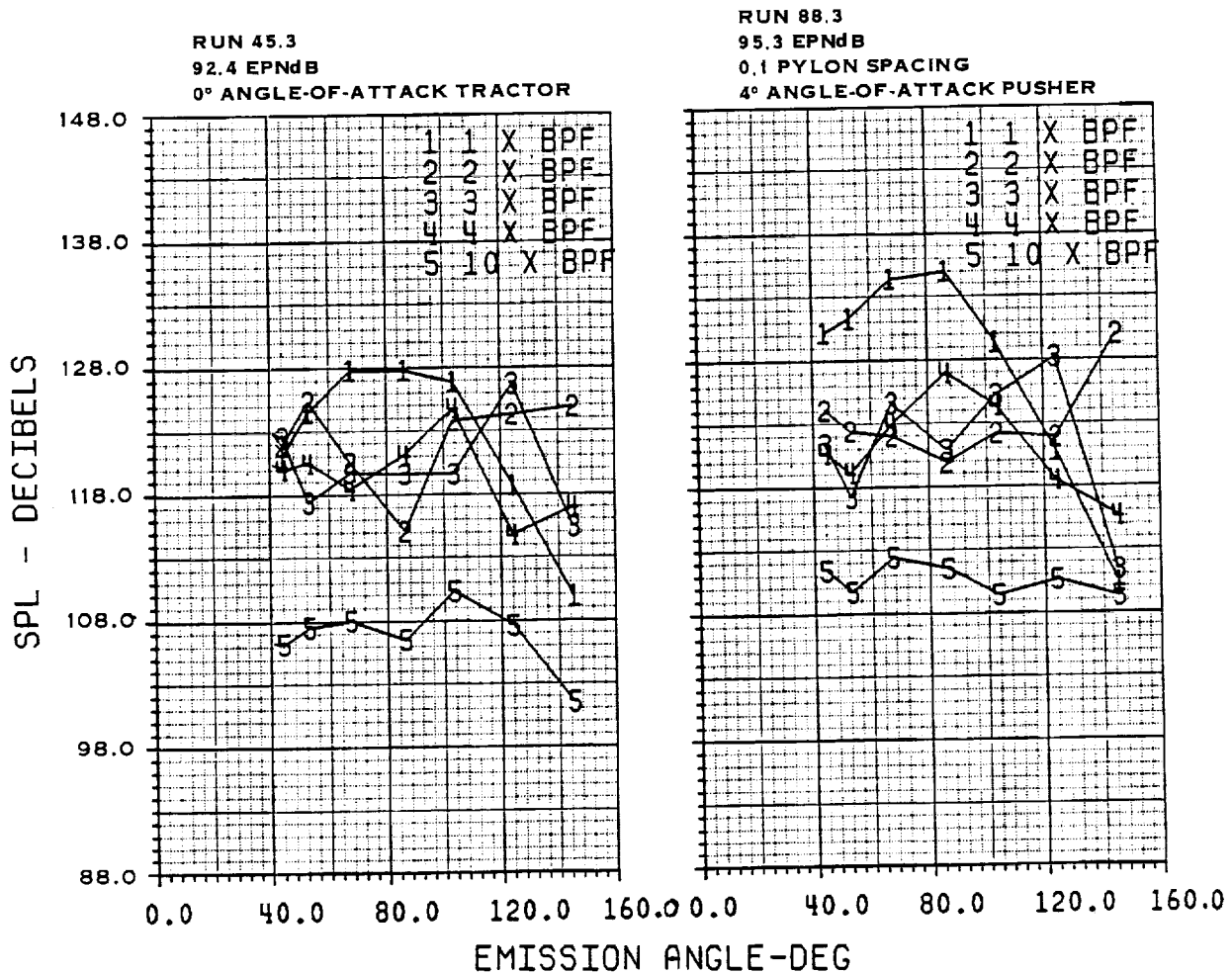
RUN 46.2
 88.7 EPNdB
 0° ANGLE-OF-ATTACK TRACTOR

RUN 89.2
 90.0 EPNdB
 0.1 PYLON SPACING
 4° ANGLE-OF-ATTACK PUSHER



EQUAL RPM DATA
 0.257D ROTOR/ROTOR SPACING
 511 KW/D² (63.7 SHP/D²)
 202 M/SEC (662 FT/SEC) TIP SPEED
 59/41 POWER SPLIT

FIGURE 82. COMPARISON OF PUSHER AT 4° ANGLE-OF-ATTACK WITH TRACTOR AT 0° ANGLE-OF-ATTACK AT LOW POWER AND LOW TIP SPEED



EQUAL RPM DATA
0.257D ROTOR/ROTOR SPACING
696 KW/D² (86.7 SHP/D²)
198 M/SEC (652 FT/SEC) TIP SPEED
58/42 POWER SPLIT

FIGURE 83. COMPARISON OF PUSHER AT 4° ANGLE-OF-ATTACK WITH TRACTOR AT 0° ANGLE-OF-ATTACK AT HIGH POWER AND LOW TIP SPEED

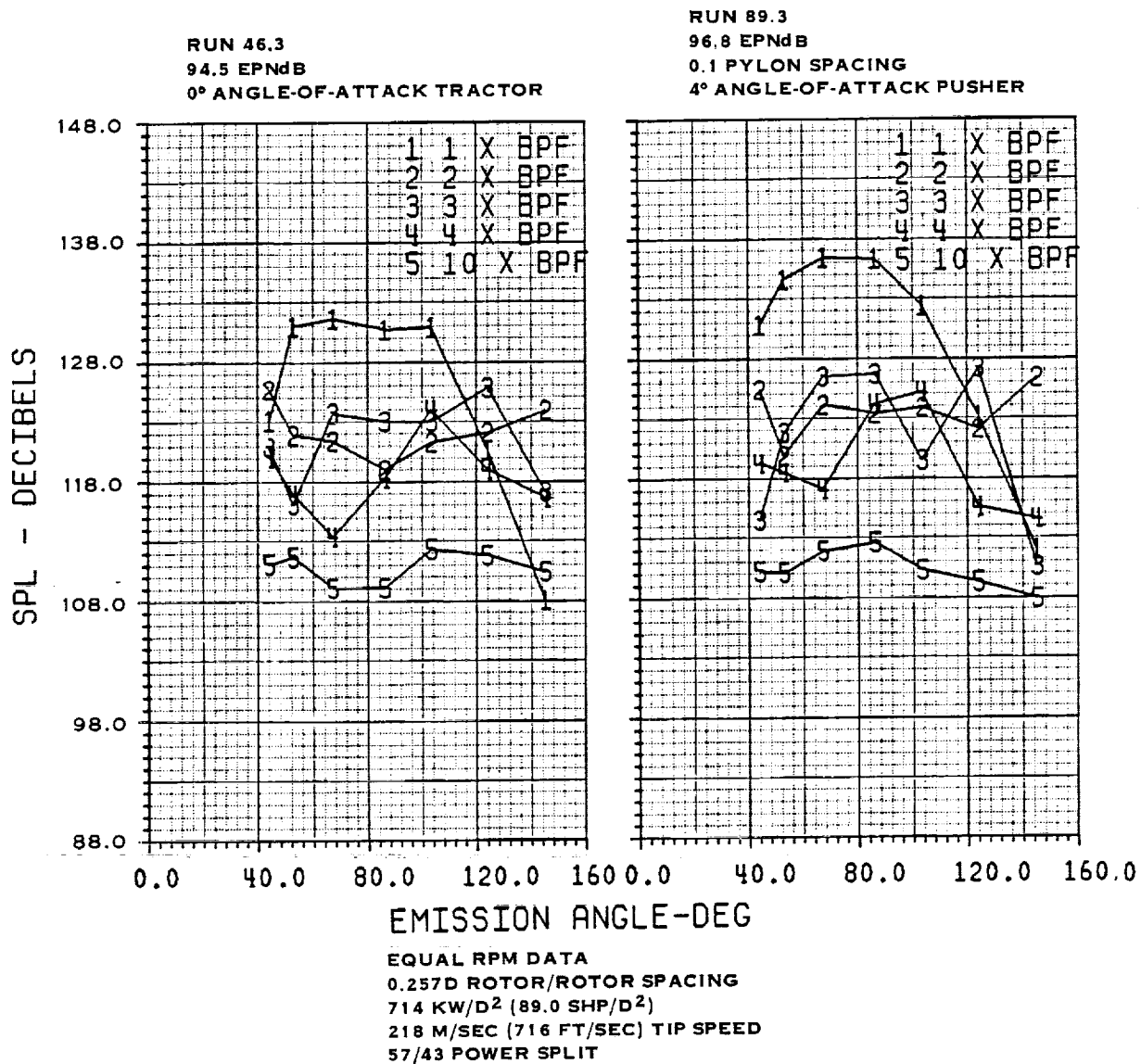
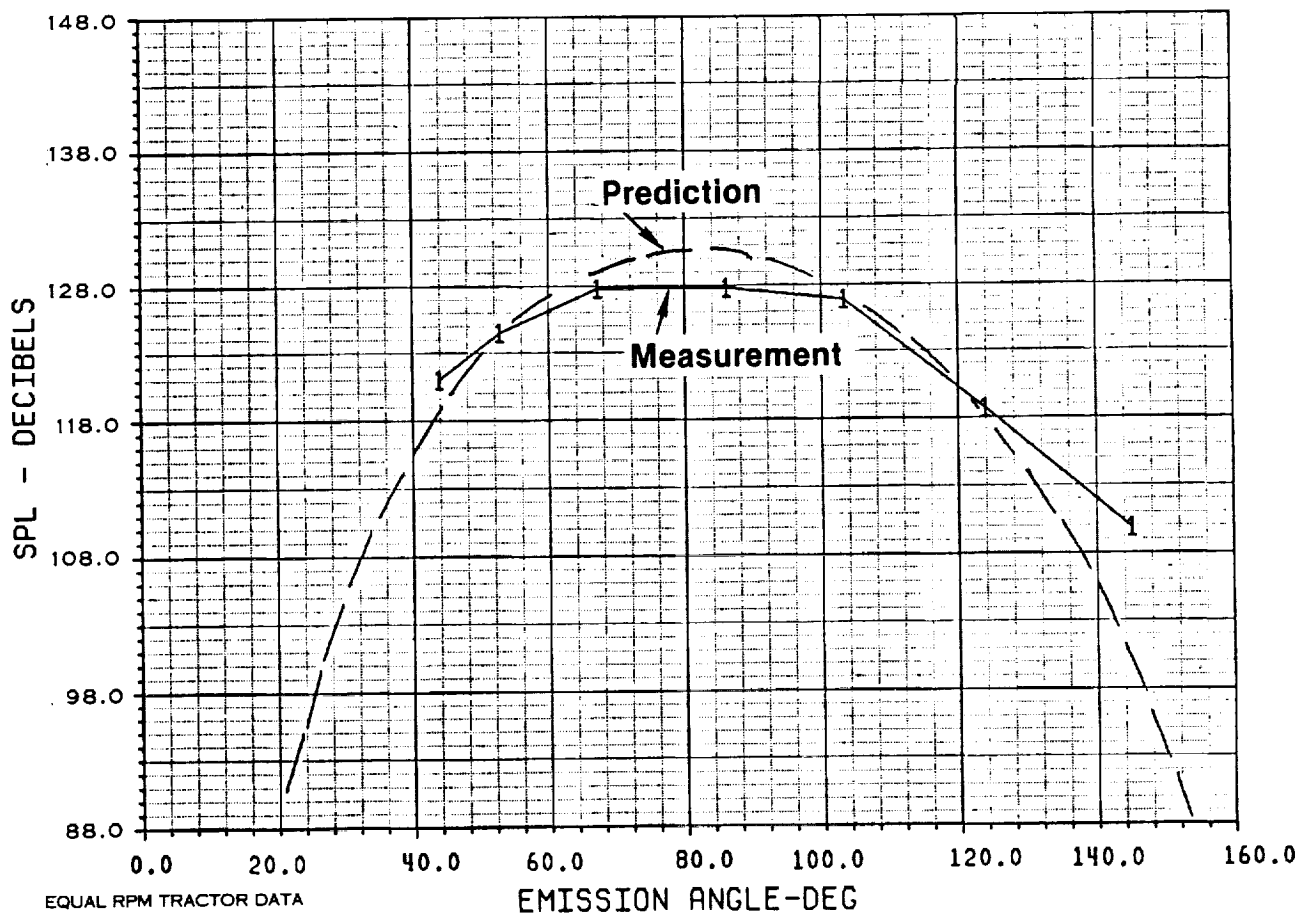


FIGURE 84. COMPARISON OF PUSHER AT 4° ANGLE-OF-ATTACK WITH TRACTOR AT 0° ANGLE-OF-ATTACK AT HIGH POWER AND HIGH TIP SPEED

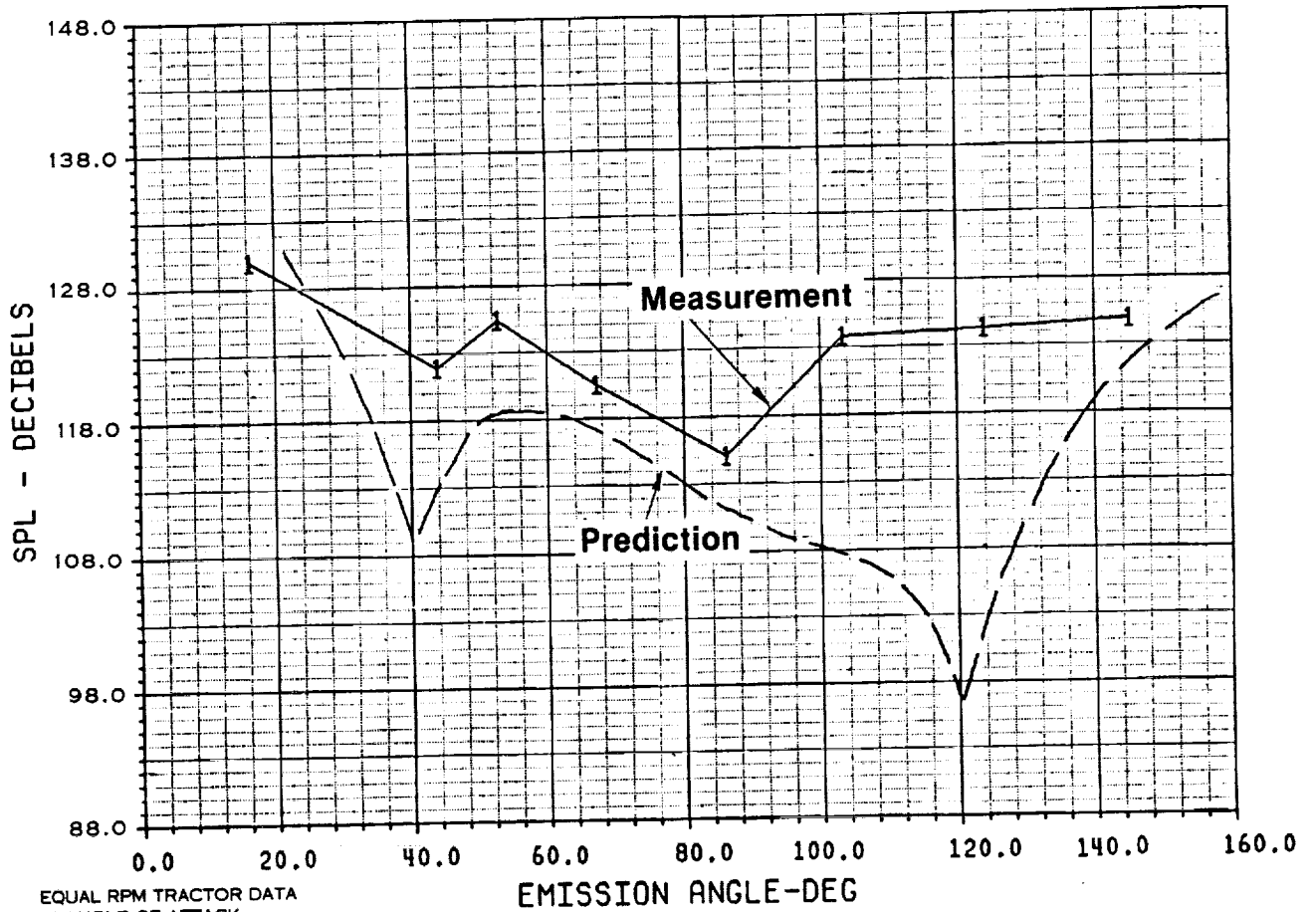
Run 45.3



EQUAL RPM TRACTOR DATA
0° ANGLE-OF-ATTACK
0.257 D ROTOR/ROTOR SPACING
696 KW/D² (86.7 SHP/D²)
199 M/SEC (652 FT/SEC) TIP SPEED
58/42 POWER SPLIT

FIGURE 85. COMPARISON OF PREDICTED AND MEASURED FAR-FIELD NOISE DIRECTIVITY AT BLADE-PASSING FREQUENCY

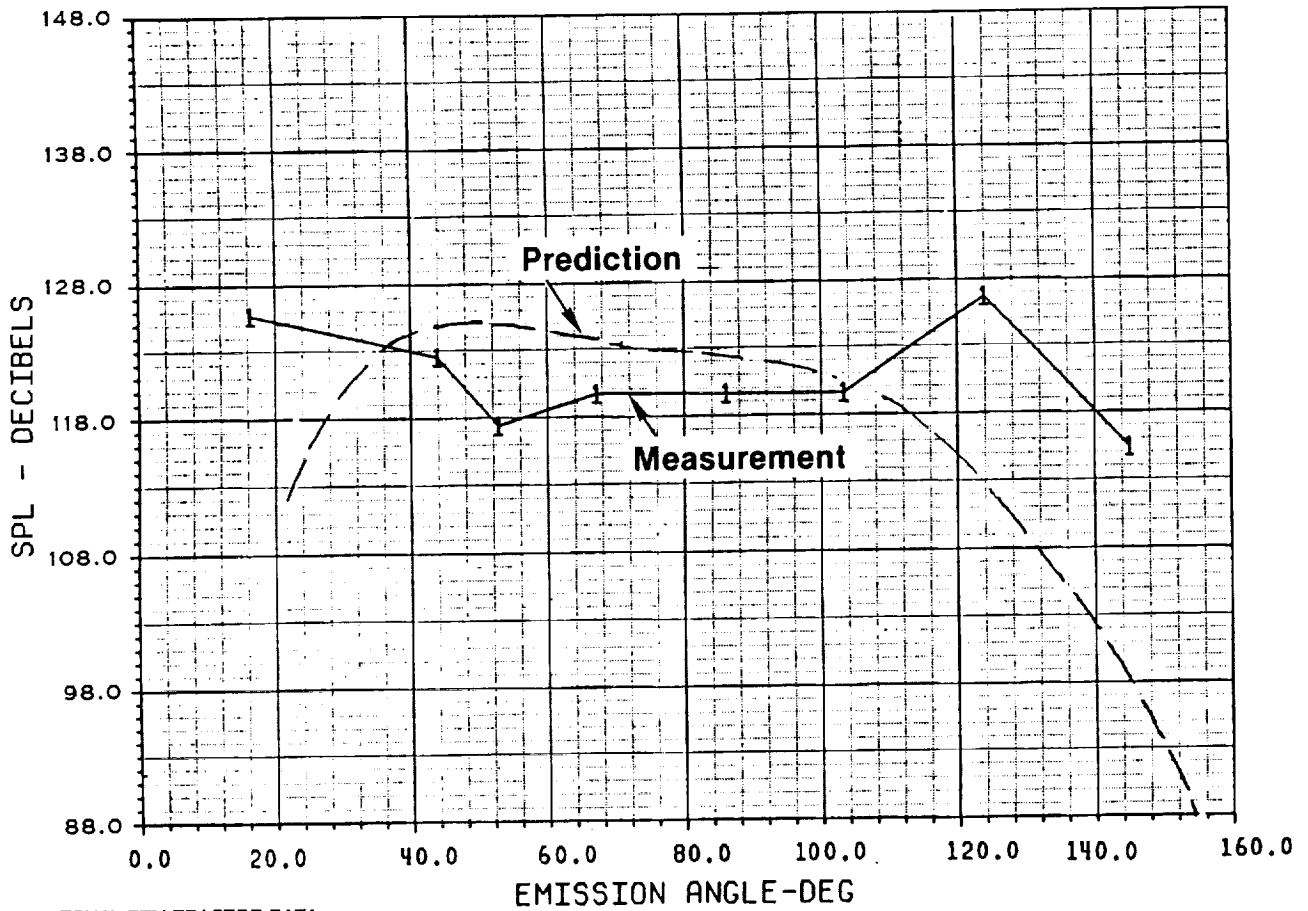
Run 45.3



EQUAL RPM TRACTOR DATA
 0° ANGLE-OF-ATTACK
 0.257 D ROTOR/ROTOR SPACING
 696 KW/D² (86.7 SHP/D²)
 199 M/SEC (652 FT/SEC) TIP SPEED
 58/42 POWER SPLIT

FIGURE 86. COMPARISON OF PREDICTED AND MEASURED FAR-FIELD NOISE DIRECTIVITY AT 2 X BPF

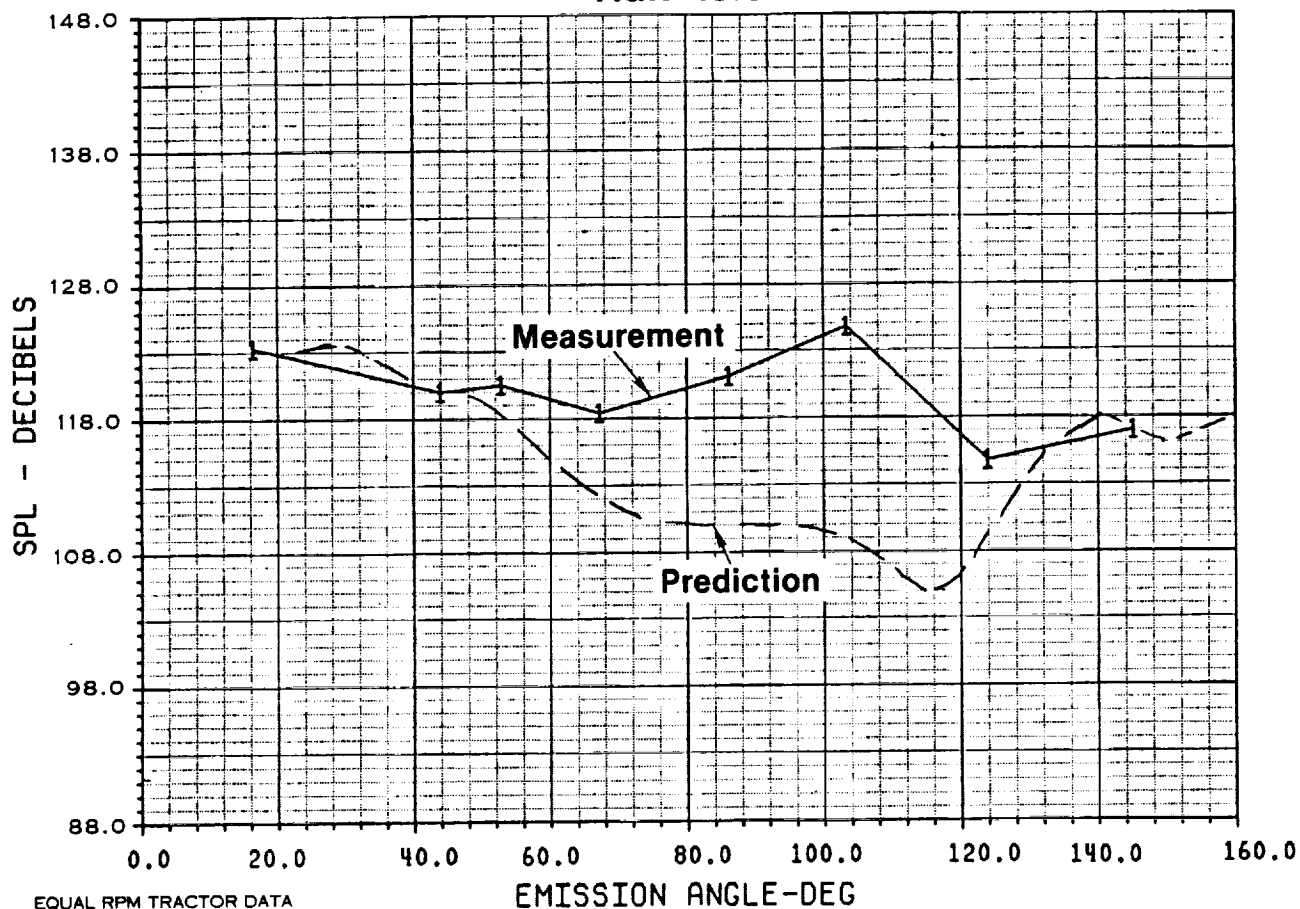
Run 45.3



EQUAL RPM TRACTOR DATA
0° ANGLE-OF-ATTACK
0.257 D ROTOR/ROTOR SPACING
696 KW/D² (86.7 SHP/D²)
199 M/SEC (652 FT/SEC) TIP SPEED
58/42 POWER SPLIT

FIGURE 87. COMPARISON OF PREDICTED AND MEASURED FAR-FIELD NOISE DIRECTIVITY AT 3 X BPF

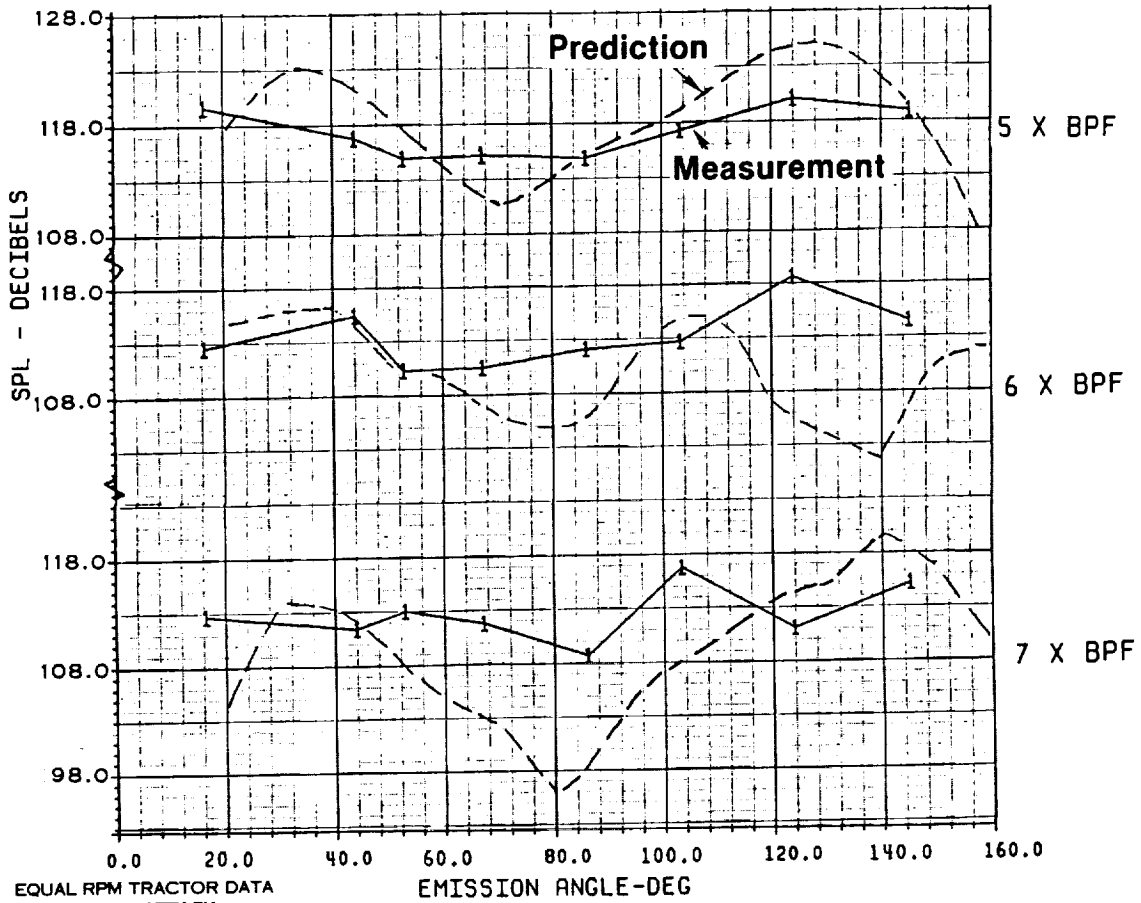
Run 45.3



EQUAL RPM TRACTOR DATA
 0° ANGLE-OF-ATTACK
 0.257 D ROTOR/ROTOR SPACING
 696 KW/D² (86.7 SHP/D²)
 199 M/SEC (652 FT/SEC) TIP SPEED
 58/42 POWER SPLIT

FIGURE 88. COMPARISON OF PREDICTED AND MEASURED FAR-FIELD NOISE DIRECTIVITY AT 4 X BPF

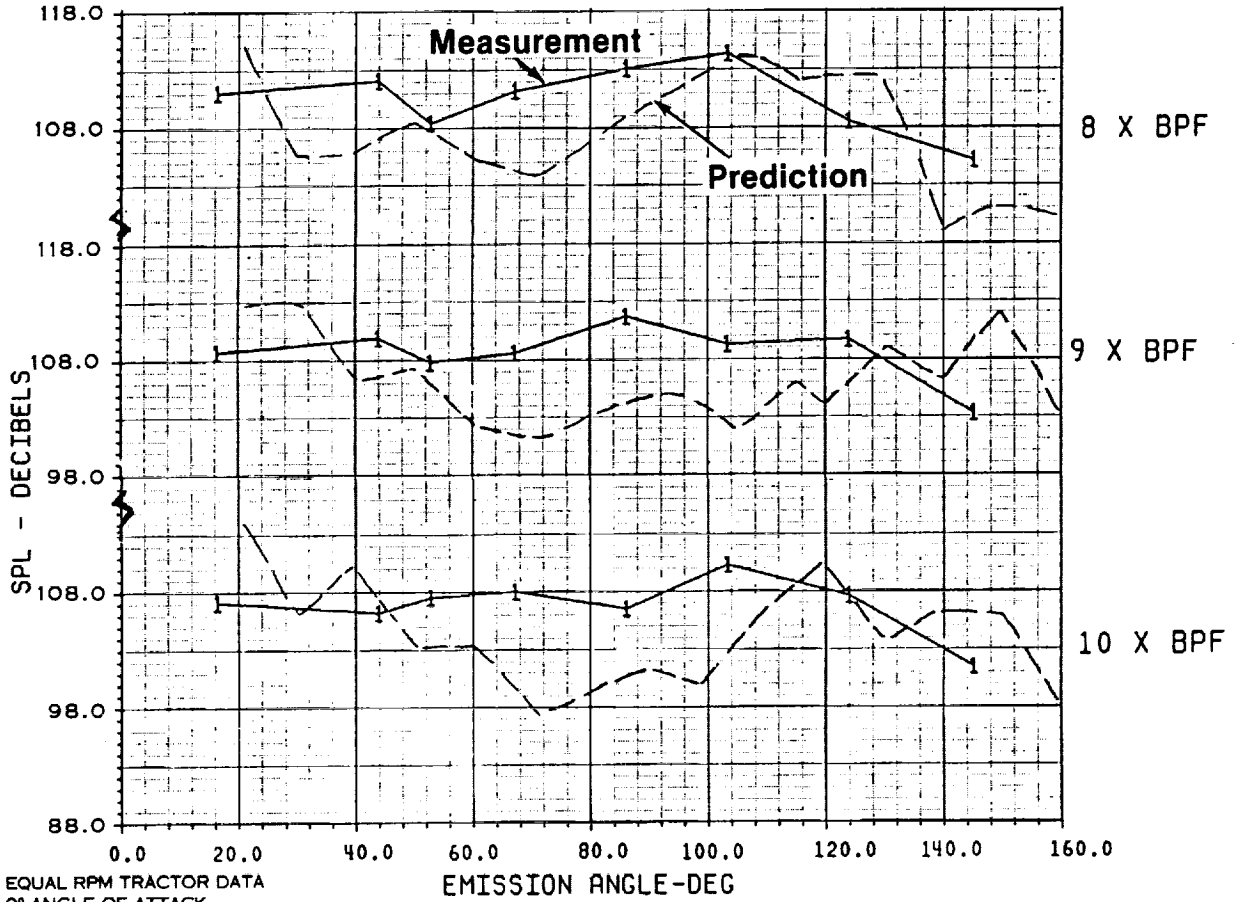
Run 45.3



EQUAL RPM TRACTOR DATA
 0° ANGLE-OF-ATTACK
 0.257 D ROTOR/ROTOR SPACING
 696 KW/D² (86.7 SHP/D²)
 199 M/SEC (652 FT/SEC) TIP SPEED
 58/42 POWER SPLIT

FIGURE 89. COMPARISON OF PREDICTED AND MEASURED FAR-FIELD NOISE DIRECTIVITY AT 5, 6, 7 X BPF

Run 45.3



EQUAL RPM TRACTOR DATA
 0° ANGLE-OF-ATTACK
 0.257 D ROTOR/ROTOR SPACING
 696 KW/D² (86.7 SHP/D²)
 199 M/SEC (652 FT/SEC) TIP SPEED
 58/42 POWER SPLIT

FIGURE 90. COMPARISON OF PREDICTED AND MEASURED FAR-FIELD NOISE DIRECTIVITY AT 8, 9, 10 X BPF

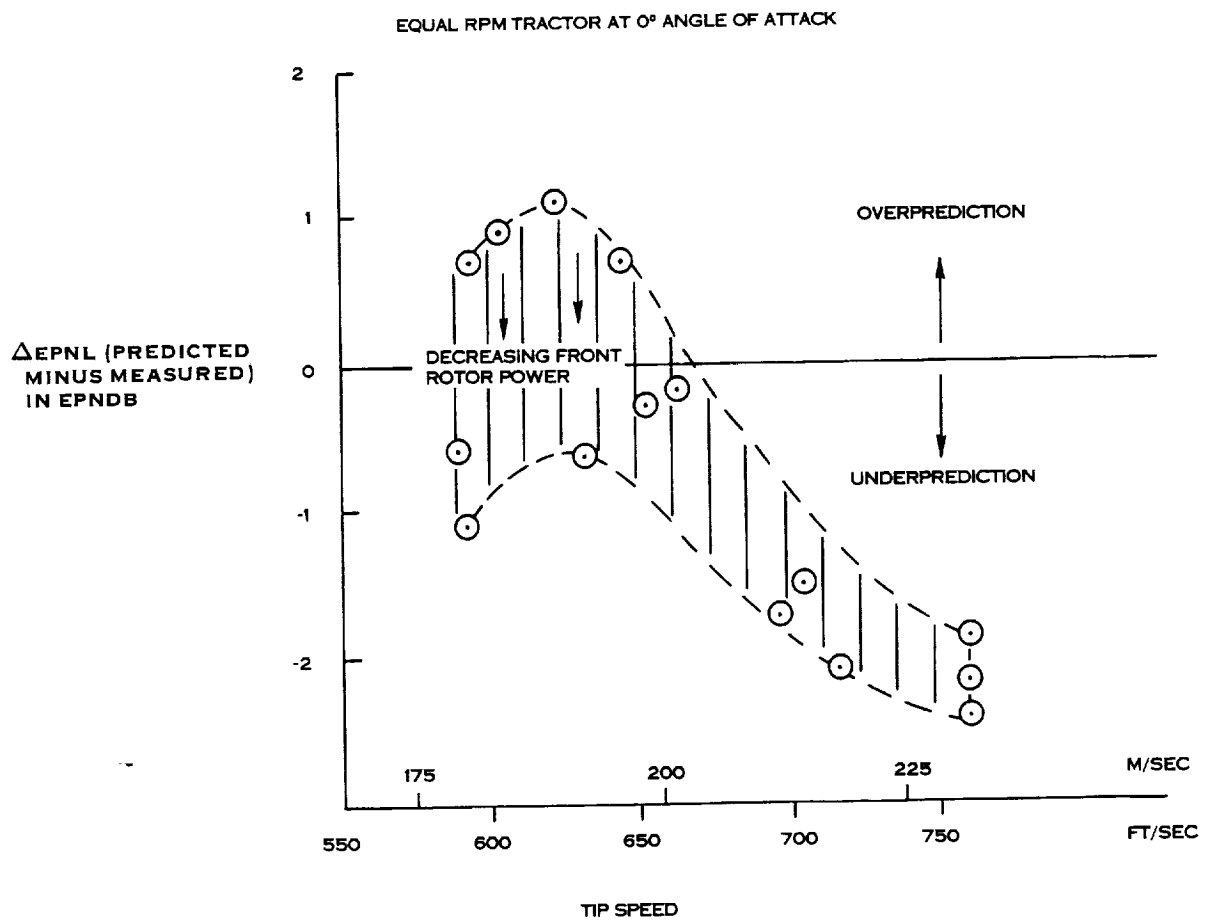


FIGURE 91. SUMMARY OF COMPARISON OF PREDICTED AND MEASURED FAR-FIELD NOISE.

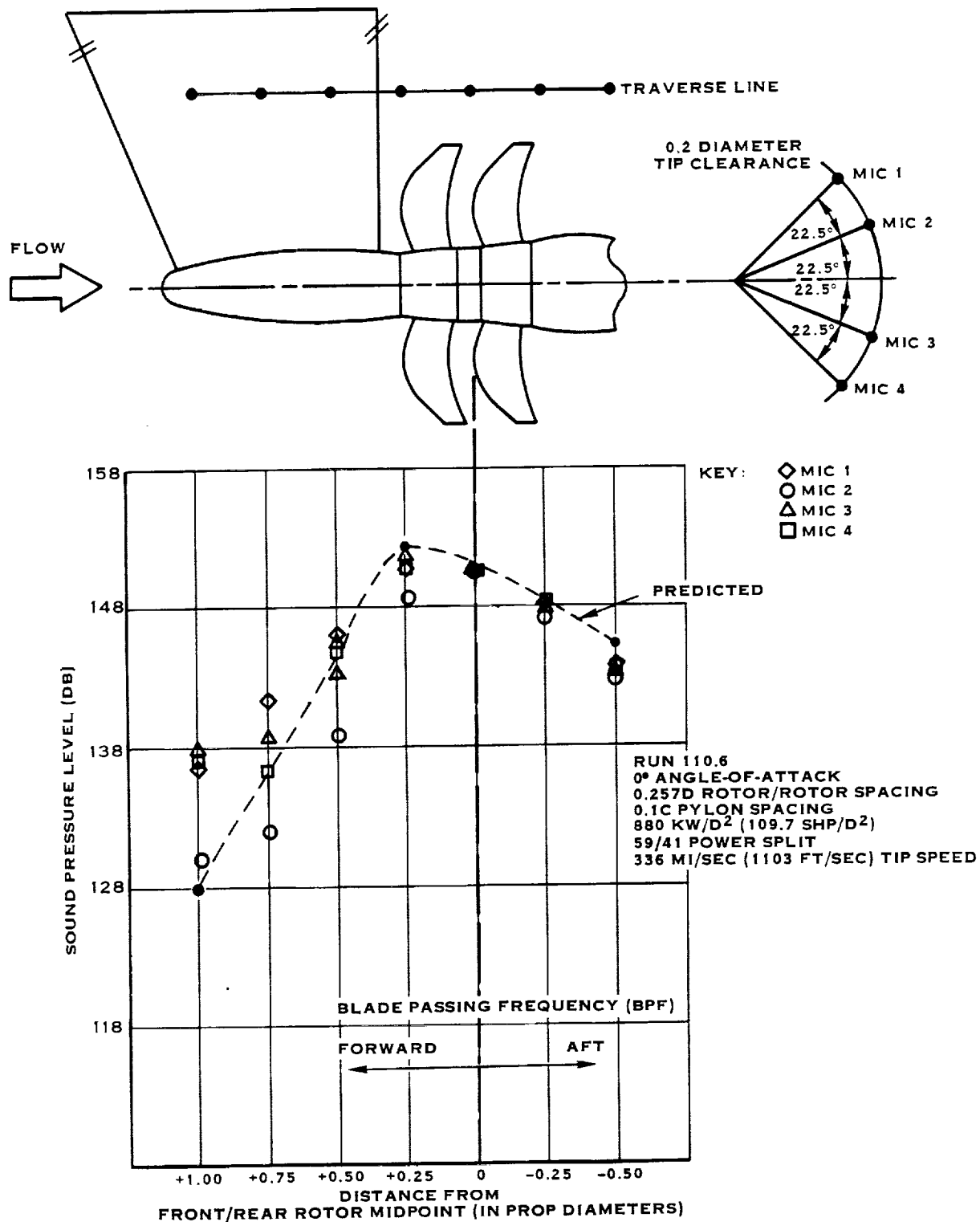


FIGURE 92. COMPARISON OF PREDICTED AND MEASURED NEAR-FIELD NOISE DIRECTIVITY AT BLADE PASSING FREQUENCY

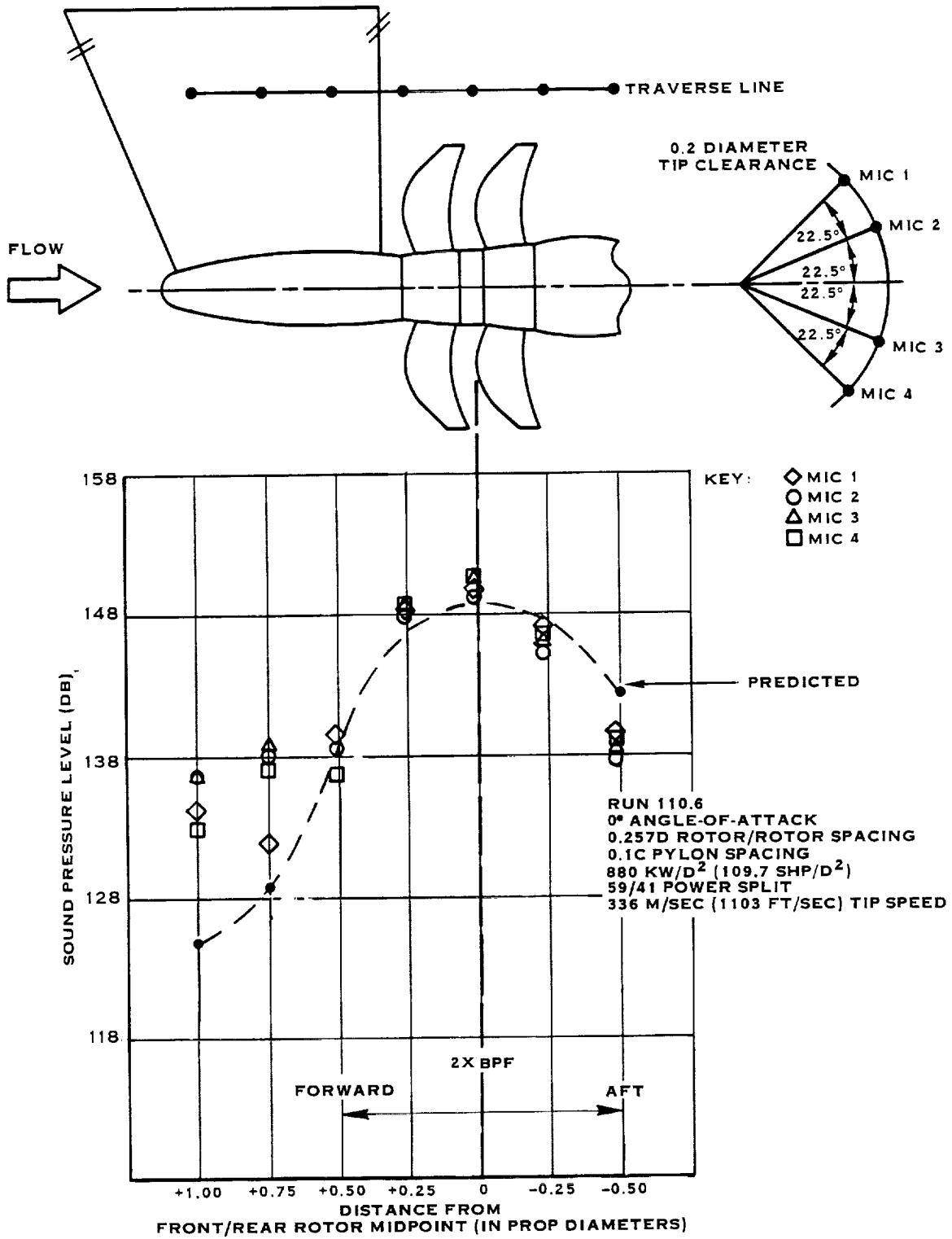


FIGURE 93. COMPARISON OF PREDICTED AND MEASURED NEAR-FIELD NOISE DIRECTIVITY AT 2X BPF

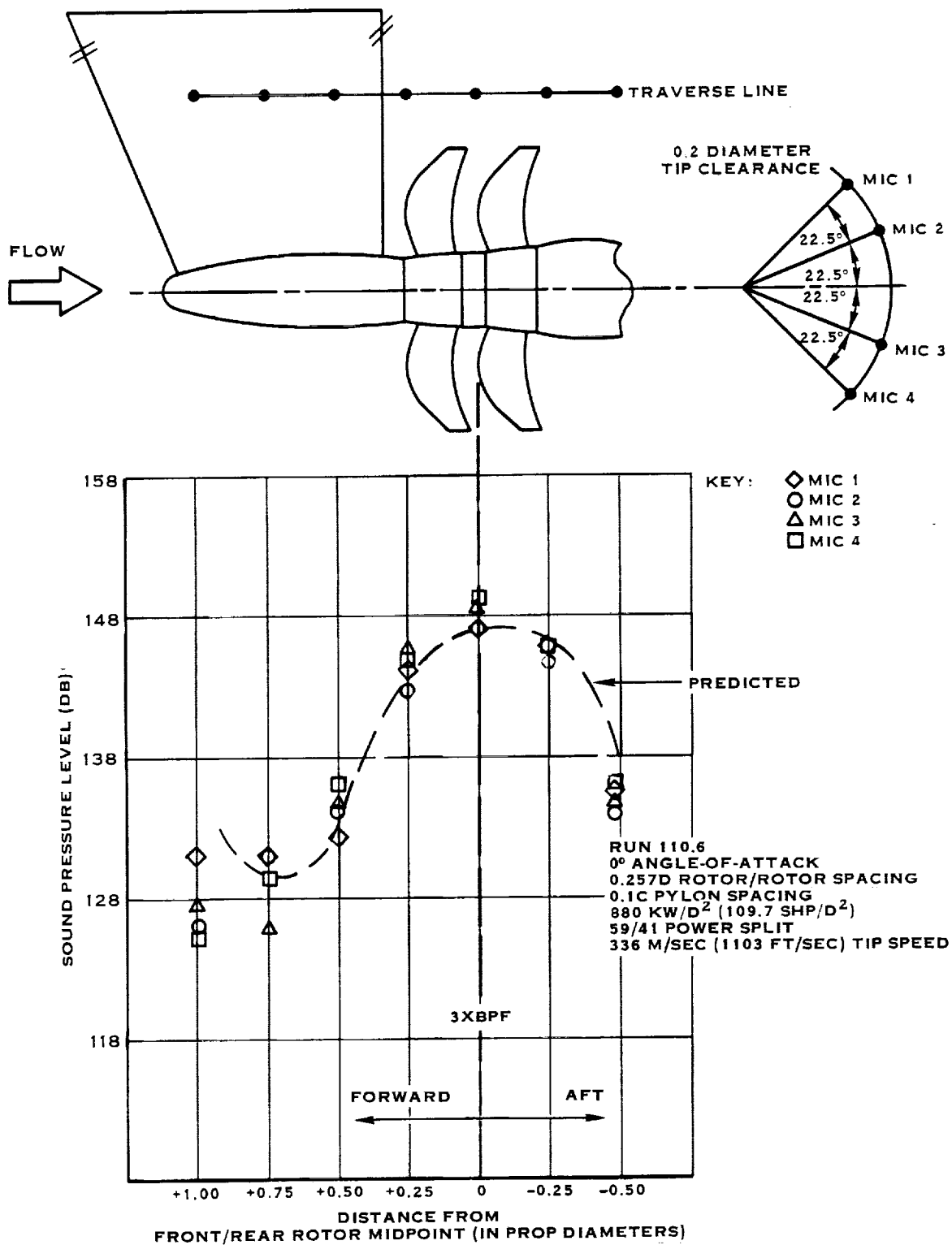


FIGURE 94. COMPARISON OF PREDICTED AND MEASURED NEAR-FIELD NOISE DIRECTIVITY AT 3X BPF

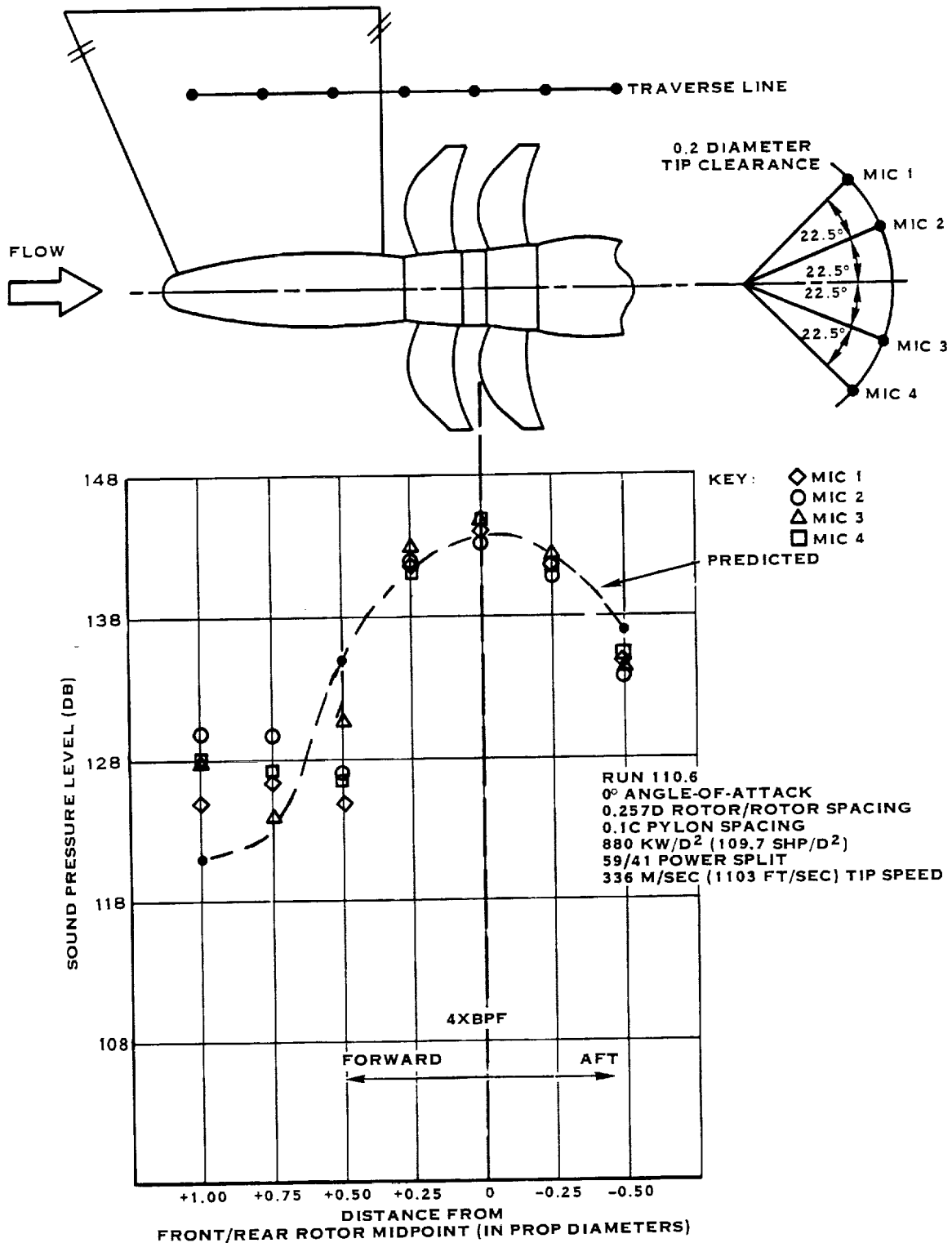


FIGURE 95. COMPARISON OF PREDICTED AND MEASURED NEAR-FIELD NOISE DIRECTIVITY AT 4X BPF

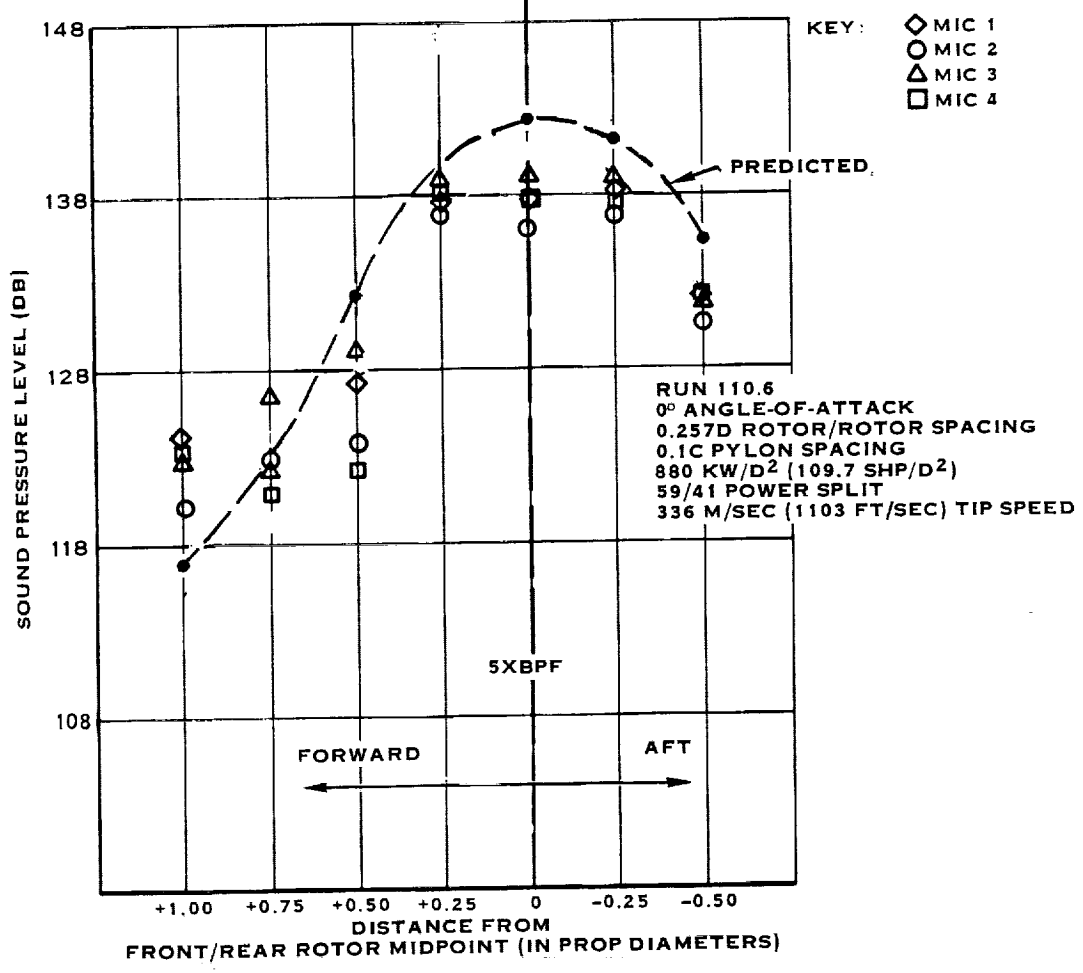
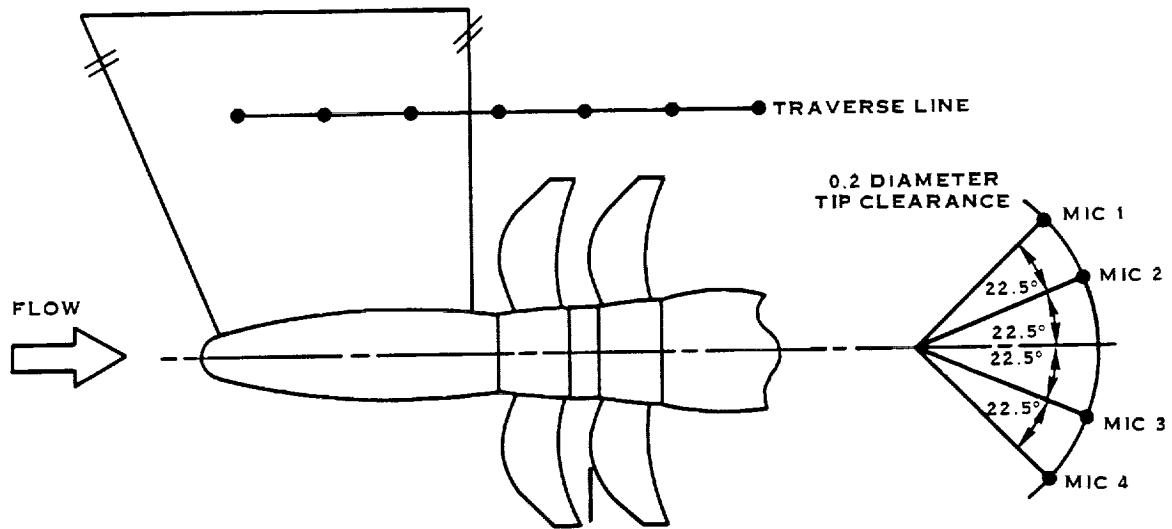


FIGURE 96. COMPARISON OF PREDICTED AND MEASURED NEAR-FIELD NOISE DIRECTIVITY AT 5X BPF

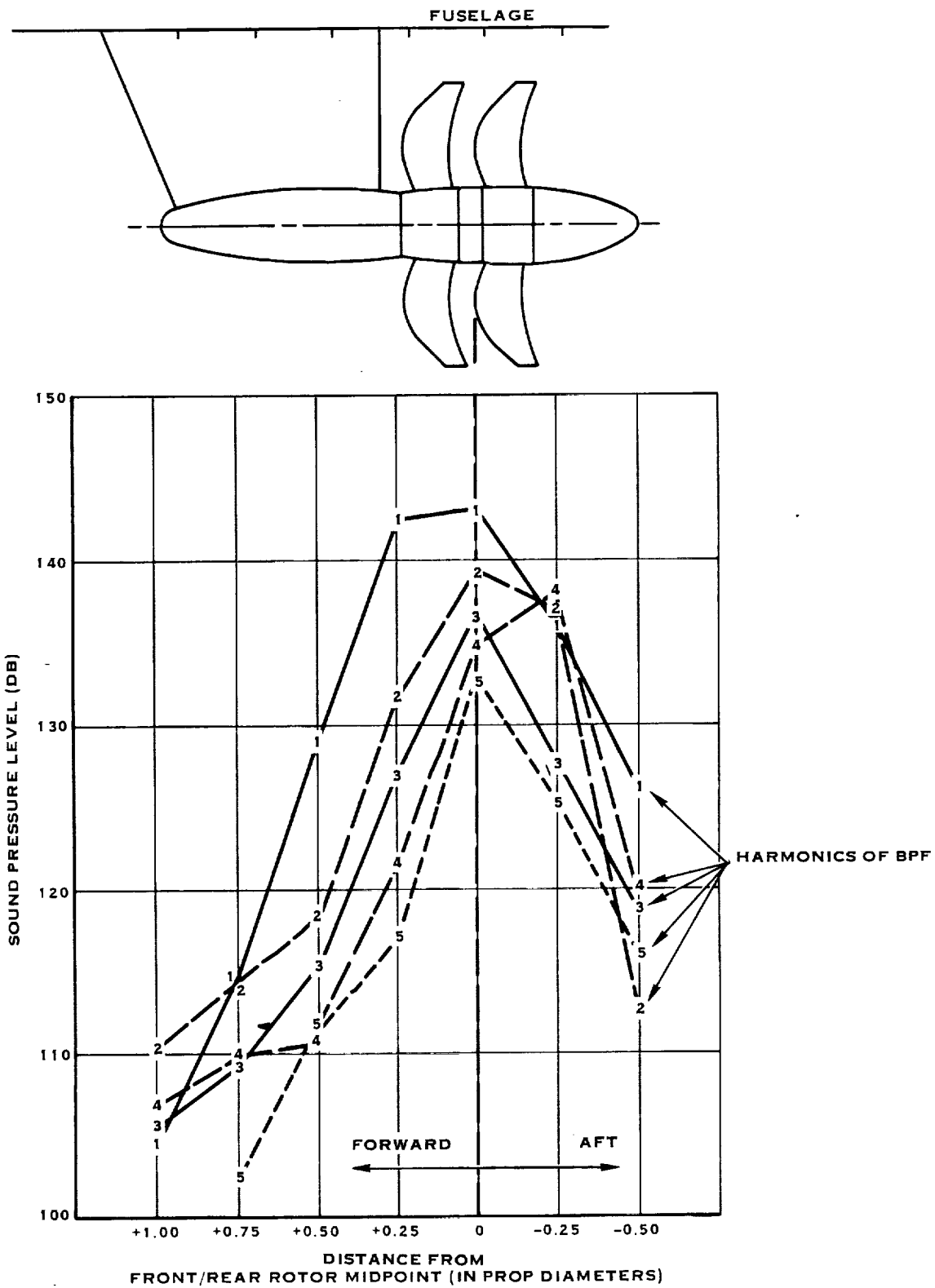


FIGURE 97. PREDICTED CRUISE NOISE AT 0.2 DIAMETER TIP CLEARANCE FOR 0.72 MN, 229 M/SEC (750 FT/SEC) TIP SPEED CONDITION

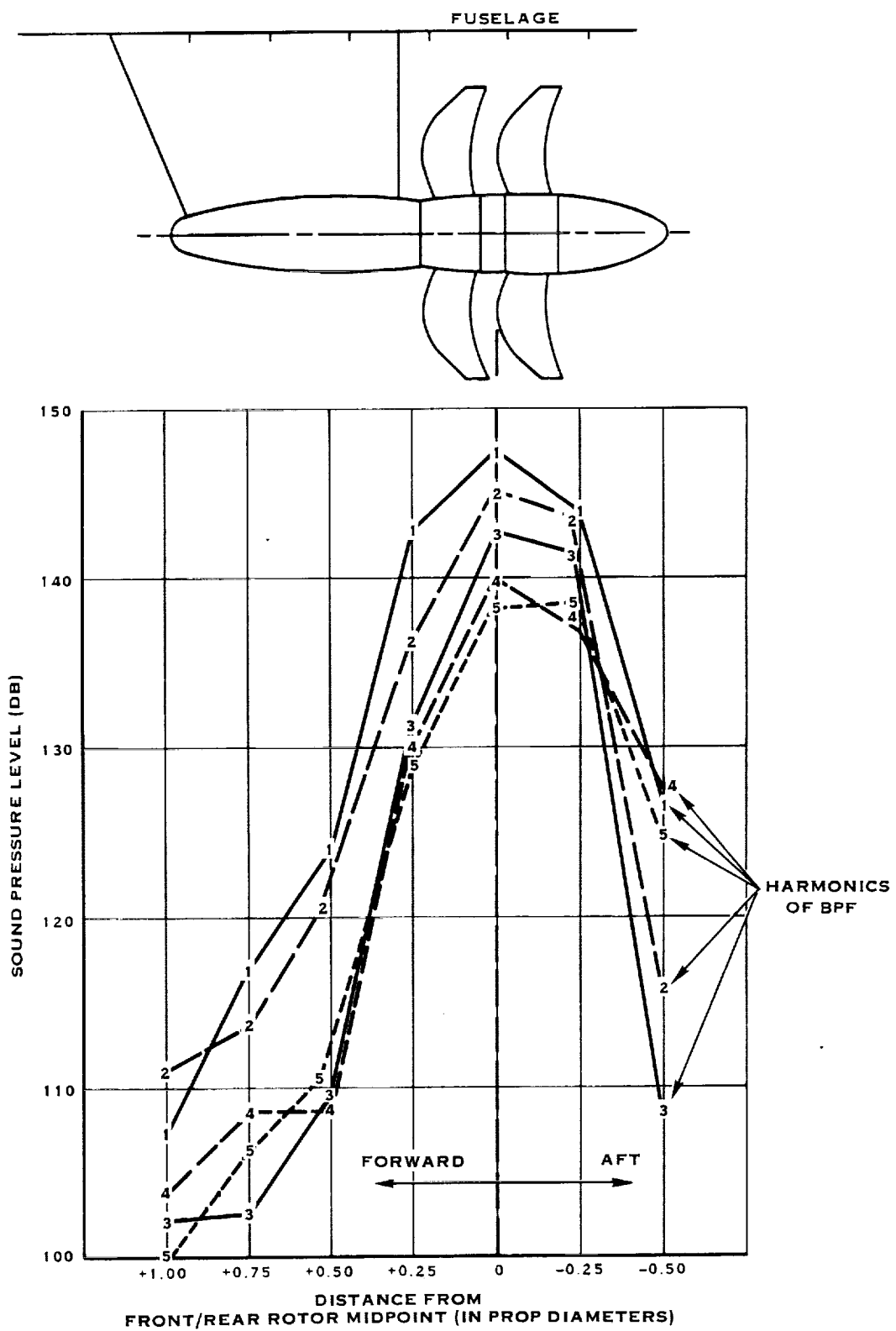


FIGURE 98. PREDICTED CRUISE NOISE AT 0.2 DIAMETER TIP CLEARANCE FOR 0.8 MN, 229 M/SEC (750 FT/SEC) TIP SPEED CONDITION

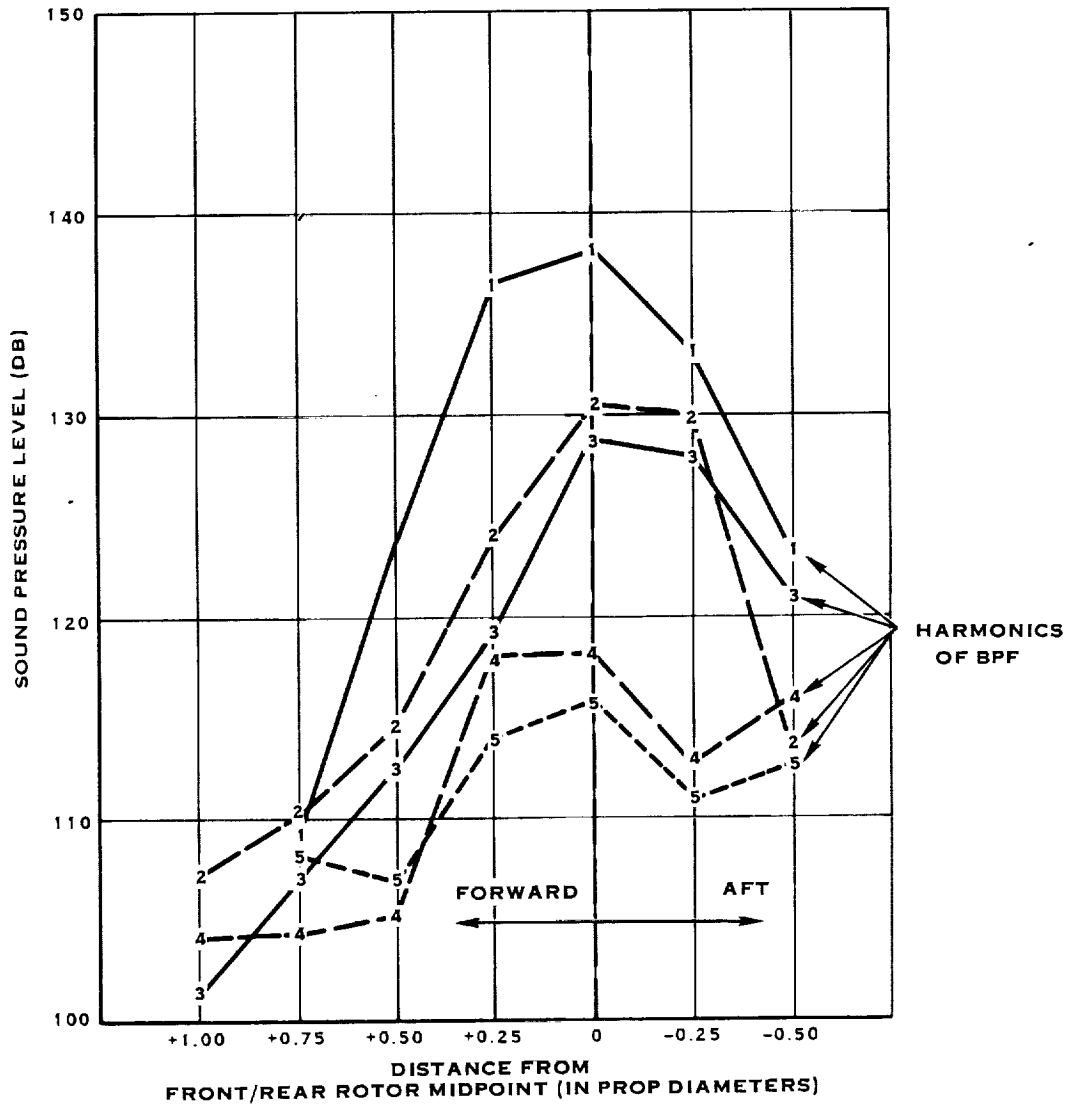
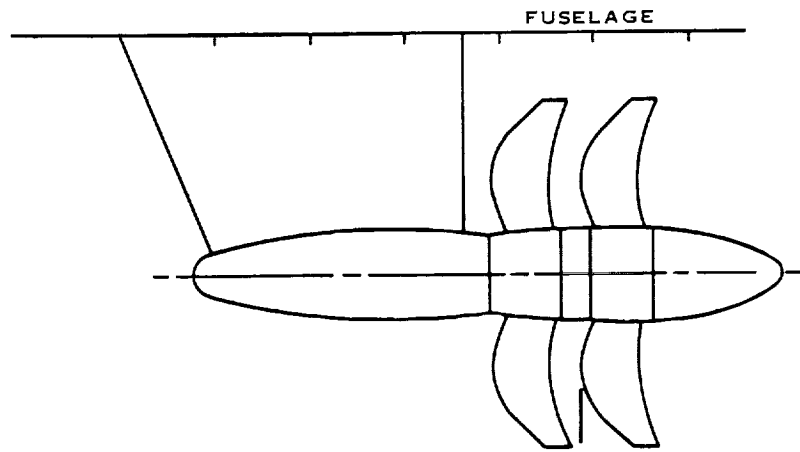


FIGURE 99. PREDICTED CRUISE NOISE AT 0.2 DIAMETER TIP CLEARANCE FOR 0.72 MN, 198 M/SEC (650 FT/SEC) TIP SPEED CONDITION

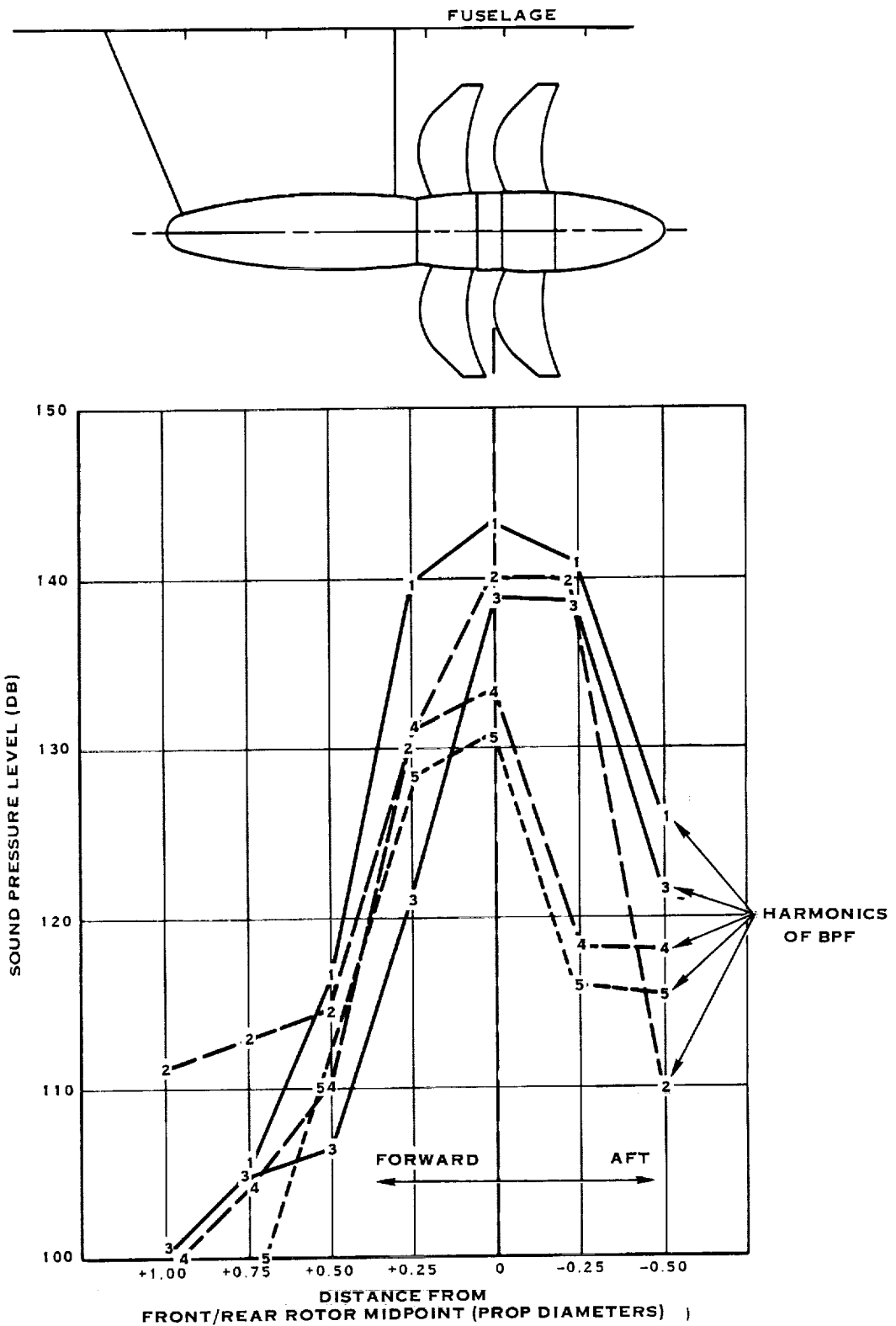


FIGURE 100. PREDICTED CRUISE NOISE AT 0.2 DIAMETER TIP CLEARANCE FOR 0.8 MN, 198 M/SEC (650 FT/SEC) TIP SPEED CONDITION

APPENDIX A

SYMBOLS AND ABBREVIATIONS

AC	Alternating current
A/D	Analog-to-digital
AF	Activity factor/blade = $100,000/16 \int_{\text{hub/tip}}^{1.0} b/D X^3 dx$
ART	Acoustic Research Tunnel
b	Blade chord
B	Number of blades per rotor
BPF	Blade passing frequency = RPM x B/60, Hz
C	Pylon chord
CRP	Counterrotating Prop-Fan
CRDR	Counterrotating Drive Rig
D	Prop-Fan diameter
dB	Decibel = $20 \text{ Log}_{10} p/p_{\text{ref}}$
dBA	A - weighted decibel
DC	Direct current
EPNdB	Effective Perceived Noise Decibel
EPNL	Effective Perceived Noise Level
FM	Frequency modulation
Hz	Hertz, cycles per second
kW/D ²	Kilowatts per diameter (in meters) squared
Mn	Mach number
M _t	Blade tip rotational Mach number
M _{th}	Blade tip helical Mach number = $\sqrt{M_t^2 + M_x^2}$

SYMBOLS AND ABBREVIATIONS (Continued)

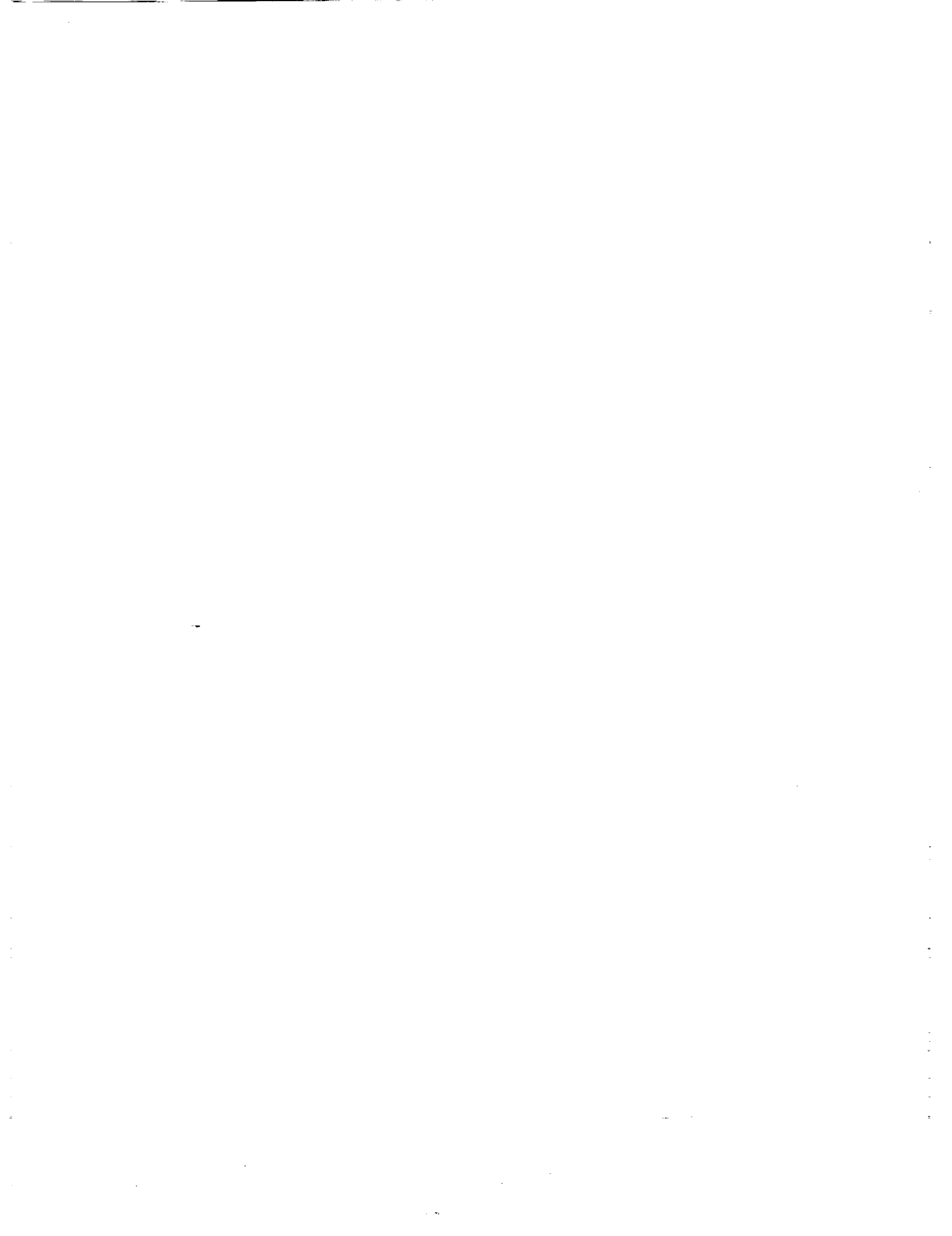
M_x	Flight Mach number
p	Acoustic pressure
P_A	Atmospheric pressure
Pa	Pascals
P_S	Static pressure
P_T	Total pressure
P_{ref}	Reference acoustic pressure = 20 μ Pa
PCA	Pitch change axis
PNL	Perceived Noise Levels
PNLT	Tone Corrected Perceived Noise Level
r	Blade radial station
R	Tip radius
R_R	Distance from source to observer
RMS	Root-mean-square
RPM	Rotations per minute
SHP	Shaft horsepower
SHP/D^2	Shaft horsepower per diameter (in feet) squared
SPL	Sound pressure level
SRP	Single Rotation Prop-Fan
T_s	Static temperature
T_r	Total temperature
\bar{U}	Mean axial velocity
V_t	Blade tip rotational velocity
X	r/R

SYMBOLS AND ABBREVIATIONS (Continued)

X_C	Corrected visual microphone location along axis of rotation (horizontal direction)*
X_M	Geometric microphone location along axis of rotation (horizontal direction)*
Y_C	Corrected visual microphone location in vertical direction *
Y_M	Geometric microphone location in vertical direction *
Z	Axial spacing between pylon trailing edge and front rotor blade leading edge
Z_C	Corrected visual microphone location *
Z_M	Geometric microphone location*
ΔdB	Shear-layer divergence correction to sound pressure level
μ	Micro = 10^{-6}
θ_R	Radiation angle, zero on axis in forward direction.

SI units of measurements used throughout. U.S. customary units may be included in parentheses.

* See Figure 9 for orientation



REFERENCES

1. Anon., CRP-X1 Model Design for Aero/Acoustic & Structural Wind Tunnel Testing, Final Report for Task Order 2 Under NASA Contract NAS3-24222, August 1984.
2. Paterson, R.W. et. al., "Design and Development of the United Aircraft Research Laboratories Acoustic Research Tunnel", J. of Aircraft, Vol 10, No. 7, 1973, pp 427-433.
3. Schlinker, R.H. and Amiet, R.K. Experimental Assessment of Theory for Refraction of Sound by a Shear-layer, NASA CR-145359, 1978.
4. Hanson, D.B., "Near-Field Frequency-Domain Theory for Propeller Noise", AIAA Journal, Vol 23, No. 4, April 1985, pp 499-504.
5. Hanson, D.B., "Noise of Counter Rotation Propellers", AIAA Paper 84-2305, October 1984.

PRECEDING PAGE BLANK NOT FILMED

1. Report No. NASA CR-179590	2. Government Accession No.	3. Recipient's Catalog No.	
4. Title and Subtitle Acoustic Test and Analysis of a Counterrotating Prop-Fan Model		5. Report Date October 1987	6. Performing Organization Code
		8. Performing Organization Report No.	
7. Author(s) Bernard Magliozzi, Paul Brown, and David Parzych		10. Work Unit No.	
9. Performing Organization Name and Address Hamilton Standard United Technologies Corporation Windsor Locks, CT 06096		11. Contract or Grant No. NAS3-24222	
		13. Type of Report and Period Covered	
12. Sponsoring Agency Name and Address National Aeronautics and Space Administration Washington, D.C. 20546		14. Sponsoring Agency Code	
		15. Supplementary Notes Final report. Project Technical Monitor, Robert Dengler NASA Lewis Research Center, Cleveland OH	
16. Abstract Results of acoustic tests of a 62.2 cm (24.5 inch) diameter model counterrotating Prop-Fan are presented. The model was tested as a tractor and a pusher downstream of a pylon, both at zero degrees and at four degrees angle-of-attack. The effects on noise of spacing between rotors and between the pylon and the rotors were also measured. Effects of rotor spacing were found to cause small changes in noise over the range of spacings tested. The presence of the pylon resulted in a 2 to 3 EPNdB increase in noise. Angle-of-attack effects showed an increase of 3 to 4 EPNdB for the tractor configuration and only about 1 EPNdB for the pusher configuration. Tip speed was found to be the strongest parameter in minimizing the noise. However, the decrease in noise with tip speeds below about 200 m/sec (650 ft/sec) became significantly smaller than at higher tip speeds. Unequal tip speeds showed small reductions in noise relative to equal tip speeds. Comparison of noise spectra between single rotation and counterrotating Prop-Fans showed that the counterrotating Prop-Fan has significantly higher levels of higher frequency noise which radiates in the forward direction. Correlation between measurements and predictions are discussed. Predictions were made of far-field noise during take-off and near-field noise during cruise.			
17. Key Words (Suggested by Author(s)) Fuel Conservation Advanced Turboprop Noise Propeller Noise Prop-Fan Noise			
		part. Date for general release: October, 1989	
19. Security Classif. (of this report) Unclassified	20. Security Classif. (of this page) Unclassified	21. No. of Pages	22. Price*